Investigations on the Pollutant Emissions of Gasoline Direct Injection Engines During Cold-Start

by

Juan Felipe Rodríguez

B.Sc., Mechanical Engineering, Universidad de los Andes (2006)
B.Sc., Mathematics, Universidad de los Andes (2008)
M.Sc., Automotive Engineering, RWTH Aachen University (2012)

Submitted to the Department of Mechanical Engineering
in partial fulfillment of the requirements for the degree of

Doctor of Philosophy in Mechanical Engineering

at the

MASSACHUSETTS INSTITUTE OF TECHNOLOGY

June 2016

Author .....
Department of Mechanical Engineering
May 18, 2016

Certified by .....
Wai K. Cheng
Professor of Mechanical Engineering
Thesis Supervisor

Accepted by .....
Rohan Abeyaratne, Quentin Berg Professor of Mechanics
Chairman, Department Committee on Graduate Students

Investigations on the Pollutant Emissions of Gasoline Direct Injection Engines During Cold-Start

by

Juan Felipe Rodríguez

Submitted to the Department of Mechanical Engineering
on May 18, 2016, in partial fulfillment of the
requirements for the degree of
Doctor of Philosophy in Mechanical Engineering

Abstract

As the CO_2 emission standards around the world become more stringent, the turbocharged downsized gasoline direct injection (GDI) engine provides a mature platform to achieve better fuel economy. For this reason, it is expected that the GDI engine will capture increasing shares of the market during the coming years. The in-cylinder liquid injection, though advantageous in most engine operation regimes, creates emissions challenges during the cold crank-start and cold fast-idle phases. The engine cold-start is responsible for a disproportionate share of the hydrocarbons (HC), nitrogen oxides (NOx) and particulate matter (PM) emitted over the certification cycle. Understanding the sources of the pollutants during this stage is necessary for the further market penetration of GDI under the constraint of tighter emission standards. This work aims to examine the formation processes of the HC, NOx and PM emissions during the cold-start phase in a GDI engine, and the sensitivity of the pollutant emissions to different operation strategies. To this end, a detailed analysis of the crank-start was carried out, in which the first three engine cycles were individually examined. For the steady-state phase, the trade-off between low fast-idle emissions and high exhaust thermal enthalpy flow, necessary for fast catalyst warm-up, is investigated under several operation strategies. The pollutant formation processes are strongly dependent on the mixture formation and on the temperature and pressure history of the combustion process. The results show that unconventional valve timing strategies with large, symmetric, negative valve overlap and delayed combustion phasing are the most effective ways to reduce engine-out emissions during both crank-start and fast-idle phases.

Thesis Supervisor: Wai K. Cheng
Title: Professor of Mechanical Engineering

Acknowledgements

The work contained in this document would have not been possible without the support of a significant number of people.

First of all, I would like to thank my advisor, Professor Wai Cheng, for providing his dedicated guidance and for giving me the opportunity and freedom to carry out my own ideas in the course of this research. I am also sincerely grateful to my doctoral committee, Professors John Heywood and Ahmed Ghoniem for their invaluable feedback and advice.

This research was supported by an industry Consortium on Engine and Fuels Research. I would like to extend my thanks to Thomas Leone from Ford; Richard Davis and Justin Ketterer from General Motors; Christopher Thomas and David Roth from BorgWarner; Kevin Freeman, Brian Hallgren, and Halim Santoso from Fiat Chrysler Automobiles, for their expert feedback during the many consortium meetings.

I would also like to thank the members of the Sloan Automotive Laboratory for their collaboration. I would like to especially express my gratitude to my lab mates Caroline Sorensen, Morgen Sullivan and Jake McKenzie, and to the lab staff members Thane DeWitt, Raymond Phan and Janet Maslow.

Thank you also to my friends in Boston for all the fun. A special thanks to my family for being my biggest source of inspiration and for encouraging me to keep moving forward.

I have been incredibly fortunate to count with the unconditional support and love of my wife, Silke. I cannot thank her enough for always being by my side throughout this adventure and for proof-reading the many versions of this document.

– Intentionally left blank –

Contents

List of Figures

List of Tables

Chapter 1

Introduction

In response to the growing concern over global warming and climate change, the greenhouse gases (GHG) emissions regulations around the world have become increasingly stringent. Figure 1-1 shows the history, enacted and proposed CO_2 emissions standards for light duty vehicles (LDV) in different parts of the world as they strive towards a goal of around 100 grams of CO_2 per kilometer during the next decade.

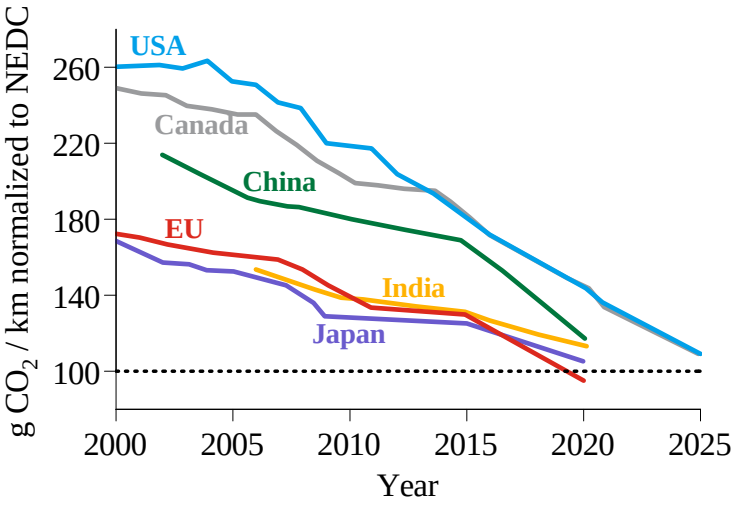

Figure 1-1: Light duty vehicles CO_2 emissions regulations around the world. Adapted from ICCT [23]

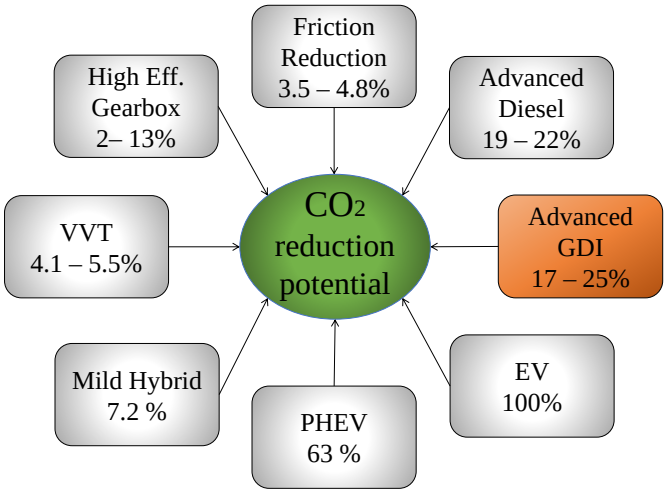

Figure 1-2: Potential for CO_2 reduction of different powertrain technologies [22]

The tightening of the fuel consumption standards, under the constrain of lower pollutant emissions, has been a driver for the adoption of new technologies during the past decade; among them gasoline direct injection (GDI) engines. According to the EPA and NHTSA estimates shown in Fig. 1-2 [22], downsized turbocharged GDI engines with cooled EGR have a potential for CO_2 emissions reduction between 17% and 25% compared to the 2008 PFI, naturally aspirated, gasoline engine used as a baseline. As this potential has been tapped during the past decade the market penetration of GDI engines has grown at an accelerated pace (see Fig. 1-3).

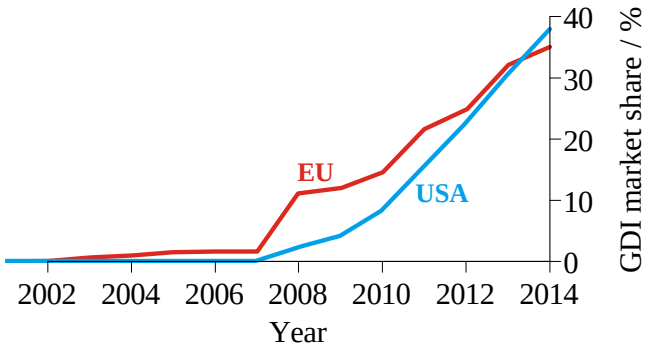

Figure 1-3: Market penetration of GDI engines in the US and the EU markets for the past decade. Data source: US [19]; EU [54]

GDI engines have better knock resistance through charge cooling, allow for aggressive scavenging to improve the low-end torque of turbo-charged engines – without the risk of short-circuiting fresh unburned mixture – and have extended lean operation limits with the associated reduction in pumping losses. On the other hand, the direct liquid injection poses some emissions challenges, especially for HC and PM during the cold-start phase.

The concern for pollutant emissions and air quality precedes the efforts undertaken to mitigate the GHG emissions of LDVs. Since the first binding emissions regulations were enacted, and came into force in 1994, the fleet average emissions standards of LDVs have been systematically tightened. Figure 1-4 shows the past, present and future federal limits for pollutant emissions that the fleets of LDV's manufacturers have to comply with. From 1994, and looking forward to 2026, the combined limit for NOx and HC emissions, which in combination are responsible for tropospheric ozone formation, will see a reduction of over 96%. Similarly, the maximum PM emissions, responsible for respiratory diseases, will reduce in 97% in the same time frame.

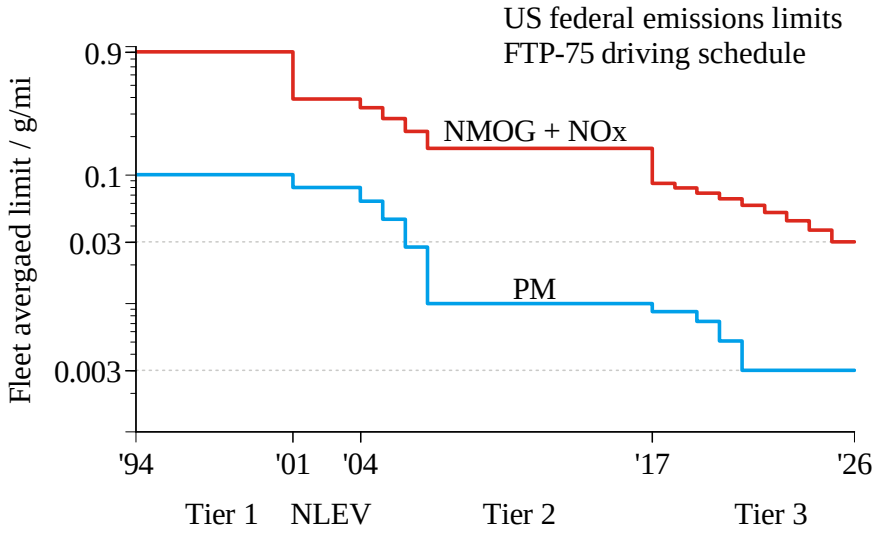

Figure 1-4: US federal fleet average emissions limits for light-duty vehicles over the FTP-75 driving schedule

Figure 1-5 shows the tailpipe NOx, HC, and PM emissions during the FTP-75 for two representative engines [1, 55]. In the representative case of Fig. 1-5, the cold-start phase is responsible for 58% of the NOx emissions, 79% of the HC emissions and 77% of the PM emissions.

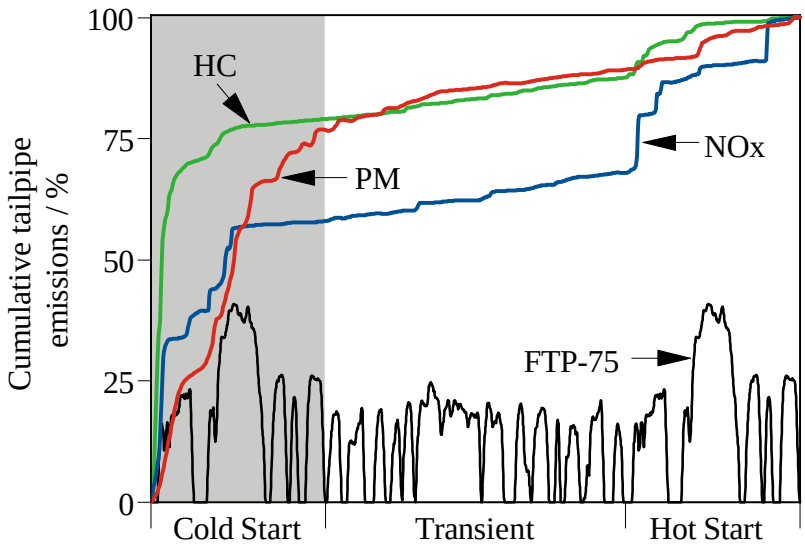

Figure 1-5: Relative cumulative tailpipe NOx, HC, and PM emissions over the FTP-75 cycle for gasoline engines. Data source: NOx and HC [1]; PM [55]

When looking deeper into the cold-start phase, it becomes evident that the engine crank-start contributes to a significant share of the cold-start emissions. Figure 1-6 shows the engine behavior during a typical cold crank-start of a GDI engine and the cumulative NOx, HC and PM emissions as a percentage of the maximum allowable emission limits for the U.S. standard T3B50/ULEV50, assuming the same HC/NOx ratio as the T2B5 standard. Prior to the 1st combustion cycle the engine is driven by the starter motor at approximately 280 *rpm*. After the 1st combustion event the engine speed increases rapidly and reaches its maximum, called speed flare, within 1 second. After the speed flare, the engine speed decreases to the targeted cold fast-idle speed. As can be seen from the cumulative engine out emissions from the example in Fig. 1-6, the engine cold crank-start is responsible for a disproportionate amount of

the cold-start phase emissions. During the initial 4 seconds (0.2% of the total FTP-75 driving schedule duration) 20 mg of NOx, 120 mg of HC and 6 mg of PM were emitted, corresponding to 9%, 36% and 17% of the overall T3B50 limit respectively. Although not regulated in the US, the European regulation limits the particulate number (PN) emissions. In this example, 2.7×10^{12} soot particles, corresponding to 40% of the Euro 6 limit, were emitted during cold crank-start.

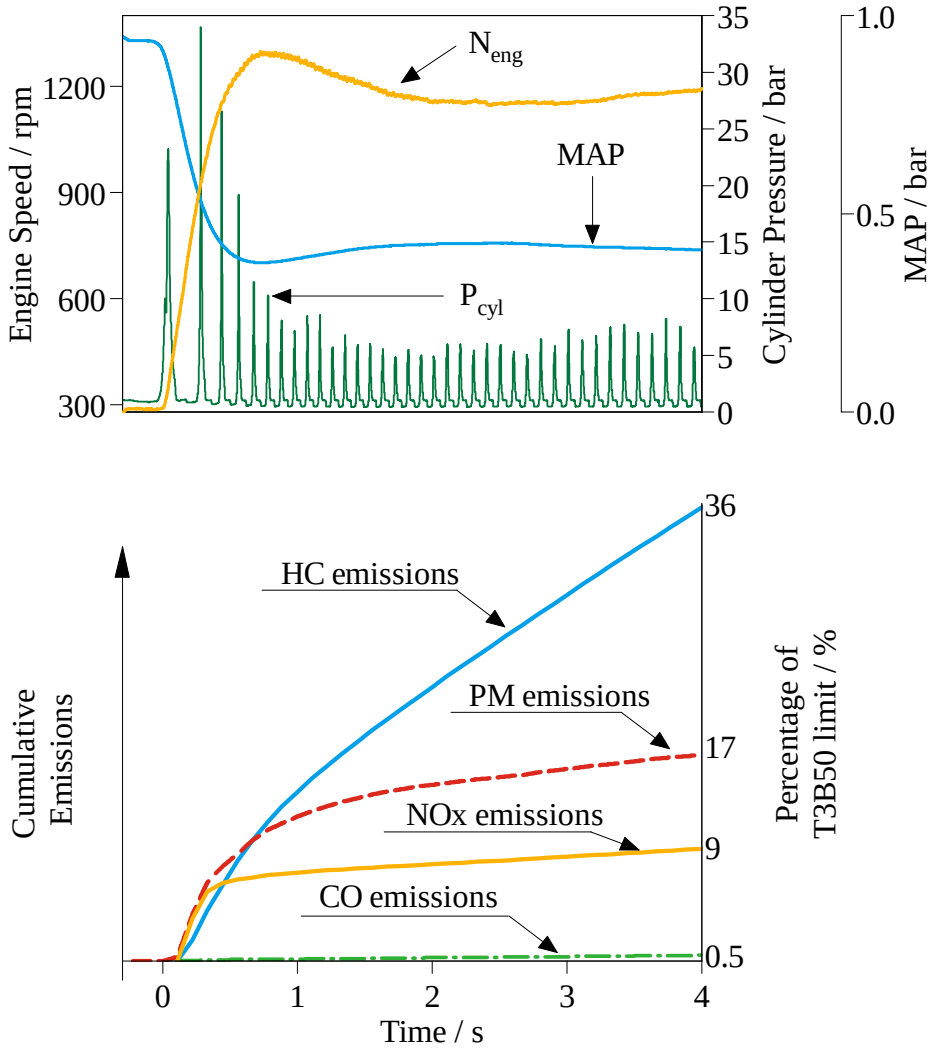

Figure 1-6: Cylinder pressure, engine speed, intake manifold pressure and cumulative emissions as percentage of the T3B50/ULEV50 limit during cold crank-start. The HC limit of T3B50 assumes the same HC/NOx ratio as the T2B5 standard

The cold cranking process has two distinctive characteristics compared to the rest of the certification cycle: Coldest cylinder wall temperatures and lowest engine speed. As a result, the fuel evaporation and mixture formation process are compromised and significant over-fueling is necessary to produce an ignitable fuel-air mixture.

Due to the increased penetration from the long injection events, a significant portion of the injected fuel lands on the cold combustion chamber surfaces. Since the combustion chamber walls are at a lower temperature than the saturation temperature of most of the species of the injected fuel; the result is the formation of fuel films which fail to evaporate completely prior to combustion. The fuel that does manage to evaporate from the spray and the films gives place to overly rich regions; these are partly responsible for the high levels of HC and PM/PN emissions during cold-start. Optical investigations conducted by Costanzo et al. [14] provide evidence of the significant role that these fuel films play on HC emissions and PM formation.

Additionally, the low temperature impacts negatively the classical HC emissions mechanisms identified by Cheng et al. [12]. Low temperature promotes the absorption of fuel into the oil layer prior to combustion. After combustion, the hot exhaust gases with low HC concentration favor the desorption of the fuel back into the bulk gases, providing an additional source for HC emissions. The low wall temperature also results in increased heat transfer away from the flame front during combustion causing a larger flame quenching distance, increasing the amount of fuel escaping combustion. Finally, the post-flame oxidation rates of the unburned HC and of the particles formed are reduced due to increased heat transfer to the cold cylinder walls.

The low cranking speed affects the charge motion. This leads to poor mixture formation, in the form of reduced evaporation of the fuel and reduced homogeneity of the charge. Additionally, the post-flame oxidation is affected by the mixing process of the unburned HC layer in the vicinity of the cylinder walls with the hot bulk gases. This mixing process scales with engine speed and is impacted during crank-start.

1.1 Previous work

The cold cranking process for GDI engines has been studied experimentally and numerically in the past. Fan et al. studied experimentally the effect of split injection on the combustion characteristics of the 1st cycle [24] and on the HC emissions behavior of the complete cranking process [25]. They identified a late intake stroke injection timing as optimal for minimizing HC emissions in their experimental setup, but provided no explanation on the reason behind it. Nevertheless, the study provides useful information for comparing trends in HC emissions as the injection timing is varied. Wiemer et al. [75] performed a similar study, including additionally the effects of fuel quantity and spark timing on the run-up speed trace and HC emissions. The study recognized that the injection and ignition timing during engine start-up must be adjusted individually for each combustion event as the engine speed increases. Furthermore, they found that the fuel quantity has a great influence on the starting behavior and HC emissions. Both studies propose fuel stratification as a possible solution for reducing HC emissions and fuel enrichment during the start-up process. However, none of them considers the impact of stratification on NOx or particulate emissions.

Whitaker et al. [74] studied in an optical engine, using laser induced fluorescence (LIF) and direct flame imaging, the effect of fuel pressure on PM emissions at cranking speed. The discussion provides a useful insight into the tradeoffs between increasing spray penetration and reduced droplet size as the fuel pressure is increased. The authors recommend the use of multiple injections to reduce spray penetration, while taking advantage of the smaller droplet size.

Using CFD analysis Kim et al [37] studied the air-fuel ratio (AFR) distribution during cranking at subzero conditions for different injection timings in a side mounted injector configuration. One of the key findings of this study is that, at cranking speed,

increased charge motion affects negatively the low AFR necessary around the spark plug for successful combustion. Since the direction of the tumble motion induced by the injection spray is opposite to the intake tumble, different combinations of intake valve opening and injection timing will result in different AFR around the spark plug, thus providing some light to explain the observations of the experimental studies presented above.

Similarly, Malaguti et al. performed numerical analysis for the initial combustion cycles, focusing on spray-wall interaction and its effect in fuel evaporation and liquid fuel film formation [52, 53]. They found that interaction between the intake valve and the injection spray results in the formation of fuel films in the cylinder head in the vicinity of the spark plug. Additionally, they found that fuel films on the combustion chamber walls are the main sources for fuel evaporation, and that the contribution from the flying fuel droplets evaporation is only relevant during the early compression stroke.

Xu et al. [78] went further in the CFD modeling of the cranking process, including engine run-up for different split injection strategies. The numerical results show that the optimum split injection strategy depends strongly on the engine speed, and therefore the injection strategy must be actively adjusted during the run-up process. In the same way as Malaguti et al. [52, 53], Xu et al. identified the importance of the rich cloud around the spark plug, and the ability of the fuel spray momentum to create flow structures that enable low AFR at the ignition point.

This paper also builds upon the methodology developed at the Sloan Automotive Laboratory at MIT for experimentally studying the 1st combustion cycle and the cranking process in port-fuel injected spark ignition engines. This previous work includes the use of fast FID and fast NDIR for HC, CO and CO_2 measurement, and of a fast response sampling system for the cycle resolved measurement of the exhaust composition [10, 11, 38, 45, 46, 65].

1.2 Project focus

This project is part of a wider effort undertaken at the Sloan Automotive Laboratory at the Massachusetts Institute of Technology to understand and mitigate the emissions challenges of gasoline direct injection engines, specifically during the cold-start phase [9, 15, 48, 57, 58, 72].

The goal of the present study is to gain a deeper understanding of the processes leading the formation of pollutants during the cold-start phase of a wall guided gasoline direct injection engine. To accomplish this, the engine-out NOx, HC and PM emissions are studied in detail for a variety of operation strategies during the cold crank-start and the cold fast-idle periods.

For the crank-start process, a special emphasis was placed on understanding the sensitivity of the mixture formation process, of the fuel pathway and of the NOx, HC, and PM emissions to the operation strategy of the individual combustion events during cranking. The effects of the heat transfer history and the residual fuel from previous injection events on the mixture formation process are also considered.

The investigations of the fast-idle period are focused on understanding and quantifying the different tradeoffs present between the engine-out emissions of pollutants, NOx, HC and PM, the combustion stability and the exhaust thermal enthalpy flow to the catalyst for several operation strategies.

An opportunity investigated in this work is the potential of unconventional valve timing, resulting in large negative valve overlap (NVO), for reducing the engine-out emissions during the cold crank-start and fast-idle phases of a GDI engine. As the authority of variable valve timing systems increases, new parked (de-energized) camshaft positions become possible. The merit of these parked positions for cold-start emissions control is studied in detail.

– Intentionally left blank –

Chapter 2

Methodology

This chapter provides a detailed description of the experimental and numerical methodology followed to quantify the engine-out emissions during the cold-start process and the energy release analysis during combustion. A special emphasis is placed on the challenges and solutions implemented for dealing with the highly transient processes taking place during engine crank-start.

2.1 Experimental setup

2.1.1 Engine base

The experiments were carried out using a commercial 4-cylinder GDI turbo-charged engine with a displacement volume of 499.5 cm^3 per cylinder, a square stroke ratio and a compression ratio of 9.2. The engine used side-mounted electromagnetic injectors, with a 52° cone angle, a 25° inclination from the horizontal and 6 holes. The engine also featured a centrally mounted spark plug and 4 valves per cylinder. The valve

timing corresponding to the stock parked position of the camshafts resulted in a negative valve overlap of 20°CA. The engine had variable valve timing (VVT) on both the intake and exhaust camshafts. The VVT system was hydraulically actuated, had an authority of 50°CA on each camshaft and allowed the advancing of the intake and the retarding of the exhaust timing. Further details are shown in Tables 2.1 and 2.2.

Engine type	In-line 4 cylinder
Displacement	1998 *cc*
Bore / Stroke	86/86 *mm*
Connecting rod	145.5 *mm*
Compression ratio	9.2 : 1
Injector type	Side mounted, 6-hole, electromagnetic
Spray cone angle	52°
Injector inclination	25°

Table 2.1: Specifications of the GM - LNF engine

Intake Valve Opening (IVO)	11°CA aTDC
Intake Valve Closing (IVC)	61°CA aBDC
Max. intake valve lift	10.3 *mm* @ 126°CA aTDC
Exhaust Valve Opening (EVO)	52°CA bBDC
Exhaust Valve Closing (EVC)	10°CA bTDC
Max. exhaust valve lift	10.3 *mm* @ 125°CA aTDC

Table 2.2: Stock parked valve timing. Valve events reported at 0.2 *mm* lift

The engine control is achieved by an in-house developed injection control software, allowing a full customization of the engine parameters such as injection and spark timings, injection duration, injection split ratio and intake/exhaust cam phasing. In actual GDI applications, typical fuel pressures for the initial injection events during crank-start ranges between 30 and 70 *bar* [4, 71] and is heavily dependent on engine speed. In the experimental setup used in this study, the fuel pressure was kept independent from engine operation and was maintained at a constant value by a hydro-pneumatic accumulator. Figure 2-1 shows further detail of the setup.

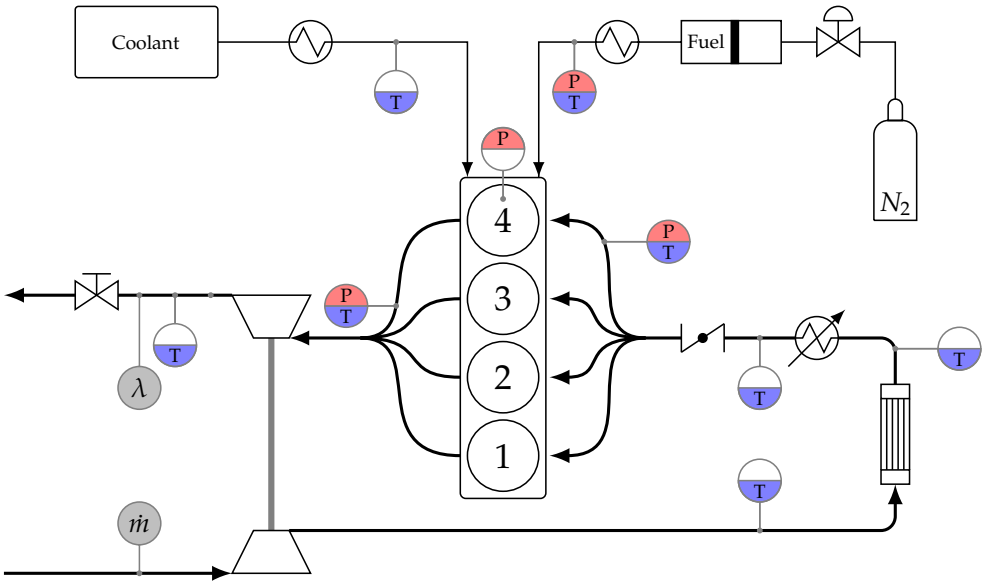

Figure 2-1: Diagram of the experimental setup and the sensor locations

The engine used a Tier II EEE certification gasoline produced by Haltermann Solutions (HF0437) with a carbon mass fraction of 86.5%, and 29% aromatics content. The fuel's RON and MON were 96.6 and 88.5 respectively. The Reid vapor pressure was 62.7 kPa with the distillation curve is shown in Fig. 2-2. The cold-start conditions were maintained as close to 20°C as possible by three independent chillers for the fuel, intake air, and engine oil and coolant.

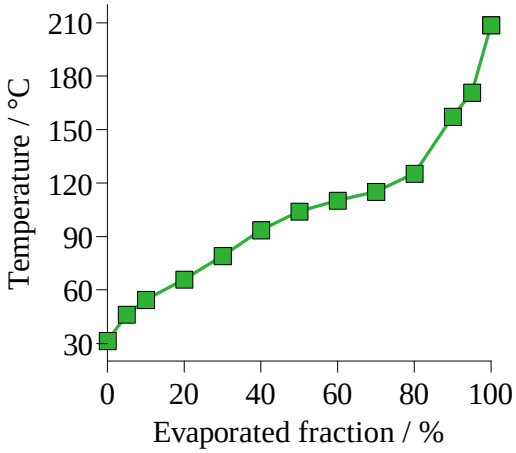

Figure 2-2: Distillation curve of the Tier II EEE certification gasoline used

2.1.2 Emissions measurement

The exhaust composition was measured using fast response analyzers from Cambustion. The wet HC mole fraction was measured using a fast flame ionization detector (FFID), model HFR400, with a response time t_{10-90} of 1 ms. The working principle of the FFID is based on the ionization of HC molecules under a hydrogen-air diffusion flame [13]. The carbon ion flow generated is attracted to the collector plate and an electrometer is used to measure the current, which is proportional to the number of carbon atoms present in the sample. Varying O_2 concentration in the sample creates difficulties for interpreting the output signal due to the competition between ion formation in the flame and their consumption by oxygen. To correct the measurements at lean operation, the change in sensitivity at different O_2 mole fractions was measured and it is shown in Fig. 2-3; the change in sensitivity is less than 5%.

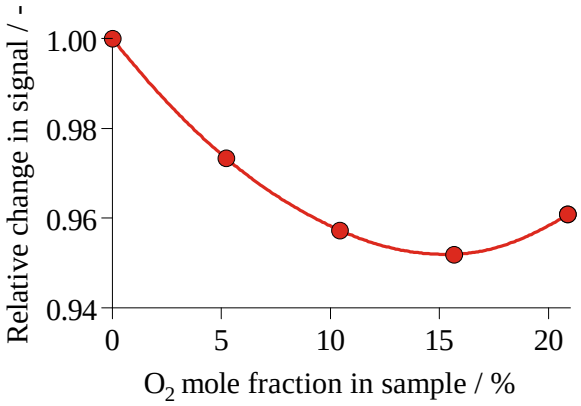

Figure 2-3: Effect of O_2 on FID. Measurement of 4500 ppm of C_3H_8; balance N_2

The CO and CO_2 wet mole fractions were measured with a fast non-dispersive infrared (NDIR) analyzer, model NDIR500, with a response time t_{10-90} of 8 ms. In NDIR sensors, a radiating IR source, usually an incandescent filament, is employed to emit a wide IR spectrum through the sensor's sample body. The amount of IR light absorbed at a certain wavelength is proportional to the concentration of the corresponding component. The light detector has a rotating filter in front of it that

eliminates all light at wavelengths other than the one being measured.

The NO wet mole fraction was measured with a fast chemiluminescence detector (CLD), model fNOx400, with a response time t_{10-90} of 4 ms. The CLD uses a discharge generator to produce ozone (O_3). In the reaction chamber, NO and O_3 react, to create form NO_2 in an electrically excited state. As the latter reverts to its ground state light is emitted and is caught by a photomultiplier detector. Since the analyzer does not measure NO_2 directly, a NO_2 to NOx ratio of 2% was assumed [30].

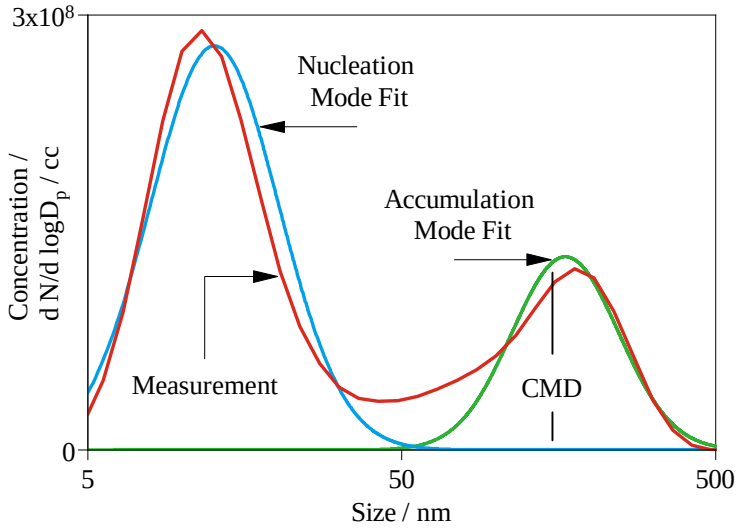

Figure 2-4: Example of particle distribution measurement for a GDI engine

The PM and PN concentrations were measured using a fast differential mobility analyzer (DMA), model DMS500, with a t_{10-90} of 300 ms. The DMS500 classifies particles in a discrete manner based on their electrical mobility, i.e. their drag to charge ratio. The particles in the sample flow through a unipolar corona discharge unit that puts a charge proportional to the surface area of the particles. The sample then flows into the classifier chamber, where it is subjected to an electric field of several kV. Depending on their electrical mobility diameter, particles in the $5 - 1000$ nm range are detected at different positions by 22 separate electrometers. A typical particle concentration vs. size spectrum is shown in Fig. 2-4. The discrete measurement is

fitted by two lognormal distributions, corresponding to the nucleation mode and to the accumulation mode. Since the European Particle Measurement Program (PMP) requires the removal of the volatile fraction, and given the low contribution of volatile particles to PM, the metric of interest is the accumulation mode. In addition the sampling temperature was kept at 150°C to prevent volatiles from condensing on the accumulation mode particles.

The number of particles per standard cubic centimeter ($\#/scc$) can be found by integrating the lognormal distribution for the accumulation mode. The volume concentration of the number of particles, $\hat{N}$ is:

$$\hat{N}\left[\frac{\#}{scc}\right] = \int_{5\ nm}^{1000\ nm} \frac{d\,N}{d\,log(D_p)} d\,log(D_p) \tag{2.1}$$

Where D_p is the particle size and $dN/dlog(D_p)$ is the particle concentration number for a the size range represented by D_p. The calculation of the mass concentration from the size spectrum measurement requires additional consideration of the morphology of the soot particles and of their specific gravity. The volume is proportional to D_p^k, where $k = 3$ is the recommended fractal dimension for GDI engines. In other words, spherical particles are assumed with a specific gravity of 1. The volume concentration of the particle mass, $\hat{M}$ is:

$$\hat{M}\left[\frac{\mu g}{scc}\right] = \int_{5\ nm}^{1000\ nm} \frac{d\,N}{d\,log(D_p)} \cdot (5.20 \times 10^{-16} \cdot Dp^3) \cdot d\,log(D_p) \tag{2.2}$$

2.1.3 Measurement of cylinder pressure

The in-cylinder pressure is measured with a high-temperature piezoelectric pressure transducer, Kistler 6125A, mounted in the cylinder head between the intake and

exhaust valves and approximately 2 cm from the cylinder wall. The charge output of the pressure sensors was amplified and converted to an analog signal using a charge amplifier, Kistler 5010b. Due to the operation principle of the metaloxidesemiconductor field-effect transistor (MOSFET) used for the charge amplifying, the signal exhibits a long-term drift at an approximate rate of 0.03 pC/s [43].

At steady-state operation the cylinder pressure can be corrected by referencing, or pegging, the pressure sensor output to a known absolute pressure level. The intake manifold absolute pressure sensor was used for this end. The pegging of the signals was done at the beginning of the compression stroke, where, due to the low piston and flow speeds, the intake manifold and the cylinder contents are in mechanical equilibrium [18].

During crank-start, an additional source of error for the measurement of the in-cylinder pressure becomes relevant. The large temperature variation during the 1^{st} combustion event during crank-start results in a large heat flux into the pressure transducer originating thermal stresses in the piezoelectric crystal; this short-term drift phenomenon is called thermal shock [59]. Despite the use of a flame arrestor on the face of the pressure sensor, the thermal shock cannot be entirely eliminated during crank-start due to the cold initial temperature of the transducer. The presence of short-term drift requires a more sophisticated pegging routine during crank-start.

The pegging approach used follows the method developed by Bertola et al. [2] for short-term drift correction. The method uses two pegging points, at the end of each of two intake strokes using the MAP sensor as a reference. Within the cycle, the pressure offset is determined by a linear interpolation between the two pegging points up to the middle of the exhaust process. From there on, till the end of the cycle, the offset is constant. This method was validated by Bertola et al. [2] for a wide range of crank-start experiments.

2.2 Mole fraction to mass conversion

2.2.1 Exhaust Mass Flow Rate Model

In order to quantify the pollutant emissions during the crank-start process it is necessary to relate the mole fraction measurements of the different species in the burned gas to the mass flow rates of the exhaust stroke. The slow response of gas flow meters make them unsuitable for the cycle-resolved analysis sought in this work. Therefore, a computational approach was used to model the exhaust mass flow rate using the cylinder pressure data and piston position as the model inputs. Given the variety of combustion events that take place during the highly transient engine crank-start, two different modeling approaches were undertaken.

The first approach follows the method described by Castaing et al. [6]. Under the assumption of ideal gas and of an isentropic gas exchange the constitutive relation for ideal gases is used as a starting point, and its time derivative is taken. This approach disregards the discharge phenomenon occurring at the exhaust valve, and focuses only on the in-cylinder gas as a whole. The following relation is obtained.

$$\frac{dp}{dt} \cdot V + p \cdot \frac{dV}{dt} = R \cdot \left(\frac{dm}{dt} \cdot T + m \cdot \frac{dT}{dt} \right) \tag{2.3}$$

Similarly, taking the relation for an isentropic process $P^{1-\gamma} \cdot T^{\gamma} = Const.$, where γ is the heat capacity ratio, and differentiating it with respect to time, the following relation is obtained.

$$\frac{\gamma - 1}{\gamma} \cdot \frac{1}{p} \cdot \frac{dp}{dt} = \frac{1}{T} \cdot \frac{dT}{dt} \tag{2.4}$$

Combining Eqs. 2.3 and 2.4 into a single equation and rearranging its terms relates the in-cylinder mass and its change with respect to time with the measured in-cylinder

pressure and volume and their respective time derivatives.

$$\frac{1}{\gamma \cdot p} \cdot \frac{dp}{dt} + \frac{1}{V} \cdot \frac{dV}{dt} = \frac{1}{m} \cdot \frac{dm}{dt} \tag{2.5}$$

To find the exhaust mass flow, Eq. 2.5 can be numerically integrated in time between EVO and EVC, taking the cylinder mass at EVO to be the air mass at IVC plus the amount of injected fuel. The air mass at IVC can be determined using the constitutive relation for the ideal gas, and assuming that the cylinder temperature matches the intake temperature. The equation for the exhaust mass flow rate is then:

$$\frac{dm_{exh}}{dt} = -\left(\frac{1}{\gamma \cdot p} \cdot \frac{dp}{dt} + \frac{1}{V} \cdot \frac{dV}{dt}\right) \cdot m \tag{2.6}$$

The second approach follows the method proposed by Lee [48]. The instantaneous mass flow rate through the exhaust valve is calculated from the equation for compressible flow through a flow restriction. The one-dimensional analysis assumes a quasi-steady, isentropic flow of an ideal gas and accounts for the real flow effects through the use of a discharge coefficient. The exhaust mass flow is defined in Eq. 2.7 using the throat area (A), flow velocity (v), and gas density (ρ).

$$\frac{dm}{dt} = \rho \cdot A \cdot v \tag{2.7}$$

The flow velocity and the gas density are related by the stagnation temperature (T_0), defined in Eq. 2.8. The flow temperature and the stagnation temperature are also related by the isentropic expansion process, Eq. 2.9, where T_0 and p_0 are the stagnation temperature and pressure respectively.

$$T_0 = T + \frac{v^2}{2 \cdot C_p} \tag{2.8}$$

$$\frac{T}{T_0} = \left(\frac{p}{p_0}\right)^{(\gamma-1)/\gamma} \tag{2.9}$$

Combining Eqs. 2.7, 2.8, and 2.9, the following relation for the isentropic mass flow rate is obtained:

$$\frac{dm}{dt} = \frac{A \cdot p_0}{\sqrt{R \cdot T_0}} \cdot \left\{ \frac{2 \cdot \gamma}{\gamma - 1} \cdot \left[1 - \left(\frac{p}{p_0}\right)^{(\gamma-1)/\gamma} \right] \right\}^{1/2} \tag{2.10}$$

For application of Eq. 2.10 to the gas exchange process in the combustion engine, an additional discharge coefficient C_D is introduced, which corrects the ideal isentropic flow to real gas flow. Additionally, due to the high in-cylinder pressures at EVO, it in necessary to consider choked flow, that is when the throat velocity matches the speed of sound (Eq. 2.11). This occurs at a certain pressure ratio across the throat, after which, any further increase in the stagnation pressure does not result in an increase of the gas velocity, and the increase on mass flow is only due to the higher gas density.

$$\frac{p}{p_0} = \begin{cases} \frac{p}{p_0} & \text{if } \frac{p}{p_0} > \left(\frac{2}{\gamma+1}\right)^{\gamma/(\gamma-1)} \\ \left(\frac{2}{\gamma+1}\right)^{\gamma/(\gamma-1)} & \text{if } \frac{p}{p_0} \leq \left(\frac{2}{\gamma+1}\right)^{\gamma/(\gamma-1)} \end{cases} \tag{2.11}$$

For the application during the exhaust process, two situations need to be considered, positive and reverse flow. For positive flow the stagnation pressure corresponds to the cylinder pressure and the throat pressure to the exhaust pressure. For reverse flow, the sign of the mass flow changes and the reverse selection of stagnation and throat pressures needs to be made.

Positive flow:

$$\frac{dm_{exh}}{dt} = \frac{C_{D,f} \cdot A_{curtain} \cdot p}{\sqrt{R \cdot T_0}} \cdot \left\{ \frac{2 \cdot \gamma}{\gamma - 1} \cdot \left[1 - \left(\frac{p_{exh}}{p}\right)^{(\gamma-1)/\gamma} \right] \right\}^{1/2} \tag{2.12}$$

Reverse flow:

$$\frac{dm_{exh}}{dt} = -\frac{C_{D,r} \cdot A_{curtain} \cdot p_{exh}}{\sqrt{R \cdot T_0}} \cdot \left\{ \frac{2 \cdot \gamma}{\gamma - 1} \cdot \left[1 - \left(\frac{p}{p_{exh}} \right)^{(\gamma-1)/\gamma} \right] \right\}^{1/2} \tag{2.13}$$

Both approaches were implemented and compared against the simulation results of commercial engine simulation packages. The first approach, described by Eq. 2.6, proved to be less sensitive to noise from the cylinder pressure signal than the second approach, described by Eqs. 2.12 and 2.13. It was also found that in the case of late combustion, the use of the first approach predicts a reverse flow at the beginning of the exhaust process. This contradicts what happens in the real flow, where a blow-down takes place when the exhaust valve is opened. This phenomenon is due to the cylinder pressure increase from the late ongoing combustion, which is accounted for by the first approach as a flow into the cylinder. Since the in-cylinder entropy is still increasing due to the ongoing combustion, the process cannot be modeled as isentropic and the first approach is not applicable. The exhaust mass flow rate model used in this work incorporates the robustness of the first approach and uses the second approach for the initial blow-down of the exhaust in the case of late combustion.

2.2.2 Transit and response delay correction

For the correct synchronization of the mole fraction measurements from the fast response analyzers with the modeled exhaust mass flow rate it is necessary to account for the transit time of the burned gas from the exhaust valve to the sampling point and for the intrinsic response time of the analyzer. Since the response and transit times are in the same order of magnitude, the latter cannot be neglected. The response time is a function of the internal flow of the analyzer and is assumed to be constant. The transit time is a function of the sampling position downstream in the exhaust runner, of the instantaneous exhaust mass flow rate, and of the exhaust gas density.

The transit time, τ_t, can be related to the distance between the tip of the sample probe and the exhaust valve, x_{probe}, by the following equation:

$$x_{probe} = \int_{t}^{t+\tau_t} v_{exh}(\xi) d\xi \tag{2.14}$$

Where the exhaust velocity, v_{exh} is calculated from the exhaust mass flow model. The exhaust gas density, ρ_{exh}, can be determined using the ideal gas constitutive relation using the cylinder temperature.

$$v_{exh}(t) = \frac{1}{A_{port} \cdot \rho_{exh}} \cdot \frac{dm_{exh}}{dt}(t) \tag{2.15}$$

Since the distance between the tip of sample probe and the exhaust valve is a known quantity, the numerical integration of Eq. 2.14 provides a method for estimating the transit time. The transport and response delay corrections can be lumped into a single term $\tau(t)$:

$$\tau(t) = \tau_t(t) + \tau_r \tag{2.16}$$

Where τ_t and τ_r are the transit time and response time respectively. The cycle mass emissions of the species k can be found by integrating the product of the species k mole fraction, $\hat{x}_k$ offset by τ, with the corresponding molecular weight ratio and the exhaust mass flow rate:

$$m_{k,cycle} = \int_{t_{EVO}}^{t_{EVC}} \hat{x}_k(t + \tau(t)) \cdot \frac{M_k}{M_{exh}} \frac{dm_{exh}}{dt} dt \tag{2.17}$$

Integrating the product of particle number and mass concentration, with the standard volumetric exhaust flow calculated based on the exhaust mass flow model and the exhaust gas density at 20°C and 1 atm, gives the total number of particles and particle mass,

$$N = \int_{t_{EVO}}^{t_{EVC}} \hat{N}(t + \tau(t)) \cdot \frac{d\,V_{exh,std}}{dt} dt \tag{2.18}$$

$$M = \int_{t_{EVO}}^{t_{EVC}} \hat{M}(t + \tau(t)) \cdot \frac{d\,V_{exh,std}}{dt} dt \tag{2.19}$$

where $\hat{N}$ and $\hat{M}$ are the particulate number and mass concentration respectively.

2.3 Lambda calculation from exhaust measurements

Based on the mole fraction measurements in the exhaust gases, the air-fuel ratio (AFR) of the combustion process can be determined. By balancing the combustion reaction, the number of moles of air per mole of fuel can be calculated. The approach used here is similar to the one developed by Silvis [68, 69]. However, the approach differs slightly given that the fast-response analyzers used in this study perform wet measurements. The general combustion reaction can be written as follows,

$$\begin{aligned} &\mathrm{C}_x\mathrm{H}_y\mathrm{O}_z + n(\mathrm{O}_2 + \alpha\mathrm{N}_2 + \beta\mathrm{CO}_2 + \chi\mathrm{H}_2\mathrm{O}) \longrightarrow \\ &\qquad a\mathrm{CO}_2 + b\mathrm{CO} + c\mathrm{H}_2 + d\mathrm{H}_2\mathrm{O} + e\mathrm{O}_2 + f\mathrm{N}_2 + g\mathrm{NOx} + h\mathrm{C}_x\mathrm{H}_y\mathrm{O}_z \end{aligned} \tag{2.20}$$

where $\alpha = 3.773$ and $\beta = 0.0018$ corresponding to a 380 ppm CO_2 mole fraction. The fuel molecule can be thought of as consisting of a single carbon atom, $x = 1$, $y = \mathrm{H/C}$, $z = \mathrm{O/C}$, where the y and z are determined by the fuel properties. The NOx mole fraction is assumed to have a negligible impact on the AFR calculation and its coefficient is set to zero, i.e. $g = 0$. Considering the total number of moles in the exhaust per input mole of fuel, n_{tot}, as an additional variable, there are a total of 10 unknowns. To solve the system, the following 10 equations (Eqs. 2.21 to 2.31) are used to determine λ from the CO_2, CO and HC measurements.

C balance:

$$x + n \cdot \beta = a + b + h \cdot x \tag{2.21}$$

H balance:

$$y + 2n \cdot \chi = 2c + 2d + y \cdot h \tag{2.22}$$

O balance:

$$z + 2n + 2n \cdot \beta + n \cdot \chi = 2a + b + d + 2e + z \cdot h \tag{2.23}$$

N balance:

$$n \cdot \alpha = f \tag{2.24}$$

Total moles:

$$n_{tot} = a + b + c + d + e + f + h \tag{2.25}$$

CO_2 from measurements:

$$a = n_{tot} \cdot \hat{x}_{\mathrm{CO_2}} \tag{2.26}$$

CO from measurements:

$$b = n_{tot} \cdot \hat{x}_{\mathrm{CO}} \tag{2.27}$$

HC from measurements:

$$h = n_{tot} \cdot \hat{x}_{\mathrm{HC}} \tag{2.28}$$

From the water-gas shift reaction (WGSR) equilibrium ($K_{WGSR} = 3.5$, [70]):

$$b\mathrm{CO} + d\mathrm{H_2O} \longrightarrow a\mathrm{CO_2} + c\mathrm{H_2} \tag{2.29}$$

$$\frac{b \cdot d}{a \cdot c} = K_{WGSR} \tag{2.30}$$

The molar water content in air due to humidity can be calculated as:

$$\chi = (1+\alpha+\beta+\chi)\cdot\frac{M_{air}}{M_{H_2O}}\cdot\frac{H_{abs}}{1000} = \frac{1+\alpha+\beta}{\frac{M_{H_2O}}{M_{air}\cdot H_{abs}}-1} \tag{2.31}$$

The absolute humidity has units of g/kg and is calculated based on the measured relative humidity (RH) and the procedure described in the Guide to Meteorological Instruments and Methods of Observation [76].

The introduction of Eq. 2.30 results in a non-linear system. For its solution an iterative method is used, requiring explicit expressions for all of the unknowns. This expressions already exist for χ, a, b, f and h. For the remaining variables, the equations system is algebraically manipulated to obtain explicit expressions for c, d, e, n and n_{tot}. From the WGSR equilibrium constant, Eq. 2.30, and the hydrogen balance equation, Eq. 2.22, expressions for c and d are obtained:

$$c = \frac{2n\cdot\chi + y\cdot(1-h)}{2} - d \tag{2.32}$$

$$d = \left(\frac{2n\cdot\chi + y\cdot(1-h)}{2}\right)\left(\frac{b}{a\cdot K_{WGSR}}+1\right)^{-1} \tag{2.33}$$

Combining the total moles equation, Eq. 2.25, and the nitrogen balance equation, Eq. 2.24, an expression for e is obtained:

$$e = \left(n_{tot}-a-b-c-d-h-\frac{2a+b+d+z\cdot(h-1)}{2+2\beta+\chi}\cdot\alpha\right)\left(1+\frac{2\alpha}{2+2\beta+\chi}\right)^{-1} \tag{2.34}$$

Reorganizing the carbon balance equation, Eq. 2.21, yields an expression for n_{tot}:

$$n_{tot} = \frac{x+n\cdot\beta}{\tilde{x}_{CO_2}+\tilde{x}_{CO}+\tilde{x}_{HC_{C1}}} \tag{2.35}$$

From the O balance equation, Eq. 2.23, the number of O_2 moles n, can be solved:

$$n = \frac{2a + b + d + 2e + z \cdot (h - 1)}{2 + 2\beta + \chi} \tag{2.36}$$

With an initial guess of $n = 1$, it takes just a few iterations to achieve a convergence interval of less than 0.1% for n. Since the stoichiometric O_2 requirement, $n_{stoich.}$, for complete combustion is known and equals $x + y/4 - z/2$, lambda can be easily calculated as $\lambda = n/n_{stoich.}$.

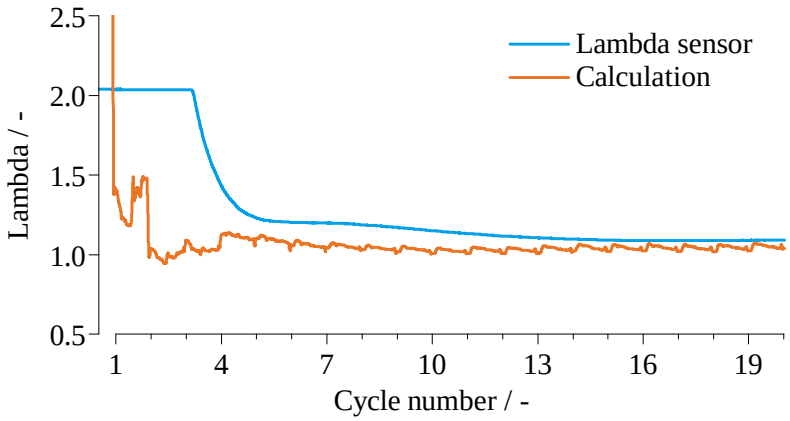

Figure 2-5: Calculated and measured λ during crank-start

The calculation of the AFR by means of the exhaust emissions measurements with fast analyzers provides certain advantages over the direct measurement of the AFR with a lambda sensor for crank start studies. First, the response time of a fully warmed-up lambda sensor is on the order of 100 ms, that is, significantly slower than the response time of the fast analyzers. Second, the lambda sensor is placed sufficiently downstream of the exhaust line to allow for a correct temperature of operation and to allow exhaust sampling from all cylinders, making it unsuitable for cycle-resolved analysis of the crank-start process. Finally, the high HC emissions during crank-start affect the characteristics of the diffusion layer of the oxygen sensor, causing a lean shift in the measurement [5]. A typical trace for the calculated and measured λ during the crank-start process can be seen in Fig. 2-5.

2.4 Energy Conversion Analysis

2.4.1 Energy accounting from mole fraction measurements

The fraction of the fuel energy released in the combustion process can be estimated from the mole fractions of carbon-containing species in the burned gases. The CO_2 and CO content in the exhaust are direct measures of how much fuel carbon was converted, and therefore how much energy was released. The calculation for the heat release, Q_b, is shown in Eq. 2.37 for the case of complete fuel oxidation,

$$Q_b = LHV_{fuel} \cdot M_{CH_y} \cdot n_{CH_y,\,b} = LHV_{fuel} \cdot M_{CH_y} \cdot n_{CO_2} \tag{2.37}$$

where M_{CH_y} is the molecular weight of the hydrocarbon CH_y ($y = 1.86$ for the certification fuel used in this study) and $n_{CH_y,\,b}$ is the moles of fuel burned. In the case of incomplete combustion, the chemical energy still contained in the exhaust gas needs to be accounted for by means of the combustion inefficiency.

$$Q_b = \eta_c \cdot (LHV_{fuel} \cdot M_{CH_y} \cdot n_{CH_y,\,b}) \tag{2.38}$$

$$= LHV_{fuel} \cdot M_{CH_y} \cdot n_{CH_y,\,b} - LHV_{CO} \cdot M_{CO} \cdot n_{CO} - LHV_{H_2} \cdot M_{H_2} \cdot n_{H_2} \tag{2.39}$$

In this case, the number of moles of fuel participating in combustion, $n_{CH_y,\,b}$, can be calculated as the sum of the CO_2 and CO moles.

$$n_{CH_y,\,b} = n_{CO_2} + n_{CO} \tag{2.40}$$

The number of moles of H_2 can be related to the CO_2 and CO content via the equilibrium constant for the water-gas shift reaction. For engine combustion, Spindt [70] suggested a value of 3.5 for the equilibrium constant in his 1965 paper.

$$\frac{n_{\mathrm{CO}} \cdot n_{\mathrm{H_2O}}}{n_{\mathrm{CO_2}} \cdot n_{\mathrm{H_2}}} = K_{WGSR} \tag{2.41}$$

The hydrogen mole balance provides the remaining piece of information to relate the CO_2 and CO content to the amount of H_2 present in the burned gases.

$$y \cdot n_{\mathrm{CH}_y,\, b} = y \cdot (n_{\mathrm{CO_2}} + n_{\mathrm{CO}}) = 2 \cdot n_{\mathrm{H_2O}} + 2 \cdot n_{\mathrm{H_2}} \tag{2.42}$$

Combining Eqs. 2.41 and 2.42 gives:

$$n_{\mathrm{H_2}} = \frac{y}{2} \cdot \frac{(n_{\mathrm{CO_2}} + n_{\mathrm{CO}}) \cdot n_{\mathrm{CO}}}{K \cdot n_{\mathrm{CO_2}} + n_{\mathrm{CO}}} \tag{2.43}$$

For a 1$^{\mathrm{st}}$ cycle analysis, care must be taken to include the residual gases, with its respective CO_2, CO and H_2 content as part of the products. For the subsequent cycles, the residual gas fraction before and after combustion are similar, and therefore it is not necessary to account them as product of the combustion. For a 1$^{\mathrm{st}}$ cycle analysis:

$$n_i = n_{i,\, Exh} + n_{i,\, Res} \tag{2.44}$$

$$n_{i,\, Res} = \left(\hat{x}_i \cdot \frac{p \cdot V}{R_u \cdot T} \right) \Bigg|_{EVC} \tag{2.45}$$

2.4.2 Heat release rate analysis

A first law analysis based on the in-cylinder pressure measurement provides crank-angle resolved data on the heat release of the combustion process. Assuming a closed system, the first law can be expressed as shown in Eq. 2.46,

$$\delta Q_b = dU + \delta W + \delta Q_{wall} \tag{2.46}$$

where δQ_b is the incremental heat release, dU represents the change in internal energy of the cylinder content, δW is the change in work and δQ_{wall} is the heat transfer to the combustion chamber walls. The work term is calculated from the cylinder pressure and the piston position:

$$\delta W = p \cdot dV \tag{2.47}$$

Under the ideal gas assumption, the change in internal energy of the closed system can be expressed using only the pressure and volume data (Eq. 2.48). Upon substitution, Eq. 2.46 transforms into Eq. 2.49,

$$dU = m \cdot c_v \cdot dT = \frac{pV}{R} \cdot c_v \cdot \frac{dT}{T} = \frac{pV}{R} \cdot c_v \cdot (\frac{dp}{p} + \frac{dV}{V}) \tag{2.48}$$

$$\delta Q_b = \frac{pV}{R} \cdot c_v \cdot (\frac{dp}{p} + \frac{dV}{V}) + p \cdot dV = \frac{c_v}{R} \cdot V \cdot dp + \frac{c_v + R}{R} \cdot p \cdot dV + \delta Q_{wall} \tag{2.49}$$

where c_v and R are the constant volume heat capacity of the gas and the ideal gas constant respectively. Following an approach similar to Gatowski et al. [26], the expression above can be manipulated algebraically to express the heat release rate as a function of the pressure, volume, and their time derivatives;

$$\frac{dQ_b}{dt} = \frac{1}{\gamma - 1} \cdot V \cdot \frac{dp}{dt} + \frac{\gamma}{\gamma - 1} \cdot p \cdot \frac{dV}{dt} + \frac{dQ_{wall}}{dt} \tag{2.50}$$

where γ is the heat capacity ratio c_p/c_v. For the calculation of the total heat release, Eq. 2.50 can be integrated from the start of combustion (SoC) until the opening of the exhaust valve, i.e. when the system stops being closed.

$$Q_b = m_{\mathrm{CH}_y,\, b} \cdot LHV_{fuel} = \int_{t_{SoC}}^{t_{EVO}} \left(\frac{1}{\gamma - 1} \cdot V \cdot \frac{dp}{dt} + \frac{\gamma}{\gamma - 1} \cdot p \cdot \frac{dV}{dt} + \frac{dQ_{wall}}{dt} \right) dt \tag{2.51}$$

The final task is to estimate the heat capacity ratio γ and the heat transfer rate to the combustion chamber walls. The correlation used for estimating of the heat capacity ratio as a function of temperature for gasoline mixtures was proposed by Brunt et al. [3] as;

$$\gamma = 1.338 - 6.0 \times 10^{-5} \cdot T + 1.0 \times 10^{-8} \cdot T^2 \tag{2.52}$$

where T is the charge temperature in K estimated from the pressure and volume data. The heat transfer rate was estimated using Woschni's approach [77] for the calculation of the heat transfer coefficient h. The model is shown in Eq. 2.53.

$$h = 0.013 \cdot d^{-0.2} \cdot p^{0.8} \cdot T^{-0.53} \cdot w^{0.8} \tag{2.53}$$

In Eq. 2.53, w is an estimate of heat-transfer-relevant gas speed as a function of engine speed and the cylinder pressure, is defined as follows:

$$w = C_1 \cdot c_m + C_2 \cdot \frac{V_d \cdot T_{IVC}}{p_{IVC} \cdot V_{IVC}} \cdot (p - p_{mot}) \tag{2.54}$$

with the mean piston speed c_m in $\frac{m}{s}$ calculated as a function of the engine speed and stroke. Woschni proposed for gasoline engines that $C_1 = 2.28$ for compression and expansion strokes and $C_2 = 3.24 \times 10^{-3} \frac{m}{sec \cdot K}$.

Lejsek et al. [49] showed that the Woschni model results in a overestimation of the wall heat flux at the low engine speeds observed during crank-start. Therefore, they proposed and validated a correction for the effective gas velocity w (Eq. 2.55) for low engine speeds between $150 - 1000\ rpm$. G_{start} and B_{start} are defined in Eq. 2.56.

$$w = G_{start} \cdot C_1 \cdot c_m + B_{start} \cdot C_2 \cdot \frac{V_d \cdot T_{IVC}}{p_{IVC} \cdot V_{IVC}} \cdot (p - p_{mot}) \tag{2.55}$$

$$G_{start} = 2.14 - 0.795 \cdot c_{m,k} + \frac{293.15}{T_{wall}} \quad \text{and} \quad B_{start} = \frac{1}{4} \cdot (\frac{V_c}{V})^{1/3} \tag{2.56}$$

Where $c_{m,k}$ is the mean piston speed during the compression stroke, and V_c is the clearance volume. Having estimated the heat transfer coefficient, the heat transfer rate can be calculated as a function of the exposed cylinder surface area A_{cyl}, the charge temperature T and the wall temperature T_{wall}.

$$\frac{dQ_{wall}}{dt} = A_{cyl}(t) \cdot h(t) \cdot \big(T(t) - T_{wall}\big) \tag{2.57}$$

Figure 2-6 shows the correlation between the two energy accounting methods developed in this section for a variety of operating conditions during the 1st cycle.

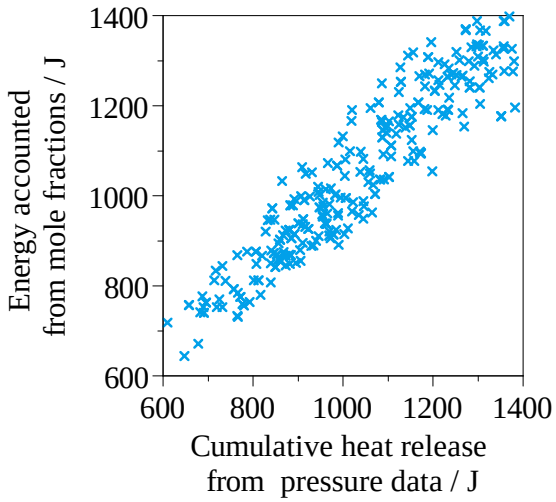

Figure 2-6: Correlation between the energy accounting methods of Section 2.4

– Intentionally left blank –

Chapter 3

Fuel accounting for the first cycle

As a part of the systematic study of the emissions in the cold-start processes of a GDI engine, this chapter deals with the fuel carbon pathway in the 1st cycle of the cold crank-start process. Since the associated particulate emissions are negligibly small in terms of the fuel carbon mass, they are not included in the following analysis. The topic of particle emissions during the 1st cycle is addressed in Chapter 4. A carbon accounting analysis is used to deconstruct the amounts of fuel participating in combustion, being exhausted as HC emissions, staying in the combustion chamber for the 2nd combustion event, and being absorbed by the oil or lost through blow-by. The engine is fired for a single cycle in one cylinder at cold start condition (20°C). The fuel carbon is accounted from CO_2, CO, and HC measurements using fast response analyzers. The parameters studied are the fuel enrichment, the injection and ignition timing, the intake and fuel pressures, and the cranking speed. Substantial fuel enrichment is needed to produce stable combustion in the 1st cycle. A share of the fuel is available for the 2nd cycle and a share goes into the oil and crank case.

Part of the results presented in this chapter have been published in the *International Journal of Engine Research* [61].

3.1 Experiments description

The engine crank-start is a highly transient process, with engine speed variations of up to 200 *rpm* within a combustion cycle. The sequence of events depends heavily on the 1st combustion event. Therefore, as an initial step to fully understand the cold-cranking emissions, the fuel pathway of 1st firing cycle is examined in detail.

To recreate the cold-start conditions, the engine coolant, engine oil, fuel, and intake air temperatures were kept at 20°C. The temperatures of the engine components under steady-state motoring at 280 *rpm* were simulated using a commercially available software; the piston temperature distribution is shown in Fig. 3-1. The cylinder liner temperature stabilizes at a value of 25°C, the piston crown temperature at 29°C, and the piston skirt at 26°C under the steady-state motoring conditions. The camshaft timing was kept at its parked position, corresponding to a negative valve overlap (NVO) of 20°CA.

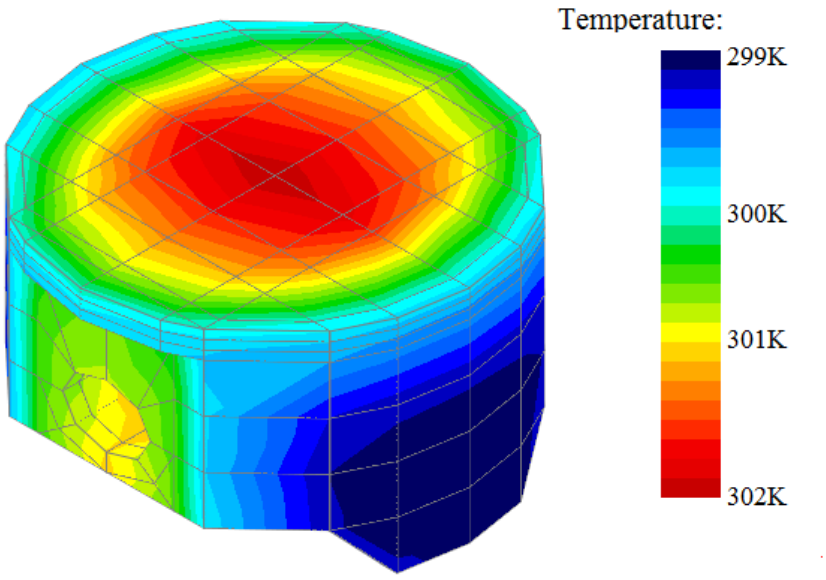

Figure 3-1: Simulated piston temperature performed with GT-Power under steady state motoring at 280 *rpm* and 20°C coolant temperature

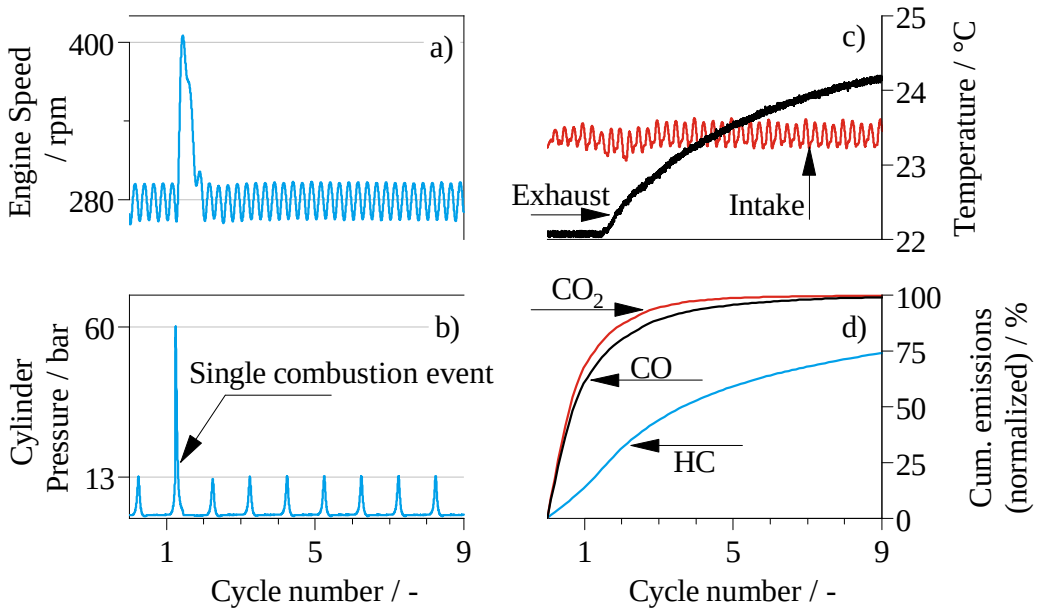

Figure 3-2: Experiment description for the 1st cycle fuel accounting. (a) Engine speed, (b) cylinder pressure, (c) intake and exhaust temperatures, and (d) normalized cumulative emissions as a function of the cycle number for a representative single fire experiment.

The experiment started with the engine being motored at the desired cranking speed (280 *rpm* except for the engine speed sweep experiments), until the temperature and exhaust HC concentration reached steady state to ensure the purging of residual hydrocarbons stored in the engine and lubricant, and to measure the background HC concentration. The throttle plate position was kept at a fixed angle. Except for the MAP sweep experiments, the position corresponded to that at fast idle (2 *bar* NIMEP at 1200 *rpm*). The resulting MAP at cranking was at 0.9 *bar*, which was slightly lower than the typical value (1 *bar*) for the actual 1st cranking cycle because the engine is motored continuously. It will be shown in the MAP sweep experiments that this difference has no material impact on the results. After this purge, a single injection and ignition event took place in cylinder # 4; a metered amount of fuel was injected followed by combustion. Thereafter, as shown in Fig. 3-2, the engine continued to be motored at cranking speed and the exhaust stream composition and

temperature measured, until steady state was achieved again. Throughout the complete experiment, the exhaust composition was measured and recorded with a 1°CA resolution. This procedure was repeated five times for each experimental condition and the results reported are the averaged values.

The exhaust composition was measured with fast-response analyzers, sampling directly from the exhaust runner of cylinder #4. The hydrocarbon concentration was measured using a fast FID unit (Cambustion model HFR400), with a response time t_{10-90} of 10 ms, and a sampling position 6 cm from the exhaust valve. The CO and CO_2 concentrations were measured with a fast NDIR unit (Cambustion model NDIR500), with a response time t_{10-90} of 20 ms, and a sampling position 8 cm from the exhaust valve. The λ value was not directly measured, since the response time of conventional λ-sensors is too slow ($\approx$ 150 ms). The λ values reported in this chapter were calculated from carbon balance using the approach presented in Section 2.3.

Parameter	**Sweep range**	**Step**	**Nominal value**
SOI [°CA $aTDC_{intake}$]	30 − 315	$\Delta = 15$	90
FEF [−]	1.9 − 3.5	$\Delta = 0.2$	2.5
Spark [°CA $aTDC_{comp.}$]	−45 − 20	$\Delta = 5$	-10
MAP [bar]	0.65 − 1	$\Delta = 50$	0.9
Fuel pressure [bar]	30 − 110	$\Delta = 20$	50
Speed [rpm]	280, 700, 1200	−	280

Table 3.1: Experimental scope for the 1st cycle fuel accounting analysis

The number of variables influencing the mixture formation and emissions behavior of the 1st firing cycle during the cranking process is extensive. Nevertheless, there are a great number of constraints during cold crank-start. The low engine speed limits the attainable pressures generated by the mechanical fuel pump; therefore constraining the fuel pressure during the 1st injection event. Due to the low temperature of the surfaces of the combustion chamber, strategies that prove to be effective under warm conditions cannot be applied during the cold-start phase.

The fuel accounting analysis was focused in six different engine parameters using a one-variable-at-a-time approach. The variables studied are: First cycle fuel enrichment factor (FEF, see Eq. 3.1), injection timing (SOI), spark timing, 1st cycle intake manifold pressure (MAP), fuel pressure and engine cranking speed. The parameters tested are summarized in Table 3.1.

Since not all the injected fuel goes into the charge mixture, a large amount of fuel has to be injected to achieve stable combustion in the 1st cycle. To quantify the amount of additional fuel required, a fuel enrichment factor (FEF) based on a speed-density calibration is defined.

$$FEF = \frac{m_{f,cyl} \cdot AFR_{stoich.}}{V_{cyl} \cdot \eta_{vol} \cdot \rho_{int}} \tag{3.1}$$

3.2 Fuel accounting methodology

3.2.1 Carbon accounting

In order to understand the fuel pathway during the 1st combustion cycle a fuel carbon accounting analysis is performed. The goal of this analysis is to quantify the amount of fuel participating in combustion, the fuel carbon fraction being exhausted as unburned hydrocarbons, and the fraction that cannot be accounted for, representing primarily the engine oil dilution by fuel and the blow-by losses. The analysis is done by translating the fuel and exhaust mass flows to equivalent carbon mass flows, and then performing a control volume analysis around the cylinder.

$$\dot{m}_{C,\ in} = \dot{m}_{C,\ out} + \dot{m}_{C,\ Engine} \tag{3.2}$$

The "in" flow corresponds exclusively to the fuel injected, while the "out" flow encompasses the carbon mass flow due to the CO_2, CO and HC content in the exhaust. The engine component of the carbon accounting represents the carbon mass that cannot be accounted for by regarding exclusively the intake and exhaust flows. This corresponds to the oil dilution by fuel and the blow-by losses. The Tier II EEE certification fuel used had a mass carbon fraction (ASTM E191) of 86.5%.

In order to relate the concentration measurements to mass flows, it is necessary to determine the exhaust mass flow and correctly synchronize it with the fast analyzers signals. Given the slow time response of the commercially available gas flow meters, the exhaust mass flow was modeled following the approach described in Section 2.2.1. Figure 3-3 shows the exhaust mass flow traces for a fired and a motored cycle.

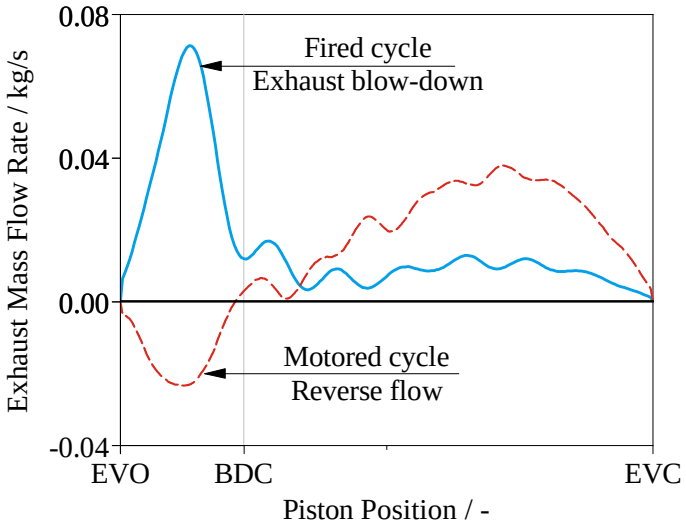

Figure 3-3: Exhaust mass flow of a fired cycle and a motored cycle

To successfully perform this type of transient analysis, the transit time of the exhaust gas from the exhaust valve to the sampling point of the analyzer needs to be considered. Since the response time of the analyzer and this transit time are in the same order of magnitude, the latter cannot be neglected. The transit time is a function of the sampling point position downstream in the exhaust runner, of the instantaneous

exhaust mass flow, and of the exhaust gas density. Following the method described in Section 2.2.2, the calculated mass flow and the exhaust temperature can be used to determine the appropriate transit delay correction to the concentration signals from the fast analyzers. Once the exhaust mass flow and the concentration signals are synchronized, the carbon mass flow due to each constituent can be calculated by multiplying the measured wet mole fraction of the component by the exhaust molar flow (using $MW_{exh} = 28.9\ g/mol$) and the molecular weight of carbon.

$$\dot{m}_{C,y} = \hat{x}_y \cdot \frac{\dot{m}_{exh}}{MW_{exh}} \cdot MW_C \tag{3.3}$$

For the motored cycles after the single-cycle firing, the cylinder pressure is lower than the exhaust pressure when the exhaust valve opens. Thus, as shown in Fig. 3-3, the exhaust flow is initially backwards until the pressure reaches equilibrium and the positive displacement flow begins. By measuring the HC mole fraction during the reverse flow, it is possible to account for the HC content flowing from the exhaust manifold into the cylinder during this period, thus avoiding double-counting of emissions for the reverse flow in the motored cycles.

The goal of the experiment is to deconstruct the pathways for the single-cycle-injected fuel and to examine how the engine parameters affect the pathways. As such, the individual carbon exhaust mass flows due to each component (CO_2, CO, and HC) are integrated for the firing and the subsequent motoring cycles, and the cycle-resolved results are summarized in three sets of numbers:

1. The first set is the HC emissions, respectively, of the 1st, 2nd, and sum of the 3rd-and-beyond cycles. The 1st (firing) cycle HC emissions give information of the emission performance; the 2nd (motoring) cycle HC emissions indicate the amount of the in-cylinder retained fuel from the 1st combustion event that would contribute to the combustible mixture of the 2nd cycle. The HC emissions

from the 3rd cycle on are caused by the slow evaporation of fuel films and the desorption of HC from the oil layer. The accounting of this HC content is necessary to estimate the amount of fuel going into the engine oil and crankcase through a total carbon balance.

2. The second set is the integrated CO_2 and CO over the complete set of recorded cycles (approximately 50). These carbon measures represent the total fuel burned and is used to provide information for the energy accounting analysis (see Section 3.2.2) and to compute the overall combustible mixture λ value.

3. The third set is the difference between the fuel carbon from the injected fuel and the cumulative carbon from the CO_2, CO, and HC measurements over the complete set of recorded cycles. This difference, labeled as the unaccounted fuel, represents the fuel that goes into the engine oil and crankcase.

3.2.2 Energy accounting

Completing the fuel accounting exercise a first law energy balance was performed using cylinder # 4 as the control volume. The Tier II EEE certification fuel used in this study had a lower heating value (LHV) of 43 MJ/kg as reported by the tests ASTM D3338 and D240. The energy content of the fuel was either converted to work, transferred as heat to the cylinder walls or exhausted in the form of thermal and chemical energy. For a given cycle:

$$(m_{f,\ in} - m_{f,\ unacc.})LHV_f = W - Q + m_{exh} \cdot c_{p,\ exh}(T_{exh} - T_0) + \sum_{species} m_i \cdot LHV_i \qquad (3.4)$$

The term W corresponds to the indicated work output of the cycle and can be calculated using the pressure measurements of the high pressure loop and the displacement volume; $W = GIMEP \cdot V_{d,\ cyl.}$.

The term Q refers to the heat transfer to the combustion chamber walls, and ultimately to the engine coolant. Its calculation is based on the classical approach presented by Woschni in the 1960's [77] with an appropiate correction for low engine speed proposed by Lejsek et al. [49]. The details of the approach can be found in Section 2.4.2.

The terms $m_{exh} \cdot c_{p,\ exh} \cdot (T_{exh} - T_0)$ and $\sum_{species} m_i \cdot LHV_i$ correspond to the sensible and chemical energy of the exhaust gases respectively. Due to the slow response time of thermocouples, measuring accurately the gas temperature of a single exhaust stroke was not possible. The thermal enthalpy was then calculated as the difference between the total heat release as calculated based on the fuel conversion to CO_2 and CO (Section 2.4.2) and the work and heat transfer terms. The chemical component of the enthalpy was calculated using the fuel carbon accounting analysis and the lower heating value (LHV_i) of the exhausted species. The species considered were total HC, CO and H_2. The H_2 content of the exhaust was not measured directly but calculated using the approach presented in Section 2.3.

Lastly, as mentioned in the previous section, a significant part of the injected fuel is dissolved into the oil layer or lost to the crankcase due to blow-by. The term $m_{f,\ unacc.} \cdot LHV_f$ represents the energy content of this lost fuel.

3.3 Injection timing sweep

The injection timing has a strong influence on the mixture formation process. As a general rule, under warm operation conditions, early injection timings result in more homogeneous mixtures, while late injection timings result in higher heterogeneity and charge turbulence prior to ignition [39]. On the other hand, for side-mounted injectors and at cold engine temperatures, the injection timing also determines the amount and

location of liquid fuel impinging on the cylinder liner, intake valves, and piston crown. This interaction of the injection spray with the combustion chamber surfaces results in the formation of liquid fuel films and in a deterioration of the mixture formation process.

Figure 3-4 shows the individual contributions of CO_2, CO and HC to the fuel carbon accounting. The combined total CO_2 and CO emissions show a monotonic increase with late injection timings. As indicated by the high CO fraction, the combustion efficiency decreases with later injection. Nevertheless, more fuel participates in the combustion process, suggesting that a lower FEF could be used to achieve an ignitable fuel-air mixture. This point is elaborated further in Section 4.2.1. The lower HC emissions after the 3rd cycle, and, more important, the lower fraction of the unaccounted fuel for late injection timings, suggest that the injection spray interaction with the piston crown reduces the amount of wall-wetting. Consequently, the amount of fuel dissolved in the oil layer is reduced.

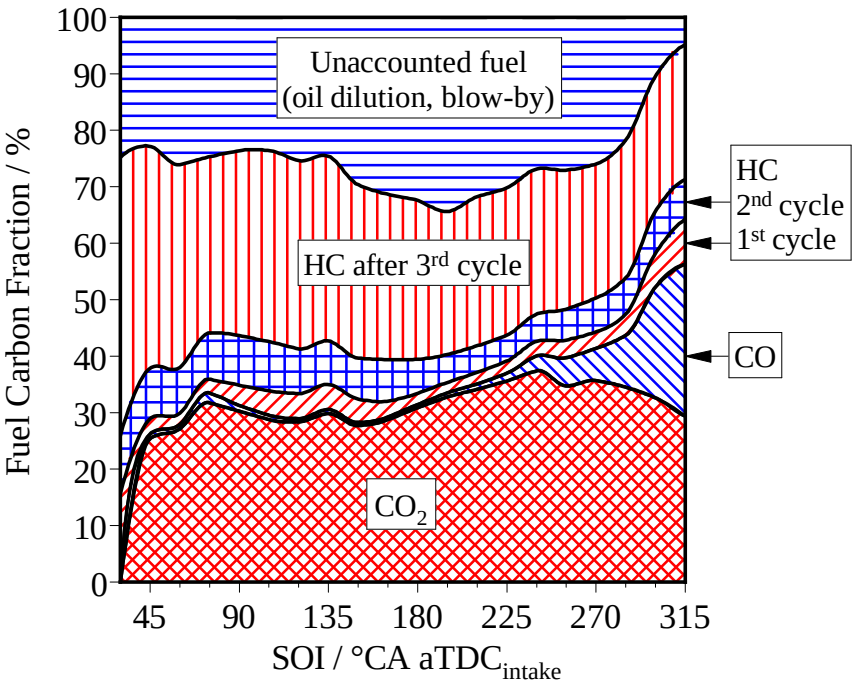

Figure 3-4: Fuel carbon pathway for the 1st cycle as a function of SOI

Figure 3-5 shows further relevant information for the 1st cycle analysis for injection timings ranging from start of injection SOI= $30° - 315°$CA aTDC$_{intake}$. The injection duration lasted approximately 6.7 ms and comprised 11°CA. Zooming in on the 1st cycle and 2nd cycle HC emissions, four zones can be identified for the 1st cycle HC emissions (Fig. 3-5-c). The first zone, ranging from SOI = 0 to 30°CA aTDC$_{intake}$, misfire occurs due to heavy impinging on the piston at reduced cylinder pressure and temperature, resulting in fuel deposits on the piston crown, that do not evaporate.

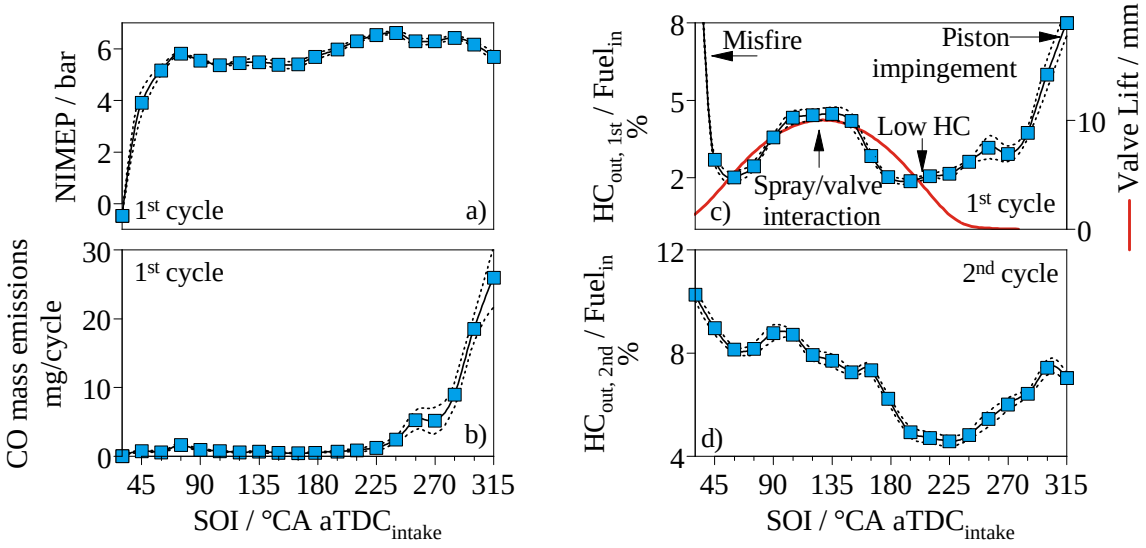

Figure 3-5: Outputs of the single-cycle-fired engine as function of SOI as follows: (a) 1st cycle NIMEP, (b) 1st cycle CO emissions, (c) 1st cycle relative HC emissions, and (d) 2nd cycle relative HC emissions. Dashed lines correspond to a one standard deviation envelope

The second zone, going from SOI $= 45 - 180°$CA aTDC$_{intake}$, is characterized by interaction between the injection spray and the intake valve. The maximum HC emissions (4.5% of injected fuel) occur in the range of SOI $= 120 - 135°$CA aTDC$_{intake}$ coinciding with the maximum lift of the intake valve. To the left and right of that maximum, HC emissions follow the intake valve lift, achieving a minimum of 1.9% of injected fuel when the intake valve lift is lower than 4 mm.

The third zone corresponds to SOI = 180 − 240°CA aTDC$_{intake}$, that is in the initial part of the compression stroke. In this zone there is not only a better fuel utilization (see Fig. 3-6), but also a flat region at low values of HC emissions.

Finally, the fourth zone corresponds to later injection timings into the compression stroke, where the interaction between piston crown and injection spray gains importance, resulting in high HC emissions. Contrary to the first zone, the interaction between the fuel spray and the upwardly moving piston occurs just before the start of combustion, resulting in a stratified mixture and rich burning region around the spark plug. From the high CO emissions observed in this SOI region, the higher HC emissions are inferred to be the result of incomplete combustion. The fuel available for the 2nd cycle combustion varies significantly with the SOI of the 1st cycle (Fig. 3-5-d), achieving a minimum value in the same range as the 1st cycle HC emissions do, that is, SOI during the early compression stroke.

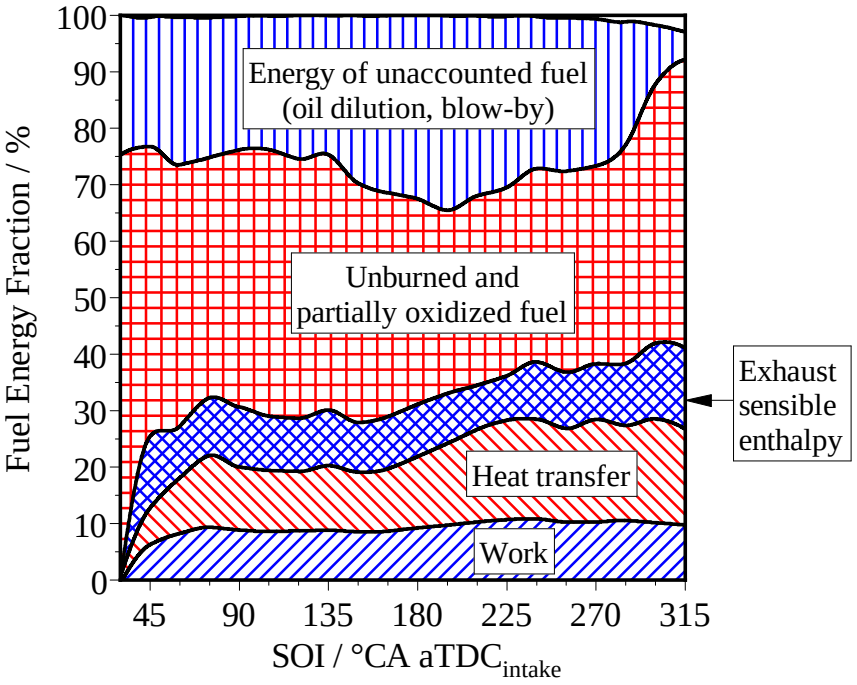

Figure 3-6: Fuel energy accounting for the 1st cycle as a function of SOI

Figure 3-6 shows the contributions of work, heat transfer, exhaust enthalpy and lost fuel to the fuel energy accounting. The amount of energy converted to work, in other words the first law efficiency, lies between 8 and 10%. Using the 1st cycle NIMEP as a measure of the work output the following analysis can be made. As shown in Fig. 3-5-a, the NIMEP increases from 0 bar at SOI= 30°CA aTDC$_{intake}$ (misfire) to 6 bar at SOI= 75°CA aTDC$_{intake}$. This zone corresponds to heavy impinging on the piston for injection timings lower than SOI= 75°CA aTDC$_{intake}$. As the piston moves downward and the impingement decreases, the NIMEP stays relatively constant for injections during the intake stroke. For compression stroke injections, the higher in-cylinder pressure reduces the injection spray penetration, allowing for a better mixture formation and increased fraction of fuel evaporated. Consequently, an increase in NIMEP for SOI up to 225°CA aTDC$_{intake}$ is observed. Up to this injection timing the homogeneity of the mixture stays relatively constant, as can be seen by the constant low values of the emitted CO. The NIMEP trend becomes flat, while the mixture becomes increasingly heterogeneous. At the injection timing SOI = 285°CA aTDC$_{intake}$ the fuel spray impinges again on the piston crown. The result is a very heterogeneous and rich mixture around the spark plug, characterized by high CO production (Fig. 3-5-b) and slightly lower NIMEP.

The heat transfer to the engine walls accounts for 10 to 18% of the total fuel energy. For injection timings during the intake stroke, the fraction of the fuel energy lost as heat transfer to the coolant between 10 and 12%. As the SOI moves into the compression stroke the heat transfer increases up to a maximum of 18% ($\approx 570\ J$) at SOI = 300°CA aTDC$_{intake}$. The heat transfer is a function of the amount and timing of the heat release rate. As argued previously, as the injection timings is delayed, more fuel takes part in combustion and the amount of heat release increases. Furthermore, as shown in Fig. 3-7, as the injection timing is delayed in the compression stroke and the mixture becomes increasingly stratified, the flame development and burn duration are shorter and the peak of heat release is shifted to an earlier point.

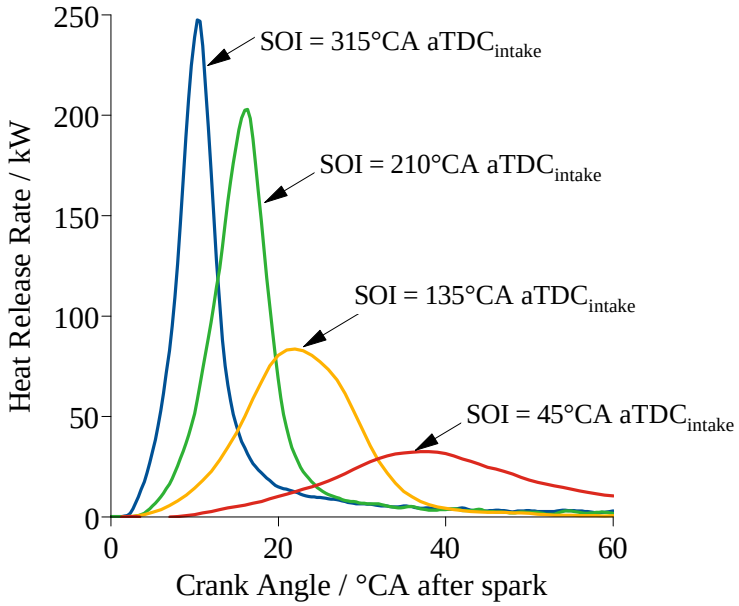

Figure 3-7: Heat release trace during the 1st cycle for different SOIs

The exhaust sensible enthalpy does not vary significantly with injection timing and stays at a value between 8 and 11% of the fuel energy content. The remaining fuel energy that was not converted to work or heat is exhausted in the form of HC, CO and H_2, or is lost to the crankcase in the form of oil dilution or blow-by. These two quantities have a high sensitivity to the injection timing as was already discussed in the fuel carbon accounting analysis.

3.4 Fuel enrichment factor

3.4.1 FEF sweep at nominal conditions

The fuel evaporation process during cranking differs significantly compared to all other operation regimes, due to the low engine speed and cold temperature. In addition, the 1st combustion cycle differs from all subsequent cycles, due to the absence of

hot residual gases during the 1st firing event. As a consequence, the necessary amount of fuel to form an ignitable mixture for the 1st cycle is significantly larger than what it is needed for the following combustion events. The fuel amount was varied between 50 and 100 mg, corresponding to fuel enrichment factors (FEF) in the range from 1.9 to 3.5. All other parameters were kept fixed at their nominal value (see Table 3.1).

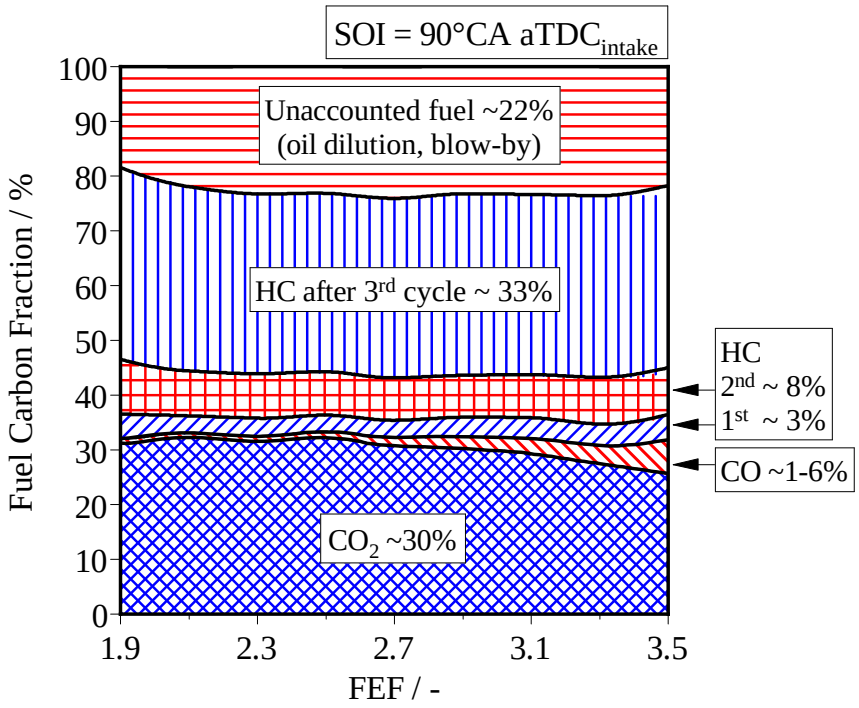

Figure 3-8: Fuel carbon pathway for the 1st cycle as a function of FEF

Figure 3-8 shows the fuel carbon pathway as a function of FEF. The combined CO_2 and CO fraction, representing the total fraction of fuel carbon burned, oscillates between 31 and 33%. Remarkably, despite the difference in injection duration, which impacts directly the spray penetration, in-flight evaporation, fuel film formation and charge turbulence, the fuel carbon accounting diagram exhibits parallel bands as the FEF is modified. Thus, for the range of FEF values tested for the 1st cranking cycle, roughly a third of the fuel takes part in combustion.

From bottom to top, the third and fourth bands in Fig. 3-8 represent the 1st HC

and 2nd HC emissions. Zooming in on these two bands, Fig. 3-9-d & -e show the relative HC emissions with respect to the mass of fuel injected. The fraction of the fuel injected coming out of the engine as unburned HC remains roughly constant with increasing FEF at values between 3 and 4%, with a slight increase for higher FEF. This 1st cycle HC emissions will contribute directly to the tailpipe emissions, since the catalyst has not reached light-off temperature.

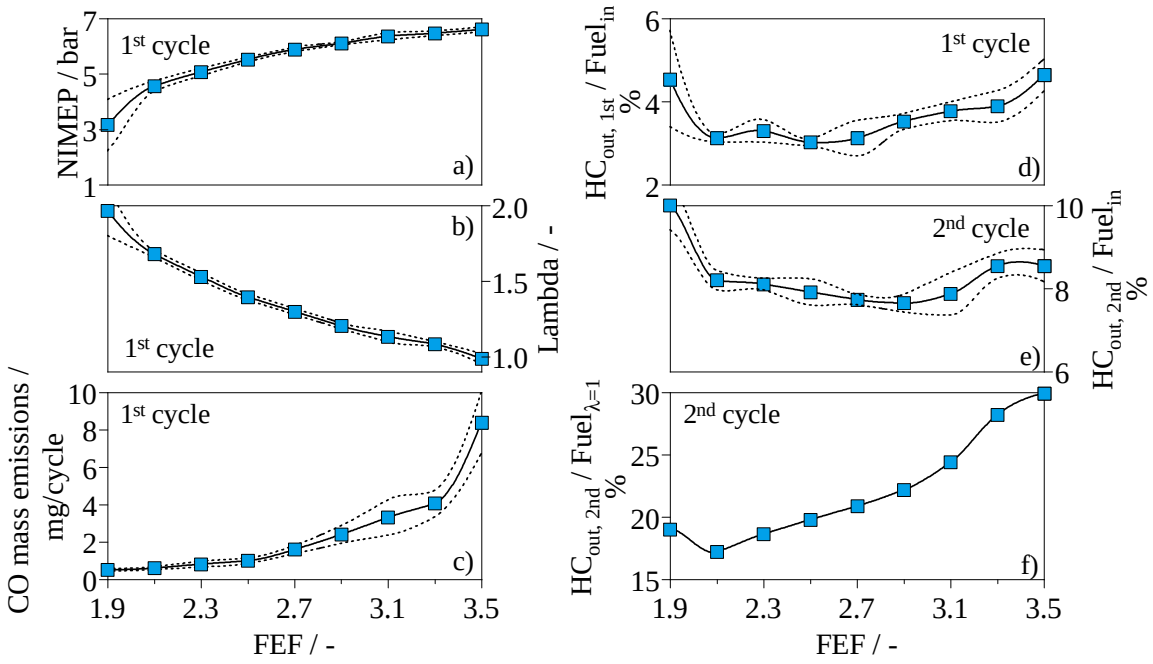

Figure 3-9: Outputs of the single-cycle-fired engine as function of FEF as follows: (a) 1st cycle NIMEP, (b) 1st cycle λ, (c) 1st cycle CO emissions, (d) 1st cycle relative HC emissions, (e) 2nd cycle relative HC emissions, and (f) 2nd cycle HC relative emissions as a percentage of the fuel mass for $\lambda = 1$. Dashed lines correspond to a one standard deviation envelope

Figure 3-9-e shows the relative HC emissions for the 2nd cycle, which is a motored cycle. This value is representative of the fuel fraction that would be available for 2nd cycle combustion, and thus, it can be used to correct the 2nd injection event, to avoid over-enrichment. The relative HC emissions for the second cycle stay roughly constant at around 8% for FEF$>$ 1.9. To understand the impact that the residual HC

could have on the second combustion event, the HC emissions are also plotted relative to the fuel necessary (based on a speed-density calibration) to achieve stoichiometric combustion. Fig. 3-9-f shows that more than 20% of the fuel necessary to achieve stoichiometric combustion for the 2nd combustion event is already in the cylinder in the form of residual HC for FEF > 2.3. The influence of residual fuel from on the 2nd cycle mixture formation and combustion will be discussed further on Section 4.3.4.

The HC emissions coming out of the engine on and after the 3rd cycle (fifth band in Fig. 3-8) due to the slow evaporation of fuel films from the combustion chamber surfaces and the desorption of the fuel dissolved in the oil layer, account to approximately 33%. Lastly, approximately 22% of the fuel cannot be accounted for. This unaccounted fuel is thought to end up as permanent oil dilution by fuel or to escape the combustion chamber as blow-by, being exhausted through a different unmonitored cylinder or through the positive crankcase ventilation (PCV) valve.

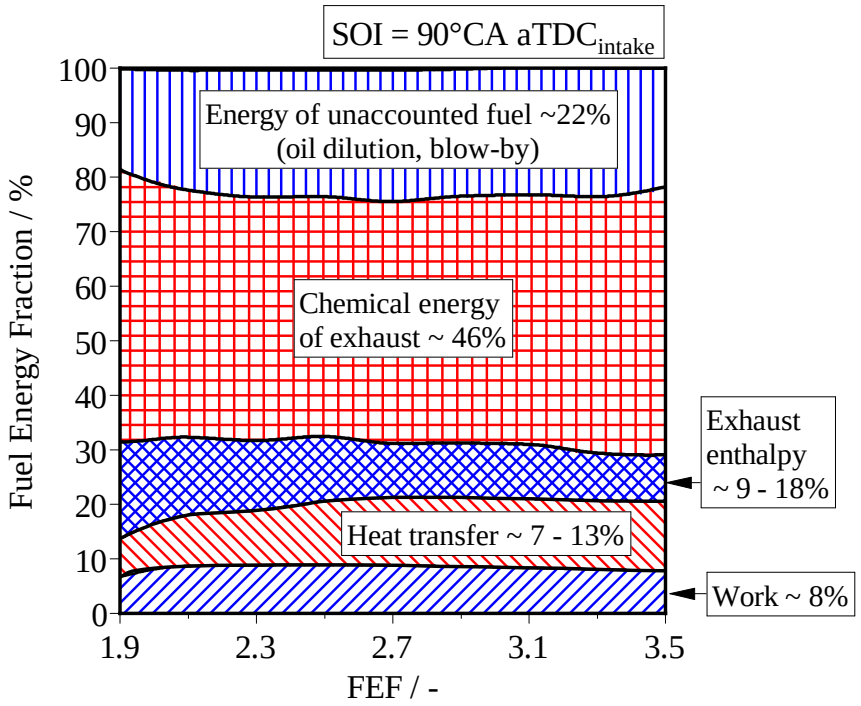

Figure 3-10: Fuel energy accounting for the 1st cycle as a function of FEF

Figure 3-10 shows the contributions of work, heat transfer, exhaust enthalpy and lost fuel to the fuel energy accounting as a function of FEF. The amount of work extracted as a fraction of the total fuel energy stays approximately constant between 7 and 9%. In absolute terms, the increase in NIMEP with increasing FEF is an expected result, since more fuel is being injected for a fixed amount of air. However, the dependence is more marked at low values, and flatter at higher FEF (Fig. 3-9-a). The results are also affected by the change in combustion phasing associated with the higher flame speeds of richer mixtures, and by the presence of locally rich pockets in the combustion chamber resulting in incomplete combustion. Since the λ value is calculated from carbon balance using the exhaust carbon values (see Section 2.3) it may be interpreted as the overall λ value of the burned mixture. For FEF increasing from 1.9 to 3.5, λ decreases from 2.8 to 1. Thus, for the whole range of FEF, the burned mixture is overall lean. Although for an FEF of 3.5 the mixture appears to be globally stoichiometric (Fig. 3-9-b), the high CO mass exhausted (Fig. 3-9-c; 8 mg CO/cycle $\approx$ 4% wet CO) indicates that the mixture was not homogeneous and that rich burning pockets were present during combustion.

The fraction of the fuel energy going to heat transfer and to the exhaust thermal enthalpy exhibit inverse trends. In the lower end of the FEF spectrum, the reduced fuel amount together with the lower flame speeds of the leaner fuel-air mixture result in reduced heat transfer and higher charge temperature at exhaust valve opening (EVO). Oppositely, at FEF = 3.5 the amount of heat release increases directly with the fuel amount, and the faster burning velocity of the richer fuel-air mixture shifts the peak of heat release to an earlier point. As a result, the balance between exhaust thermal enthalpy and heat trasnfer is shifted to the latter.

Lastly, the exhaust chemical enthalpy and the fraction of energy that cannot be accounted for mirror the results presented in the fuel carbon analysis for the total HC emissions and the fuel fraction lost to the crankcase.

3.4.2 FEF sweeps at different injection timings

As presented in Section 3.3, the injection timing has a significant impact on the fuel pathway of the 1st cranking cycle. To further examine the interdependence between the injection timing and the fuel enrichment requirement, the fuel accounting analysis was extended to the three injection strategies presented in Table 3.2.

Injection strategy	**FEF range**
$SOI = 195°\text{CA aTDC}_{\text{intake}}$	$1.9 - 3.3;\ \Delta = 0.2$
$SOI = 345°\text{CA aTDC}_{\text{intake}}$	$0.5 - 1.3;\ \Delta = 0.2$
$SOI_1 = 195°\text{CA aTDC}_{\text{intake}}$ $SOI_2 = 330°\text{CA aTDC}_{\text{intake}}$ $m_{fuel,SOI2} = 6\ mg$	$0.7 - 2.5;\ \Delta = 0.2$

Table 3.2: Extended injection strategy study of the 1st cycle's FEF

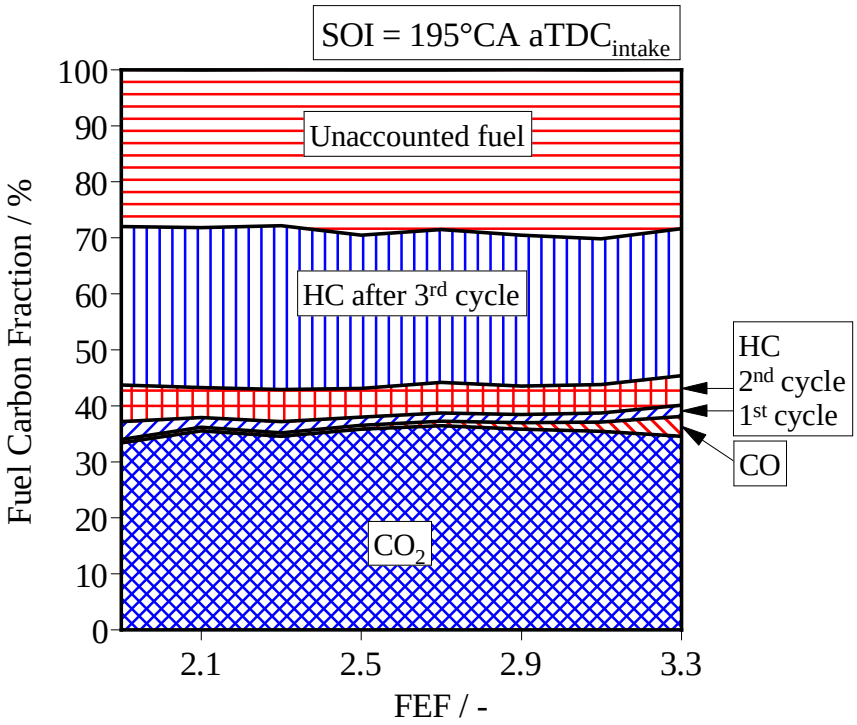

Figure 3-11: Fuel accounting for the 1st cycle vs. FEF for early compression SOI

Figure 3-11 shows the fuel accounting diagram as a function of FEF for a single injection during the early compression stroke at SOI= 195°CA $aTDC_{intake}$. As shown in Fig. 3-5, this injection timing provides advantages over the intake injection in terms of HC emissions and fuel utilization. The combined CO_2 and CO share for the early compression injection strategy is approximately 36%; roughly 4% higher than the intake SOI strategy (see Fig. 3-4). On the other hand, the greater interaction between the injection spray and the cylinder liner at SOI = 195°CA $aTDC_{intake}$ results in a larger amount of lost fuel due to oil dilution. Nevertheless, in spite of the aforementioned differences, the carbon fraction bands remain parallel.

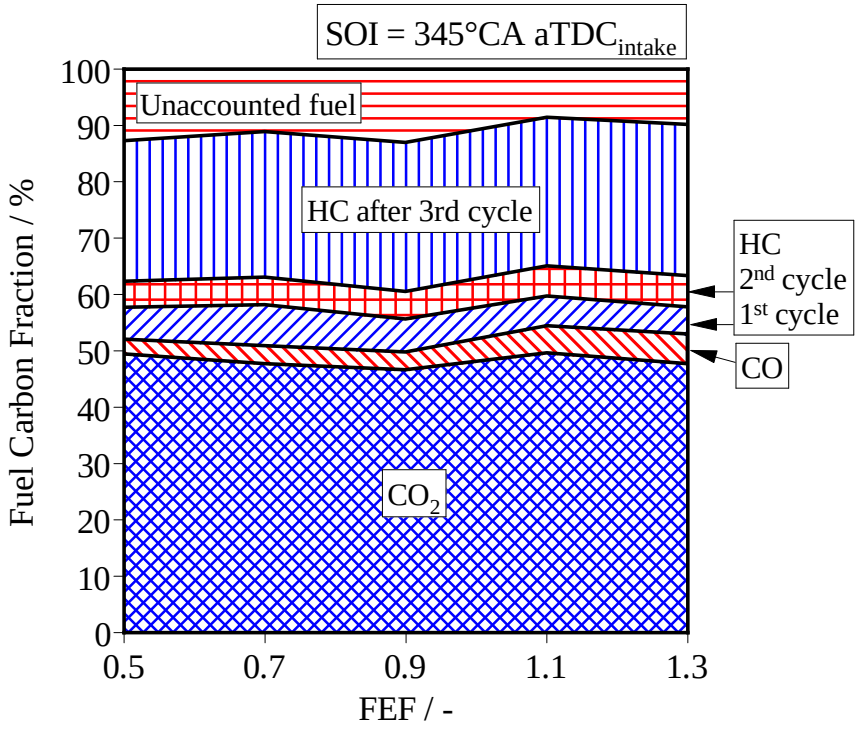

Figure 3-12: Fuel accounting for the 1st cycle vs. FEF for late compression SOI

Late injection during the compression stroke, allows for mixture stratification around the spark plug, therefore reducing the enrichment (FEF) required to form an ignitable mixture. Figure 3-12 shows the fuel accounting diagram as a function of FEF for a single injection during the late compression stroke (SOI = 345°CA $aTDC_{intake}$). Mix-

ture stratification has the advantage of better fuel utilization as shown by the CO_2 fraction close to 50% with the disadvantage of higher CO production due to rich burning regions. Additionally, the heavy piston impingement results in a significant increase in 1st cycle HC emissions while at the same time eliminating the spray/liner interaction reducing the amount of fuel lost as oil dilution.

Lastly the combination of the previous strategies is shown in Figure 3-13. The early compression injection corresponds to the main event and was used to adjust the FEF. The late compression injection mass was kept at 6 mg. For low FEF, the leaner mixture resulted in partial burn and high 1st cycle HC emissions. At FEF = 1.7, the maximum fuel utilization is achieved with a combined CO_2 and CO share at 48%. As the share of the main injection increases with FEF, the unaccounted fuel increases due to the spray/liner interaction and the oil dilution associated with it.

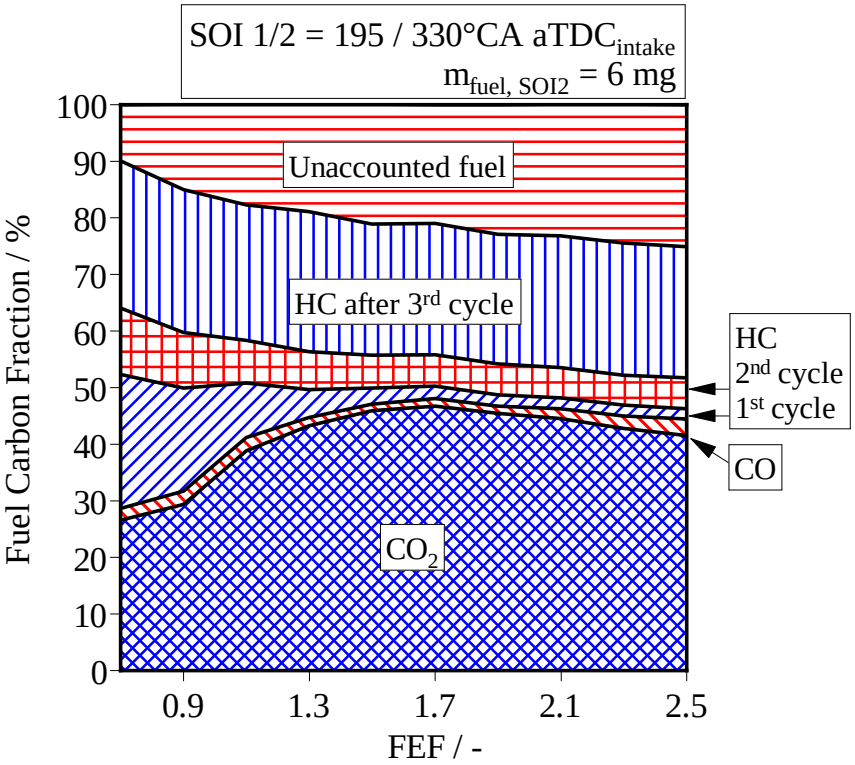

Figure 3-13: Fuel accounting for the 1st cycle vs. FEF for split injection strategy

3.5 Spark timing sweep

The use of delayed combustion phasing has been established as a common practice in the industry to increase the thermal enthalpy flow to the catalyst, reducing its light-off time, while keeping the engine-out HC emissions under control [21, 27]. In contrast, the influence of ignition timing on the 1st combustion cycle characteristics has been characterized in only a few studies for a reduced set on spark timings before TDC [25, 75].

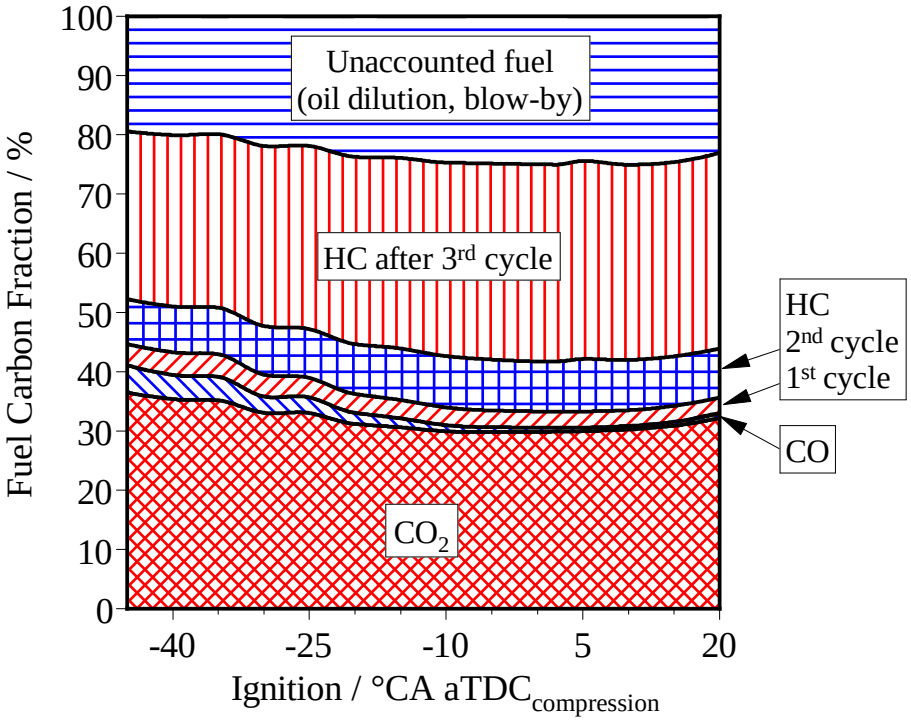

Figure 3-14: Fuel carbon pathway for the 1st cycle as a function of spark timing

Figure 3-14 shows the fuel carbon accounting diagram for the spark timing sweep. The CO_2 and CO production exhibit a high sensitivity to spark timing; earlier combustion phasing results in an increased production of both species. This is a rather striking result, given that the amount of fuel, injection timing, fuel pressure and engine speed are kept constant; therefore, the mixture formation process is similar for all

spark timings studied. The increased production of CO_2 and CO is believed to occur due to a combination of the higher in-cylinder temperatures associated with advanced combustion timing and the AFR around the spark plug at ignition timing. Higher combustion temperatures result in higher unburned-gas temperatures and higher wall heat transfer (see Fig. 3-16), thus aiding in the evaporation of fuel films in the combustion chamber and increasing the amount of fuel taking part in combustion. The engine-out CO emissions are additionally affected at advanced spark timing by the lower burned gas temperature during expansion, reducing the post-flame oxidation rate of CO.

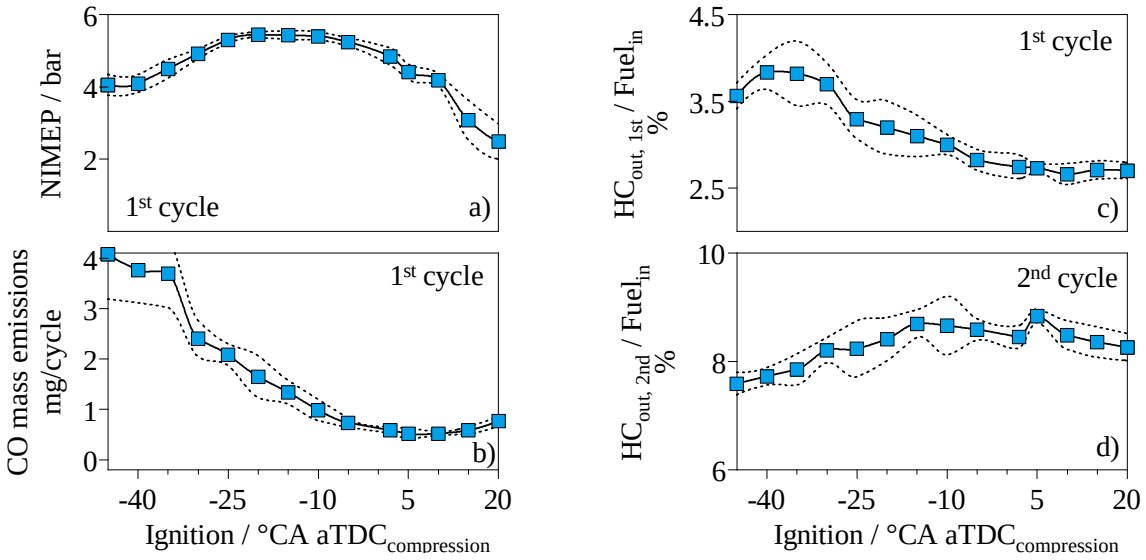

Figure 3-15: Outputs of the single-cycle-fired engine as function of spark timing as follows: (a) 1st cycle NIMEP, (b) 1st cycle CO emissions, (c) 1st cycle relative HC emissions, and (d) 2nd cycle relative HC emissions. Dashed lines correspond to a one standard deviation envelope

The HC emissions bands (1st, 2nd and 3rd-on) show a relatively constant thickness (see Fig. 3-14) indicating that the HC emissions sources are not significantly affected by spark timing. Taking a closer look at the 1st cycle HC emissions (Fig. 3-15-c) it is observed that later ignition timings have a small positive impact on the HC emissions; however, they exhibit a significant lower sensitivity compared to the CO production.

The higher burned gas temperatures resulting from spark retard, favor the post-flame oxidation of unburned HC in the bulk gas, but also promote fuel evaporation from crevices and cylinder surfaces [16]. These two competing effects result in the lower sensitivity observed for HC. The net effect is a decrease in HC as a fraction of the fuel from ≈ 3.7% to 2.8%. The fuel available for the second cycle combustion (Fig. 3-15-d) follows an inverse trend, that is, it increases slightly with retarded spark timing. The lower HC emissions after the third cycle, and the lower fraction of the unaccounted fuel for advanced spark timings (Fig. 3-14) are a direct consequence from the increased fraction of fuel taking part in combustion during the 1st cycle.

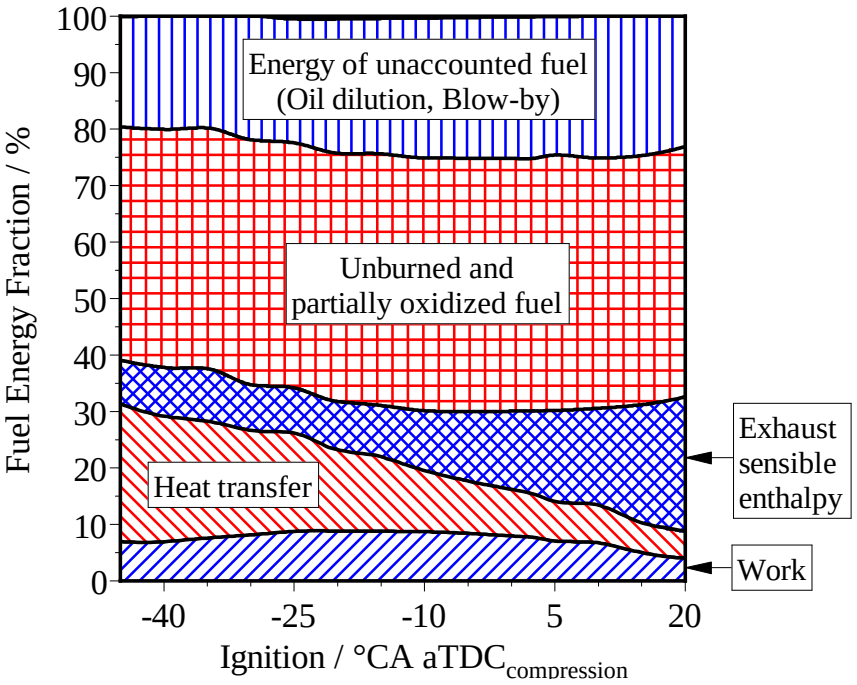

Figure 3-16: Energy accounting for the 1st cycle as a function of spark timing

The fuel energy accounting diagram is shown in Fig. 3-16. From bottom to top, the first band represents the work output of the 1st cycle with a share of 4 - 9% of the fuel energy. The 1st cycle NIMEP as a function of spark timing is shown in Fig. 3-15-a. For both extremes of the spark timing spectrum there is a reduction in work output, with a higher impact on the side of late ignition. The maximum NIMEP is achieved

in a plateau region from ignition timing -25 to -5°CA aTDC$_{\text{comp.}}$. Due to the low, but rapidly changing, engine speed, the usual notion of proper combustion phasing for MBT ($CA50 \approx 7$°CA aTDC$_{\text{comp.}}$ and $P_{max} \approx 15$°CA aTDC$_{\text{comp.}}$) does not apply [11]. The NIMEP plateau region is a result of the competing effects between heat transfer to the cylinder walls and the location of the maximum cylinder pressure.

As the spark timing is varied from -45 to 20°CA aTDC$_{\text{comp.}}$ the wall heat transfer and the exhaust sensible enthalpy exhibit opposite trends. Delaying the combustion phasing reduces the peak temperature of combustion and, consequently, the heat transfer to the combustion chamber walls. Conversely, the lower heat transfer results in a higher charge temperature at exhaust valve opening, thus, increasing the sensible enthalpy of the exhausted gases. The exhaust chemical enthalpy and the fraction of energy that cannot be accounted for mirror the results of the fuel carbon analysis.

3.6 Intake pressure sweep

Lower cylinder pressure can be beneficial for the evaporation of fuel films formed during the injection process [46]. Furthermore, given the reduced volumetric efficiency respect to the atmospheric conditions, less vaporized fuel is needed to form a combustible mixture. The most direct way to influence the in-cylinder pressure is by means of the manifold absolute pressure (MAP). During cranking, MAP is a function of engine speed and throttle position. During this analysis, to isolate the effect of MAP from that of engine speed, the throttle position was the modified parameter, achieving a minimum MAP value of 650 $mbar$ at a cranking speed of 280 rpm, for a fully closed throttle valve.

The distribution of the fuel carbon as a function of MAP is shown in Fig. 3-17. The production of CO_2 increases with lower MAP values suggesting an improved mixture

formation, plausibly caused by better fuel evaporation at lower cylinder pressure. The CO production is independent from MAP remaining at 1% throughout the sweep.

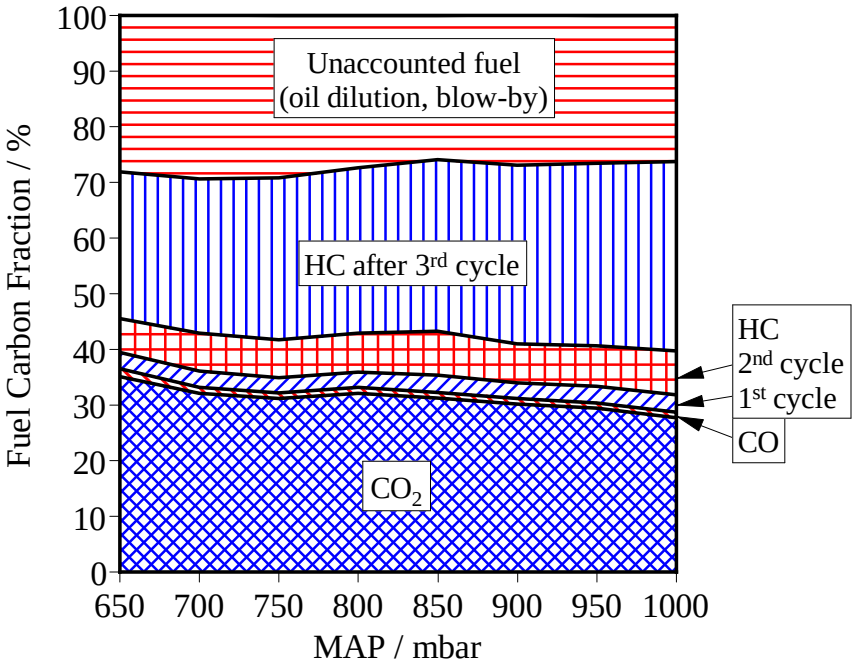

Figure 3-17: Fuel carbon pathway for the 1st cycle as a function of MAP

As MAP increases, while the relative HC emissions stay relatively constant for the 1st and 2nd cycles, the amount of 3rd cycle-on HC increases. This observation may be explained by the increase in the oil layer temperature because more fuel is burned with the increased MAP so that there is more desorption in the subsequent motoring cycle. The corresponding decrease in the oil dilution and blow-by amount lends support to this explanation. Despite the better fuel utilization at lower MAP values, the relative first cycle engine-out emissions (Fig. 3-18-d) increase modestly with intake pressure. Nevertheless, in absolute terms, lower MAP allows a reduction in the injected fuel amount without over-leaning of the mixture, and resulting in lower absolute HC emissions for the 1st cycle (Fig. 3-18-e).

Since the engine was calibrated using a speed-density approach, the injected amount of fuel, and logically the cycle work output, is a function of MAP (Figs. 3-18-a and -c).

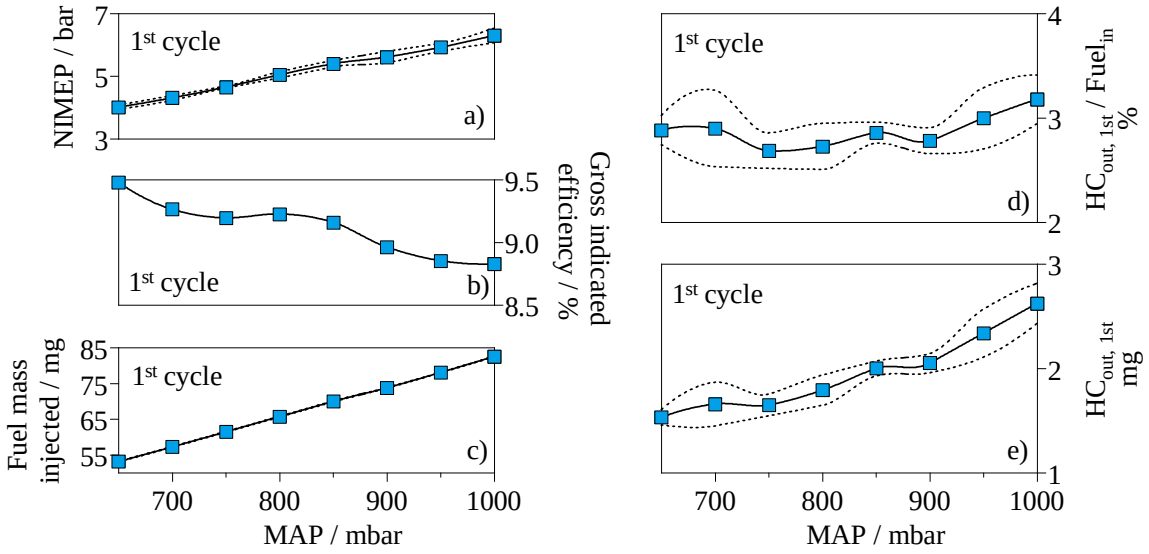

Figure 3-18: Outputs of the single-cycle-fired engine as function of MAP as follows: (a) 1st cycle NIMEP, (b) 1st cycle gross indicated efficiency, (c) 1st cycle injected fuel mass, (d) 1st cycle HC relative emissions, and (e) 1st cycle HC absolute emissions. Dashed lines correspond to a one standard deviation envelope

To assess the fuel evaporation behavior for different MAP values, the gross indicated fuel conversion efficiency ($\eta_{i,g}$) is a useful tool. In the MAP sweep, the combustion phasing and hence the gross thermal efficiency of the burned fuel are approximately the same; hence, $\eta_{i,g}$ becomes the ratio of the mass of fuel burned to the injected fuel; a measure of the fuel utilization efficiency. For increasing MAP values from 650 to 1000 $mbar$, $\eta_{i,g}$ decreases slightly from 9.5% to 8.8%. Thus, the fuel utilization decreases with more injected fuel.

Figure 3-19 shows the fuel energy accounting for the MAP sweep. The first lower band, corresponding to the fraction of energy converted to work, is equivalent to the gross indicated fuel conversion efficiency discussed above. As the MAP is increased from 650 to 1000 $mbar$ the heat transfer share decreases from 15% to 10%, as the heat transfer processes is driven by the temperature gradient in the combustion chamber and does not scale with MAP, remaining roughly constant at 340 J. Therefore, as the fuel amount increases with MAP, the contribution of heat transfer to the

energy accounting decreases. The sensible enthalpy, on the other hand, is directly proportional to the mass of the trapped charge. Therefore, it scales directly with MAP and fuel mass and its contribution remains constant at approximately 10.5%. As it was the case in the previous sections, the exhaust chemical enthalpy and the fraction of energy that cannot be accounted for correspond to the results from the fuel carbon accounting.

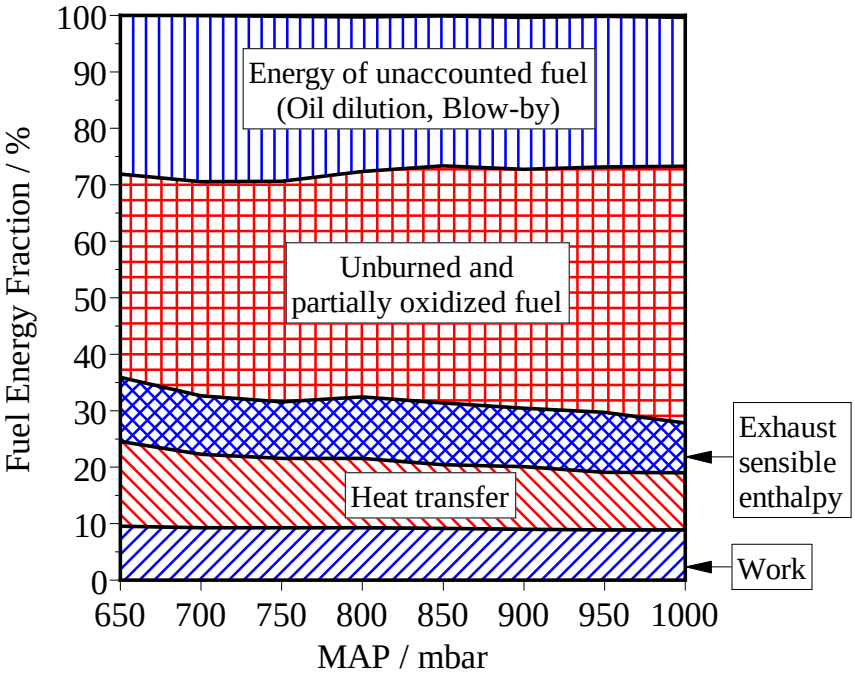

Figure 3-19: Fuel energy accounting for the 1st cycle as a function of MAP

3.7 Fuel pressure sweep

The fuel injection pressure has a strong influence on the mixture formation of GDI engines through different mechanisms, especially for the 1st combustion event. On the one hand, the increase in fuel pressure results in a decrease in fuel droplet diameter (SMD). The smaller droplets have better evaporation. They also have a lower inertia

and exchange momentum readily with the charge; thus, spray penetration and wall impingement are reduced. On the other hand, higher fuel pressures result in higher nozzle velocities, and therefore in higher momentum and penetration of the injection spray. This results in increased wall wetting, hindering the fuel evaporation. The balance between these conflicting effects has been studied in the past, in the fuel pressure range from 5 to 40 *bar* [20, 41, 44]. In this range, the droplet size decreases sharply with increasing injection pressure from 100 μm at 5 *bar* to roughly 30 μm at 40 *bar* and the advantages in reduction of droplet size are more significant than the disadvantages of increased spray penetration, resulting in better mixture formation and lower emissions.

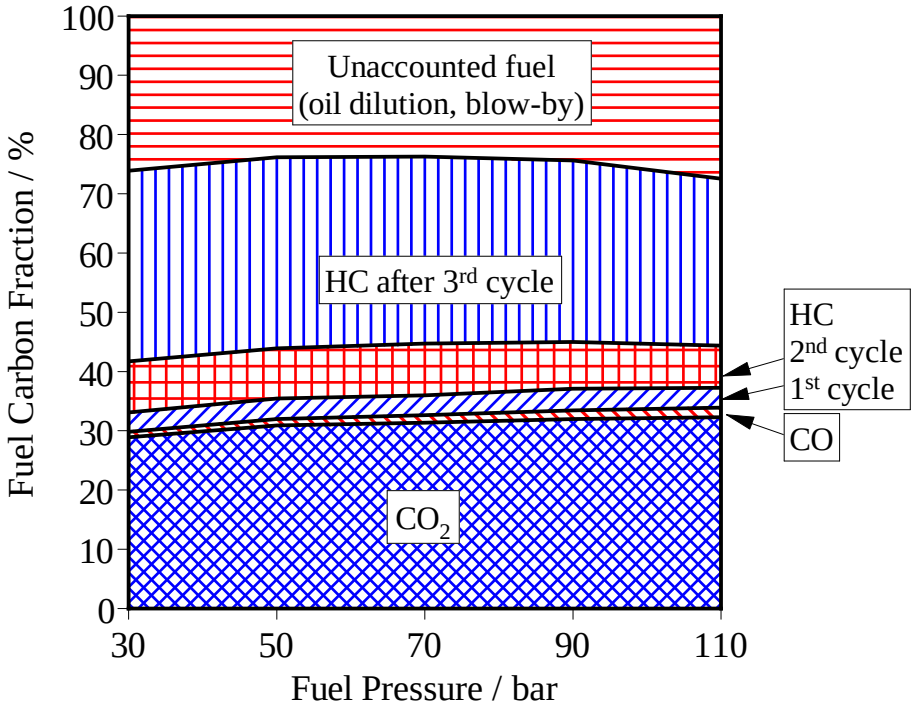

Figure 3-20: Fuel carbon pathway for the 1st cycle as a function of fuel pressure

In this study, the fuel pressure range of $30 - 110$ *bar* is examined. The lower value corresponds to what a modern fuel pump could supply for the 1st injection cycle [44]; however, only modest reductions in fuel droplet size are achievable in this pressure

range (e.g. from $\approx 35-18\ \mu m$, as reported by Landenfeld et al. [44]). The fuel pulse width was adjusted to account for the different injection pressures and keep the fuel amount constant. At 30 *bar* the injection event has a duration of 14.5°CA, while at 110 *bar* the duration is only 7.5°CA.

The mixture formation is favored by higher injection pressures, as can be seen from the higher CO_2 production associated with them (Fig. 3-20). The CO production increases with fuel pressure from 0.9% at 30 *bar* to 1.7% at 110 *bar*. On the other hand, the 1st cycle HC emissions are insensitive to the injection pressure. It is worth to point out, that the injection timing for this set of experiments was kept constant at 90°CA $aTDC_{intake}$, during the intake valve opening; an injection timing that proved to result in higher HC emissions due to spray interaction with the intake valve. The detail of the 1st cycle HC emissions is presented in Fig. 3-5-c.

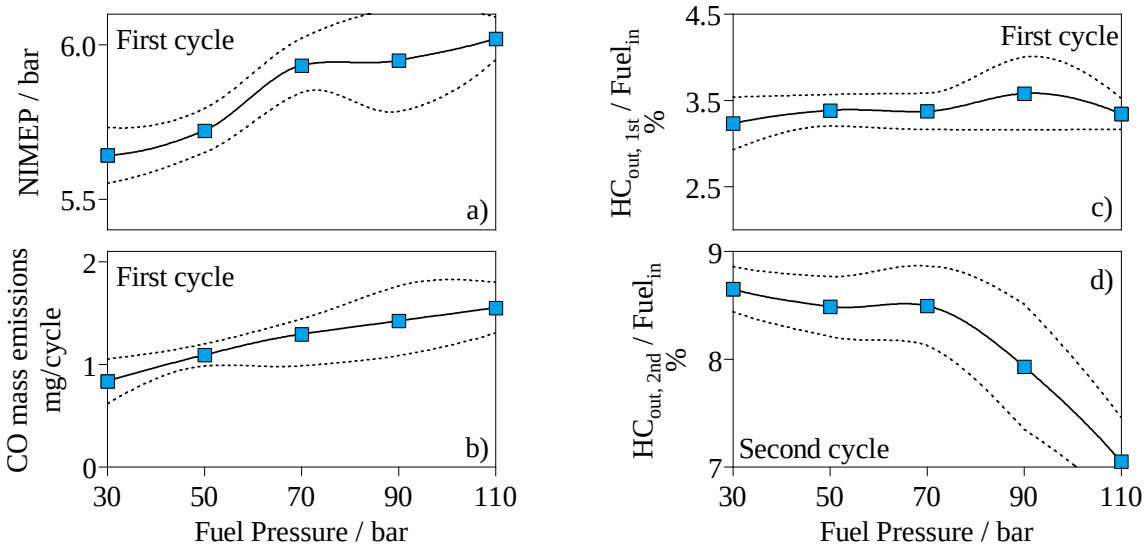

Figure 3-21: Outputs of the single-cycle-fired engine as function of fuel pressure as follows: (a) 1st cycle NIMEP, (b) 1st cycle CO emissions, (c) 1st cycle relative HC emissions, and (d) 2nd cycle relative HC emissions. Dashed lines correspond to a one standard deviation envelope

The results for the 2nd cycle HC emissions, as well as the HC emissions after the 3rd cycle (Fig. 3-20) indicate that despite the higher fuel pressure, and the corresponding

increase in spray penetration, the fuel remaining in the combustion chamber after the 1st combustion event decreases with higher fuel pressures. The detail of the 2nd cycle HC emissions is presented in Fig. 3-5-d. The overall effect is that for injection pressure increasing from 30 to 110 *bar*, the fraction of fuel burned (as indicated by the fuel carbon used) only increases modestly, from 33% to 37%; the 1st cycle HC emissions as fraction of fuel remain approximately constant.

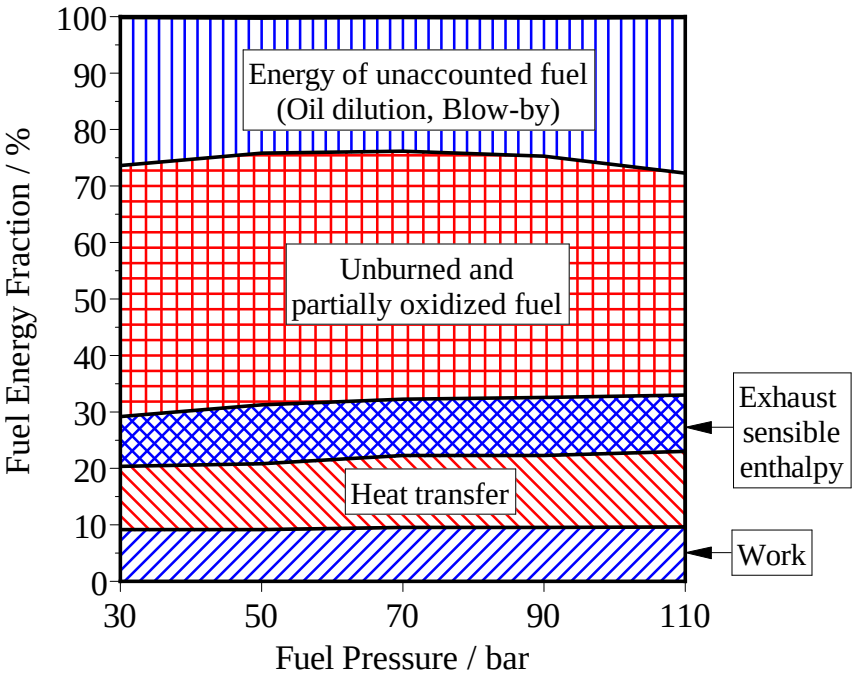

Figure 3-22: Fuel energy accounting for the 1st cycle as a function of fuel pressure

Figure 3-22 shows the fuel energy accounting for the 1st cycle as a function of fuel pressure. Due to the better mixture formation achieved with higher fuel pressure the work share of the fuel energy accounting increases with fuel pressure (see also Fig. 3-5-a). For the same reason, the flame development angle and burn duration is reduced, resulting in the higher wall heat transfer fraction observed. The exhaust sensible enthalpy is not affected by fuel pressure variations.

3.8 Engine speed sweep

With the increased market share of start-stop systems and hybrid powertrains, the engine cranking speed is not limited anymore to the low speed of conventional starters, providing a further dimension for engine start optimization. To gain a better understanding on how engine speed affects the mixture formation and emissions behavior of the 1st combustion cycle, three different engine speeds were considered. These correspond to conventional cranking speed (280 *rpm*), idle (700 *rpm*) and fast idle (1200 *rpm*). Given that the burning velocity changes with engine speed due to the effect of turbulence, the combustion phasing is a function of engine speed, if all other parameters are left constant. To decouple the effect of engine speed from the combustion phasing, the spark timing was adjusted for each engine speed studied to achieve a comparable combustion phasing as quantified by the 50% mass fraction burned point (CA50, see Fig. 3-24-b).

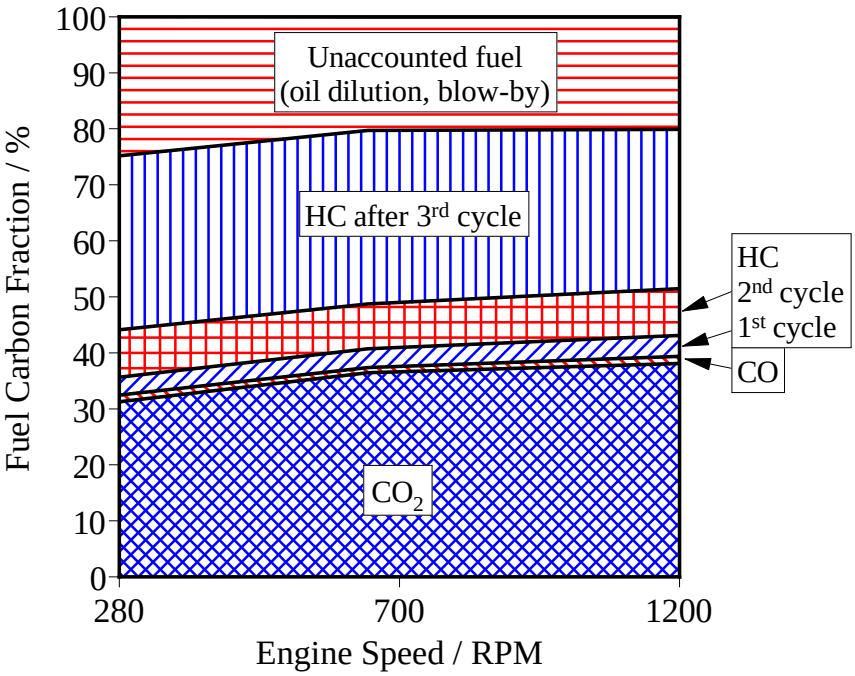

Figure 3-23: Fuel carbon pathway for the 1st cycle as a function of engine speed

The increase in engine speed results in better fuel utilization due to the improved mixture formation resulting from higher turbulence. For higher engine speeds this effect is observed in Fig. 3-23 as an increase in the production of CO_2 and in Fig. 3-25 as an increase in the combined work, heat transfer and sensible enthalpy fractions. The fuel utilization, as measured by the fraction of fuel carbon conversion to CO and CO_2, improves by 20% (from 0.35 to 0.42), see Figure 3-23. Additionally the NIMEP increases in 49% from 5.5 *bar* for 280 *rpm* to 8.2 *bar* for 1200 *rpm* (see Fig. 3-24-a). This improved mixture formation from the higher turbulence more than compensates for the shorter preparation time at the higher speed. This improvement partially explains the amount of NIMEP increase. The remaining improvement is due to the reduction in heat loss with an increase in engine speed.

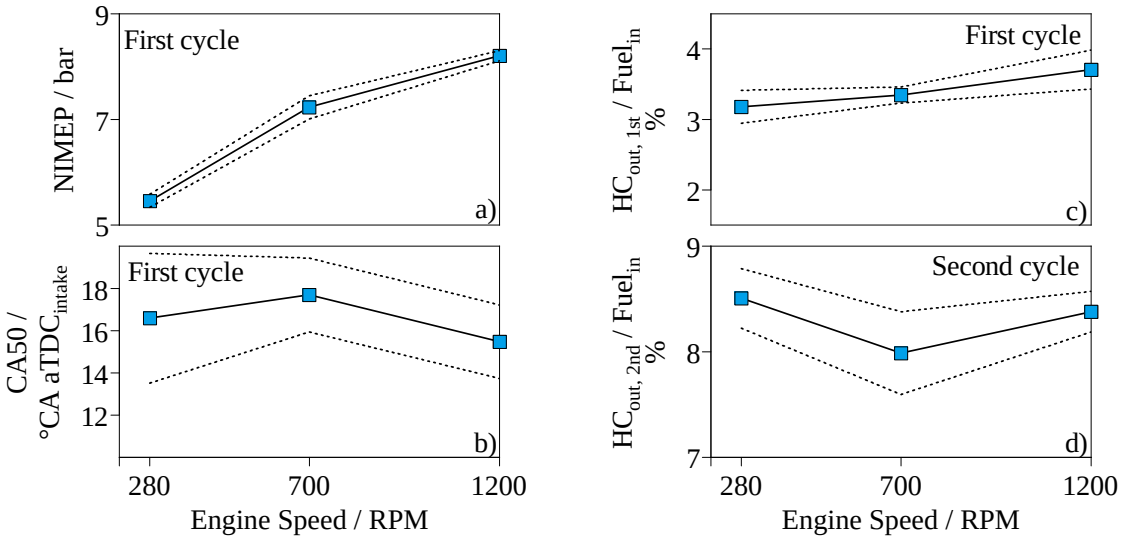

Figure 3-24: Outputs of the single-cycle-fired engine as function of engine speed as follows: (a) 1st cycle NIMEP, (b) 1st cycle CO emissions, (c) 1st cycle relative HC emissions, and (d) 2nd cycle relative HC emissions. Dashed lines correspond to a one standard deviation envelope

Despite the better mixture formation, the HC emissions for the 1st cycle show a slight increase with increasing engine speed (Fig. 3-24-c). This result can be traced back to two opposing effects. On one side, the higher turbulence results in better

fuel atomization and evaporation, increasing the amount of fuel that participates in combustion, and decreasing the total amount of unburned hydrocarbons remaining in the combustion chamber. On the other side, higher engine speed results in lower heat transfer to the cylinder walls, resulting in higher burned gas temperatures during the expansion and the exhaust strokes. This promotes the desorption of HC from the oil layer and the evaporation of liquid films in the combustion chamber. The net effect is a slight increase in the 1st cycle HC emissions. It is important to point out, that if a certain value of NIMEP is targeted, the 1st cycle FEF can be reduced for higher engine speeds, resulting in lower absolute HC emissions.

Since the cycle temperature for the motored cycles does not vary with engine speed as significantly as for the 1st fired cycle, the 2nd cycle HC emissions (Fig. 3-24-d) as well as the HC emitted from the 3rd cycle on (Fig. 3-23) remain insensitive to engine speed. The fraction of unaccounted fuel is mainly a function of the difference in CO_2 production, and therefore reduces with increasing engine speed.

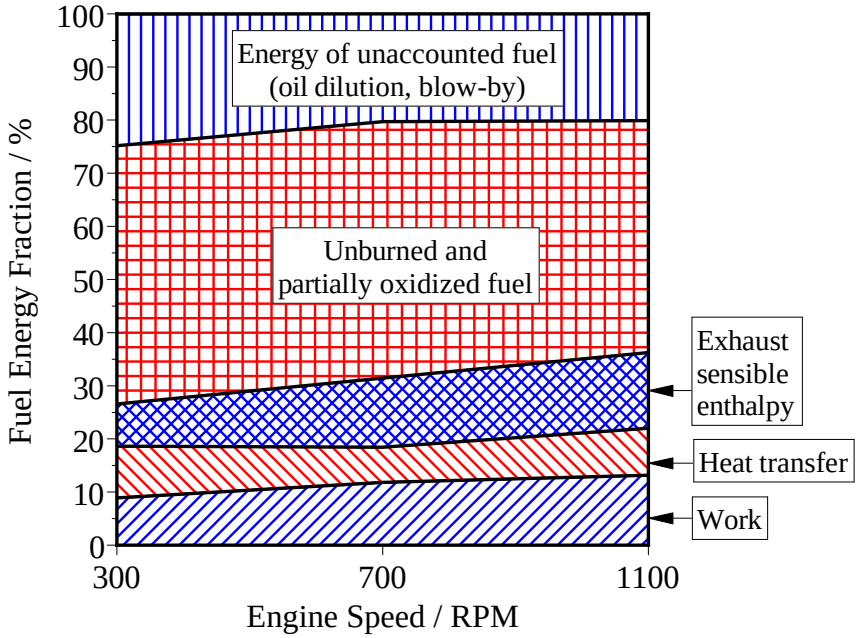

Figure 3-25: Fuel energy accounting for the 1st cycle as a function of engine speed

3.9 Findings

Using a fuel carbon accounting analysis for the 1st combustion cycle, the study presented in this paper aims to quantify the amount of fuel participating in combustion as well as the amount of unburned HC left after combustion leading to HC emissions and residual fuel in the combustion chamber. A one-variable-at-a-time approach was used to isolate the effects of the different parameters affecting the 1st combustion cycle. The study focused in the effects of fuel enrichment, injection and ignition timing, intake manifold and fuel pressure, and engine speed, with the following key findings:

- The injection timing determines the type and degree of interaction between the injection spray and the elements of the combustion chamber. For this particular configuration, it was found that injection during the early compression stroke results in lower HC emissions, due to reduced interaction with the intake valve and piston crown. Injection events close to BDC result in increased liner wetting, therefore increasing the amount of fuel lost as oil dilution.

- The 1st cycle fuel enrichment affects on a one-to-one proportion the absolute 1st cycle HC emissions. Thus, reducing the fuel enrichment is beneficial for HC emissions reduction, but increases the probability of a partial burn or a misfire, which would result in unacceptably high HC emissions. Despite the fuel conversion efficiency being constant at 30% for all FEFs, the energy distribution changes significantly. For low FEF, the late combustion phasing causes increased charge temperatures at EVO and lower temperatures during combustion. As a result the exhaust sensible enthalpy is larger while the wall heat transfer is reduced.

- The spark timing, and the associated combustion phasing, impacts both the amount of fuel participating in combustion as well as the rate of post-flame oxidation. As a general trend, later spark timing results in reduced CO and

slightly lower HC emissions at the cost of lower work output. As already mentioned in the previous point, late combustion phasing affects directly the charge temperatures at exhaust valve opening and the maximum temperature during combustion. Consequently, the exhaust sensible enthalpy and the wall heat transfer follow inverse trends and are highly sensitive to spark timing.

- A reduced intake manifold pressure has a positive influence in mixture preparation, resulting in more fuel participating in combustion. The relative HC emissions are not sensitive to MAP. Due to the reduced amount of fuel injected (at constant enrichment factor), the absolute HC emissions are lower at the cost of lower work output.

- The decrease in droplet size from higher injection pressures is offset by the increase in fuel spray penetration. Fuel utilization increases with injection pressure. The relative HC emissions, however, are not sensitive to injection pressure.

- Higher engine speed promotes turbulence. The improvement in turbulent mass transfer more than compensates for the reduction in mixture preparation time; hence, fuel utilization improves with engine speed. The relative HC emissions increase modestly with higher engine speeds. At the same combustion phasing, NIMEP increases with engine speed because of the better fuel utilization and of the heat loss reduction. For a targeted NIMEP value, therefore, less fuel is needed at the higher engine speed, resulting in reduction of the absolute HC emissions.

Chapter 4

Cycle-by-cycle analysis of cold crank-start

This chapter seeks to expand the understanding of the CO, HC, NOx, and PM/PN emissions behavior during the cold crank-start process of a GDI engine. For that purpose the initial 3 engine cycles are analyzed individually under a set of parameters that include among others the mass of injected fuel, the start of injection (SOI), and the ignition timing. The focus is on the dependence of the CO, HC, PM/PN and NOx emissions. Additionally, the interactions between cycles are also considered by studying the impact that the heat transfer history and the residual fuel from previous injection events have on the mixture formation and FEF requirement.

The PM/PN emissions per cycle decrease by more than an order of magnitude as the crank-start progresses from the 1st to the 3rd cycle, while the HC emissions stay relatively constant. The wall heat transfer during the previous cycles, as controlled by the combustion phasing, has a more significant influence on the mixture formation process for the current cycle than the amount of residual fuel. The results show that the rise in HC emissions caused by the injection spray interacting with the intake

valves and piston crown is reduced as the cranking process progresses. Combustion phasing retard significantly reduces the PM emission. The HC emissions, however, are relatively not sensitive to combustion phasing in the range of interest. NOx emissions mirror the maximum cylinder temperature when mixture stratification is not present.

Part of the results presented in this chapter have been published in the *SAE International Journal of Engines* [60, 62].

4.1 Experiments description

In order to quantify the pollutant mass emissions of the individual engine cycles during crank-start the sampling probes of the fast response analyzers were located as close as possible to the exhaust valve. The methodology for converting concentration measurements to mass emissions is found in Section 2.2.2. The focus of this study was placed on cylinder #4. To suppress pressure, temperature and composition interactions from neighboring cylinders, the engine was operated in single-cylinder mode. As a consequence, the engine was unable to achieve a speed transient that is representative of a 4-cylinder engine during crank-start. To circumvent this, the engine was torque-assisted by a 10 *hp* electric motor during the simulated crank-start experiments. The motor triggering point and speed-ramp were tuned to achieve similar speed traces between multi-cylinder and single-cylinder crank-start. Each experiment starts with the engine motoring at cranking speed until steady state conditions are achieved. After the steady-state motoring, and depending on the engine cycle of interest, 1, 2 or 3 combustion events take place in cylinder #4 (see Fig. 4-1 a-c). Thereafter, engine is motored while the exhaust flow composition and temperatures are recorded until the purging of residual HC is completed and the steady-state conditions are attained. Five experiments were run for each experimental condition; the average values are reported.

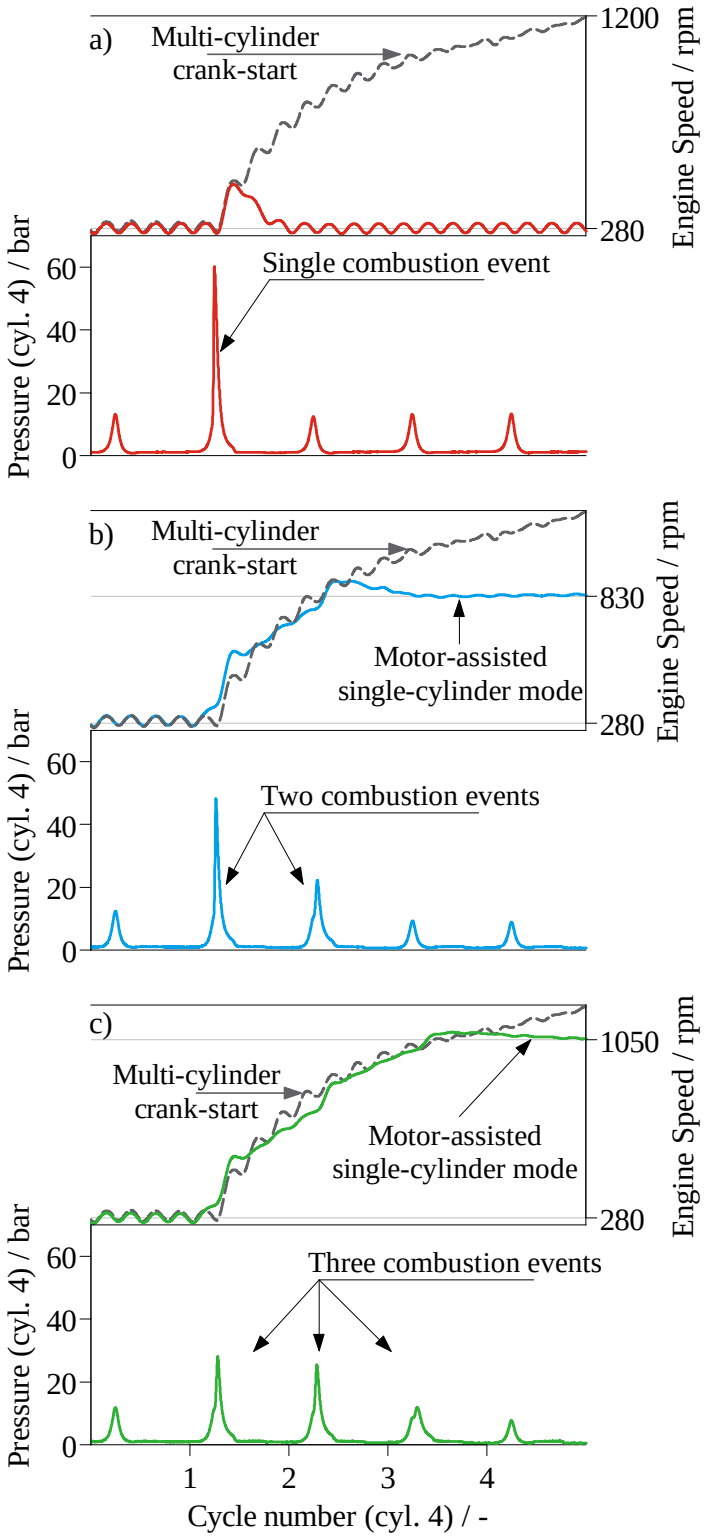

Figure 4-1: Representative traces for the 1st (a), 2nd (b), and 3rd (c) cycle experiments

Throughout all of the experiments the throttle opening was fixed at the fast-idle position (2 *bar* NIMEP, 1200 *rpm*). The engine operated in open-loop mode with the fuel amount being a function of the demanded enrichment, the engine speed and the intake manifold pressure (speed-density calibration). Table 4.1 contains a summary of the typical values of the relevant parameters for the initial 3 engine cycles.

Parameter	**1st cycle**	**2nd cycle**	**3rd cycle**
Fuel mass for FEF = 1 [*mg*]	29.5	26	21
MAP [*bar*]	0.9	0.75	0.6
Speed [*rpm*]	280	800	1050

Table 4.1: 1st cycle strategy for 2nd cycle experiments

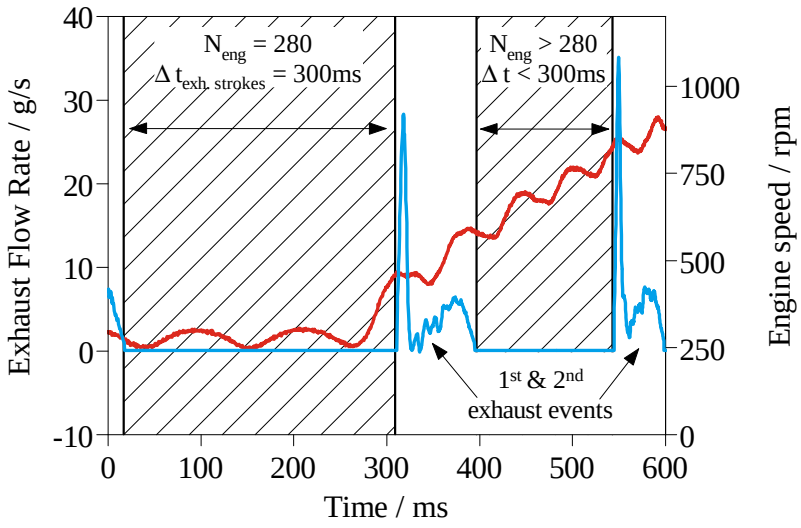

Figure 4-2: Continuous measurement of the particle spectrum does not achieve a cycle-by-cycle resolution

A further particularity of the experiment design has to do with the transit and response delay of the fast analyzers. In comparison to the fast FID and fast NDIR and fast CLD analyzers, the time response of the particle differential mobility analyzer (DMS) is two orders of magnitude slower, precluding crank-angle resolved measurements of the particle spectrum. Still, at $t_{10-90} = 300\ ms$, the instrument's response

time is sufficient to allow cycle-resolved measurement at speeds lower than 280 *rpm*. However, as illustrated in Fig. 4-2, when the engine speed increases during crank-start the DMS is not able to completely differentiate between two engine cycles.

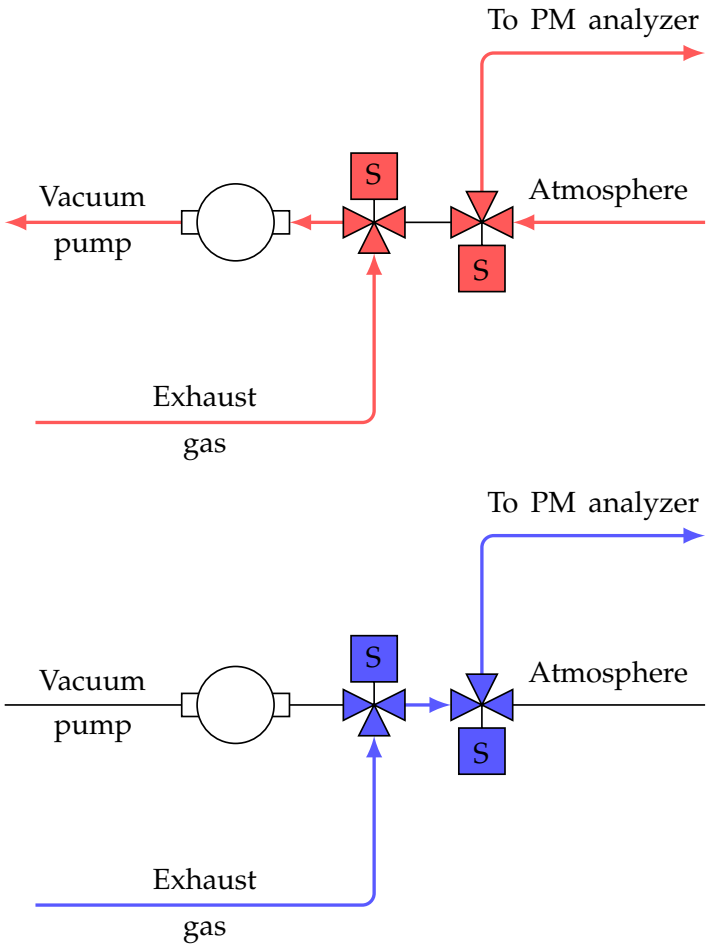

Figure 4-3: Exhaust gas sampling system (EGSS) for cycle-resolved particle spectrum measurement. Top: Closed position feeds ambient air to the analyzer and circulates the exhaust gases to minimize the dead volume. Bottom: Open position feeds exhaust sample to the analyzer

To overcome this obstacle for performing a cycle-resolved analysis of the initial three engine cycles, an exhaust gas sampling system (EGSS) is employed. The objective of the EGSS is to supply to the analyzer only the exhaust gases from the desired cycle, while blocking the exhaust gases from previous and following cycles. The EGSS is

located upstream of the DMS and consists of two three-way solenoid valves connected in series. In the "closed" position (Fig. 4-3-top), the exhaust gas is circulated around the system by a rotary vane vacuum pump in order to minimize dead volumes, while the DMS is allowed to sample ambient air in order to maintain its internal pressure within range. In the "open" position (Fig. 4-3-bottom) the exhaust and sample flows are connected, and the DMS is able to carry out defectively the particle spectrum measurement for the desired engine cycle. The solenoid valves have a 3/32" orifice and an opening time of 10 ms. The EGSS is controlled by a programmable micro-controller that uses the crankshaft encoder signal as an input for the timely actuation of the solenoid valves.

4.2 First cycle analysis

A number of variables influence the mixture formation process and the emissions behavior of the 1st firing cycle during the cranking process. This section focuses on the four most relevant injection parameters using a one-variable-at-a-time approach. The variables studied are: Start of injection (SOI), fuel enrichment factor (FEF), ignition timing, and fuel pressure. The swept ranges and the nominal points are presented in Table 4.2. Unless otherwise stated, all the variables stay constant at the nominal values during the different sweeps.

Parameter	**Sweep range**		**Nominal value**
SOI [°CA aTDC$_{\text{intake}}$]	30 − 315	$\Delta = 15$	90
FEF [−]	1.7 − 3.5	$\Delta = 0.2$	2.5
Spark [°CA aTDC$_{\text{comp.}}$]	−45 − 20	$\Delta = 5$	-10
Fuel pressure [bar]	30 − 110	$\Delta = 20$	50

Table 4.2: Experimental scope for the 1st cycle emissions

4.2.1 First Cycle: Start of Injection and Fuel Enrichment

The two most important variables affecting the mixture formation and the combustion and emissions behavior are the SOI and the FEF. Figure 4-4 shows the dependence of the CO, NOx and HC emissions on the injection timing, while keeping the rest of the variables at the nominal values shown in Table 4.2. As seen in Fig. 4-4-top, the CO emissions stay below 3 mg for SOI $\leq$ 240°CA aTDC$_{intake}$. For later injection timings, the enrichment around the spark-plug increases as a result of mixture stratification, and the CO emissions increase rapidly.

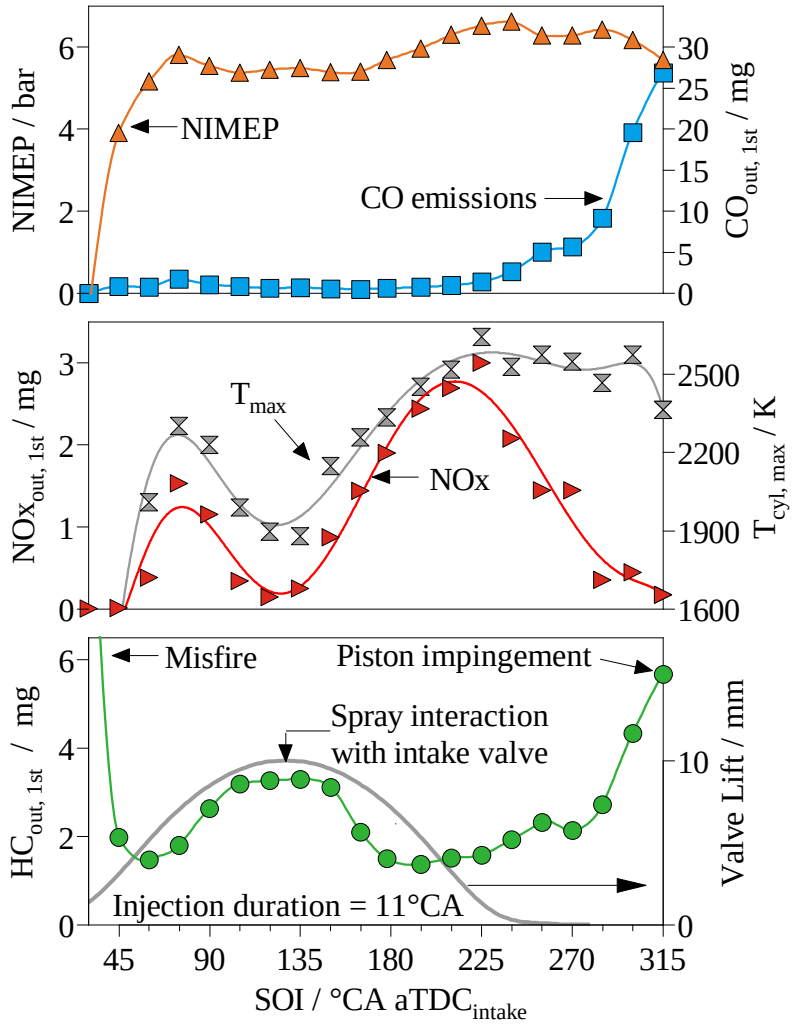

Figure 4-4: 1st cycle CO, NOx and HC emissions as a function of the SOI

The NOx emissions show a strong dependence with SOI covering a range from $0.1 - 3$ mg (Fig. 4-4-middle). As discussed in section 3.3, the injection timing influences the amount and timing of the heat release from combustion as well as the spatial distribution of the AFR. Given that NOx formation is driven by both temperature and oxygen availability [30], the cylinder averaged temperatures serves as a good first order indicator. As observed in Fig. 4-4 up to SOI = 225°CA $\text{aTDC}_{\text{intake}}$, the maximum cylinder-averaged temperature and the NOx emissions exhibit very similar trends. For later injection timings, as the mixture becomes stratified, the oxygen availability in the high-temperature zone is reduced leading to lower NO production.

Due to the interaction of the spray with the piston at very early injections (SOI $\leq$ 30°CA $\text{aTDC}_{\text{intake}}$) the engine misfires resulting in negative NIMEP and high HC emissions. For SOI between 45 to 75°CA $\text{aTDC}_{\text{intake}}$ significant piston impingement is avoided and the relative HC emissions are reduced to 1.5 mg while the NIMEP increases from 4 to 6 bar. For the SOI range from 90 to 180°CA $\text{aTDC}_{\text{intake}}$ the HC emissions increase to a peak value of 3.3 mg and then decrease again to 1.5 mg, due to the interaction between the injection spray with the intake valve (notice in Fig. 4-4 that the maximum valve lift coincides with the highest HC emissions). As the valve recedes into its seat during the early part of the compression stroke, SOI ranging from 180 to 225°CA $\text{aTDC}_{\text{intake}}$ results in consistently lower HC emissions at approximately 1.5 mg while the NIMEP increases from 5.5 to 6.8 bar, suggesting better mixture formation. Lastly, for injection during the late compression stroke (SOI = 240 to 315°CA $\text{aTDC}_{\text{intake}}$) the HC and CO emissions increase significantly, while the NIMEP goes down slightly. At this late SOI, the interaction between the injection spray and the piston promotes the formation of fuel films on the piston crown, as well as an overly enriched air-fuel mixture around the spark-plug.

The PM/PN emissions (Fig. 4-5) exhibit some similarities to the HC emissions

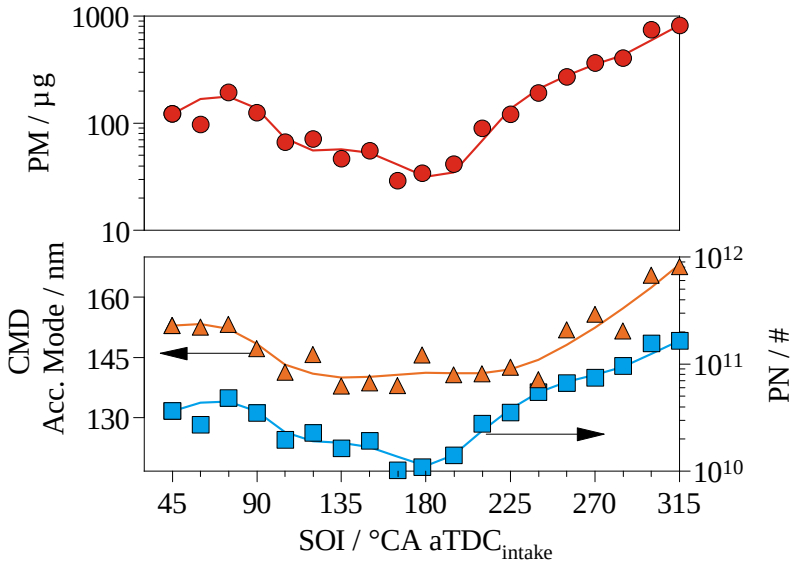

Figure 4-5: 1st cycle PM/PN emissions and median particle size as a function of SOI

(Fig. 4-4-bottom), especially for SOI during the compression stroke. For SOI during the intake stroke, the soot emissions decrease monotonically to a minimum of 30 μg and 10^{10} number of particles. The count median diameter (CMD) of the particles is also slightly reduced from 150 nm to 140 nm. The interaction of the fuel spray with the intake valve has no noticeable effect, and the trends are dominated by the interaction with the piston. As the SOI moves into the compression stroke, the particle emissions increase significantly, both in number and size, reaching 1.6×10^{11} and 168 nm respectively, corresponding to a PM emission of 800 μg.

Having analyzed the impact of the injection timing on the emissions behavior of the 1st cycle, the attention is now placed on the injected fuel amount as quantified by the fuel enrichment factor (FEF). It is desirable for any cold transient to maximize the work output while at the same time minimizing the pollutant emissions. In this regard, the crank-start process is not different. Figure 4-6-top presents the 1st cycle NIMEP as a function of the FEF for 4 different injection strategies. The respective tradeoffs between NIMEP and pollutant emissions are presented in Fig. 4-6 for CO

and HC (middle and bottom), in Fig. 4-7 for PM/PN and in Fig. 4-8 for NOx. Four different injection strategies were selected for the FEF sweep:

1. Injection during intake valve opening (SOI = 90°CA aTDC$_{\text{intake}}$).
2. Early compression stroke injection (SOI = 195°CA aTDC$_{\text{intake}}$).
3. Split injection with a fixed second injection mass at 6 mg (SOI 1/2 = 195/330°CA aTDC$_{\text{intake}}$).
4. Late compression stroke injection (SOI = 345°CA aTDC$_{\text{intake}}$).

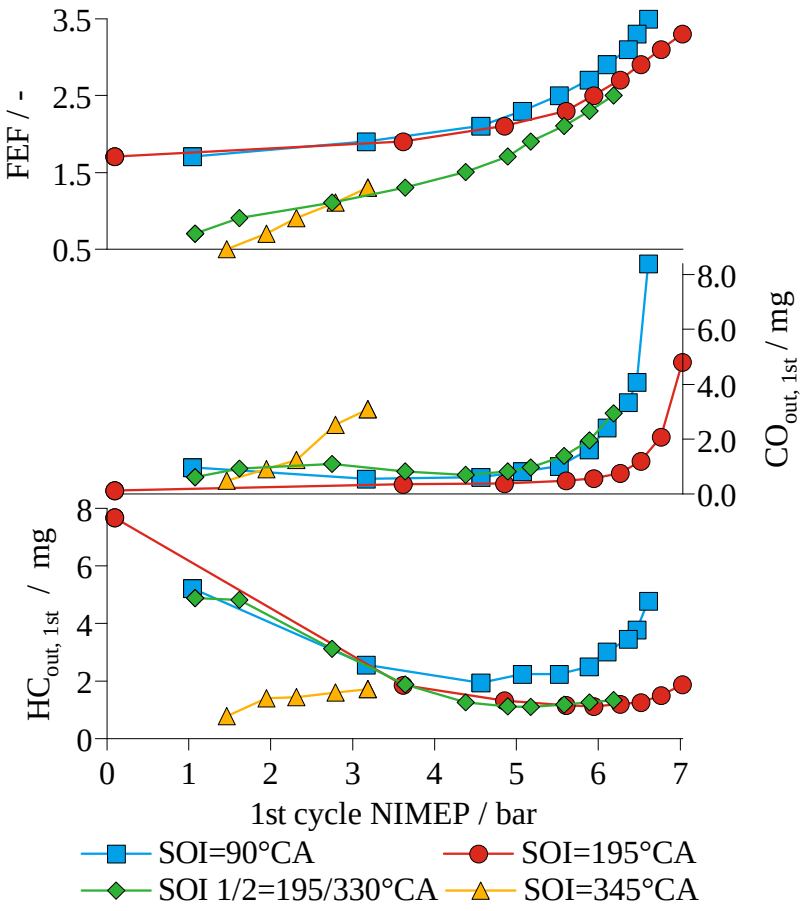

Figure 4-6: Effect of FEF on NIMEP, CO, and HC emissions for the 1$^{\text{st}}$ cycle for injection strategies 1 trough 4

In general, the NIMEP increases monotonically with FEF, with a reduced trend when the mixture becomes overly enriched around the spark-plug, as can be inferred from the increasing partial oxidation of the fuel to CO (Fig. 4-6-middle). The late injection strategy (SOI = 345°CA $aTDC_{intake}$) reduces the minimum FEF requirement for avoiding a partial burn or a misfire, while keeping the HC emissions at a low level. On the other hand, the soot emissions (Fig. 4-7) increase dramatically in number and size even at low NIMEP, making this injection strategy unattractive.

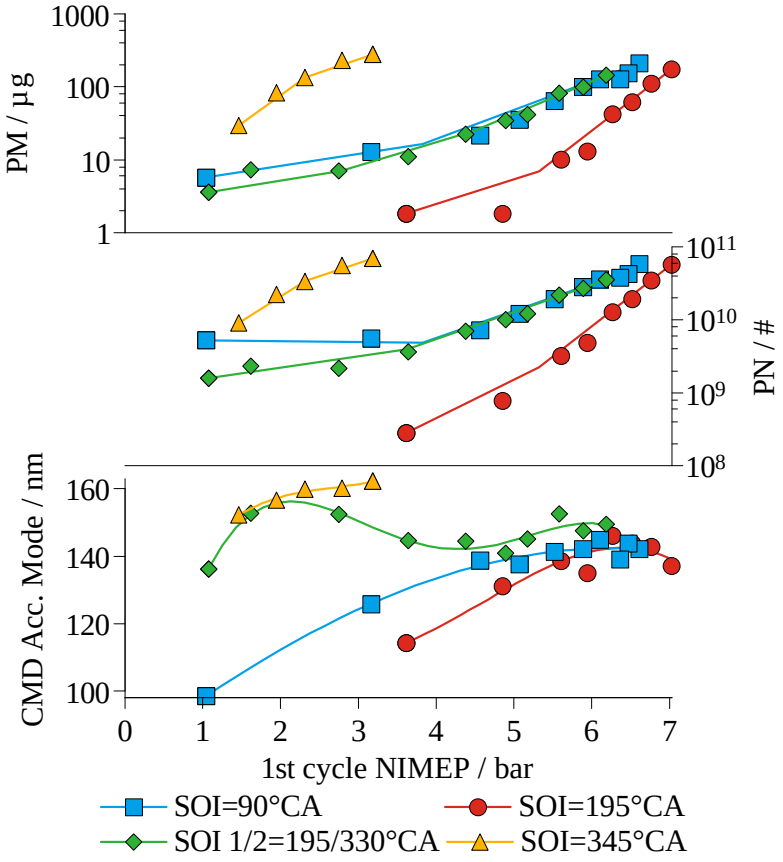

Figure 4-7: Effect of FEF on PM/PN emissions and median particle size for the 1st cycle for injection strategies 1 trough 4

Injection during intake valve opening (SOI = 90°CA $aTDC_{intake}$) results in the highest HC emissions and increased FEF requirement for a given NIMEP (see Fig. 4-6). In comparison to closed valve injection, the soot emissions are also deteriorated exhibiting PM emissions up to an order of magnitude higher.

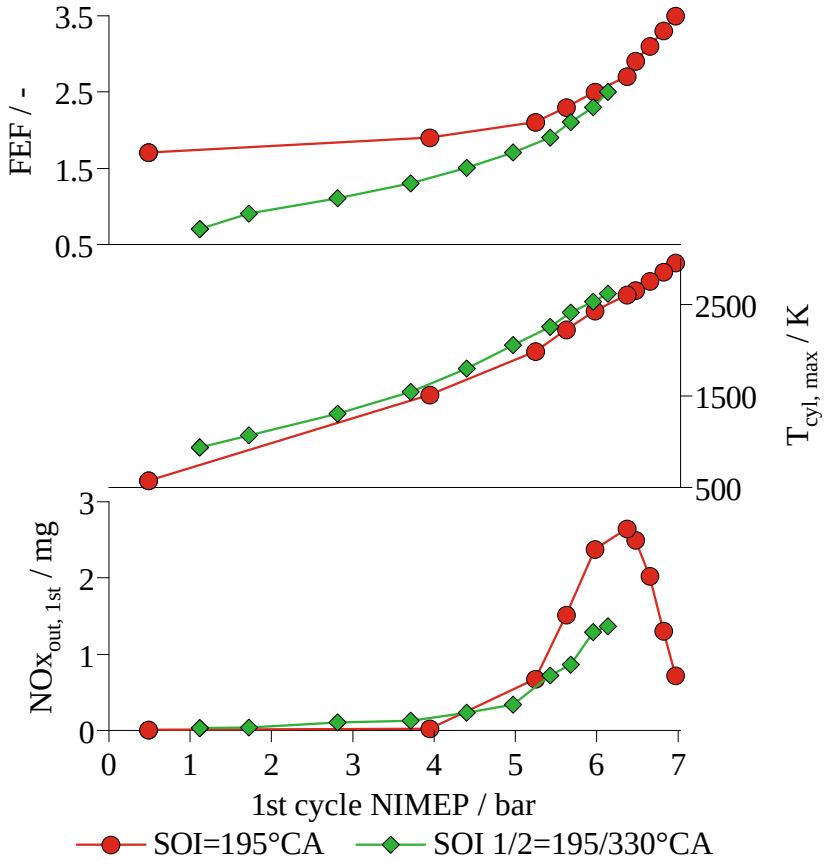

Figure 4-8: Effect of FEF on NIMEP, cylinder-averaged maximum temperature, and NOx emissions for the 1st cycle for injection strategies 2 and 3

A common strategy used by OEMs during engine crank-start is the so called high-pressure stratified start [20, 41, 42]. The split injection strategy used in this study aims to reproduce such approach. The injection of a small amount of fuel (6 mg) late in the compression stroke reduces the FEF requirement for a given NIMEP, by creating a stratified mixture around the spark-plug. Furthermore, the HC emissions for a given NIMEP remain at the same level of the single injection in the early compression stroke (SOI = 195°CA $aTDC_{intake}$), suggesting that the reduction in FEF compensates for the increase HC production caused by piston impingement (Fig. 4-6-bottom). As shown in Fig. 4-8, the high-pressure stratified start is also advantageous for reducing NOx emissions. The mixture enrichment at the spark-plug reduced the

oxygen availability during the high temperature phase of the flame development. As the flame propagation transitions to the homogeneous mixture, the piston downward displacement lowers the cylinder temperature and reduces NO formation. Although the piston interaction has a negligible effect on the HC emissions, its effect on the PM/PN emissions (Fig. 4-7) is significant as it increases the soot mass emissions up to an order of magnitude, achieving similar values as the open valve injection strategy.

Lastly, injection during the early compression stroke (SOI = 195°CA $aTDC_{intake}$) results in the most favorable injection strategy in terms of pollutant emissions for a given NIMEP, if the risk of partial burn or misfire is correctly managed by adjusting the minimum FEF appropriately. The HC and PM emissions are the lowest compared to the other three strategies evaluated. Given that the NO production is a function of both temperature history and oxygen availability, the NOx emissions peak at FEF = 2.7; for lower FEF the amount of heat realease is reduced, for larger FEF values, the O_2 concentration in the high temperature zone is reduced. As a result, in order to control the NO production with a homogeneous injection strategy without drastically increasing the FEF it is necessary to reduce the 1^{st} cycle NIMEP to below 6 *bar*; this corresponds to FEF less than 2.5.

In summary, in comparison to the early compression stroke single injection strategy (SOI = 195°CA $aTDC_{intake}$), the open valve injection results in increased HC and PM emissions. Late compression injection, increases the combustion robustness at the cost of very high PM emissions. The high-pressure stratified start strategy, increases the combustion robustness and achieves the same HC emissions performance, reduces NOx emissions, but increases the PM emissions by an order of magnitude. The saddle shape of the 2-D sweep depicted in Fig. 4-9 shows that the increased stratification of late injection timings can improve the HC emissions at low FEF as a consequence of faster burn rates reducing the amount of fuel that is only partially oxidized. At higher FEF, when partial burn is no longer a concern, later SOI results in higher HC

emissions due to piston impingement. The dependence of PN on SOI and FEF for compression injection is monotonous. Later SOI and higher FEF result invariably in higher soot emissions.

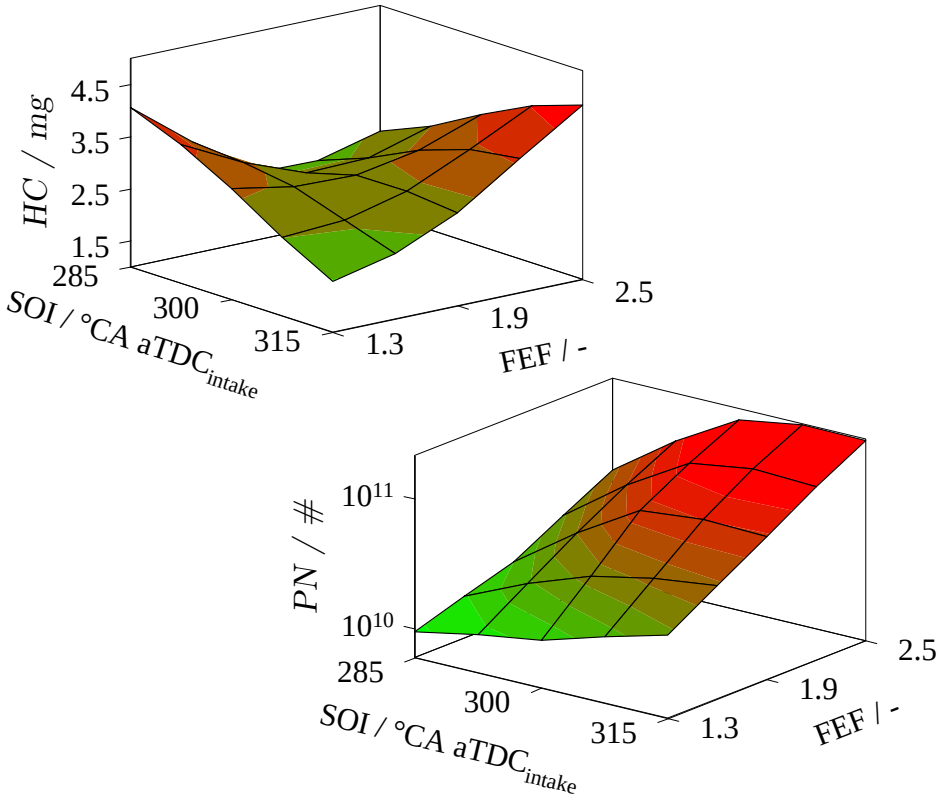

Figure 4-9: HC and PN dependence on late SOI and FEF for the 1st cycle

The effect of the FEF on the combustion phasing can be seen in Fig. 4-10. Open valve injection results in the highest sensitivity of the mass fraction burned (MFB) to FEF. As injection is delayed to the early compression stroke, the sensitivity is reduced. Further reduction is achieved by the split injection strategy, achieving a constant CA10 and CA50, with CA90 remaining a function of FEF. In the case of very late single injection, the dependence of combustion phasing to FEF disappears.

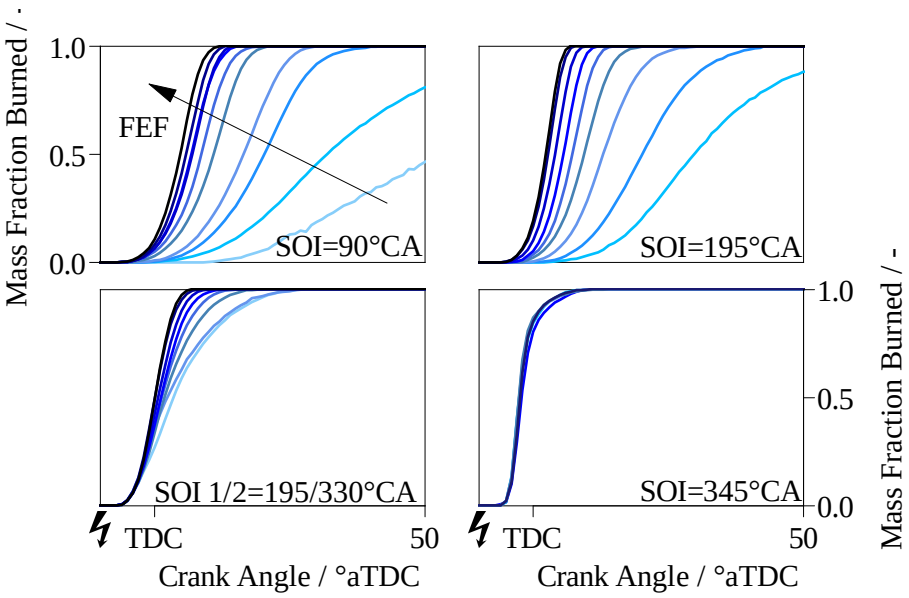

Figure 4-10: Effect of the FEF on the combustion phasing for 4 different injection strategies

4.2.2 First cycle: Ignition timing

A well-known strategy for the reduction of engine-out HC emissions and fast catalyst warm-up during steady state operation consists on retarding of the spark timing [7, 8, 21]. The reduction in HC emissions with spark retard is mainly associated with the in-cylinder consumption of the fresh mixture stored in the crevice volumes by the flame, with post-flame and exhaust runner oxidation playing less important roles [21]. During the cold crank-start of GDI engines, the significant over-fueling necessary to form a combustible mixture results in the formation of fuel films. The liquid fuel films become a dominant source for HC emissions, comparable to or greater than the crevice storage mechanism [14]. Higher burned gas temperatures in the expansion process with retarded timing promotes both the evaporation and oxidation of the HC contained in the fuel films. Thus, the impact of late combustion phasing on crank-start HC emissions in not straight forward.

Three different injection strategies were tested:

1. Injection during intake valve opening (SOI = 90°CA aTDC$_{intake}$).

2. Early compression stroke injection (SOI = 195°CA aTDC$_{intake}$).

3. Split injection with a fixed second injection mass at 6 *mg* (SOI 1/2 = 195/330°CA aTDC$_{intake}$).

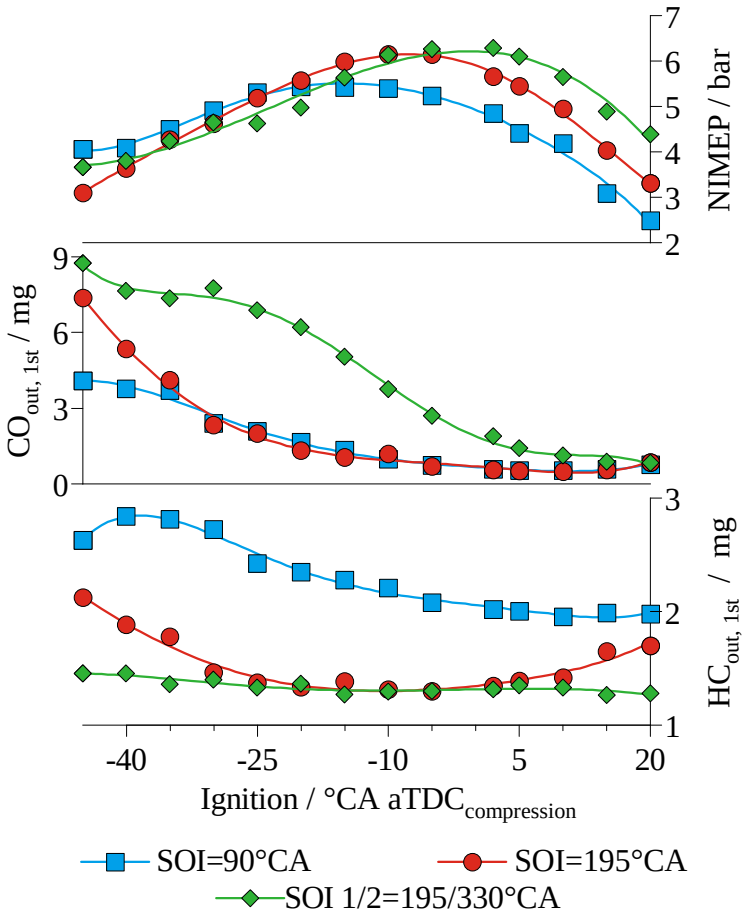

Figure 4-11: Effect of spark timing on 1st cycle NIMEP, CO and HC emissions for injection strategies 1 trough 3

Figure 4-11 shows the HC emissions as a function of the ignition timing for strategies 1 through 3, all other parameters remaining constant at their nominal value (see Table 4.2). The ignition timing was varied from -45 to 20°CA aTDC$_{comp.}$. Higher CO emissions for advanced ignition timings can be observed for all injection strategies.

Advanced ignition results in higher unburned gas temperatures in the fresh mixture ahead of the flame front. This promotes the evaporation of the fuel films on the cylinder walls, leading to the formation of a richer mixture for the last gas elements participating in combustion, increasing the formation of CO and CO_2. Additionally, advancing the spark timing reduces the time between the end of injection and the ignition point. As a result, the spatial distribution of the AFR around the spark plug at ignition timing influences the production of CO.

In the case of open valve injection, advanced ignition results in higher relative HC emissions at 2.8 mg. The retarding of the ignition timing to 2°CA $aTDC_{comp.}$ results in a HC emissions reduction to 2 mg (≈ 0.8 mg reduction). Further spark retard does not lead to an additional benefit, and does result in a sharp decrease in NIMEP. In the case of early compression injection, the relative HC emissions are insensitive to spark timing in the ignition range from -30 to 10°CA $aTDC_{comp.}$, remaining constant at approximately 1.3 mg, and exhibiting an increase for very early or very late ignition. The HC emissions of the split injection are insensitive to ignition timing, remaining in the range 1.3 to 1.4 mg for the entire sweep.

In normal engine operation, substantial reduction in HC is observed with spark retard, which increases the charge temperature in the later part of the expansion process and facilitates the oxidation of the crevice HC, which is a major source [12]. In the 1^{st} cycle of the cranking process, however, the major HC source is the fuel vapor from the fuel film on the cylinder surfaces. The amount of HC is substantial, and, unlike the crevice HC, it is not premixed with air. Thus the amount of HC that gets oxidized is small compared to the total amount. Therefore the HC emissions are not sensitive to the extent of secondary oxidation. Hence spark timing, which influences secondary oxidation, does not materially affect the HC emissions.

On the other hand, the particulate emissions are very sensitive to the spark timing as can be seen in Fig. 4-12. For injection strategies 1 and 3 (early injection timing

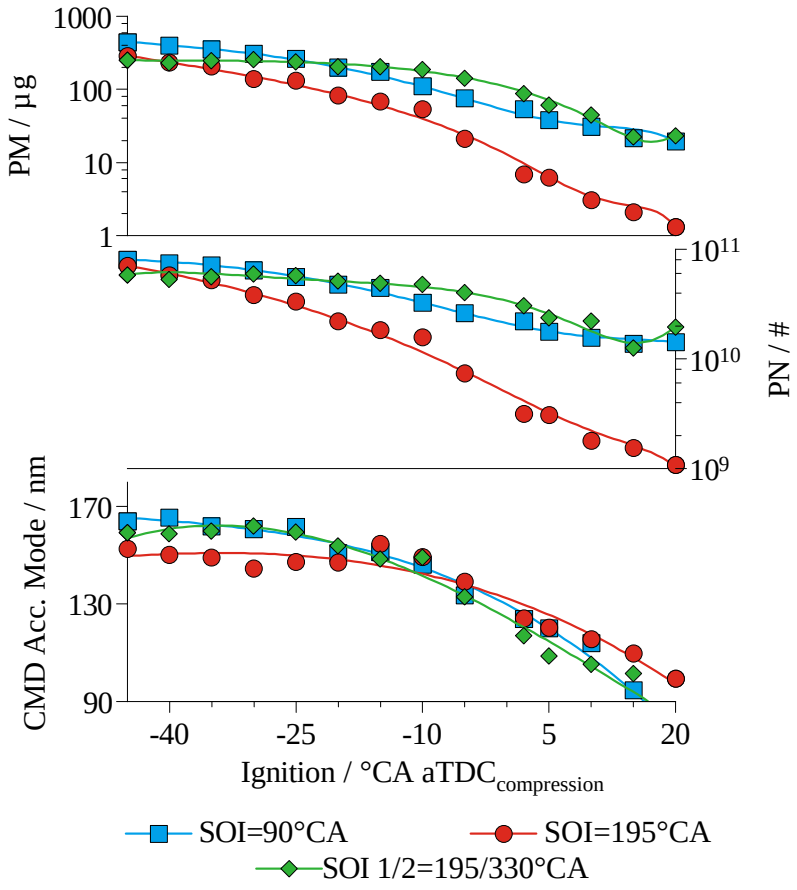

Figure 4-12: Effect of spark timing on 1st cycle PM/PN emissions for injection strategies 1 trough 3

and split injection) the retard in spark timing from −45 to 20°CA aTDC$_{comp.}$, results in a PM reduction of an order on magnitude. This result is driven by both a reduction in PN, as well as by the halving of the particle size. In the case of early compression injection (SOI = 195°CA aTDC$_{intake}$), the reduction in PM with spark timing is even more significant covering over 2 orders of magnitude (250 μg at −45°CA aTDC$_{comp.}$ to 1.3 μg at 20°CA aTDC$_{comp.}$). The result is driven by both the reduction in particle formation (PN) and a reduction of the accumulation process resulting in smaller particles (CMD). For the PM emission, the formation of the particulates is a result of the post-flame pyrolysis of the rich unburned mixture formed from the fuel vapor that evaporates from the in-cylinder liquid fuel film [35]. With spark retard, the

flame arrival to the cylinder wall is delayed. This reduces the time available for the pyrolysis to occur, thereby reducing both the amount of particle formation and their growth.

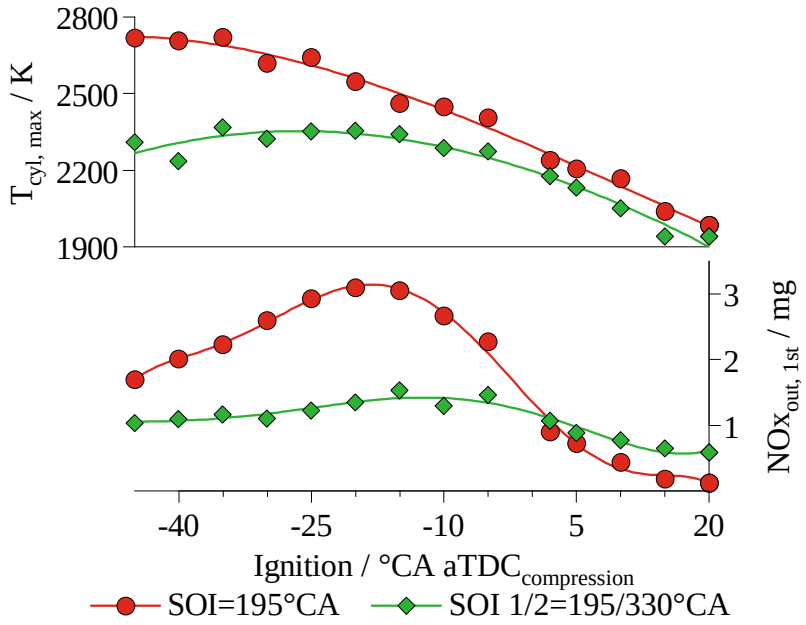

Figure 4-13: Effect of spark timing on 1st cycle NOx emissions for injection strategies 2 and 3

Figure 4-13 shows the 1st cycle NOx emissions for injection strategies 2 and 3 (early compression injection and split stratified injection). For both strategies, the NOx emissions peak at a spark timing of -15°CA $aTDC_{comp.}$. However, as already pointed out in Section 4.2.1, the split injection strategy results in significant lower NOx emissions. Focusing on the early compression injection strategy (red line in Fig. 4-13), the NOx emissions vary greatly with ignition timing between 0.1 and 3 mg. The reduction of NOx with later combustion phasing has a straight forward explanation; delay ignition reduces the peak combustion temperatures and thus NO formation. On the other hand, advancing the spark timing earlier than -15°CA $aTDC_{comp.}$ results too in NOx emissions reduction, despite the increase in cylinder-averaged maximum temperature.

The trend observed in Fig. 4-13 can be explained by considering the time available for mixture formation. As the spark timing is advanced, the time between end of injection and ignition is reduced, leading to a more heterogeneous mixture. As a result, the local and temporal enrichment of the mxiture around spark plug for advanced ignition timings reduces the O_2 availability and limits the NO formation. Furthermore, looking closer at the burned gas temperature and residence time in the hot temperature zone gives further insight. Figure 4-14 shows simulated results during a spark sweep for the burned gas temperature, mass fraction burned and in-cylinder pressure. Advancing the combustion phasing significantly increases the peak combustion temperature but also reduces the residence time of the burned gases in the high temperature region. Additionally, the evaporation of fuel films towards the end of the flame propagation at advanced spark timings results in a richer end-gas mixture with a reduced oxygen availability. The combined effect is the reduction in NO formation with spark advance earlier than $-15°$CA aTDC$_{\text{comp.}}$.

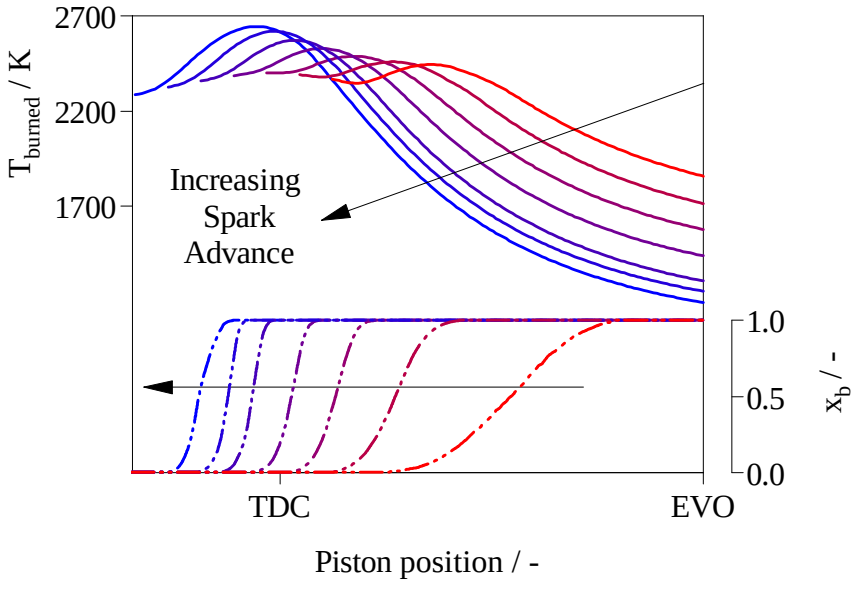

Figure 4-14: Simulated burned gas temperature, combustion phasing and cylinder pressure for different ignition timings

4.2.3 First cycle: Fuel pressure

The injection pressure has a direct influence in the mixture formation process due to its impact in fuel droplet size and momentum affecting the evaporation behavior, wall wetting and charge turbulence. Emissions performance and combustion behavior of current GDI injection systems benefit from increased injection pressures, with 200 *bar* being today's standard pressure [32]. During engine cranking the fuel pressure must increase from around 5 *bar* (low pressure pump) to the targeted 1st cycle injection pressure. The pressure build-up is a function of the cranking time before the 1st cycle injection and the cranking speed. A typical 1st cycle fuel pressure lies between $30 - 50$ *bar* [4].

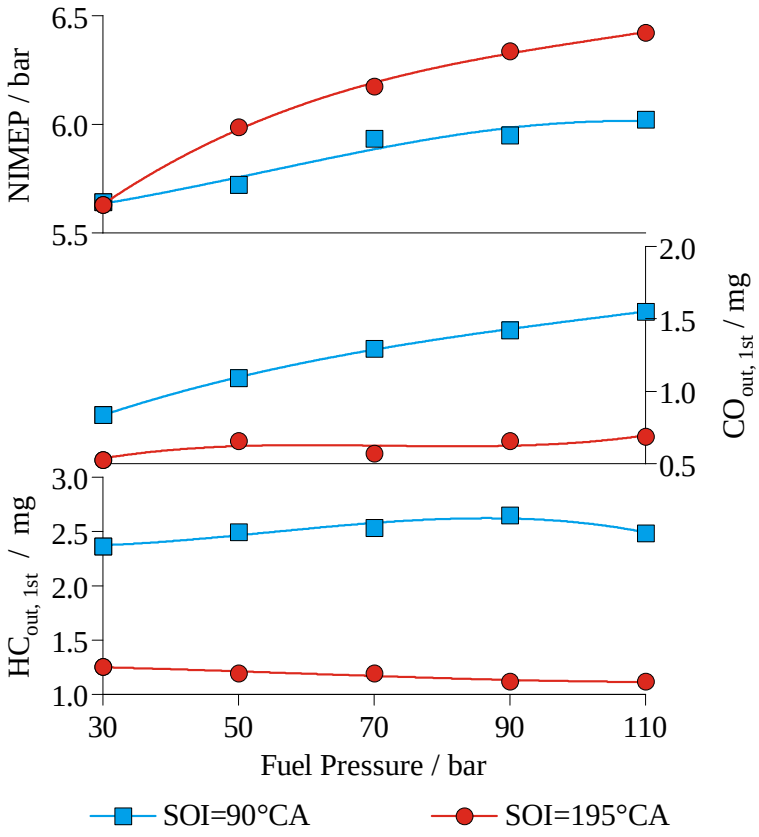

Figure 4-15: Effect of fuel pressure on 1st cycle NIMEP, CO and HC emissions

This section concerns itself with the effect of increasing the 1st cycle fuel pressure on the HC, PM/PN and NOx emissions. Two different injection strategies were tested:

1. Injection during intake valve opening (SOI = 90°CA aTDC$_{intake}$).

2. Early compression stroke injection (SOI = 195°CA aTDC$_{intake}$).

Higher fuel pressure results in better mixture formation as can be inferred from the increasing NIMEP (Fig. 4-15-top). CO emissions are insensitive for early compression injection (SOI = 195°CA aTDC$_{intake}$), while they increased with higher fuel pressure for the open valve injection strategy (SOI = 90°CA aTDC$_{intake}$) due to interaction of the spray with the intake valve. A similar observation was made for the HC emissions; insensitive for early compression injection, and a slight increase with fuel pressure for open valve injection (Fig. 4-15-bottom).

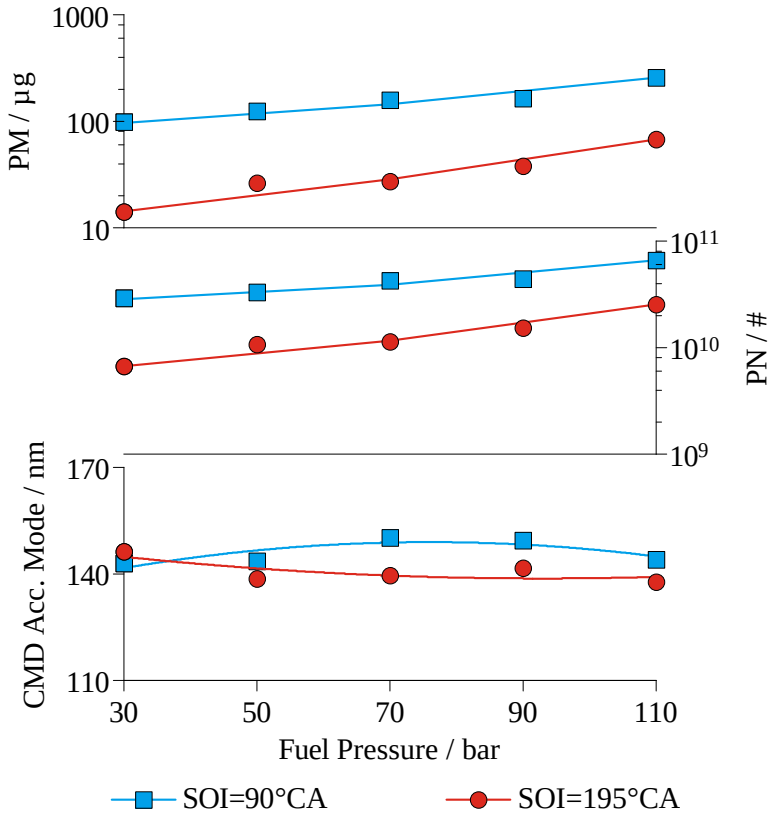

Figure 4-16: Effect of fuel pressure on 1st cycle PM/PN emissions

As was already observed during the investigation of the other parameters in Table 4.2, PM/PN emissions have a higher sensitivity to the injection strategy, in this case to fuel pressure. As shown in Fig. 4-16, open valve injection (SOI = 90°CA $aTDC_{intake}$) results in a PM emissions increase of 2.5 times going from 100 μg at 30 bar to 250 μg at 110 bar. For early compression injection (SOI = 195°CA $aTDC_{intake}$), the relative increase is more substantial going from 14 μg to 67 μg in the same range. In both cases the increase on PM was driven by an increase in particle nucleation (PN), since the fuel pressure showed no significant effect on the particles median size (Fig. 4-16-bottom).

Figure 4-17 shows the NOx emissions as a function of fuel pressure for the early compression injection strategy (SOI = 195°CA $aTDC_{intake}$). The NOx emissions and the peak cylinder-averaged temperature correlate well for lower fuel pressures. For $P_{fuel} > 70$ bar, the NOx emissions stay constant despite the higher cylinder temperature. This is likely to be due to changes in spatial distribution of the AFR with changing fuel pressure.

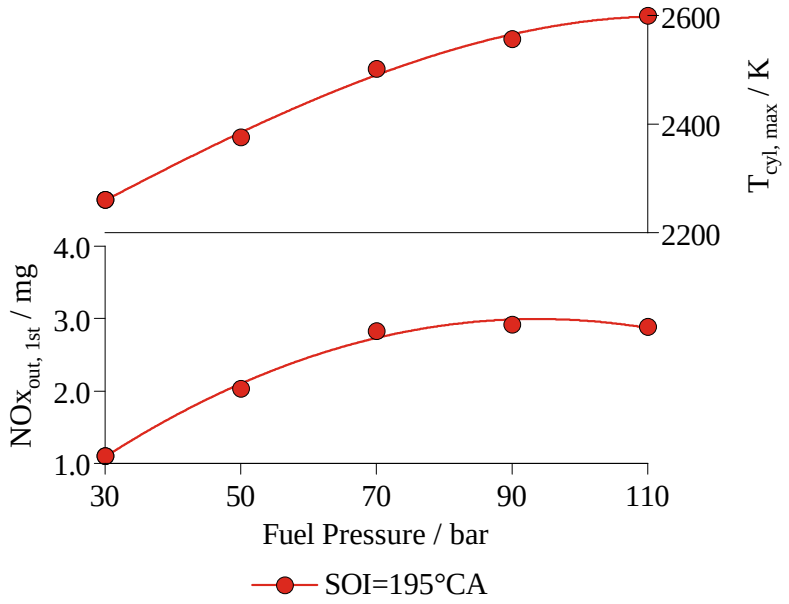

Figure 4-17: Effect of fuel pressure on 1st cycle NOx emissions

In summary, increasing the 1st cycle fuel pressure from the levels found in today's GDI engines has only a reduced benefit on the 1st cycle NIMEP, which is more than offset by the worse performance in PM/PN emissions. The HC emissions behavior was linked to the SOI, with increased HC emissions for injection during IVO at higher fuel pressures; and insensitive behavior for early compression stroke SOI. Although reducing the fuel pressures below 50 *bar* improves the emissions performance, it is not recommended since it would pose a constraint for late SOI strategies.

4.3 Second cycle analysis

The 2nd engine cycle during crank-start differs significantly from the 1st cycle previously described in the main following points:

- Presence of residual fuel from previous injection event.
- Wall heating from previous combustion event.
- Presence of residual exhaust gases during the mixture formation.
- Higher engine speed and lower manifold pressure.

This section focuses on the three of the most relevant injection parameters using a one-variable-at-a-time approach. The variables studied are: Start of injection (SOI), fuel enrichment factor (FEF), and ignition timing. The swept ranges can be found in Table 4.3. In order to decouple the effects of the 1st cycle injection strategy on the 2nd cycle emission analysis, the 1st cycle strategy was kept constant as shown in Table 4.4.

Lastly, the interactions between the 1st and 2nd cycles are also studied by considering the impact that the heat transfer history and the residual fuel from the previous

injection event have on the mixture formation and fuel enrichment requirement of the 2nd cycle. The results can be found in Section 4.3.4.

Parameter	Sweep range		Nominal value
SOI [°CA aTDC$_{\text{intake}}$]	30 − 315	$\Delta = 15$	180
FEF [−]	1.3 − 2.1	$\Delta = 0.2$	1.7
Spark [°CA aTDC$_{\text{comp.}}$]	−45 − 5	$\Delta = 5$	-10

Table 4.3: Experimental scope for the 2nd cycle emissions

Parameter	1st cycle
SOI [°CA aTDC$_{\text{intake}}$]	180
FEF [−]	2.5
Spark [°CA aTDC$_{\text{comp.}}$]	−10

Table 4.4: 1st cycle strategy for 2nd cycle experiments

4.3.1 Second cycle: Fuel Enrichment Factor

Figure 4-18 shows the 2nd cycle emissions behavior as a function of FEF. The combustion λ decreases linearly with FEF with a slope of -0.49, in other words increasing FEF by 0.2 would decrease combustion λ by approximately 0.1. As the combustion λ decreases below 1.1, the CO emissions show a steep increase. This indicates that, despite having a lean global AFR, there are rich regions in the air-fuel mixture responsible for the CO production. The NOx emissions increase from a minimum of 0.2 mg at FEF = 1.3 to a maximum of 1.3 mg at FEF = 1.9 driven by the increase in combustion temperature. For FEF > 1.9 the NOx emissions decrease due to the lower O_2 availability of the over-enriched mixture. With the exception of FEF = 1.3 (partial burn), the HC emissions exhibit a slight monotonic increase with FEF at a rate of 0.07 mg of HC for a 0.2 step in FEF. The PM emissions increase

is more substantial with FEF, for a 0.2 step in FEF, the 2nd cycle PM emissions increase in $\approx 2.5\ \mu g$. A fuel enrichment factor of 1.7 provides a good balance between emissions behavior and the combustion robustness.

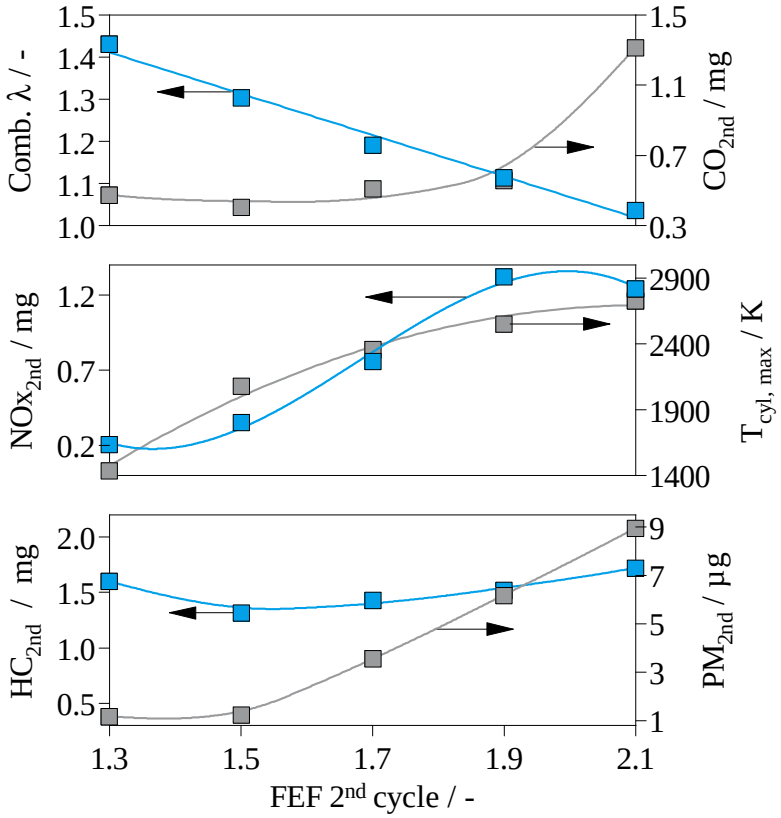

Figure 4-18: 2nd cycle CO, NOx, HC and PM emissions as a function of FEF

4.3.2 Second cycle: Start of injection

Following a similar approach as in Section 4.2.1, the analysis is extended to the 2nd cycle dependence on the injection timing. The FEF and spark timing were held constant at 1.7 and -10°CA aTDC$_{\text{comp.}}$ throughout the sweep as well as the injection strategy of the 1st cycle. The FEF selection for the 2nd cycle is based on the trends presented in Section 4.3.1 and resulted in a fuel mass of approximately 44 mg and an injection duration of 15°CA.

The NIMEP, CO and HC emissions as a function of the injection timing are shown in Fig. 4-19. The trends observed in the SOI sweep are similar in shape for the 1st cycle (see Fig. 4-4), although the magnitudes differ. Injection timings earlier than 45°CA $aTDC_{intake}$ cause significant piston impingement and poor mixture formation. As SOI is retarded the piston impingement is reduced, favoring the mixture preparation and resulting in a sharp increase in NIMEP. At SOI = 75°CA $aTDC_{intake}$ the NIMEP reaches a local maximum and the HC emissions start to increase rapidly due to spray interaction with the intake valve. From SOI = 75 to 180°CA $aTDC_{intake}$ the intake valve wetting reduces the work output (NIMEP), increases the HC emissions and has no effect on the CO production. The maximum intake valve lift corresponds with a local minimum in NIMEP and a local maximum in HC emissions. However, compared to the 1st cycle (Fig. 4-4), the spray/valve interaction has a lower absolute impact on HC emissions and an greater impact on NIMEP. Under the assumption that the fuel mass required to form a fuel film on the back of the intake valve is independent from the injected amount, it can be argued that the relative amount of fuel lost due to valve wetting increases as the injected fuel mass decreases.

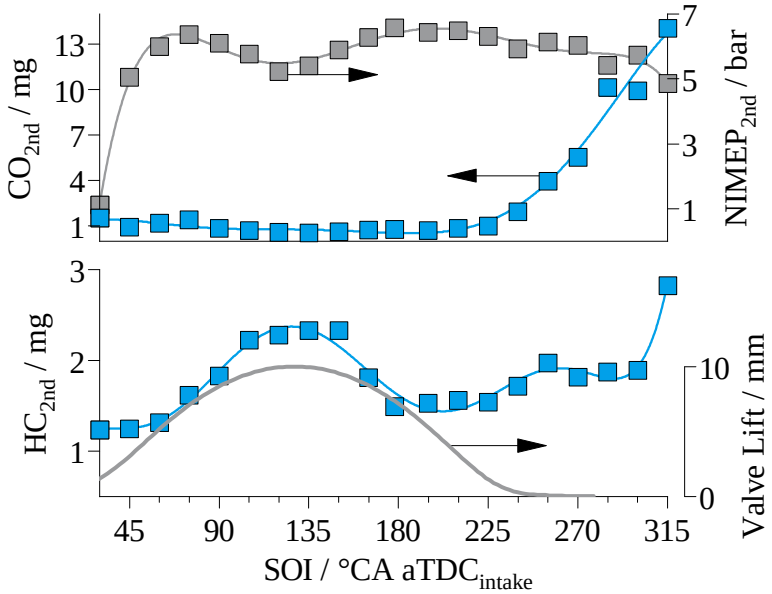

Figure 4-19: 2nd cycle NIMEP, CO, and HC emissions as a function of SOI

Injection timings in the initial part of the compression stroke, where the intake valve lift is lower than 6 mm, result in a flat region of low HC emissions. As the SOI is further delayed between 240 and 300°CA $aTDC_{intake}$, the HC emissions increase due to the decay in turbulence intensity and its negative effect on mixture formation [35]. After SOI=300°CA $aTDC_{intake}$, the spray/piston interaction results in mixture stratification in the vicinity of the spark plug, resulting in an increase in HC emissions.

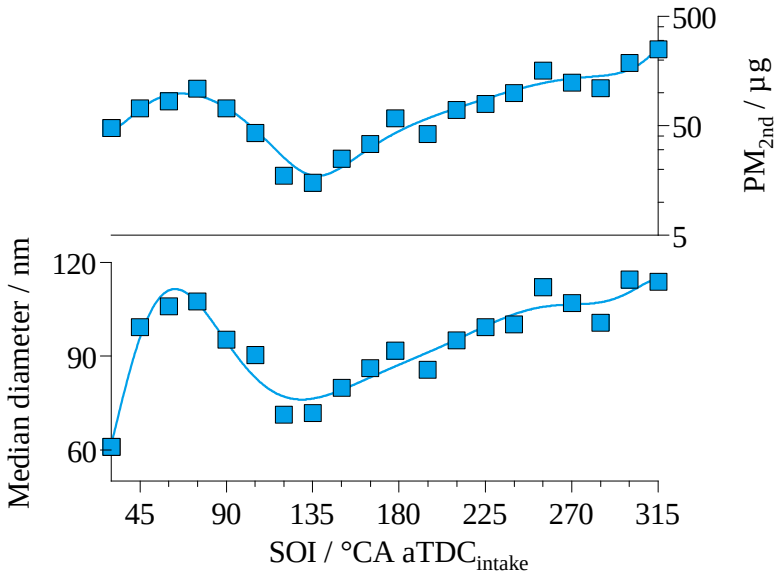

Figure 4-20: 2nd cycle PM emissions as a function of SOI

Figure 4-20 shows the PM emissions as a function of the SOI for the 2nd cycle. Injection timings in the first half of the intake stroke result in higher PM emissions in comparison to SOI in the late intake stroke. In contrast to the HC emissions, the interaction spray/valve interaction leads to a reduction in PM emissions; presumably from a reduction of the fuel delivered to the combustion chamber due to wetting of the back of the intake valve. The 2nd cycle PM dependence on SOI shows a similar behavior as the 1st cycle PM (Fig. 4-5). The minimum PM emissions are achieved for SOI in the region of maximum intake valve lift, at approximately SOI=135°CA $aTDC_{intake}$; after this point the PM emissions increase monotonically with SOI retard. The decrease in turbulence intensity and the interaction with the

piston crown drives the PM emissions up. In comparison to the 1st cycle PM (Fig. 4-5), the 2nd cycle PM is an order of magnitude lower, and the median particle size a 30% smaller.

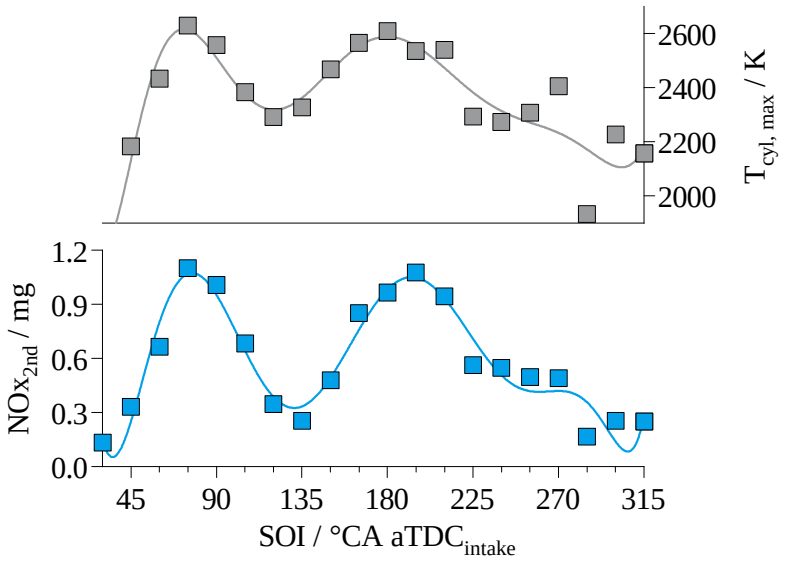

Figure 4-21: 2nd cycle NOx emissions as a function of SOI

Lastly, the NOx emissions as a function of SOI for the 2nd cycle are plotted in Fig. 4-21. As was the case for the 1st cycle analysis, for start of injection before 225°CA $aTDC_{intake}$, the NOx formation correlate very well with combustion temperature. For later SOI timing, mixture stratification starts to affect oxygen availability during the early stages of combustion. Consequently, the cylinder-averaged maximum temperature and the NO production are not as tightly coupled.

4.3.3 Second cycle: Ignition timing

Figures 4-22, 4-23 and 4-24 show the dependence of HC, PM and NOx emissions on the ignition timing. The FEF and SOI were held constant at 1.7 and 180°CA $aTDC_{intake}$ respectively. The selection of FEF and SOI for the 2nd cycle was based on the emissions and NIMEP trends presented on the preceding sections.

The HC emissions of the 2nd cycle are reduced as combustion phasing is delayed, going from a maximum of 1.9 mg of HC at the most advanced spark timing tested (-45°CA aTDC$_{comp.}$) to a minimum of 1.36 mg for -10°CA aTDC$_{comp.}$ spark timing; further delay in the spark timing did not have an impact on the HC emissions of the 2nd cycle. This observation suggests that the HC emissions during the initial cranking cycles are impacted by the evaporation of liquid films after end of combustion. Unlike the HC stored in the combustion chamber crevices, the fuel vapor from liquid films is not premixed with air, and its oxidation is less sensitive to increased post-flame temperatures associated with the combustion retard.

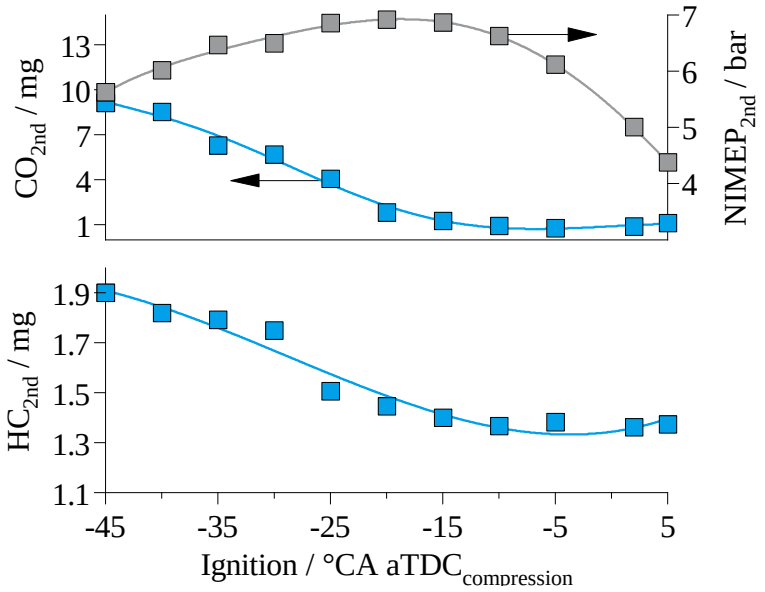

Figure 4-22: 2nd cycle NIMEP, CO, and HC emissions as a function of ignition timing

The formation of the particulates is driven by the pyrolysis of the fuel rich mixture created by evaporation of the liquid fuel films [35]. As combustion is delayed, the time available for the mixing of the vapor originating from the liquid fuel films increases while the time for particulate nucleation through fuel vapor pyrolysis and accumulation through HC condensation is reduced. As a result the PM is reduced by more than one order of magnitude with late combustion phasing, due to lower particulate number and smaller median particulate size. It is worth noticing that although the

trends observed in Fig. 4-23 for the median particulate size and the particulate mass appear to be parallel, the PM scale is logarithmic while the CMD scale is linear.

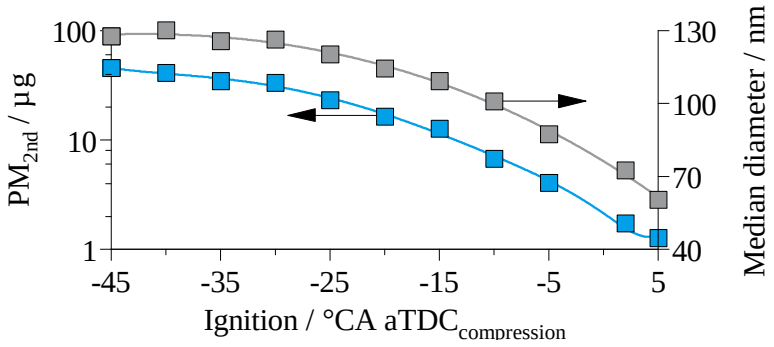

Figure 4-23: 2nd cycle PM emissions as a function of ignition timing

As it was the case for the 1st cycle (see Fig. 4-13), NOx emissions peak at a spark timing of -20°CA aTDC$_{comp.}$. For later combustion phasing, the peak temperatures are lower, therefore reducing the formation rate of NO. For earlier combustion timing, despite higher peak temperatures, the evaporation of fuel films due to the higher unburned temperatures decreases the oxygen availability. Additionally, the higher heat transfer rates to the cold cylinder walls reduces the residence time of the mixture in the high temperature zone. As a result, there is a slight reduction of NO production for spark timings earlier than -20°CA aTDC$_{comp.}$.

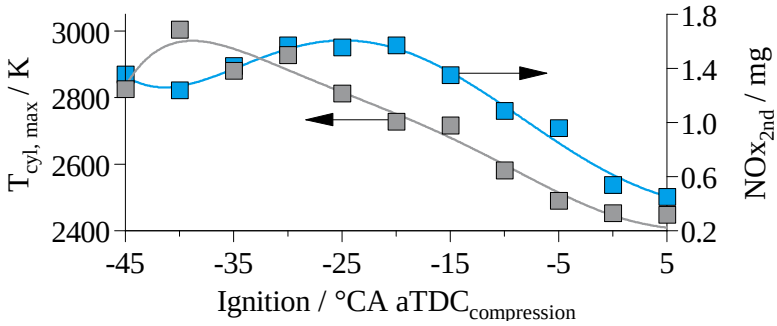

Figure 4-24: 2nd cycle NOx emissions as a function of ignition timing

4.3.4 Second cycle dependence on first cycle strategy

As can be inferred from the 1st cycle fuel accounting analysis (e.g. Fig. 3-8), more than half of the fuel injected in the 1st injection event does not participate in combustion. The remaining fuel is either pushed back into the intake manifold before IVC, absorbed into the lubricant oil, stored in the combustion chamber in the form of fuel films or lost to the crank-case in the form of blow-by gases. Some of this fuel will return to the cylinder, desorb from the oil layer or evaporate from the fuel films before the 2nd cycle ignition point and participate in combustion. Given the importance of the residual fuel on the mixture formation process, it must be included in the analysis of the 2nd cycle FEF_{2nd} requirement. In Chapter 3 the residual fuel available for combustion was quantified for the 2nd cycle by means of fuel carbon accounting using the HC exhausted from a non-firing 2nd cycle (see Fig. 4-25-bottom).

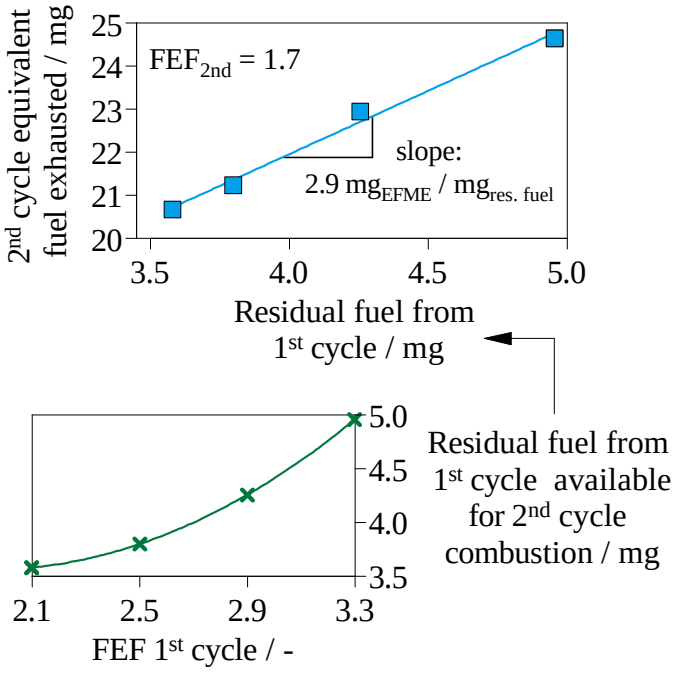

Figure 4-25: Top: 2nd cycle equivalent fuel mass exhausted as a function of the residual fuel for $FEF_{2nd} = 1.7$. Bottom: Residual fuel from the 1st cycle as a function of FEF_{1st}.

The concept of the equivalent fuel mass exhausted (EFME) is introduced to facilitate the study of the impact that the residual fuel from the 1st cycle has on the mixture formation of the 2nd cycle. The EFME represents the amount of fuel necessary to produce the observed carbon mass exhausted, in the form of CO_2, CO and HC, in a given cycle (see Eq. 4.1).

$$EFME = m_{HC} + \frac{1}{x_{C,\ fuel}} \cdot \left(m_{CO_2} \frac{MW_C}{MW_{CO_2}} + m_{CO} \frac{MW_C}{MW_{CO}} \right) \tag{4.1}$$

Where m_i, MW_i and $x_{C,\ fuel}$ represent the mass emissions, molecular weight and fuel carbon content respectively. Thus EFME represents the amount of fuel vapor available for combustion in the cycle. Figure 4-25-top shows the EFME of the 2nd cycle as a function of the residual fuel for the case $FEF_{2nd} = 1.7$. The EFME increases linearly with the residual fuel. The resulting slope shows that an increase in 1 mg in residual fuel would result in an increase of 2.9 mg in EFME. To verify the observed trend, the experiment was repeated at FEF_{2nd} values of 1.5, 1.9 and 2.1; the results exhibited a similar slope.

The faster increase of equivalent fuel mass exhausted (EFME) in comparison to the increase in residual fuel can be explained as follows. The impact of the 1st cycle FEF_{1st} on the 2nd cycle mixture formation goes beyond the contribution of residual fuel from the 1st to the 2nd cycle. The 1st cycle fuel amount has a significant effect on the $NIMEP_{1st}$ and on the combustion phasing at fixed spark timing. As the heat release increases and is shifted to earlier points with higher 1st cycle FEF_{1st}, the wall heat transfer during the 1st cycle increases as well. Figure 4-26 shows the total wall heat transfer as a function of FEF_{1st} during the 1st cycle. The heat transfer rate was calculated using the Woschni [77] correlation corrected for low engine speeds [50]. Considering the magnitude of the increase in heat transfer during the 1st combustion event when going from $FEF_{1st} = 2.1$ to 3.3 (Fig. 4-26) the increase in surface tem-

perature can be estimated. Using the thermal diffusivity, density and heat capacity of cast iron, the cylinder liner's thermal diffusion layer thickness is estimated to be $\approx 2.5\ mm$. Therefore, for an increase in heat transfer of $\Delta Q = 500\ J$ the liner surface temperature increases by $\Delta T_{surf.} \approx 8\ K$.

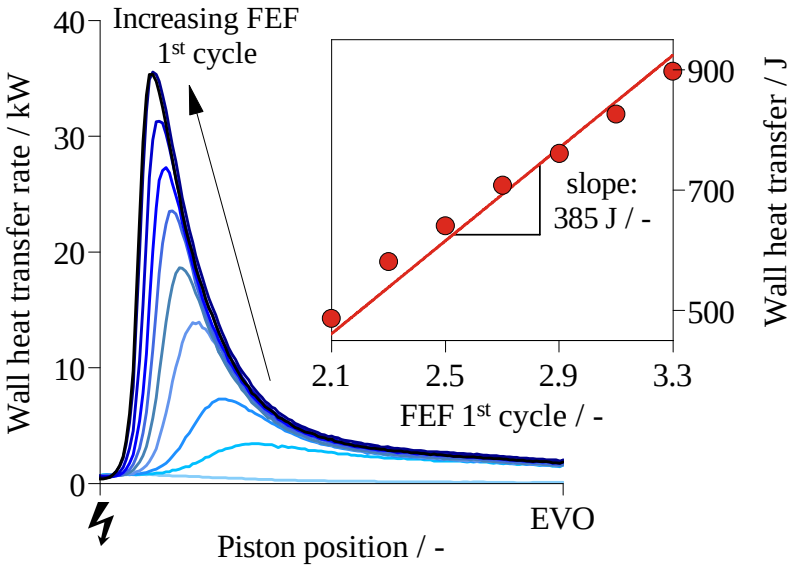

Figure 4-26: Wall heat transfer as a function of FEF_{1st} for the 1st cycle

This estimated increase in cylinder wall temperature is enough to have an observable influence on the mixture formation process of the 2nd cycle, as it favors the evaporation of the light fraction of the injected fuel. In order to assess the impact of the wall heating during the 1st cycle on the 2nd cycle mixture formation, the effect of residual fuel is separated from that of wall heating via two sets of experiments:

1. 1st cycle wall heat transfer sweep, controlled with 1st cycle spark timing, at constant FEF_{1st} and residual fuel.

2. Residual fuel sweep at constant wall heat transfer in the 1st cycle. The procedure is achieved by suppressing the spark so that the 1st cycle does not fire; i.e. there is no combustion heat transfer.

As shown in Fig. 4-27, for the first set of experiments, the wall heat transfer increases with spark advance; at the same time the residual fuel mass remains approximately unchanged. The spark timing sweep range was selected to achieve a similar heat transfer range as the one resulting from the 1st cycle FEF_{1st} sweep. The dependence of the 2nd cycle equivalent fuel mass exhausted as a function of the 1st cycle total wall heat transfer for the case $FEF_{2nd} = 1.7$ is shown in Fig. 4-28. As the 1st cycle wall heat transfer is increased (through 1st cycle spark advance) the 2nd cycle EFME increases. Using a linear fit, the slope indicates that a 100 J increase in heat transfer would result in a 1 mg increase in EFME. To further confirm the validity of these observations, the experiment was carried out at FEF_{2nd} values of 1.5, 1.9 and 2.1; a similar dependence of the EFME on the 1st cycle heat transfer was observed in all cases.

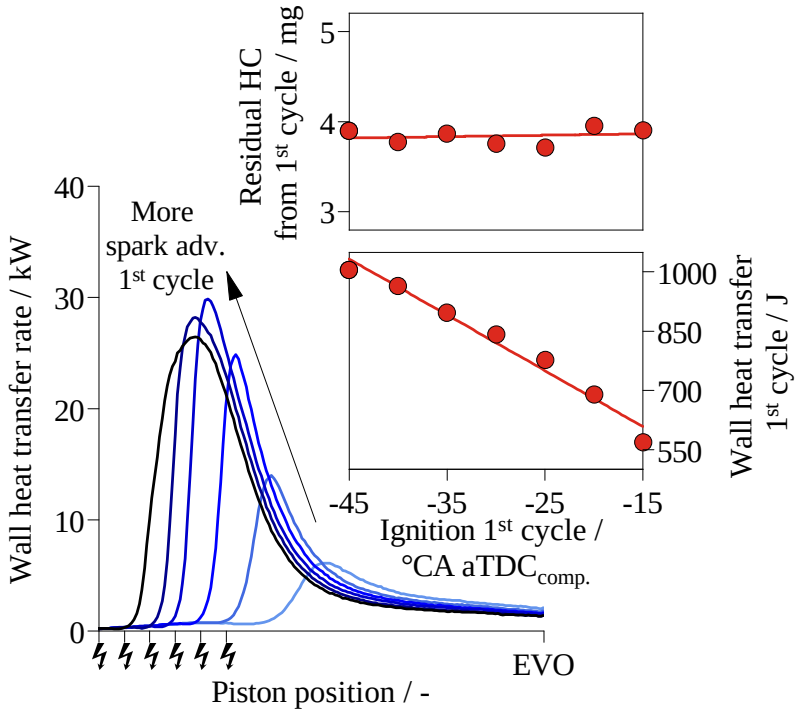

Figure 4-27: Wall heat transfer and residual fuel as a function of spark timing for the 1st cycle

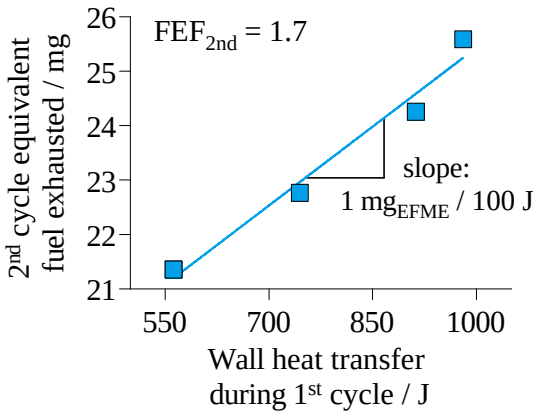

Figure 4-28: 2nd cycle equivalent fuel mass exhausted as a function of the wall heat transfer during the 1st cycle at constant residual fuel

For the second set of experiments with constant 1st cycle wall heat transfer, the 2nd cycle EFME is shown as a function of the residual fuel in Fig. 4-29. The constant heat transfer condition was obtained by suppressing the ignition during the 1st cycle. In this way, the wall heat transfer is only a result of the mixture compression. The residual fuel range achieved with this approach is between 3.5 and 6.5 mg. As shown in Fig. 4-29, the increase in 2nd cycle EFME exhibits a monotonic trend with residual fuel. When the results are fitted linearly, the observed slope shows almost a 1-to-1 correspondence. Thus in the absence of change in wall temperature due to change in heat transfer, the increase in EFME corresponds to the increase in residual fuel from the previous cycle. For consistency, the experiment was repeated at FEF_{2nd} values of 1.9 and 2.1, and a similar trend of 2nd cycle EFME against the residual fuel from the 1st cycle (constant 1st cycle heat transfer) was observed.

The relative importance of the residual fuel and the wall heating effects on EFME of the 2nd cycle may be assessed as follows:

$$\Delta EFME = \frac{\partial EFME}{\partial m_R}\Delta m_R + \frac{\partial EFME}{\partial Q}\frac{\partial Q}{\partial FEF_{1st}}\Delta FEF_{1st} \tag{4.2}$$

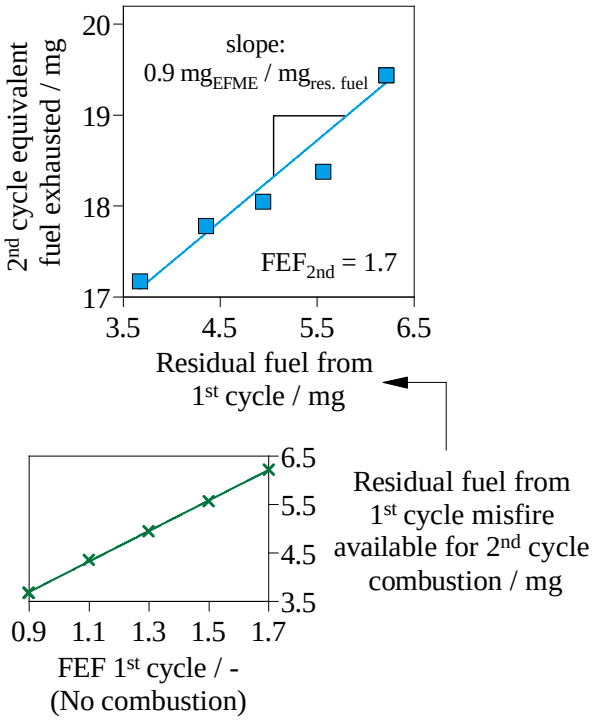

Figure 4-29: 2nd cycle equivalent fuel mass exhausted as a function of the residual fuel from the 1st cycle at constant heat transfer (1st cycle misfire)

Where m_R is the residual fuel mass from the 1st cycle and Q is the wall heat transfer in the 1st cycle. On the right-hand-side of Eq. 4.2, the first term represents the change of EFME in the 2nd cycle due to the presence of the residual fuel from the 1st cycle; the second term represents the change of that due to the change in wall heat transfer in the 1st cycle. The partial derivatives may be estimated from the experimental data:

- From Fig. 4-29, $\frac{\partial EFME}{\partial m_R} = 0.9$
- From Fig. 4-28, $\frac{\partial EFME}{\partial Q} = 10^{-2}\ mg/J$
- From Fig. 4-26, $\frac{\partial EFME}{\partial FEF_{1st}} = 385\ J$

For the data shown in Fig. 4-25, for a change of 1st cycle FEF_{1st} from 2.1 to 3.3 ($\Delta FEF_{1st} = 1.2$), m_R increases from 3.6 to 4.95 mg ($\Delta m_R = 1.35\ mg$). Then numerical values for Eq. 4.2 become:

$$\Delta EFME = 1.22\ mg + 4.62\ mg = 5.84\ mg \tag{4.3}$$

The above value is in line with the observed value of $\Delta EFME = 4.1\ mg$ in Fig. 4-25. More importantly, Eq. 4.3 shows that the effect of the change of the wall heat transfer in the 1st cycle on the 2nd cycle EFME is approximately 4 times that of the residual fuel amount.

4.4 Third cycle analysis

Closing the cycle-by-cycle analysis, this section focuses on the 3rd engine cycle during crank-start. In comparison to the preceding cycles, the 3rd cycle mixture formation is improved due to the higher engine speed, reduced amount of injected fuel from the lower intake manifold pressure, warmer cylinder walls and increased fraction of residual fuel and gases. As it was done in the preceding section, the analysis is focused on the start of injection (SOI), fuel enrichment factor (FEF), and ignition timing using a one-variable-at-a-time approach. The swept ranges can be found in Table 4.5.

Parameter	**Sweep range**		**Nominal value**
SOI [°CA aTDC$_{\text{intake}}$]	30 − 315	$\Delta = 15$	180
FEF [−]	1.3 − 1.9	$\Delta = 0.2$	1.5
Spark [°CA aTDC$_{\text{comp.}}$]	−45 − −5	$\Delta = 5$	-10

Table 4.5: Experimental scope for the 3rd cycle emissions

Once again, to decouple the effects of the 1st and 2nd cycle injection strategy on the 3rd cycle emission analysis, the 1st and 2nd cycle strategies were kept constant as shown in Table 4.6.

Parameter	1st cycle	2nd cycle
SOI [°CA aTDC$_{intake}$]	180	180
FEF [−]	2.5	2.5
Spark [°CA aTDC$_{comp.}$]	−10	−10

Table 4.6: 1st and 2nd cycle strategies for 3rd cycle experiments

4.4.1 Third cycle: Fuel Enrichment Factor

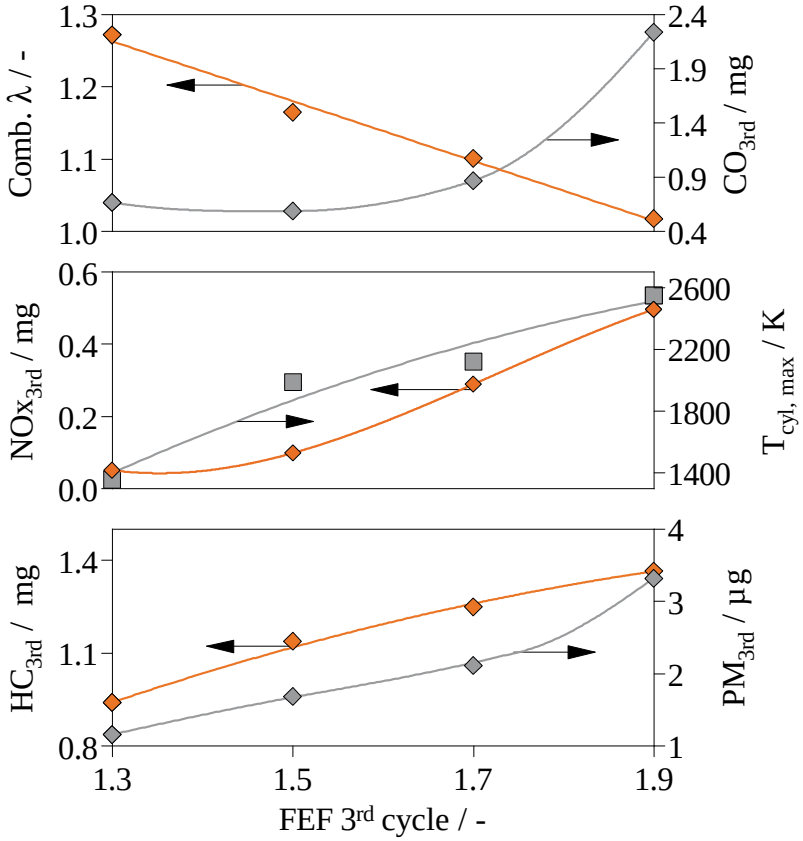

Figure 4-30: 3rd cycle CO, NOx, HC and PM emissions as a function of FEF

The 3rd cycle emissions behavior as a function of FEF is shown in Figure 4-30. Similar to the 2nd cycle, λ decreases linearly with FEF with a slope of -0.41. Despite the mixture being globally lean at $\lambda = 1.1$, the CO emissions show an inflection point at FEF = 1.7. The NOx emissions increase from a minimum of 0.05 *mg*

at FEF = 1.3 to a maximum of 0.5 mg at FEF = 1.9 driven by the increase in combustion temperature. The HC emissions increase with FEF at the same rate of the 2nd cycle, that is 0.07 mg HC for a 0.2 step in FEF. The PM emissions increase with FEF is less pronounced than for the preceding two cycles; for a 0.2 step in FEF, the 3rd cycle PM emissions increase in $\approx 0.7\ \mu g$.

4.4.2 Third cycle: Start of injection

Figures 4-31 and 4-32 show the results for the injection timing sweep during the 3rd engine cycle during crank-start. The fuel enrichment factor and spark timing were held constant at 1.5 and -10°CA aTDC$_{\text{comp.}}$ respectively throughout the SOI sweep. Furthermore, the injection strategy of the two previous cycles was also held constant at the values shown in Table 4.6. The FEF selected for the 3rd cycle resulted in an injected fuel mass of approximately 32 mg and the injection event had a crank-angle duration of 16°CA.

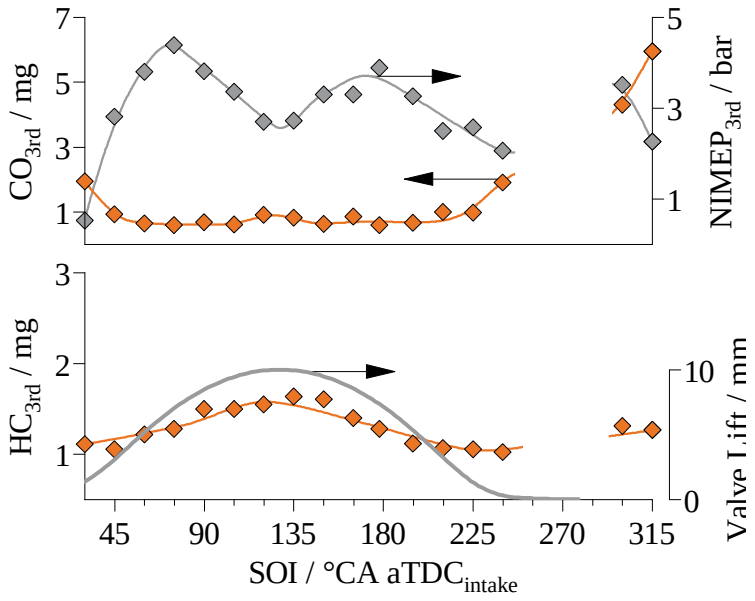

Figure 4-31: 3rd cycle NIMEP, CO, and HC emissions as a function of SOI

The general shape of the NIMEP, CO, and HC trends with varying SOI is similar to what was already discussed in Section 4.3.2 for the 2nd cycle. However, in comparison to the two preceding cycles, open valve injection has a lower impact on the HC emissions and a more significant impact on NIMEP. Table 4.7 shows quantitatively the observed differences between the initial three cycles during crank-start. Under the assumption that the fuel film mass on the back of the intake valve is only a function of the valve geometry and temperature, the fuel film mass is independent from the injected fuel mass. Consequently the relative amount of fuel that does not participate in combustion due to the valve wetting increases as the injected fuel mass decreases. Due to a decrease in turbulence intensity, SOI between 240 and 300°CA $aTDC_{intake}$ results in engine misfire.

Parameter	**1st cycle**	**2nd cycle**	**3rd cycle**
NIMEP @ SOI=75°CA $aTDC_{intake}$	5.8 *bar*	6.4 *bar*	4.4 *bar*
NIMEP @ SOI=120°CA $aTDC_{intake}$	5.4 *bar*	5.2 *bar*	2.7 *bar*
Change in NIMEP	-7%	-19%	-39%
HC @ SOI=75°CA $aTDC_{intake}$	1.5 *mg*	1.3 *mg*	1.2 *mg*
HC @ SOI=120°CA $aTDC_{intake}$	3.3 *mg*	2.3 *mg*	1.6 *mg*
Change in HC	+120%	+77%	+33%

Table 4.7: Effect of spray/valve interaction on NIMEP and HC emissions.

Figure 4-32 shows the PM and NOx emissions as a function of the SOI for the 3rd cycle. The trends observed mimic the results for the 2nd cycle already discussed. The PM emissions are driven by spray interaction with the piston crown, increasing both the number and size of the emitted particles. For injection timings between 105 and 225°CA $aTDC_{intake}$ the particle median diameter and mass remain relatively constant. NOx emissions correlate very well with the maximum cylinder-averaged temperature. However, due to the lower MAP, fuel mass injected and NIMEP, the NO formation is significantly lower when compared to the measured values of the two preceding cycles.

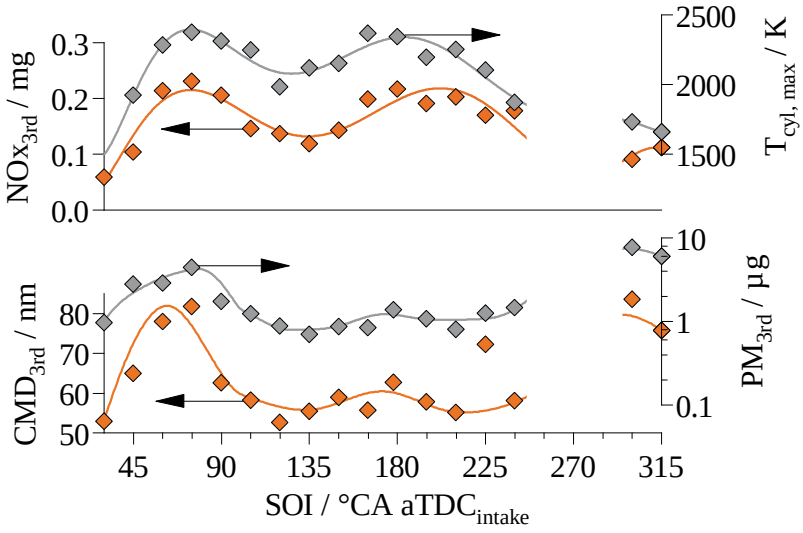

Figure 4-32: 3rd cycle PM and NOx emissions as a function of SOI

4.4.3 Third cycle: Ignition timing

Figures 4-33 and 4-34 show the dependence of the pollutant emissions on the ignition timing for the 3rd engine cycle during cold crank-start.

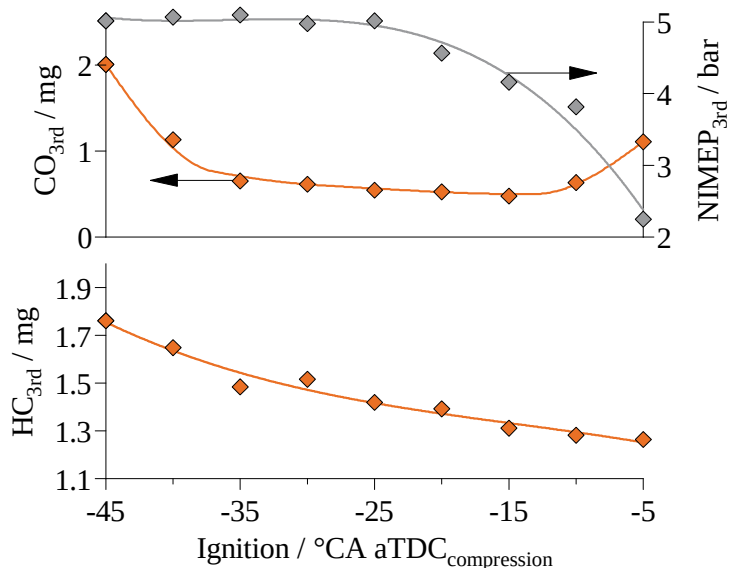

Figure 4-33: 3rd cycle NIMEP, CO, and HC emissions as a function of spark timing

The FEF and SOI were held constant for each cycle at 1.5 and 180°CA $aTDC_{intake}$ respectively. The HC emissions of the 3rd cycle follow a monotonic downwards trend as combustion phasing is delayed. The reduction range is similar to the one observed for the 2nd cycle ($\approx 1.3 - 1.9\ mg$).

PM emissions are also reduced with later spark timing due to the shorter time available for fuel pyrolysis and for particle growth between end of combustion and EVO.

The NOx emissions curve in Fig. 4-34 follows the averaged maximum temperature. As opposed to the 1st and 2nd cycles, as the engine speed increases the impact of the flow structure on the spatial distribution of the AFR ratio decreases, achieving a more homogeneous mixture at the ignition point, even for advanced spark timing.

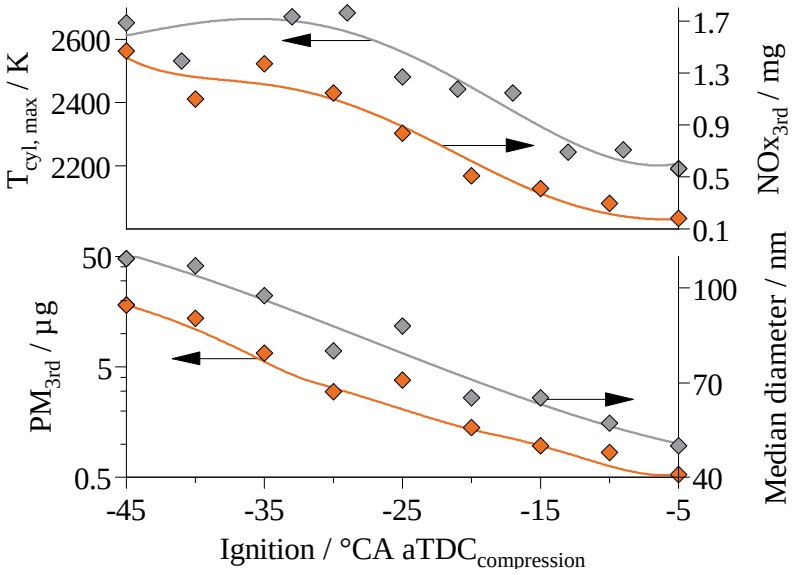

Figure 4-34: 3rd cycle PM and NOx emissions as a function of spark timing

4.5 Findings

The effects of fuel amount, injection timing and spark timing on the HC and PM emissions of the initial 3 cycles during cold crank-start were studied in a wall guided gasoline direct injection engine. The main results can be summarized as follows:

- The adverse conditions of temperature and charge motion during cold crank-start result in mixture inhomogeneity. Consequently, aiming for an overall combustion λ of 1 is not a viable strategy as it increases the CO, HC and PM emissions. The amount of fuel injected needs to be large enough to reduce the risk of misfire or partial burn, and sufficiently small to control the engine out emissions. The results show that the optimum enrichment for the initial 3 cycles are $\mathrm{FEF_{1st}} = 2.5$, $\mathrm{FEF_{2nd}} = 1.7$ and $\mathrm{FEF_{3rd}} = 1.5$.

- The sensitivity of the HC emissions to the FEF is roughly the same for all 3 cycles, while the PM sensitivity decreases significantly as the cycle number increases. In a similar way, the HC emissions for the initial 3 cycles are in the same order of magnitude; between 1 and 1.5 $mg/cyl./cycle$. In contrast, the PM emissions per cycle are reduced in more than an order of magnitude as the crank-start progresses form the 1^{st} to the 3^{rd} cycle.

- The FEF history has an influence on the mixture formation through two mechanisms. First, as the FEF of previous cycles increases, so does the residual fuel mass. Second, the amount and point of heat release for the previous cycles is a function of FEF. The heat release increase of the previous cycles translates into wall heating, impacting the fuel evaporation and mixture formation process.

- The SOI selection for minimizing the pollutant emissions presents a tradeoff. The lowest HC emissions are achieved for SOI during the first half of the intake stroke, for intake valve lifts lower than 5 mm. Contrary, the minimum PM

emissions are achieved for SOI during the intake stroke and the intake valve lift greater than 5 mm. Injection during the early compression stroke results in a good compromise for both HC and PM emissions.

- The effect of fuel spray interaction with the intake valve in HC emissions is reduced as the crank-start progresses form the 1^{st} to the 3^{rd} cycle. In contrast, its impact of NIMEP increases.

- The HC emissions of the 1^{st} cycle are insensitive to combustion phasing in the range of interest. For the 2^{nd} and 3^{rd} cycles, spark timing retard results in approximately a 30% reduction as the spark timing goes from -45 to 10°CA $\text{aTDC}_{\text{comp.}}$. For the 3 cycles studied, the observed PM reduction with combustion retard is larger than an order of magnitude as the spark timing is delayed from -45 to 10°CA $\text{aTDC}_{\text{comp.}}$.

- NOx emissions are driven by combustion temperature and correlate well with the maximum cylinder-averaged temperature. In the case of mixture inhomogeneities due to mixture stratification or flow structure, rich zone can result in a reduction of oxygen availability and consequently lead to lower NOx emissions.

– Intentionally left blank –

Chapter 5

Valve timing effect on crank-start

The goal of this chapter is to assess the potential of unconventional valve timings for reducing the engine-out hydrocarbon, particulate matter and nitrogen oxides emissions during the cold crank-start of a gasoline direct injection engine. With variable valve timing (VVT) systems, the selection of the de-energized position (parked position) of the camshafts is limited by the authority of the phasing system (in °CA) and the desired maximum intake advance and exhaust retard during warm operation. As the authority of VVT systems increases, new camshaft parked positions become possible. The merit of these alternative parked positions for cold crank-start emissions control is discussed in this chapter. The four different valve timing settings that were studied in detail are as follows:

1. Baseline stock valve timing
2. Late intake opening/closing
3. Early exhaust opening/closing
4. Late intake phasing combined with early exhaust phasing

Delaying the intake valve opening improves the mixture formation process and results in approximately a 25% reduction of HC and PM/PN emissions. Early exhaust valve phasing results in a deterioration of the HC and PM/PN emissions performance. The combined strategy consisting of late intake and early exhaust phasing shows a considerable reduction in the cold crank-start HC and PM/PN emissions of 30%.

Part of the results presented in this chapter have been published in the *SAE International Journal of Engines* [63].

5.1 Experiments description

The four different valve timing investigated in this study correspond to the different combinations of exhaust timing advance and intake timing retard, as shown in Fig. 5-1. The experimental matrix with the resulting valve timings is shown in Table 5.1.

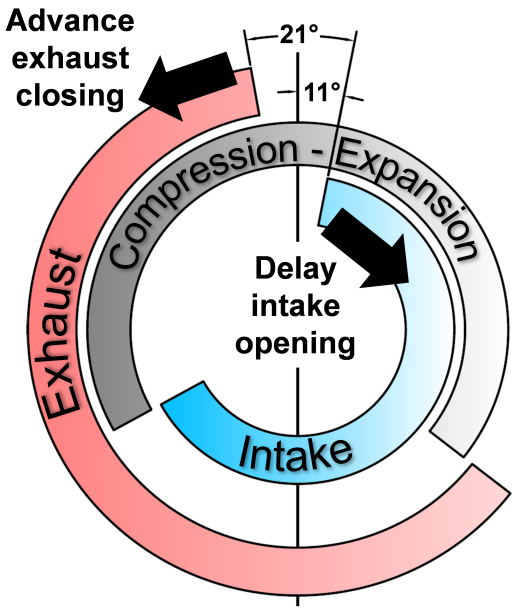

Figure 5-1: Baseline intake and exhaust timings and direction of phasing for the other investigated valve timings

Case name	Intake timing*	Exhaust timing*
Baseline	IVO = 11°CA aTDC IVC = 61°CA aBDC	EVC = 10°CA bTDC EVO = 52°CA bBDC
Late IVO	IVO = 42°CA aTDC IVC = 92°CA aBDC	EVC = 10°CA bTDC EVO = 52°CA bBDC
Early EVC	IVO = 11°CA aTDC IVC = 61°CA aBDC	EVC = 41°CA bTDC EVO = 83°CA bBDC
Symmetric NVO	IVO = 42°CA aTDC IVC = 92°CA aBDC	EVC = 41°CA bTDC EVO = 83°CA bBDC

*The valve events reported correspond to a 0.2 *mm* valve lift.

Table 5.1: Valve setting cases for the crank-start study

With the purpose of separating the effects of valve timing on the cold crank-start emissions from other parameters, the injected fuel mass for each cycle was adjusted to result in a comparable combustion λ during crank-start for all valve timing cases. The combustion λ was calculated following the approach described in Section 2.3 using the CO and CO_2 mole fractions and disregarding the HC content. The resulting λ values during crank-start are shown in Fig. 5-2. The spark timing for each cycle was adjusted for the first three cycles, so that the point for 50% of heat release (CA50) was at a similar location for all valve timing cases studied. From the 4^{th} cycle on, the spark timing was held constant for the rest of the crank-start process, resulting in later combustion phasing as the engine speed increased (see Fig. 5-2). For each valve timing setting, the throttle position was fixed throughout the cranking process at a position resulting in fast-idle conditions of 2 *bar* NIMEP at 1200 *rpm*. For each experimental case, the injection timing was adjusted individually for the first three cycles and was chosen to minimize HC and PM emissions. From the 4^{th} cycle on, the injection event took place during the mid-intake stroke (SOI = 105°CA $aTDC_{intake}$) for all cases. Each experimental condition was repeated 5 times, and the results reported correspond to the average values.

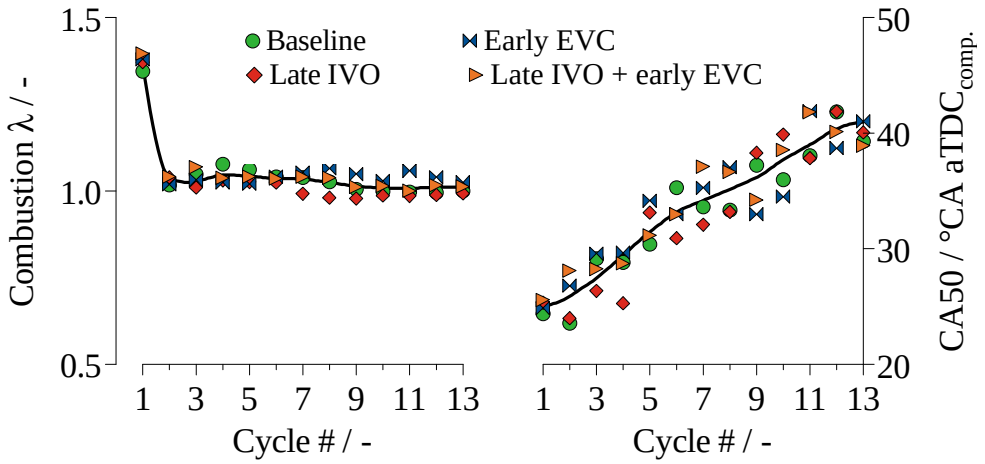

Figure 5-2: Combustion lambda and CA50 during the crank-start process for all four valve timings studied

5.2 Crank-start with late intake timing

Delaying the intake valve timing has a number of positive potential effects on the mixture preparation process in GDI engines at cold temperature.

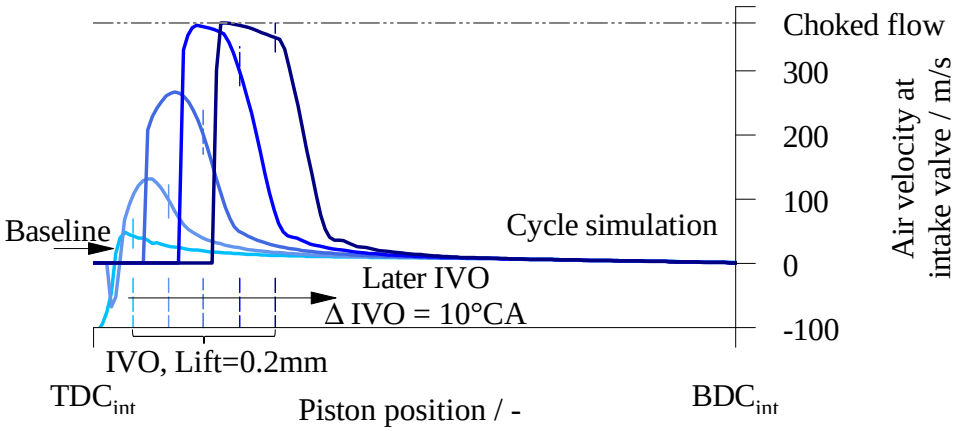

Figure 5-3: Air velocity at intake valve as a function of IVO timing; simulation results

As the intake timing is delayed, the intake valves remain closed during the initial part of the intake stroke resulting in a drop in the cylinder pressure. As the intake

valves open, the pressure differential across the valve at IVO increases, results in higher air velocity and increased turbulence intensity during the initial portion of the intake stroke [46, 64, 67]. These flow features promote fuel-air mixing. Figure 5-3 shows the results of a cycle simulation for the air velocity at the intake valve for different IVO timings. Compared to the baseline, the peak air velocity can increase up to 8 times for the latest IVO considered; note that the maximum velocity is limited by choked flow conditions.

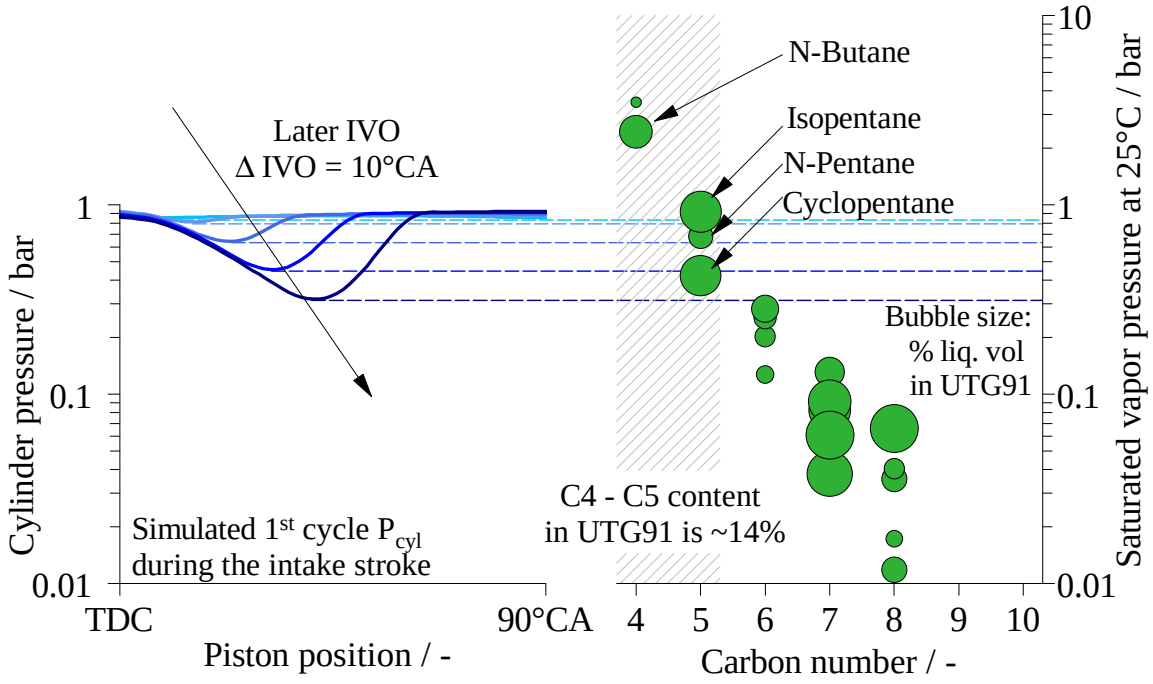

Figure 5-4: Left: Simulated in-cylinder pressure during intake stroke for the first engine cycle and different IVO timings. Right: Saturated vapor pressure at 25°C of the main constituents of the certification gasoline UTG-91

The pressure drop during the intake stroke at late IVO timings could also have a direct impact on the fuel spray evaporation. As the in-cylinder pressure decreases, the potential for flash-boiling of the more volatile fraction of the fuel increases, improving the spray breakup and aiding in the spray evaporation and the mixture formation process [40, 66]. Figure 5-4 shows the saturated vapor pressure for the main fuel

species of a certification gasoline (UTG-91); the bubble size represents the volumetric fraction of the species in the fuel. The saturated vapor pressure was calculated using the Antoine equation (Eq. 5.1) where the A, B, and C parameters were obtained from NIST [51] for the different fuel species.

$$log_{10}(P_{sat}) = A - \frac{B}{C+T} \tag{5.1}$$

As shown in Fig.5-4, a delay in IVO of 40°CA results in a minimum pressure of 300 *mbar* for the 1st engine cycle during crank-start, which is below the saturation pressure of all the C4 and C5 content of the fuel. Of particular relevance are the species Isopentane (4.4 $\%^{vol}$, $P_{sat} = 0.91$ *bar*), N-Pentane (1.4 $\%^{vol}$, $P_{sat} = 0.68$ *bar*) and Cyclopentane (4.3 $\%^{vol}$, $P_{sat} = 0.42$ *bar*) as together they represent 10% of the fuel content and their saturation pressures at ambient temperature are in the range achievable by the late IVO setting. It is worth pointing out that the minimum in-cylinder pressure is attained during the first half of the intake stroke. Thus, a fuel injection event during the minimum pressure region might result in piston impingement; offsetting the advantages of improved evaporation through flash-boiling.

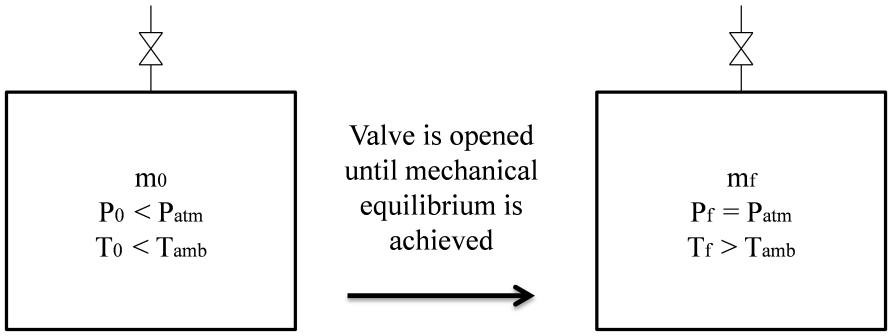

Figure 5-5: Simplified thermodynamic analysis of the filling process

Delayed intake timing also benefits the fuel vaporiaztion process as a result of the higher charge temperature at the end of the intake stroke. The increase in charge

temperature is a result of the flow work occurring during the cylinder filling in the intake stroke. To illustrate this, consider the isochoric filling process with an ideal gas of an adiabatic cylinder, whose contents have been expanded isentropically from P_{atm} and T_{amb} to P_0 and T_0 (see Fig. 5-5). Under the assumption of a constant volume, adiabatic process, the 1st law for open system considered is reduced to Eq. 5.2.

$$\frac{d(mc_vT)}{dt} = \frac{dm}{dt}c_pT_{amb} \tag{5.2}$$

After integrating from t_0 (valve opening) to t_f (mechanical equilibrium) and manipulating algebraically the expression with the ideal gas law, the following expression for the final cylinder temperature is obtained:

$$\frac{T_f}{T_0} = \left[\left(1 - \frac{P_0}{P_{atm}}\right)\frac{c_v}{c_p}\frac{T_0}{T_{amb}} + \frac{P_0}{P_{atm}}\right]^{-1} \tag{5.3}$$

Since T_0 isrelated to P_0 from the isentropic expansion, the resulting relation for T_f as a function of P_0 is shown in 5.4. Using $P_{atm} = 1\ bar$, $T_{amb} = 300\ K$ and $\gamma = c_p/c_v = 1.4$, the final charge temperature as a function of the cylinder pressure at valve opening is shown in Fig. 5-6.

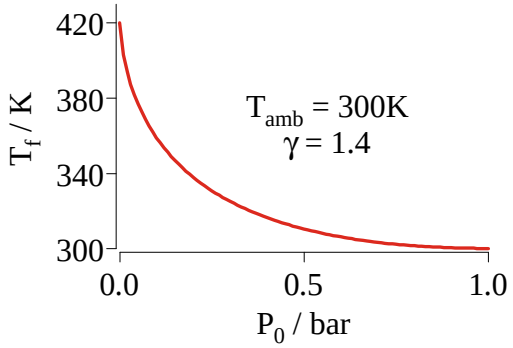

Figure 5-6: Final temperature after cylinder filling as a function of pressure at IVO for the simplified system

$$T_f = T_{amb}\left[\left(1 - \frac{P_0}{P_{atm}}\right)\frac{1}{\gamma} + \left(\frac{P_0}{P_{atm}}\right)^{1/\gamma}\right]^{-1} \tag{5.4}$$

The idealized model presented above provides an upper boundary for the temperature increase expected at the end of compression for different IVO timings. Figure 5-7 shows the result of a cycle simulation for the charge temperature throughout the intake stroke of the 1st engine cycle during crank-start. Retarding the IVO event 40°CA results in an increase in 20°C at the end of the intake stroke. The same increase in fuel temperature would approximately double the saturated vapor pressure of the different fuel species.

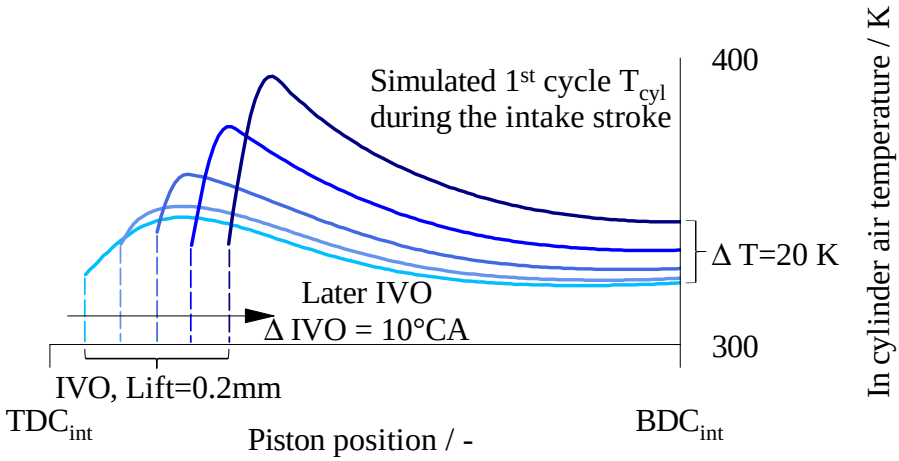

Figure 5-7: Simulated in-cylinder temperature during the intake stroke for the first engine cycle and different IVO timings

As a last consideration regarding the impact of late intake timing on the crank-start behavior, Fig. 5-8 shows the effective compression ratio and the peak motoring pressure at 280 *rpm*. Reducing the effective compression (ECR) ratio during engine crank-start is beneficial for improving the NVH behavior. Lower ECR results in a lower rate of pressure rise (ROPR) and lower vibration dose value. On the other hand, as the ECR is reduced the effective work output of the initial engine cycles is reduced and consequently the duration of the crank-start process is extended.

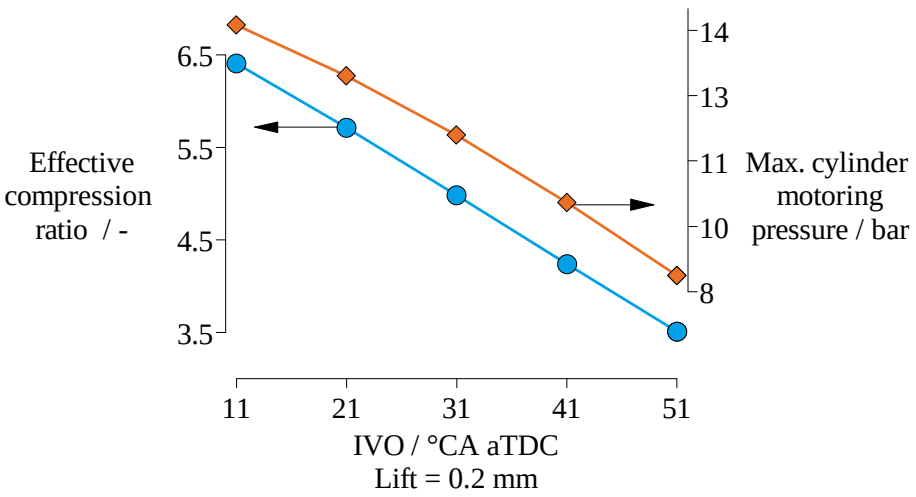

Figure 5-8: Effective compression ratio for the 1st cycle as a function of IVO

To experimentally test the effect of late IVO, the intake valve timing was delayed by approximately 31°CA. The new intake timing is achieved by retarding the intake camshaft phasing 2 teeth. Cam sprockets have 46 teeth; a 2 teeth rotation corresponds to a change in IVO of 31.3°CA. The resulting valve timing is shown in Fig. 5-9.

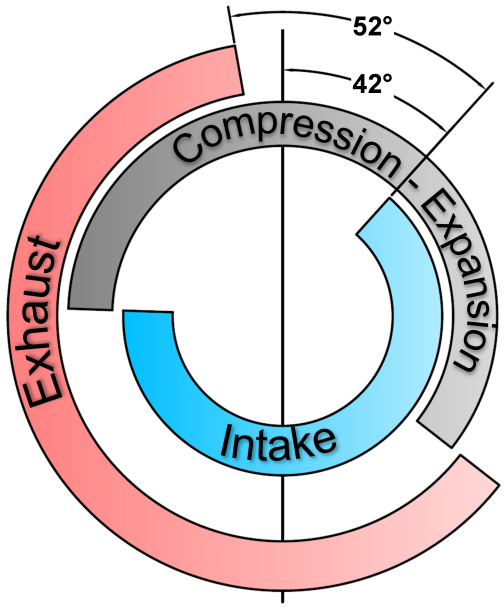

Figure 5-9: Valve timing diagram for the late IVO/IVC setting

Figure 5-10 shows the required fuel mass to attain a given combustion lambda during the 1st cycle for both the baseline and late IVO valve timing configurations. For the 1st combustion event during cold crank-start, the target combustion lambda is between 1.2 and 1.4; leaner mixtures increase the risk of partial burn or misfire, while lambda values closer to 1 result in locally fuel rich pockets responsible for significant CO production (see Section 3.4). From the previous considerations about the impact of late IVO on the mixture formation, for a given combustion lambda in the window of interest, the late IVO case results in approximately a 13% reduction in the fuel requirement, as more fuel evaporates and participates in combustion.

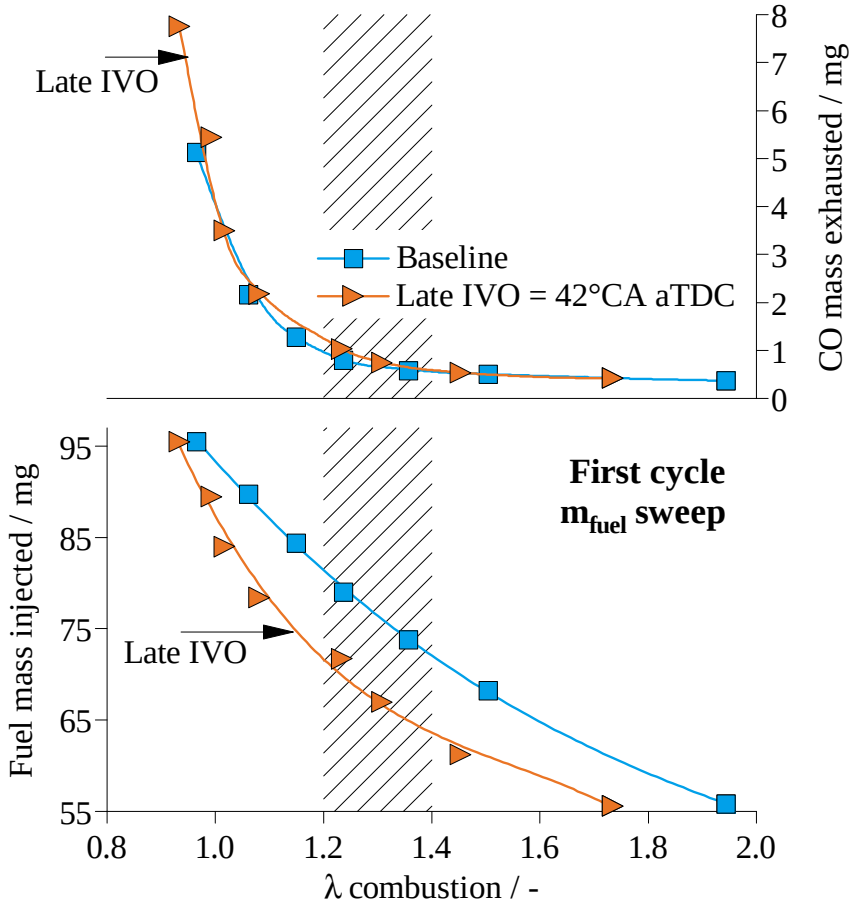

Figure 5-10: CO production (top) and 1st cycle fuel requirement (bottom) as a function of combustion λ for baseline and late IVO settings

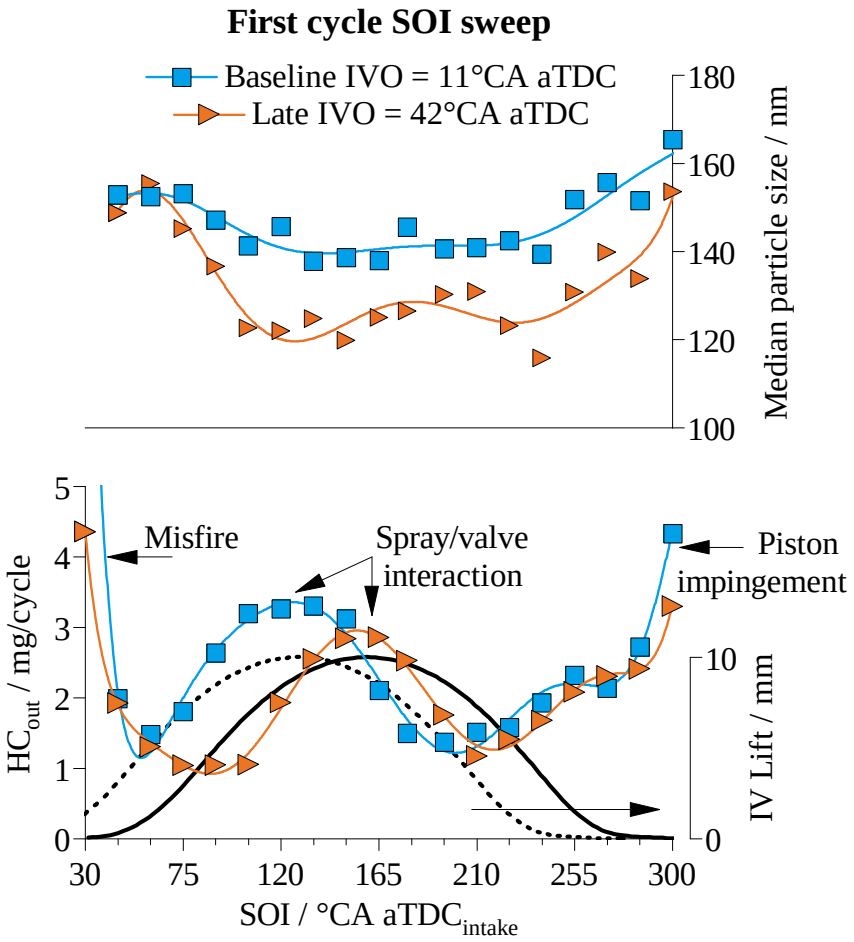

Figure 5-11: 1st cycle HC emissions and particle median size as a function of SOI for both baseline and late IVO cases

As argued in Section 4.2.1, the optimum injection strategy for lowest 1st cycle emissions with the baseline configuration consists of a single injection event during the early compression stroke to avoid piston and intake valve interaction with the fuel spray. As the IVO timing is delayed, the interaction zone between the fuel spray and the intake valve is shifted to a later point in the intake stroke (see Fig. 5-11). This shift enables injection during the first half of the intake stroke without interfering with the intake valve so that fuel bounce to the cylinder head is reduced. The latter is a major cause of the HC emissions for early injection (the high HC emissions region at the left-hand-side of Fig. 5-11). The results of the SOI sweep during the 1st cycle

for both the baseline and late IVO cases at constant fuel mass shows that the SOI for lowest HC emissions is shifted from 195°CA $aTDC_{intake}$ for the baseline case, to 105°CA $aTDC_{intake}$ for late IVO, and the minimum HC emissions change from 1.5 to 1 $mg/cycle$. Furthermore, the better evaporation behavior of the fuel, and the reduced amount of unburned HC favors a reduction in the particle number and size respectively. The top diagram in Fig. 5-11 shows a sustained reduction in the median size of the particle accumulation mode throughout the SOI sweep.

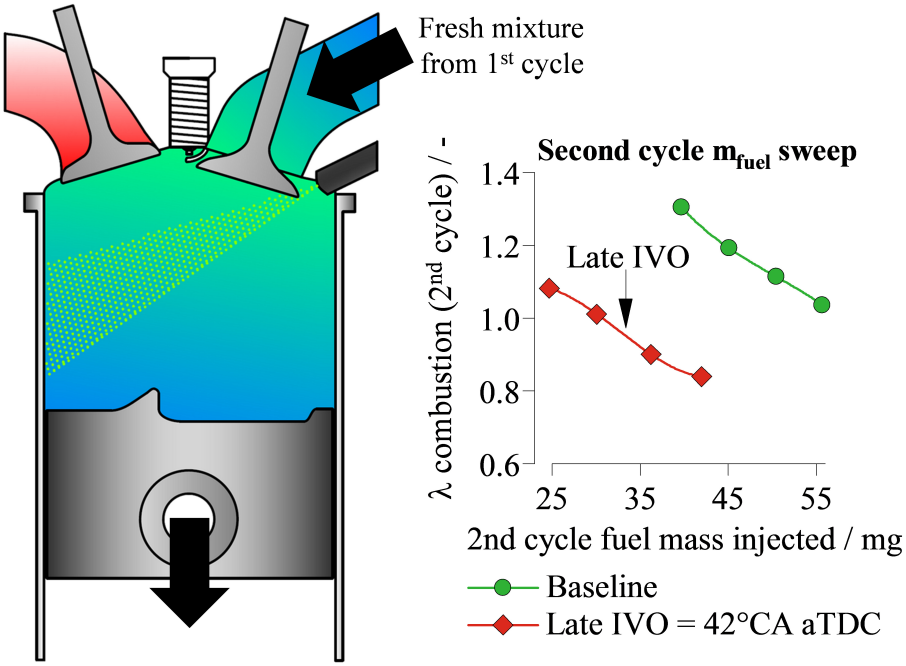

Figure 5-12: Mixture formation process during the 2nd cycle

As the IVO timing is delayed, the IVC timing is shifted to the mid-compression stroke. Consequently, part of the fresh mixture formed during the 1st engine cycle is pushed into the intake manifold, and is available for the 2nd cycle. As a result, the required mass of direct injected fuel during the 2nd cycle for a given combustion lambda is reduced, diminishing the formation of fuel films during the injection process. This effect is illustrated in Fig. 5-12

The first 2 seconds of the cold crank-start, comprising the period between the start of cranking till the maximum engine speed is achieved (speed flare), for both the baseline and late IVO cases are shown in Figs. 5-13 and 5-14. Fig. 5-13 shows that the late IVO setting results in lower NIMEP for the first 2 engine cycles and consequently, in a slower engine speed run-up and reduced speed-flare. This is a consequence of the reduced trapped mass and lower effective compression ratio resulting from late IVC. As the intake manifold is pumped down by the engine, the manifold pressure decreases more rapidly in the baseline case due to the narrower throttle opening necessary to achieve 2 *bar* of NIMEP at steady state. After the 3rd engine cycle, however, the lower cylinder volumetric efficiency of the late IVO setting is compensated by the wider throttle opening and comparable NIMEP traces are obtained.

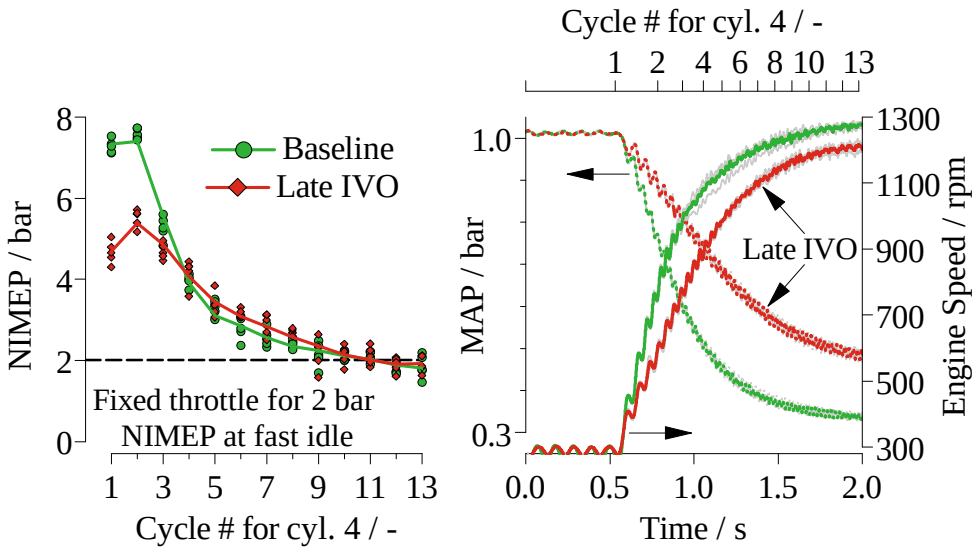

Figure 5-13: NIMEP, engine speed and MAP traces during cold crank-start for baseline and late IVO. Symbols are for individual run results; colored lines represent average values of 5 separate runs

Regarding the engine out emissions, Fig. 5-14 shows the NOx, HC, and PM traces during cold crank-start for the initial 13 engine cycles ($\approx$ 2 s). The NOx emissions are driven by the in-cylinder temperature during the combustion process, and therefore correlate well with NIMEP. The peak NOx emissions occur during the 1st

cycle and decrease monotonically thereafter to a steady-state value of approximately 0.05 $mg/cyl./cycle$. The HC emissions peak at the 2nd cycle and approach a steady-state value around 0.4 $mg/cyl./cycle$. As the crank-start progresses, the reduction in HC is caused by better mixture formation driven by the increase in engine speed and in cylinder wall temperature. The PM emissions show a similar trend, peaking at the 1st or 2nd cycle, and approaching steady-state values between $0.015 - 0.04$ $\mu g/cyl./cycle$. PM formation is a complex process with competing processes of nucleation, agglomeration and oxidation [28, 29]. As the engine speed increases there is better fuel-air mixing and less time for liquid fuel pyrolysis, post-flame agglomeration and particle coagulation. The end result is a reduction in the number and size of the particulates.

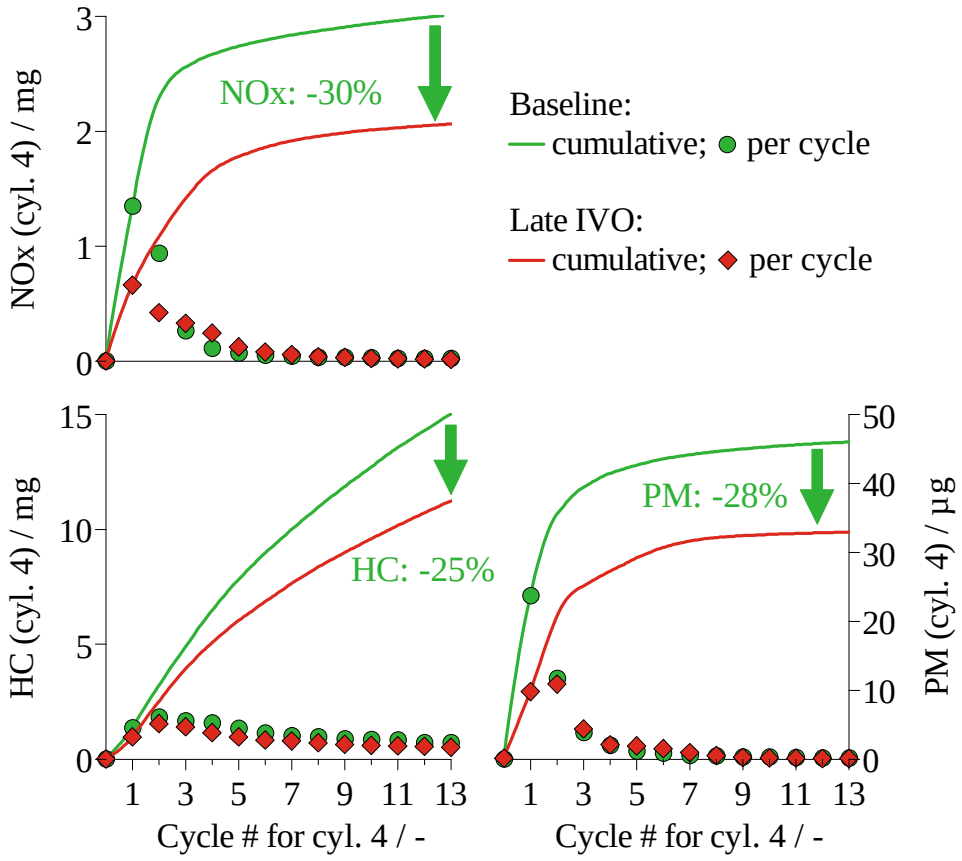

Figure 5-14: Cycle-by-cycle and cumulative NOx, HC, and PM emissions of cylinder 4 during cold crank-start for the baseline and late IVO settings

As argued at the beginning of this section, the late IVO setting promotes the mixture formation and reduces the effective compression ratio. The lower ECR results in lower NIMEP in the initial 3 cycles and as a consequence, lower NOx emissions. The cumulative reduction in NOx amounts to 30% in the time interval considered. Similarly, late IVO leads to a reduction in HC emissions of 25%. Contrary to the observations for NOx and PM emissions, the HC reduction is not constrained to the first cycles and is observed throughout the entire crank-start. Lastly, a 28% reduction in cumulative mass emissions of particulates was observed for the late IVO setting during the initial 13 cycles. This reduction is mainly attributed to a reduction in the 1^{st} cycle PM emissions, while the subsequent cycles show comparable PM emissions for both valve timing cases.

5.3 Crank-start with early exhaust timing

Advancing the exhaust valve timing has a direct impact on the residual gas fraction and the charge temperature during crank-start. When the EVC timing is advanced, the effective portion of the exhaust stroke is reduced, thereby increasing the amount of exhaust gas trapped at the end of the stroke. As the residual gas fraction increases, so does the charge temperature at the end of the intake stroke. Figure 5-15 shows the results of a cycle simulation at cranking speed ($280rpm$) for different values of exhaust valve advance; the results are representative of the conditions at the beginning of the 2nd engine cycle. As the EVC is advanced from the baseline position to a maximum of 40°CA, the residual gas fraction increases from 10% to 25%. The resulting increase in charge temperature during the intake stroke, due to the higher residuals, is on the order of 100°C. Such a temperature increase has the potential to improve the fuel spray evaporation and to reduce the formation of fuel films on the cylinder walls and piston crown.

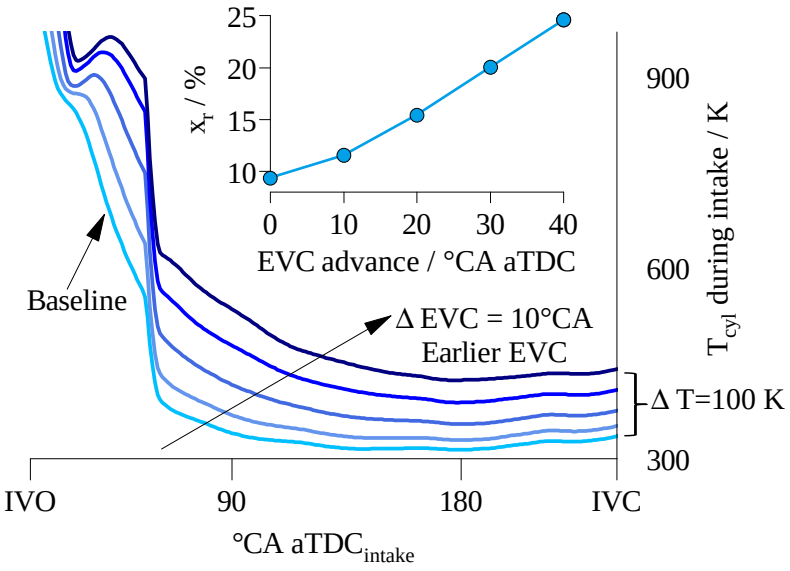

Figure 5-15: Simulated residual gas fraction and in-cylinder temperature during the intake stroke for the 2nd engine cycle and different EVC timings

Experimentally, the exhaust valve timing was advanced by rotating the exhaust camshaft 2 cam-sprocket teeth from the baseline position. The corresponding change in EVO/EVC is approximately 31°CA. Fig. 5-16 shows resulting valve timing.

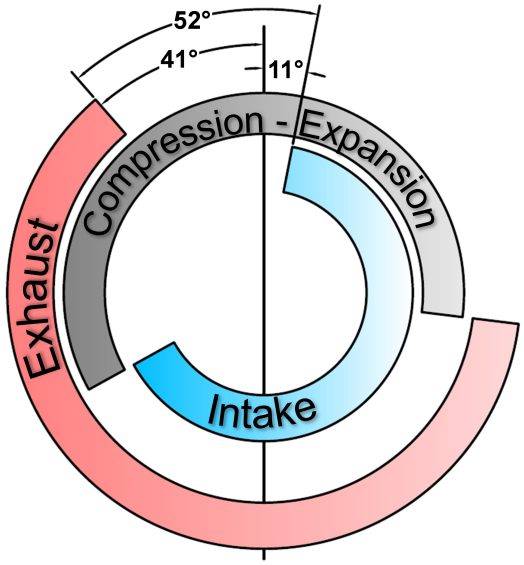

Figure 5-16: Valve timing diagram for the early EVO/EVC setting

The 1st engine cycle is characterized by the absence of residual gases. Thus, as it is observed in Fig. 5-17, the mixture formation process is not affected by the valve timing change, and the dependence of the combustion lambda on the injected fuel mass is similar for both the baseline and the early EVC setting. For the 2nd cycle, however, the presence of residual gases results in a 15% lower fuel requirement for a given lambda of combustion. To determine if the reduction in fuel requirement is associated to the potential improvement in fuel evaporation from the higher charge temperatures, it is necessary to analyze the effect of charge dilution by residual gases. When the increase of residual gas fraction for the early EVC setting is accounted for (increasing from 9% in the baseline case to 22% in the early EVC setting) a 15% reduction in volumetric efficiency is expected. Therefore, the reduction in required fuel for a given combustion lambda is attributed to the air displacement by the residual gas. The greater residual gas fraction with early EVC does not play a significant role in the in-flight spray evaporation and mixture formation processes.

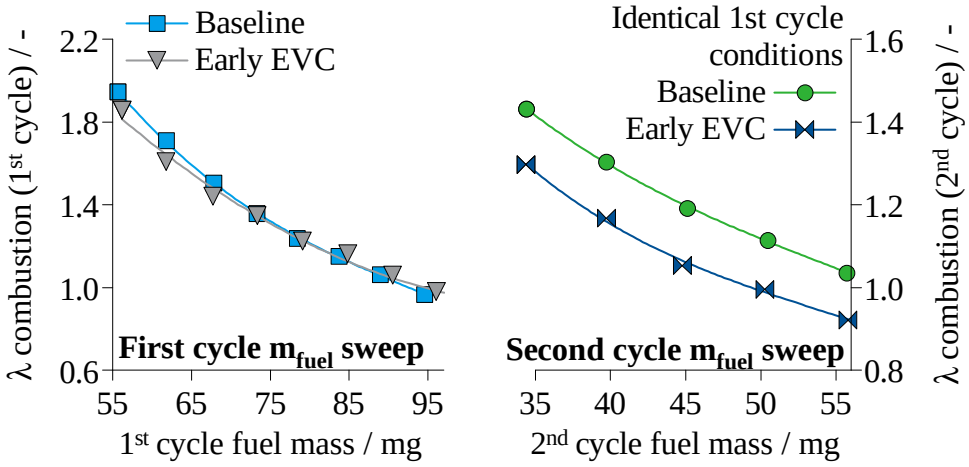

Figure 5-17: Baseline and early EVC results for the lambda of combustion as a function of the injected fuel amount for the 1st and 2nd engine cycles

Figure 5-18 shows the first 2 seconds of the cold crank-start, between the start of cranking and the speed flare, for both the baseline and early EVC cases. It is observed during the 1st cycle that despite the similar mixture formation process (Fig. 5-17)

and same intake manifold pressure during the intake stroke (Fig. 5-18), the early EVC setting resulted in lower work output. The differences in NIMEP are explained by the GIMEP loss associated with early EVO, and the increase in pumping losses caused by the early EVC (see Fig. 5-19). The impact of the lower 1st cycle NIMEP is seen in the slightly slower engine speed run-up during the 1st cycle, and the reduced speed-flare. As the engine speed increases and the intake manifold is pumped down, the early EVO/EVC work losses are compensated by a wider throttle opening, and the NIMEP traces are comparable after the 2nd engine cycle.

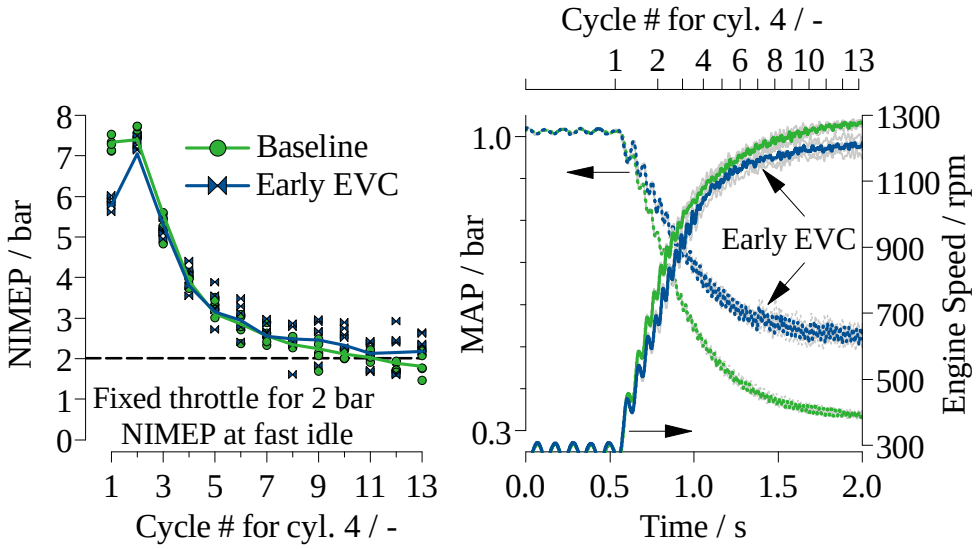

Figure 5-18: NIMEP, engine speed and MAP traces during cold crank-start for baseline and early EVC. Symbols are for individual run results; colored lines represent mean values of 5 separate runs

The NOx, HC, and PM cycle-by-cycle and cumulative emissions are shown in Fig. 5-20. During the initial 13 cycles, early EVC setting results in a 26% reduction in cumulative NOx emissions and in a 20% and 48% increase in cumulative HC and PM emissions respectively. The 1st cycle NOx, HC, and PM emissions are equivalent for both baseline and early EVC settings due to the absence of residual gases. From the 2nd cycle on, the increased internal EGR caused by early EVC starts to have an impact on the emissions behavior.

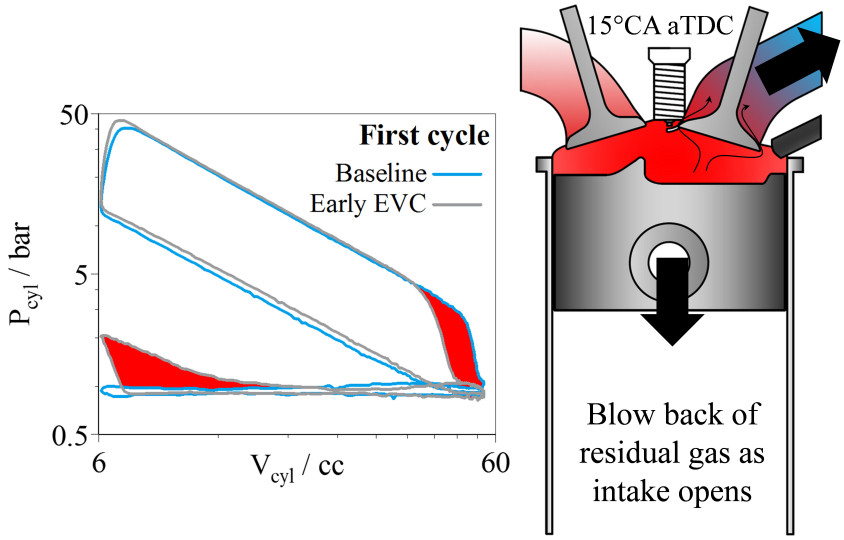

Figure 5-19: Work output losses caused by early EVO/EVC

The reduction in NOx emissions with early EVC is a direct result of the increased residual gas fraction. The charge dilution achieved after the 2nd cycle lowers the peak temperatures during combustion and results in an approximate 50% reduction in NO production and emission.

Increased internal EGR rates have competing effects on the HC emissions. Given that a significant part of the HC flow during the exhaust process occurs due to roll-up vortex formed during the later part of the exhaust stroke by the scraping of the boundary-layer gases off the cylinder wall [30], it is expected that the early EVC results in more trapping of this HC rich gases, thus leading to a reduction in HC emissions [21]. On the other hand, the increased residual fraction reduces the combustion and post-flame temperatures and limits the oxidation rate of the fuel that managed to escape combustion.

The PM formation stages can be summarized as nucleation, oxidation, and growth [28]. Particle nucleation is a function of temperature and availability of precursors, such as liquid fuel and overly rich regions. While the amount of liquid fuel is inferred to be similar for both baseline and early EVC timings (see Fig. 5-17 and

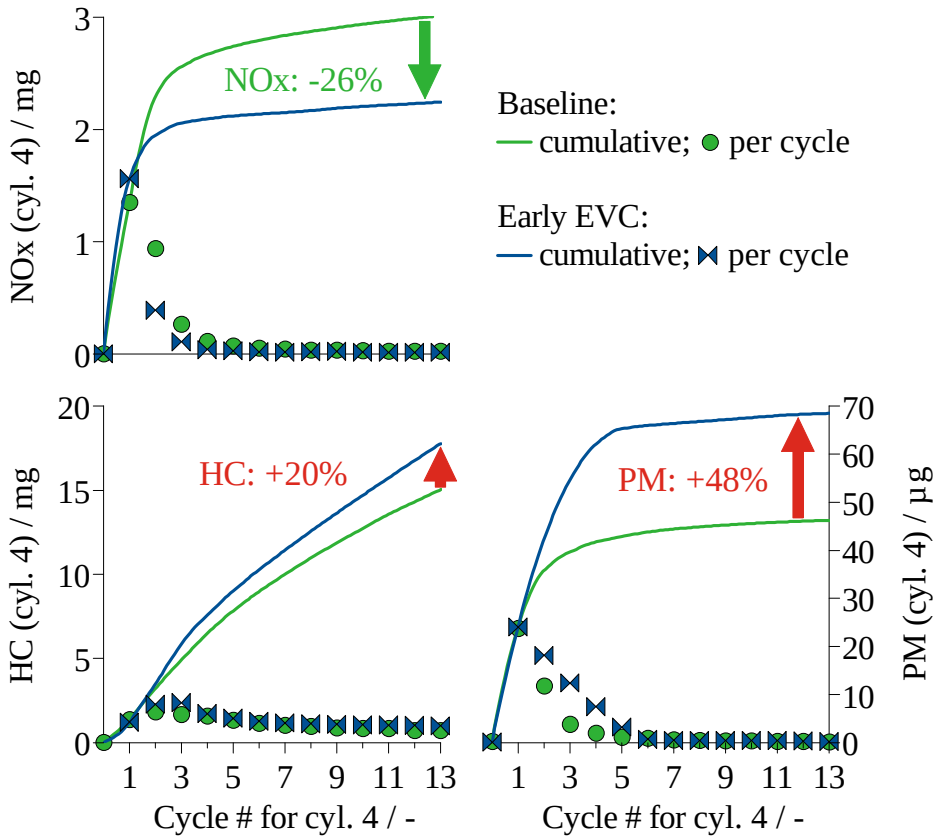

Figure 5-20: Cycle-by-cycle and cumulative NOx, HC, and PM emissions of cylinder 4 during cold crank-start for the baseline and early EVC settings

its discussion), the spatial distribution of the AFR is dependent on the intake flow structure, which could be affected by the blow-back of residual gases at IVO. This effect, however, cannot be estimated with the tools used in this study. Additionally, the particles contained in the residual gases which fail to burn completely in the combustion process, could serve as additional nucleation sites. On the other hand, early EVC reduces the in-cylinder temperatures through charge dilution, which has the effect of reducing the particle nucleation rate, while concurrently reducing the oxidation rate of the incipient particles. Particle growth is affected by amount of HC in the post-flame gases available for agglomeration, the particles surface area, and the coagulation through particle collisions. In this regard, early EVC could affect the particle growth potential as it impacts the post-flame HC concentration [29]. In

summary, early EVC results in higher HC and PM emissions during crank-start as a result of competing effects of formation and oxidation due to the increased residual gas fraction.

5.4 Crank-start with late intake and early exhaust timing

The final valve timing strategy studied, referenced as symmetric NVO, is a combination of late IVO and early EVC. The intake valve timing was delayed by the same amount the exhaust valve timing was advanced. Each camshaft was rotated 31°CA (2 cam-sprocket teeth) from the baseline position in the respective direction. The resulting valve timing, shown in Fig. 5-21, has a symmetric negative valve overlap (NVO) of 83°CA.

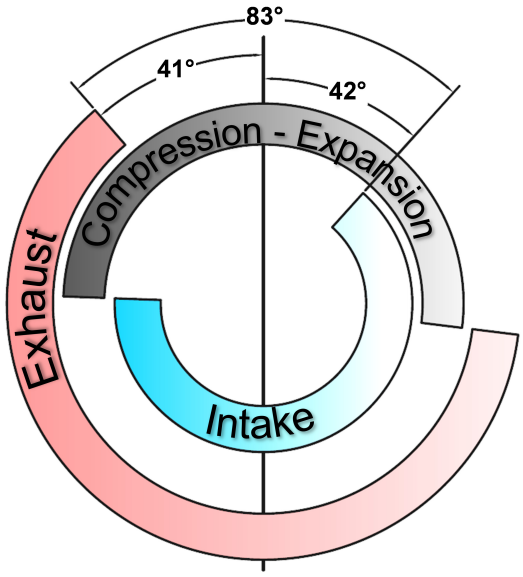

Figure 5-21: Valve timing diagram for the early EVO/EVC setting

The main features of the symmetric NVO strategy are the increase in charge motion

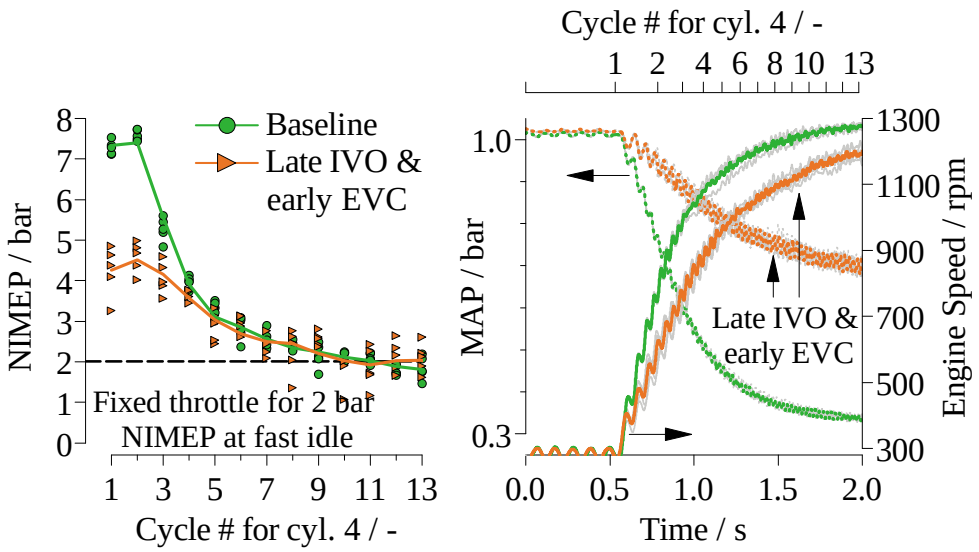

Figure 5-22: NIMEP, engine speed and MAP traces during cold crank-start for baseline and symmetric NVO. Symbols are for individual run results; colored lines represent mean values of 5 separate runs

and reduction in cylinder pressure during the early intake stroke due to late IVO and the increase in residual gas fraction brought along by early EVC. Additionally, the reduction in effective compression ratio due to late IVC and the reduction in effective expansion ratio due to early EVO have an impact in the work output of the first few engine cycles. In comparison to the early EVC strategy, the symmetric NVO setting reduces the blow-back of the trapped residual gases, as the late IVO allows for the expansion of the residual gases prior to IVO. Figure 5-22 shows the progression of the cold crank-start during the first two seconds for the baseline and symmetric NVO cases. A sharp reduction in NIMEP can be observed for the first three engine cycles of the symmetric NVO case. This is a result of the reduction in fresh mixture trapped at IVC and of the increase in losses from early EVO/EVC (Fig. 5-19). The resulting speed trace resembles the late IVO case, with a reduced speed transient and flare. For the later cycles, these effects are compensated for by the throttle setting which takes into effect as the MAP adjusts to the steady-state value. In order to achieve 2 *bar* NIMEP, the throttle position results in a MAP value of 0.65 *bar* after 2 seconds

(for comparison, ≈ 0.3 *bar* for baseline and 0.5 *bar* for late IVO or early EVC). It was also noted that for any given cycle after the 1st combustion event, the higher internal EGR causes greater variability in NIMEP with symmetric NVO strategy.

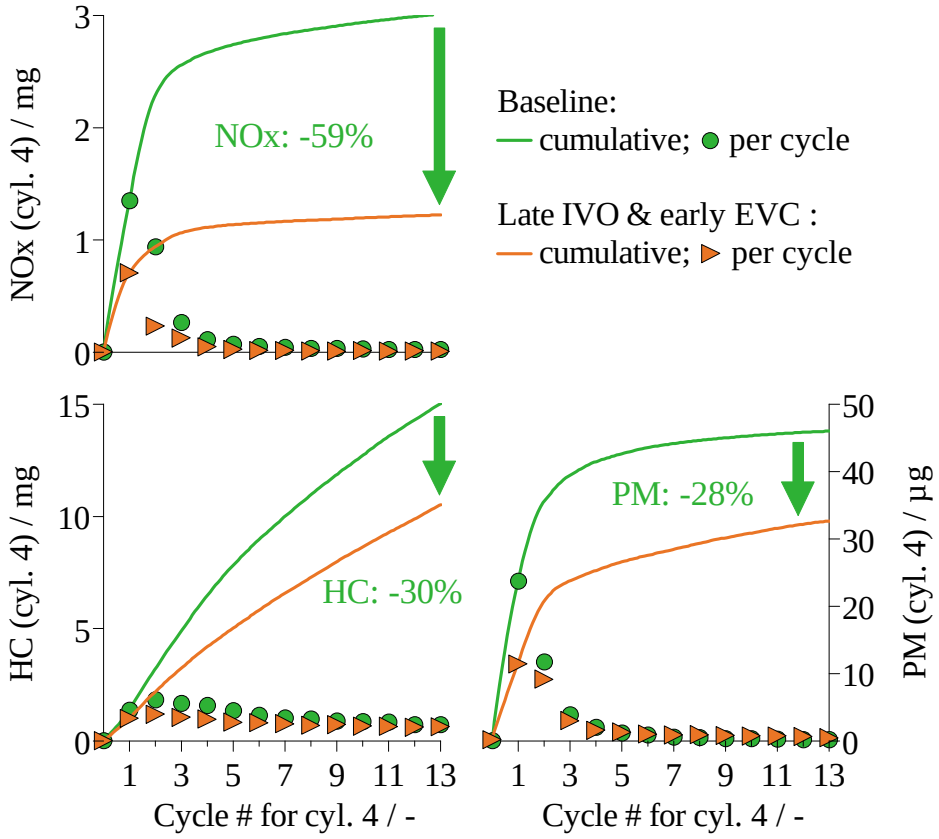

Figure 5-23: Cycle-by-cycle and cumulative NOx, HC, and PM emissions of cylinder 4 during cold crank-start for the baseline and symmetric NVO settings

Figure 5-23 shows the cycle-by-cycle and cumulative NOx, HC and, PM emissions for both the baseline and symmetric NVO strategies. Compared to the baseline, the cumulative NOx emissions achieved with the symmetric NVO setting show a significant reduction of 59%. The lower cumulative NOx emissions are the combined result of 2 effects. First, late IVO/IVC result in a reduced ECR and thus in lower NIMEP during the initial engine cycles. Second, the increased residual gas fraction after the 2nd cycle dilutes the charge, lowering the combustion temperature and reducing the NO production.

Comparing the symmetric NVO to the previous two strategies discussed (late IVO: Fig. 5-14; early EVC: Fig. 5-20), the measurements show a greater resemblance to the HC and PM emissions reduction achieved with late IVO, as they are reduced in 30% and 28% correspondingly with respect to the baseline. The reduction in HC emissions is more prominent during the initial five engine cycles, with the difference becoming smaller as the crank-start progresses. As in the late IVO case, the reduction in PM stems mainly from the 1^{st} cycle.

Late IVO alone was advantageous in the mixture formation process, improving spray evaporation and reducing the amount of fuel films serving as HC and PM sources. Additionally, the lower volumetric efficiency caused by the late IVC event, reduces the total mass exhausted during the critical 1^{st} cycle, for which the intake pressure is close to atmospheric. Conversely, the early EVC results described in the previous section showed an increase in HC and PM emissions, due to the unbalance of the competing effects of increased internal EGR on the HC and PM formation and oxidation. From a simplified analysis, the emissions behavior of the combined strategy was expected to fall between the two cases previously described. However, the combined effect of late IVO and early EVC on the temporal and spatial evolution of the inlet flow, AFR, EGR, charge temperature and fuel films cannot be assessed with the experimental capabilities of this study and no further explanation can be provided for the observed trends.

5.5 Findings

The effects of four valve timing settings on the cold-start NOx, HC and PM emissions during crank-start were studied in a wall guided gasoline direct injection engine. The valve timings examined were the stock position, late IVO, early EVC and a combination of the latter, dubbed symmetric NVO. The following conclusions are drawn:

- Late IVO improves the mixture formation process in cold crank-start and reduces the exhaust mass flow during the critical 1st cycle exhaust event. The delayed intake timing results in 25% and 28% reduction of the cumulative HC and PM cold crank-start emissions respectively. During the initial cycles, late IVC results in lower NIMEP and in-cylinder temperatures reducing the rate of NO formation.

- The effect of early EVC timing on the crank-start emissions is due to the increase in residual gas fraction. For this reason it does not have any effect on the 1st cycle. Early EVC results in an improvement in NOx emissions after the 2nd engine cycle and in a deterioration of the HC and PM/PN emissions in cold crank-start. The increase in cumulative HC and PM emissions comprises mainly the contributions from the early cycles (2nd through 5th).

- The combined strategy consisting of late intake and early exhaust phasing shows a significant reduction in the cumulative crank-start NOx emissions due to the combination of increased residuals and lower NIMEP of the initial cycles. Furthermore, the reduction in cumulative HC and PM/PN emissions is similar in magnitude and cycle-to-cycle progression to the late IVO case. Thus early EVC has less impact on the crank-start HC and PM emissions compared to late IVO.

– Intentionally left blank –

Chapter 6

Cold fast-idle emissions

This chapter deals with the emissions behavior during the cold fast-idle of a gasoline direction engine. The cold fast-idle is a short quasi-steady (see Table 6.1) period between the end of the crank-start and the first acceleration event in the certification cycle. In the case of the FTP-75 and the NEDC, two of the most widespread used certification cycles, the idling period before the first transient has a duration of 20 seconds. The objectives during the cold fast-idle are twofold: To provide a high thermal enthalpy flow to the three-way-catalyst (TWC) to reduce th light-off time, while keeping the engine-out pollutant emissions as low as possible during the TWC warm-up process.

Engine speed	1200 *rpm*
NIMEP	2.3 *bar*
External EGR	0%
Coolant, oil and fuel temperature	20°C
Fuel pressure	50 *bar*
Number of cycles in average	150

Table 6.1: Experimental conditions for cold fast-idle experiments

6.1 Experiments descripton

Due to the steady-state nature of the cold fast-idle experiments, the metrics of interest are different in comparison to the single cycle and crank-start experiments presented in the previous chapters. The exhaust gas composition was measured at the exit of the turbine, or TWC inlet in real applications. The HC mole fraction was measured using a fast response FID analyzer (Cambustion model HFR400), the CO and CO_2 mole fractions were measured with a fast response NDIR analyzer (Cambustion model NDIR500), and the NOx mole fraction with a fast response CLD analyzer (Cambustion model fNOx400). The PM and PN concentrations were measured using a fast response differential mobolity analyzer (Cambustion model DMS500). Additionally, the temperature and pressure of the working fluids was monitored on several positions. The location of the different sensors is shown in Fig. 6-1.

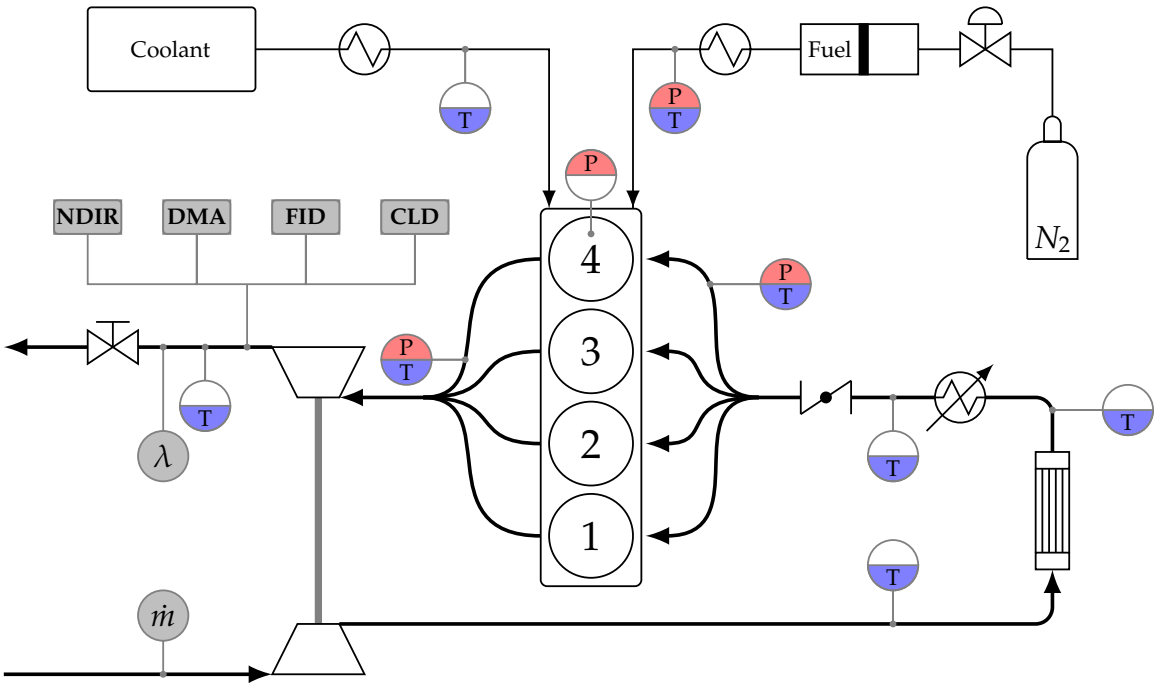

Figure 6-1: Diagram of the experimental setup and the sensor locations

Previous work at MIT has focused on extensively characterizing the cold fast-idle emissions of HC [9] and particulates [36]. The experiments presented in this chapter seek to expand the previous analysis to include NOx emissions and unconventional valve timing. The variables studied and object of the following sections are:

1. Air-fuel equivalence ratio
2. Split-injection strategies
3. Combustion phasing
4. Valve timing

6.2 Air-fuel equivalence ratio

During the normal operation of stoichiometric gasoline engines, the air-fuel equivalence ratio is carefully regulated around $\lambda = 1$ to ensure that the TWC catalyst mantains a certain level of oxygen storage so that it can effectively oxide HC and CO emissions to CO_2 and reduce NOx emissions to N_2. However, during cold fast-idle, this constrain is lifted due to the catalytic inactivity of the TWC. This section presents the effect of lambda on the engine out emissions, exhaust enthalpy and engine stability. Table 6.2 presents the specific details of the air-fuel equivalence ratio experiments, in addition to the operating conditions presented in Table 6.1.

Spark timing	5°CA $aTDC_{comp.}$
Start of Injection	105°CA $aTDC_{intake}$
Injection pulse duration	1520 μs
Injected mass	17.1 mg
Valve timing	Baseline (Table 5.1)

Table 6.2: Injection strategy for lambda sweep

The experiments were conducted at constant spark timing and constant fuel mass. The air-fuel ratio was controlled by the throttle position. Figures 6-2 and 6-3 show the emissions characteristics of the three pollutants studied.

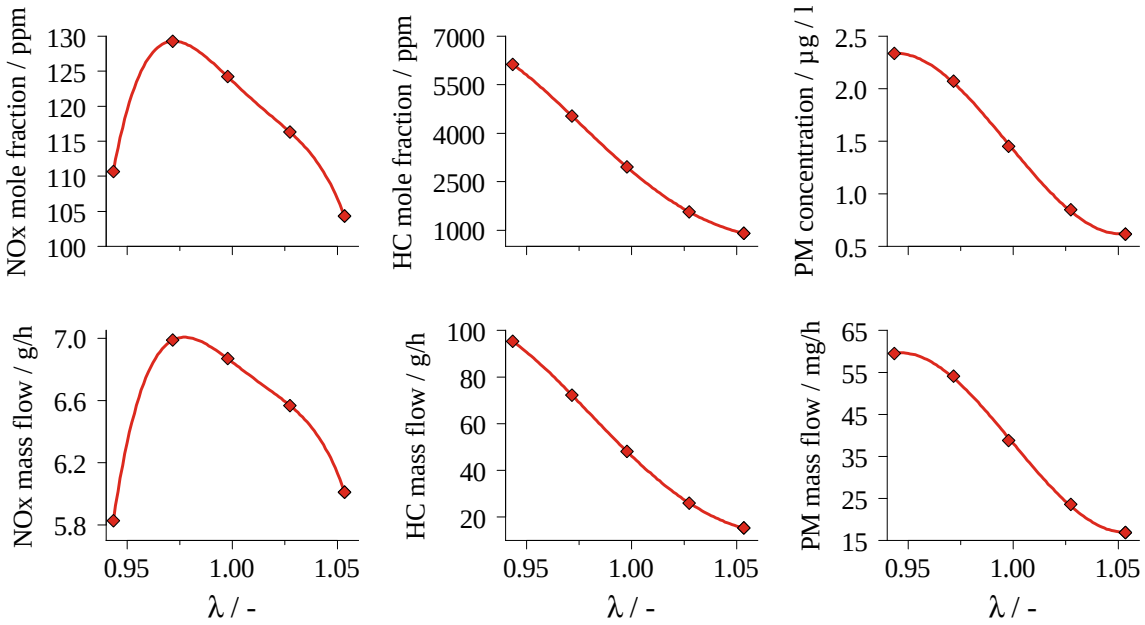

Figure 6-2: Concentration and mass flow of NOx, HC and PM as a function of lambda

NOx mole fraction and mass emissions peak at a slight rich mixture of $\lambda = 0.975$. The reduced flame speed of the leaner mixture and the constant spark timing results in a delay in combustion phasing as shown in Fig. 6-4 and consequently i a reduction in peak temperature. As the mixture becomes leaner at constant fuel mass, the adiabatic flame temperature decreases slightly while the oxygen concentration increases. For richer mixtures there is a lack of O_2 available for NO formation. The combined effect of reduction in temperature due to the later combustion phasing and the oxygen availability result in NOx emissions peaking at a slightly fuel-rich AFR.

The HC and PM emissions exhibit a monotonic reduction with increasing lambda. Increasing the AFR results in higher O_2 concentration and higher burned gas temperature due to later combustion phasing. The higher post-combustion temperature

results in higher post-flame oxidation rates of the fuel-air mixture resulting from the quenching layer close to the cylinder liner and the out-gassing of mixture stored in crevices and in-between the piston lands [34]. The PM emissions decrease is driven by a reduction in particle number as the median particle size remains constant at approximately 45 nm (Fig. 6-3). The particle formation and growth during cold-start takes place mainly in the fuel-rich regions in the combustion chamber [35]. As such, the O_2 increase and higher burned temperature of leaner mixtures reduces the amount of fuel available for pyrolysis through post-flame oxidation, but does not affect the nucleation and growth processes occurring in the fuel vapor plume from fuel films.

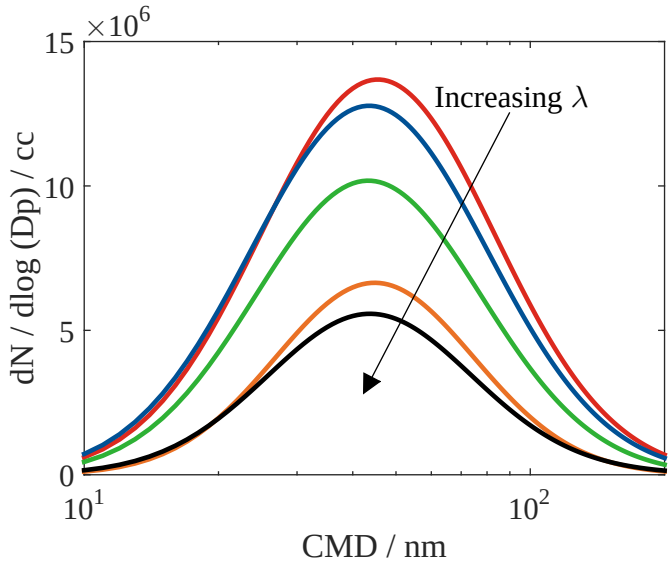

Figure 6-3: Particle size distribution of the accumulation mode (lognormal fit) as a function of lambda ($\lambda = 0.95 - 1.05$ and a 0.025 step)

From the emissions trends observed, it is evident that leaner mixtures are favorable for reducing the cold fast-idle emissions. However, the application of such a strategy is limited by engine stability as quantified by the covariance of the NIMEP ($\text{CoV}_{\text{NIMEP}}$). Figure 6-4 shows how the cycle-to-cycle variability increases proportionately to λ. However, as the experiment was performed at constant spark timing, the effects of later combustion phasing and leaner mixture are confounded. Section 6.3 examines some injection strategies aiming to improve the $\text{CoV}_{\text{NIMEP}}$.

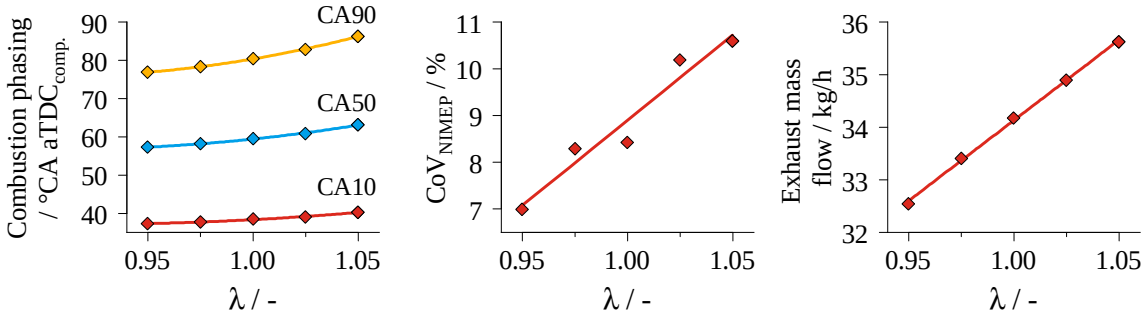

Figure 6-4: Combustion phasing, CoV of NIMEP and exhaust mass flow as a function of lambda

6.3 Split-injection strategies

This section assesses the effect of three different split injection strategies on engine out emissions and combustion stability during cold fast-idle. The injection strategies investigated are presented in Tables 6.3, 6.4 and 6.5. In all cases the spark timing was kept constant at 5°CA aTDC$_{comp.}$ and the valve timing setting was in the baseline position.

SOI1	105°CA aTDC$_{intake}$
SOI2	165°CA aTDC$_{intake}$
Injection split y_1/y_2	100/0; 75/25; 50/50; 25/75; 0/100
Air fuel ratio	$\lambda = 1$
NIMEP	2.3 *bar*

Table 6.3: Split injection strategy A

SOI1	45°CA aTDC$_{intake}$
SOI2	105°CA aTDC$_{intake}$
Injection split y_1/y_2	100/0; 75/25; 50/50; 25/75; 0/100
Air fuel ratio	$\lambda = 1$
NIMEP	2.3 *bar*

Table 6.4: Split injection strategy B

SOI1	105°CA $aTDC_{intake}$
SOI2	364°CA $aTDC_{intake}$ (1°CA before spark)
Main injection pulse	1550 μs
Injected mass	17.4 mg
Late injection pulse (PW2)	$200 - 250$ μs; 10 μs step
Air mass flow	38 kg/h

Table 6.5: Split injection strategy C

The fuel spray penetration is proportional to the duration of injection for a fixed fuel pressure. Depending on the injection timing, an increased fuel spray penetration could result on impingement of the piston crown, back of the intake valve, or cylinder liner and it's respective oil layer. If the fuel amount to be delivered is split into multiple injections events the penetration length of the separate injection pulses can be reduced [74].

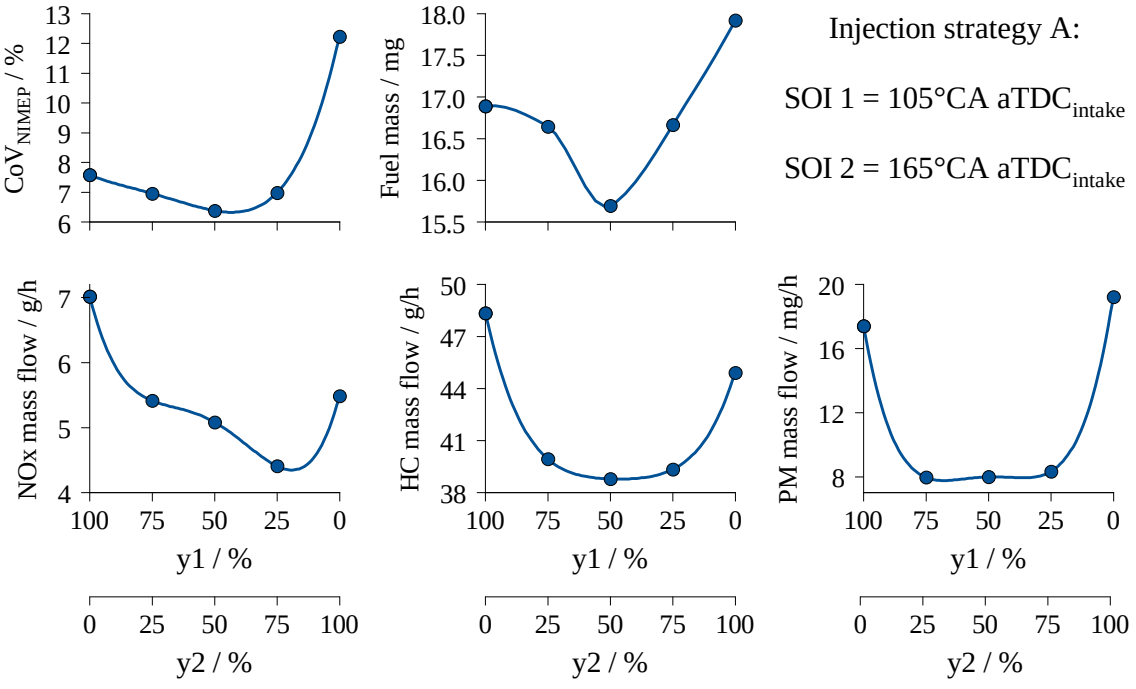

Figure 6-5: Split injection strategy A: Combustion stability and mass flow emissions of NOx, HC and PM as a function of split ratio

Figure 6-5 shows the emissions and CoV behavior of the split injection strategy A. The x-axis extremes correspond to a single injection event at the respective SOI specified in Table 6.3. As a result of the reduced fuel impingement on the intake valve and the cylinder liner with split injection, the HC and PM emissions are lowered in approximately 30% and 65% respectively. Given that the tendency to form liquid fuel films is reduced, the less fuel is necessary to achieve the targeted NIMEP and lambda, with a minimum of 15.7 mg at $y_1/y_2 = 50/50$. The NOx emissions show a minimum for a split ratio $y_1/y_2 = 25/75$ presumably as a consequence of a more homogeneous mixture minimizing the regions experiencing high temperatures with high oxygen availability. Park et al. [56] also report lower NO formation with split injection strategies.

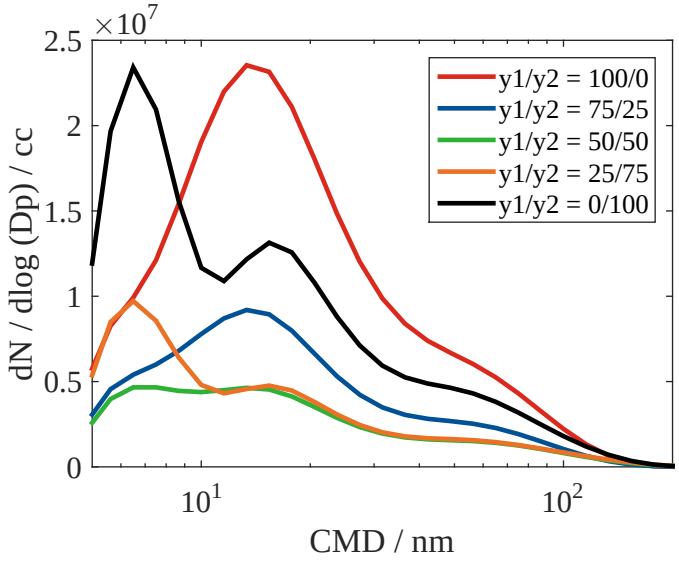

Figure 6-6: Split injection strategy A: Particle size distribution of the measured spectrum as a function of split ratio

The spray interaction with the cylinder liner and the corresponding oil layer shows a distinctive behavior in the particulate emissions. As shown in Fig. 6-6, as the fraction of fuel injected in the second injection (SOI2 = 165°CA $\text{aTDC}_{\text{intake}}$) increases, an additional aerosol mode appears in the particle distribution different from the nucleation and accumulation modes. This tri-modal particle distribution, with the

distinct peak between $6-7$ nm has been observed by other studies [73] and it is attributed to organic hydrocarbons. The size range of the molecule detected falls outside of the size range of the paraffins found in gasoline [33]; e.g. n-Octane has a chain length of 13 Å. The $6-7$ nm peak detected can be linked to larger HC molecules being detached from the oil layer on the liner due to the interaction with the fuel spray.

Concerning combustion stability, split injection has a positive effect on the CoV of NIMEP achieving a minimum of 6.4% at $y_1/y_2 = 50/50$. This represents a 15% improvement with respect to a single injection during IVO and a 48% improvement compared to single injection close to BDC.

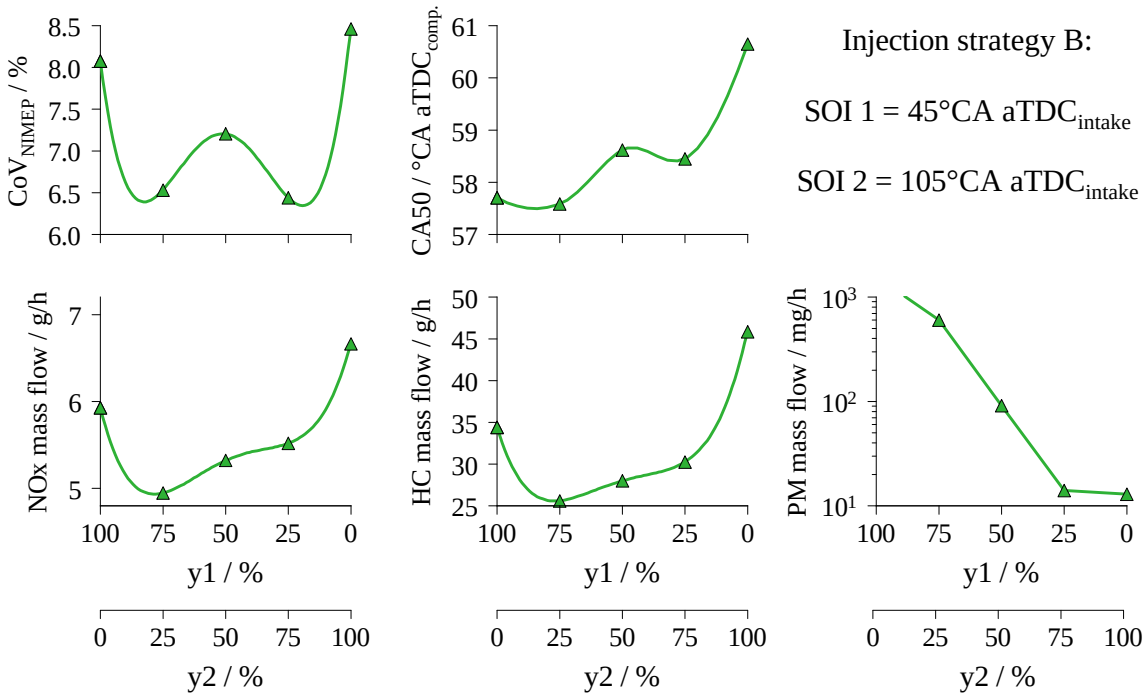

Figure 6-7: Split injection strategy B: Combustion stability and mass flow emissions of NOx, HC and PM as a function of split ratio

The focus is now placed on the split injection strategy B (Table 6.4). The early SOI of the first injection event results in spray interaction with the piston crown.

The second injection takes place at open intake valve. As shown in Fig. 6-7, the spray interaction with the piston crown has little impact on HC emissions, and, in comparison to liner and intake valve interaction, it is even beneficial. The PM formation increases sharply with increasing spray/piston interaction covering more than 2 orders of magnitude as the injection is shifted from a single injection event at 45°CA $aTDC_{intake}$ to a single injection at 105°CA $aTDC_{intake}$. As the fraction of the first injection is reduced to 25%, the injection duration is short enough that the penetration length is less that the distance to the piston. Therefore, the split ratios $y_1/y_2 = 25/75$ and $y_1/y_2 = 0/100$ show similar PM emissions and comparable particle size distributions (see Fig. 6-8).

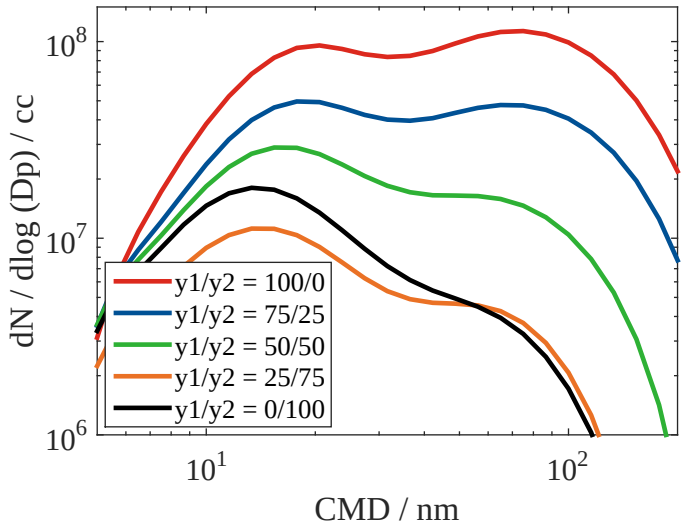

Figure 6-8: Split injection strategy B: Particle size distribution of the measured spectrum as a function of split ratio

The NOx emissions as a function of the split ratio of injection strategy B are shown in Fig. 6-7. The increase in NOx emissions as the split ratio is shifted towards injection during IVO is correlated with the change in combustion phasing. As CA50 is retarded, the temperature of the residual gases increases and the residual mass fraction is reduced. Lower residual gas fraction results in higher combustion temperatures and consequently higher NO formation. Lastly, the improvement in

cycle-to-cycle variability of injection strategy B is in the same range of strategy A going from a maximum of 8.5% for single injection during intake opening to 6.5% for $y_1/y_2 = 25/75$ and $y_1/y_2 = 75/25$.

Lastly, split injection strategy C is examined. Strategy C consists of an early main injection during the intake stroke resulting in a homogeneous air-fuel mixture with $\lambda = 1.05$ and a very late injection immediately before the ignition timing, in order to enrich the mixture in the vicinity of the spark plug to favor the the early stages of the flame development and propagation and improve the combustion stability [17]. The pulse width of the late injection was varied in the ballistic range of the solenoid injector; i.e. the injection pulse is outside of the linear range of operation resulting from the partial opening of the nozzle needle, also referred to a "free-flight".

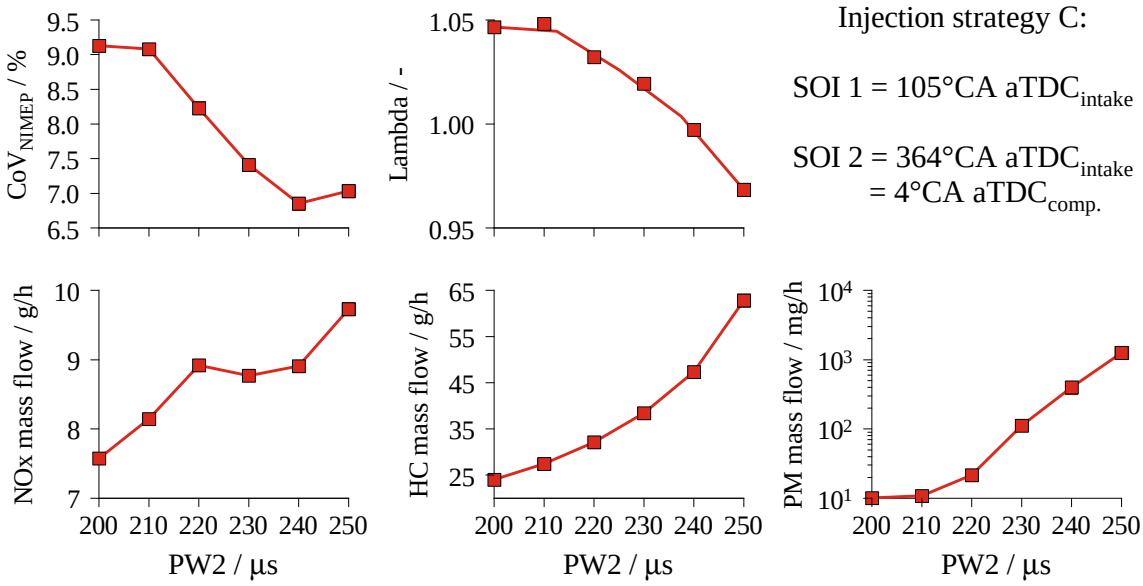

Figure 6-9: Split injection strategy C: Combustion stability and mass flow emissions of NOx, HC and PM as a function of late injection pulse duration

Figure 6-9 shows the NOx, HC and PM emissions as a function of the pulse width of the late injection. Injection pulses shorter or equal than 210 μs are not long enough to result in a measurable enrichment of the air-fuel mixture as can be seen

in the lambda results. From an injection pulse of 220 μs, the mixture enrichment can be measured and the exhaust lambda decreases monotonically. The combustion stability also increases approximately a percentage point while all engine out emissions increase. The increase in NOx emissions with late injection pulse is driven by the higher NIMEP and the resulting hotter combustion temperatures. Since the mixture is stratified, the oxygen availability in the bulk of the charge remains unchanged for most of the combustion process.

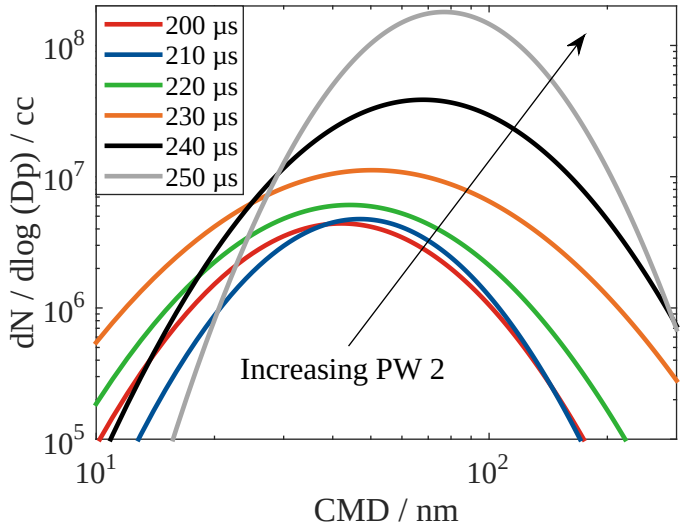

Figure 6-10: Split injection strategy C: Particle size distribution of the accumulation mode (lognormal fit) as a function of late injection pulse duration

HC and PM emissions are driven up by the formation of fuel films from the piston impingement resulting at longer late injection pulses. The HC emissions more than doubled as the injection pulse is increased from 200 μs to 250 μs. The particulate emissions increase is more significant as it covers more than two orders of magnitude in the late injection range tested. As shown in the particle size distribution in Fig. 6-10, the higher PM is the result of an increase in the size and number of particles being produced. The median particle diameter of the accumulation mode is 1.8 times larger for PW2 = 250 μs in comparison to the homogeneous case. That increase in particle size alone results in a sixfold increase in particulate mass.

6.4 Combustion phasing

The effect of retarded combustion phasing on the engine-out NOx, HC and PM emissions is presented in this section. Delayed spark timing is the most common strategy used to reduce the light-off time of the three-way catalyst during cold-start. However, combustion delay also impacts directly the engine-out pollutant emissions. Three injection strategies selected for the combustion phasing study are based on the lessons learned in Sections 6.2 and 6.3 and are shown in Table 6.6.

	Single	**Double**	**Triple**
SOI1 [°CA $aTDC_{intake}$]	105	105	105
SOI2 [°CA $aTDC_{intake}$]	–	165	165
SOI3 [°CA before spark]	–	–	1
Injection split y_1/y_2	100/0	50/50	50/50
Late injection (PW3) [μs]	–	–	230
Air-fuel ratio	$\lambda = 1.05$	$\lambda = 1.05$	$\lambda = 1.05$
NIMEP [bar]	2.3	2.3	2.3

Table 6.6: Strategies used for the combustion phasing study at cold fast-idle

The **Single** strategy consists of only one injection event during intake valve opening. The **Double** strategy uses an equal-parts split for the injection even, half being injected during intake valve opening and half during the last part of the intake stroke. Lastly, the **Triple** strategy is based on the **Double** with an additional third late injection of a small quantity of fuel immediately before spark timing. In all cases the overall air-fuel ratio was kept at $\lambda = 1.05$ and the NIMEP at 2.3 bar.

As combustion phasing is delayed, the thermal efficiency of the engine decreases. As a result the air and fuel mass flow rates necessary to keep the targeted NIMEP constant increase. In order to separate the effects of increased exhaust mass flow from the effects of volumetric pollutant formation two different metrics are used. To track the changes in pollutant emissions on a per mass basis, the mole fraction

measurements are translated into mass emissions and then referenced to the amount of fuel injected. This metric is referred to as emissions index (EI, Eq. 6.1) and as such is independent of the air and fuel mass flow rates. To account for the change in emissions as a consequence of a change in air mass flow, the net indicated specific emissions is used as a metric (NISE, Eq. 6.2).

$$\mathrm{EI} = \hat{x}_i \cdot \frac{MW_i}{MW_{exh}} \cdot \frac{\dot{m}_{exh}}{\dot{m}_{fuel}} \tag{6.1}$$

$$\mathrm{NISE} = \hat{x}_i \cdot \frac{MW_i}{MW_{exh}} \cdot \dot{m}_{exh} \cdot \frac{2}{NIMEP \cdot V_d \cdot N_{eng}} \tag{6.2}$$

Figure 6-11 shows the emissions behavior for all three injection strategies as a function of the crank angle at which 50% of the fuel has been burned (CA50).

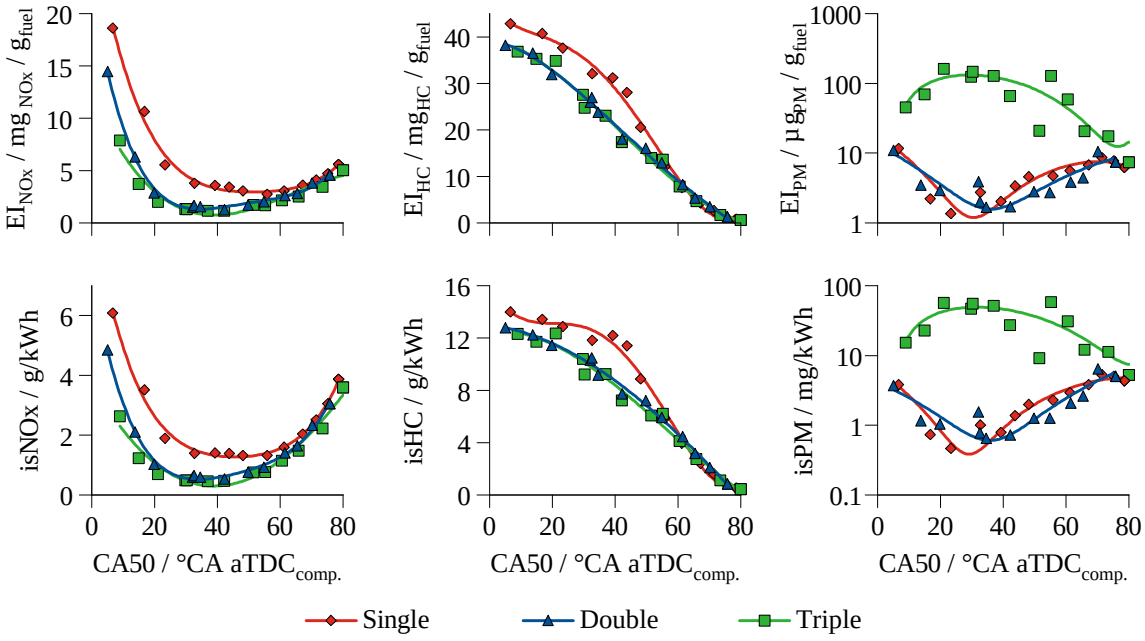

Figure 6-11: Emissions indices and indicated specific emissions of NOx, HC and PM as a function of CA50 for three different injection strategies

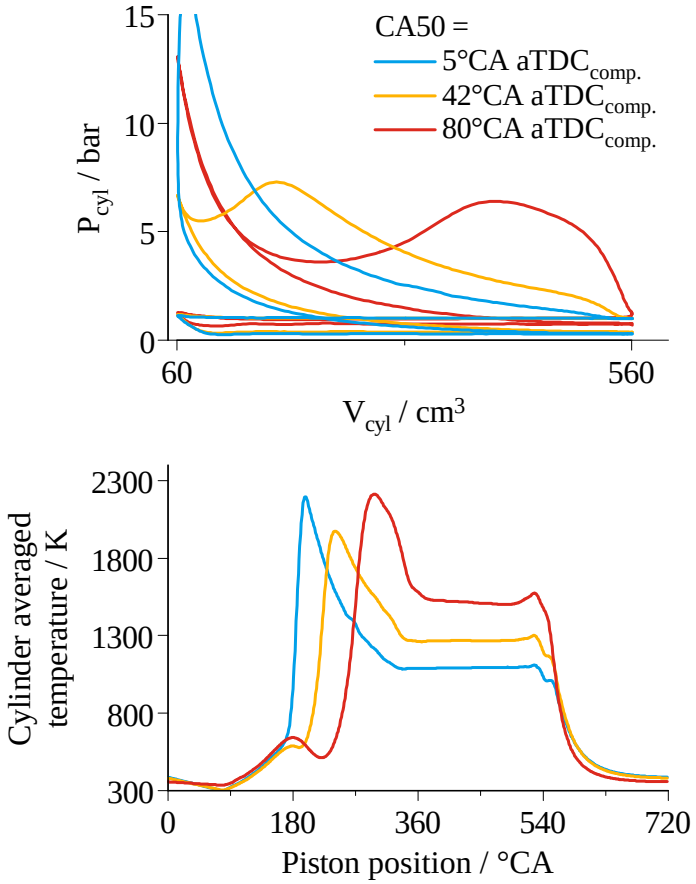

Figure 6-12: Experimental P-V diagram and cylinder temperature for three different combustion phasing using the **Double** injection strategy

NOx emissions are reduced significantly as the CA50 goes from the most advanced point ($\approx$ 5°CA aTDC$_{comp.}$) to approximately CA50 = 40°CA aTDC$_{comp.}$. This reduction is driven by a reduction in the peak temperatures as a larger fraction of the combustion process occurs at larger cylinder volumes. For later combustion phasing, the combination of an increase in the NOx emissions index with higher exhaust mass flows results in a steep increase in the NOx specific emissions. As combustion phasing is delayed, the thermal efficiency of the engine decreases. To compensate for that reduction, larger amounts of fuel need to be injected to maintain constant NIMEP (area inside the curve in Fig. 6-12, top). Even though the peak combustion pressure is reduced monotonically with later combustion phasing, the peak cylinder temperatures

do not. At CA50 ≈ 40°CA aTDC$_{comp.}$ the maximum cylinder averaged temperature exhibits a minimum; for earlier CA50 the combustion at lower volume increases the peak temperatures, while at later combustion phasing the larger amount of fuel involved results in the same effect. Experimental traces illustrating this phenomena are shown in Fig. 6-12.

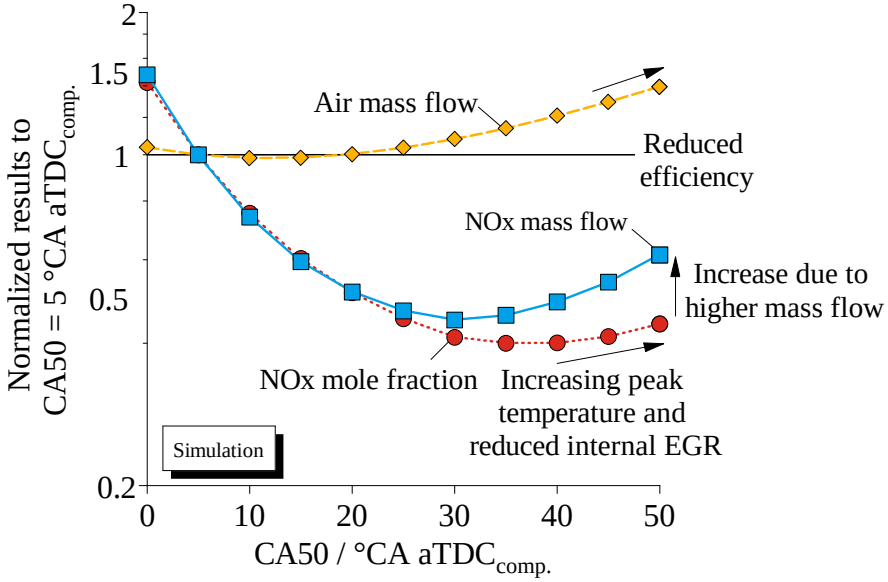

Figure 6-13: Simulated NOx emissions as a function of CA50

Furthermore, the burned gas temperature after combustion increases with late CA50, decreasing the density of the exhaust gases and of the residual burned gases. The end result is a reduction in the residual gas fraction as combustion phasing is delayed. The lower mass of inert residual gases is less effective at diluting the fresh charge resulting in increasing combustion temperature and higher rates of NO formation. This processes are illustrated by means of a cycle simulation in Fig. 6-13.

Throughout the CA50 sweep, the **Single** injection strategy exhibited approximately double the NOx emissions as the split strategies. Furthermore, due to increased fuel stratification in the beginning of the combustion process the **Triple** injection strategy showed 10% lower NOx emissions as its **Double** counterpart.

Delayed combustion phasing affects the in-cylinder conditions by reducing the peak pressure during combustion and increasing the burned gas temperature behind the flame front and during exhaust. Regarding the HC emissions, a reduction in peak pressure is beneficial for the reduction in crevice storage of unburned mixture. Higher post-flame and exhaust temperature increase the post-oxidation rate of the unburned HC content in the bulk gases and exiting the crevices during the exhaust stroke. However, late combustion phasing also reduces the HC residence time in the hot burned gases before EVO. Nevertheless, if the combustion phasing is retarded enough to maintain high temperatures during the exhaust process significant post-oxidation will take place in the exhaust runner and manifold. This phenomenon was observed for the three injection strategies tested.

The EI_{HC} and isHC decreased monotonically with later combustion and approached zero for very late CA50. The oxidation in the exhaust manifold is responsible for the reduction of HC emissions to close to zero values. Evidence for exhaust manifold post-oxidation is observed in Fig. 6-14; for CA50 later than 65°CA $aTDC_{comp.}$, the after-turbine temperature is higher than the exhaust port temperature due to the post-oxidation process. It should be mentioned as a last remark that the **Single** injection results in higher HC emissions in comparison to the other two strategies. Furthermore, the late ballistic injection before ignition has no effect in the HC emissions and the HC emissions traces overlap for the **Double** and **Triple** strategies overlap.

Combustion phasing impacts PM emissions by altering the nucleation, oxidation and growth processes. As combustion is delayed, the time available for nucleation through fuel film and droplet pyrolysis is reduced, while at the same time the nucleation rate increases due to the higher gas temperatures. The oxidation rate of the incipient particles increases, while the time between end of combustion and EVO is reduced. If the temperatures during the exhaust stroke are high enough, significant particle oxidation can occur after EVO as the exhaust flows through the manifold.

Lastly, as the HC concentration in the burned gases drops with late combustion phasing, particle growth through surface adsorption/absorption is also limited.

As observed in Fig. 6-11, the **Single** and **Double** strategies exhibit similar PM emissions behavior. The PM emissions index and specific emissions decrease from MBT combustion phasing to a minimum located at CA50 $\approx$ 35°CA aTDC$_{\text{comp.}}$. After this point the PM emissions increase again with further combustion delay. Due to the decreasing thermal efficiency later combustion phasing, the amount of fuel necessary to keep NIMEP constant increases. Consequently, the higher particle nucleation and growth rate stemming form larger fuel quantities injected cannot be counterbalanced by the rates of post-flame oxidation in the hotter exhaust gases during expansion and exhaust stroke. The **Triple** injection strategy behaves differently from the other two strategies studied. The late injection event immediately before ignition results liquid fuel droplets that do not fully evaporate and mix with the rest of the cylinder contents, therefore increasing by over an order of magnitude the PM emissions. The PM emissions peak when CA50 $\approx$ 35°CA aTDC$_{\text{comp.}}$ and decrease for earlier or later combustion phasing. The spark timing corresponding to that CA50 point is close to TDC. Therefore, the late injection event has higher possibility of impinging on the piston crown. The sharper decrease towards late combustion phasing is attributed to particle oxidation. Since the particles formed from the late injection event are located close to the spark-plug, that is close to the first burning elements in the cylinder charge, the time for particle oxidation before EVO is longer. As combustion phasing is delayed significantly most of this particles are oxidized and the PM emissions of the three injection strategies converge at CA50 = 80°CA aTDC$_{\text{comp.}}$.

Lastly, it is also important to address the combustion stability and thermal enthalpy flow during the cold fast-idle period. Figure 6-14 shows the CoV and LNV of NIMEP for the three injection strategies. CoV increased monotonically with CA50 in all cases. Comparing the different injection strategies, the **Single** injection re-

sulted in approximately 20% higher CoV. On the other hand the **Double** and **Triple** strategies exhibited similar CoV suggesting that the late ballistic injection had no effect on stabilizing combustion and that the effects identified in Section 6.3 are not additive. The lowest normalized value of NIMEP (LNV_{NIMEP}) is a metric introduced by Hoard and Rehagen [31] to characterize the subjective idle quality. It is defined as the lowest single NIMEP in a data set divided by the average NIMEP. Hoard and Rehagen argued that LNV needs to be higher than 75% for customer acceptability [31]. Similarly to CoV, **Single** injection resulted in worse LNV while the **Double** and **Triple** strategies showed similar trends.

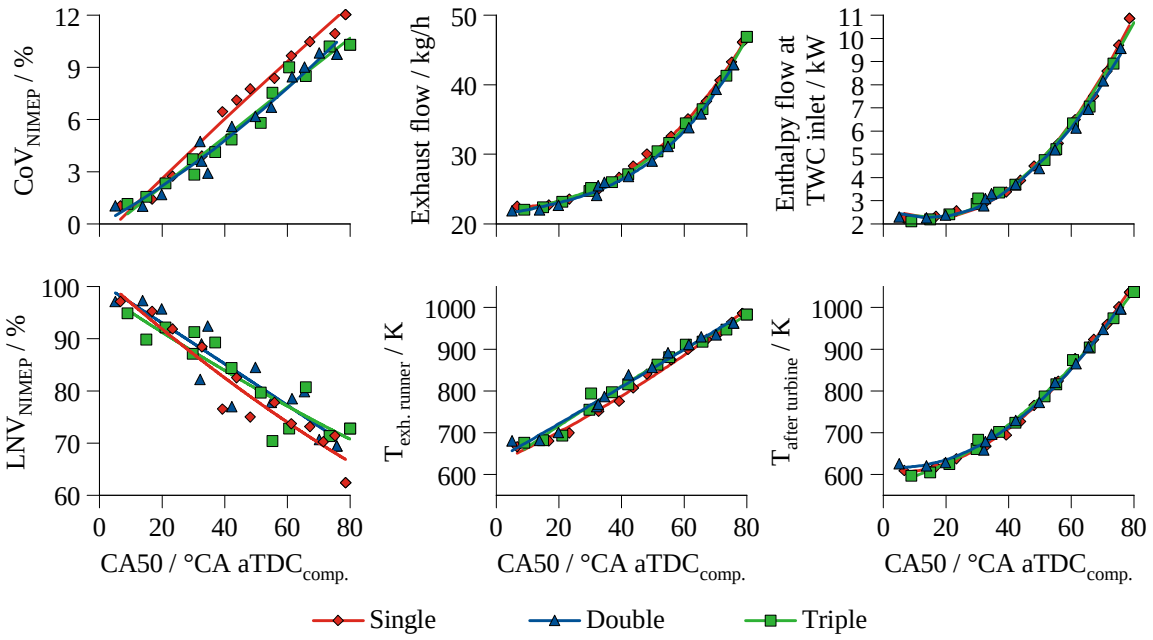

Figure 6-14: Combustion stability and exhaust thermal enthalpy as a function of CA50 for three different injection strategies

The exhaust thermal enthalpy was not influenced by the selection of the injection strategy and appears to be a function of CA50 only. As the combustion phasing is delayed the exhaust mass flow and exhaust gas temperature increase due to the lower conversion efficiency of the engine. As a result the thermal enthalpy flow to after turbine increases proportionally to the square of CA50: $\dot{Q}_{exh} \propto 0.002 \cdot \mathrm{CA50}^2$.

6.5 Valve timing

This section deals with the effects of unconventional valve timing on the engine-out NOx, HC and PM emissions. It has been documented that the combustion phasing has a significant impact on the fast idle HC [7] and PM [35] emissions; however those studies focus on the conventional direction of cam phasing, namely intake advance and exhaust retard. As illustrated in Fig. 6-15, the approach followed in this study is in the opposite direction of cam phasing; that is intake retard and exhaust advance.

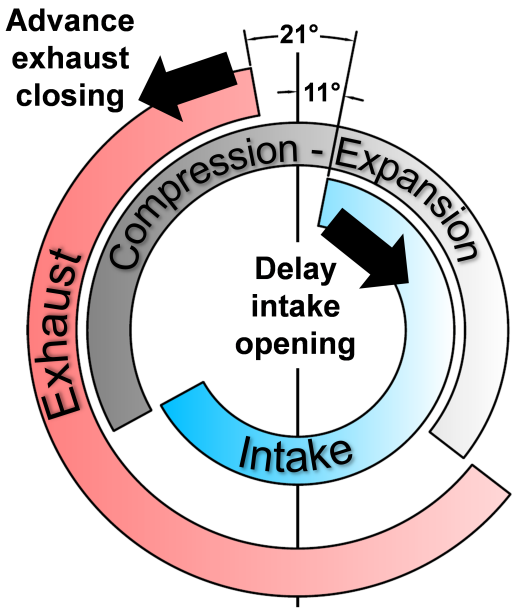

Figure 6-15: Baseline intake and exhaust timings and direction of phasing for the other investigated valve timings

The fast-idle experiments were carried out at the different valve timings summarized in Table 6.7. For each valve timing studied, a combustion phasing sweep was performed to identify the possible trade-offs between combustion stability, TWC feed-gas enthalpy and engine-out emissions. Based on the lessons learned form the results presented in Sections 6.4 and 6.3, the injection strategy selected was the **Double** described in Table 6.6.

	Intake delay	Exhaust advance
Baseline	$\Delta IV = 0°CA$	$\Delta EV = 0°CA$
Early EVC	$\Delta IV = 0°CA$ $\Delta IV = 0°CA$	$\Delta EV = 16°CA$ $\Delta EV = 31°CA$
Symmetric NVO	$\Delta IV = 12°CA$ $\Delta IV = 24°CA$	$\Delta EV = 12°CA$ $\Delta EV = 24°CA$

Table 6.7: Valve setting cases for the cold fast-idle study

The direction of phasing of the valve timing strategies studied result in an increase in residual gas fraction (x_r) due to the truncation of the later part of the exhaust stroke by the early EVC event. In the region of negative valve overlap, the residual gas fraction is only a function of the exhaust advance and independent from the intake timing. The resulting residual gas fractions for the valve settings presented in Table 6.7 are shown in Fig. 6-16.

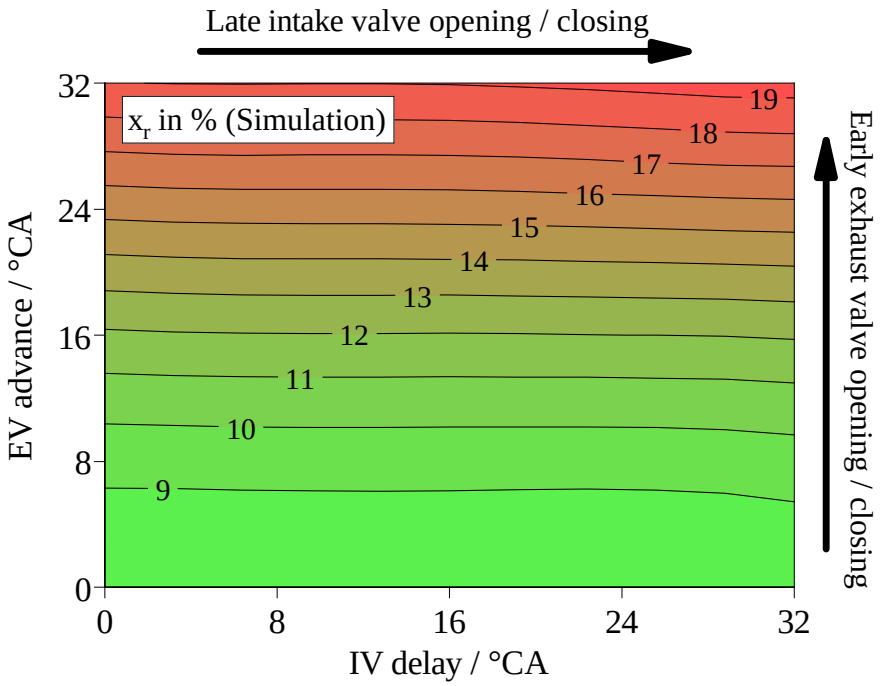

Figure 6-16: Residual gas fraction at cold fast-idle as a function of valve timing

6.5.1 Early EVC

The engine-out emissions performance of the two different levels of exhaust timing advance investigated (16°CA and 31°CA) are presented in Fig. 6-18. NOx emissions show a significant improvement with EVC advance. Early exhaust phasing increases the residual gas fraction. The higher heat capacities of CO_2 and H_2O in comparison to N_2 and O_2, make the internal EGR an effective diluent for reducing the peak temperatures in the combustion chamber and limiting the NO production. The reduction in NOx emissions is more prominent in the early end of the CA50s tested. For CA50 later than 30°CA $aTDC_{comp.}$, the reduction with early EVC is approximately constant. For an EV advance of 16°CA a 35% reduction is observed, while an advance of 31°CA results in 60% NOx reduction compared to the baseline.

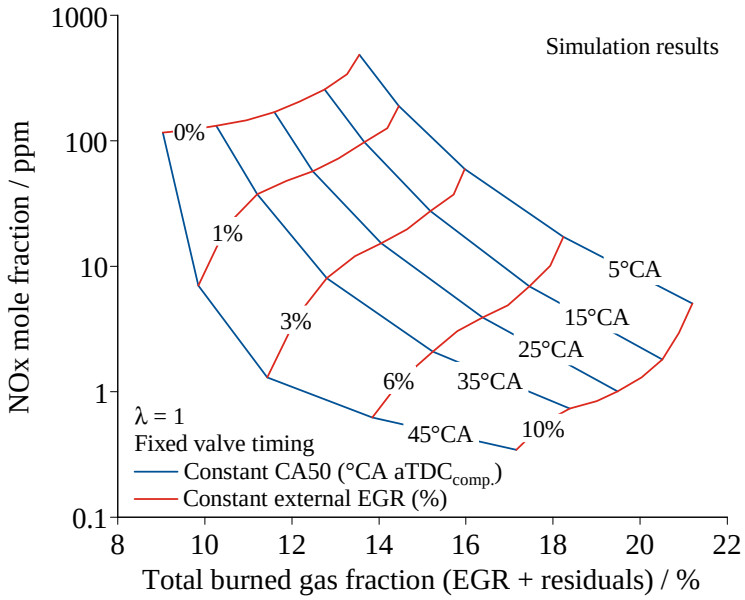

Figure 6-17: Simulated engine-out NOx mole fraction during cold fast-idle for EGR rates and combustion phasing at stoichiometric combustion and fixed valve timing

Fig. 6-17 shows the simulation results of the NOx mole fraction in the exhaust for different combustion phasing and different rates of EGR. The simulations were run with an added external EGR in an effort to separate the effects of total burned

gas fraction from those of combustion phasing. At constant combustion phasing, the change in total burned gas fraction is achieved with the help of external EGR. As expected the higher burned gas fraction results in a reduction of NO production from the lower peak temperatures achieved by the charge dilution. Conversely, at constant external EGR, the delay in combustion phasing results initially in a reduction of peak combustion temperatures and in a reduction of the total burned gas fraction. The latter effect, together with the deteriorated engine efficiency at late combustion (see Fig. 6-12) result in diminishing reduction in NOx as the combustion phasing is further delayed. The trend is ultimately reversed for very late combustion phasing, resulting in higher NOx emissions. The use of early EVC strategies provide an additional degree of freedom to control the total burned gas fraction in the fresh mixture in the same way that the external EGR loop from the example does.

The engine-out HC emissions exhibit a slight improvement for moderate exhaust advance and a significant deterioration for the most advanced exhaust timing. The sources of HC emissions at cold fast-idle are diverse and include crevice storage of fresh mixture, absorption of fuel vapors in the oil layer, flame quenching at the cold cylinder walls and the presence of liquid fuel films [12]. Changes in valve timing are not expected to have a significant impact on the oil layer, flame quenching and liquid fuel mechanism. However, the dilution of the fresh mixture with residual gases reduces the HC mole fraction of the mixture stored in the combustion chamber crevices and can be beneficial for reducing HC emissions. Furthermore, given that a significant share of the HC stored in-between the piston rings returns to the combustion chamber during the later part of the exhaust stroke in the form roll-up vortex formed by the scraping of the boundary-layer gases off the cylinder wall [30], early EVC results in more trapping of this HC rich gases, thus leading to a reduction in HC emissions [21]. On the other hand, the increased residual fraction has some negative effects. First, it reduces the combustion and post-flame temperatures, limiting the oxidation rate of the fuel that managed to escape combustion. Second, it increases the cylinder

pressure during the mixture formation process, which in turn hinders the evaporation of the injected fuel. The combination of these effects results in the trends observed in Fig. 6-18. For moderate exhaust advance the increase in residual gas fraction benefits the crevice mechanism and has no observable impact on the post-combustion temperature as can be inferred from the measured exhaust runner temperature (Fig. 6-19). The sharp increase in x_r from 31°CA exhaust advance, however, reduces the expansion temperature significantly and slows down the post-combustion oxidation of the remaining HC content. Nevertheless, as CA50 is delayed after 50°CA aTDC$_{comp.}$ the HC emissions of both exhaust advance settings start to converge driven by the increase in post-combustion temperature.

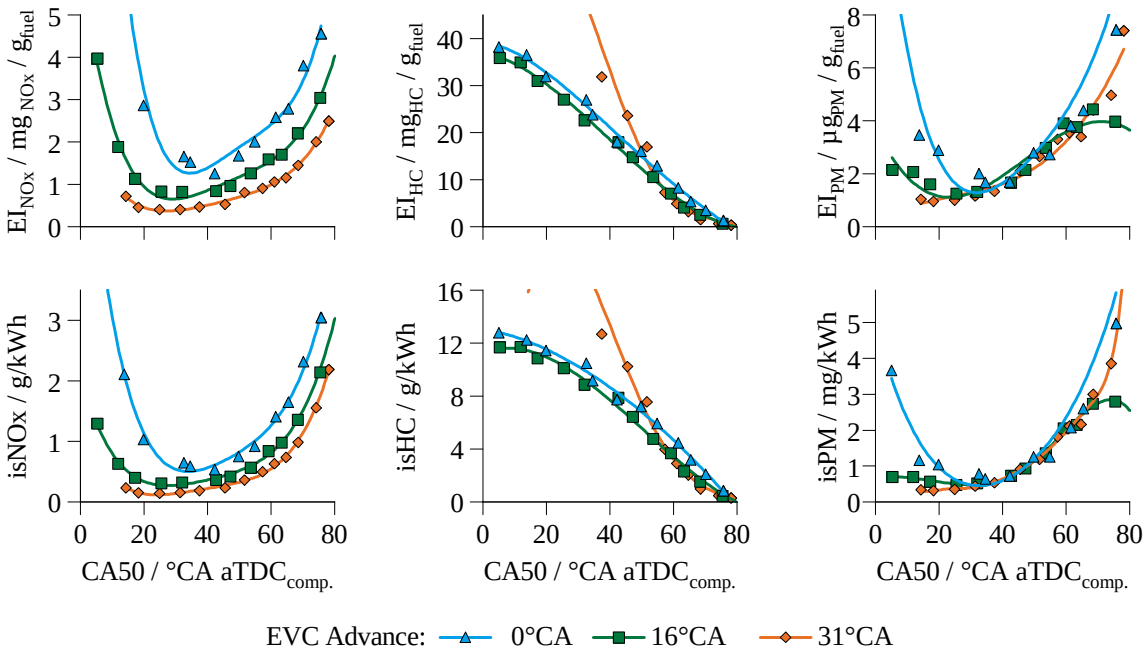

Figure 6-18: Emissions indices and indicated specific emissions of NOx, HC and PM as a function of CA50 for baseline and two early EVC settings

Exhaust advance can impact the PM emissions in a number of ways. First, it reduces the in-cylinder temperatures through charge dilution by internal EGR. Lower temperatures reduce the particle nucleation rate through fuel pyrolysis, while at the same time reducing the oxidation rate of the incipient particles. Furthermore, the

effect exhaust advance on the post-flame oxidation of the HC content can affect the particle growth by surface agglomeration of HC on the formed particles. These competing effects result in the PM trends observed in Fig. 6-18. Particulate emissions show a significant improvement with exhaust advance for CA50 timings earlier than 20°CA aTDC$_{comp.}$. From CA50 in the range of $20-70$°CA aTDC$_{comp.}$, the PM emissions are independent of the valve timing. The latest CA50 point tested suggests an impact of early EVC on particle reduction; however, given the combustion instability at this late spark timing the significance of that point is reduced.

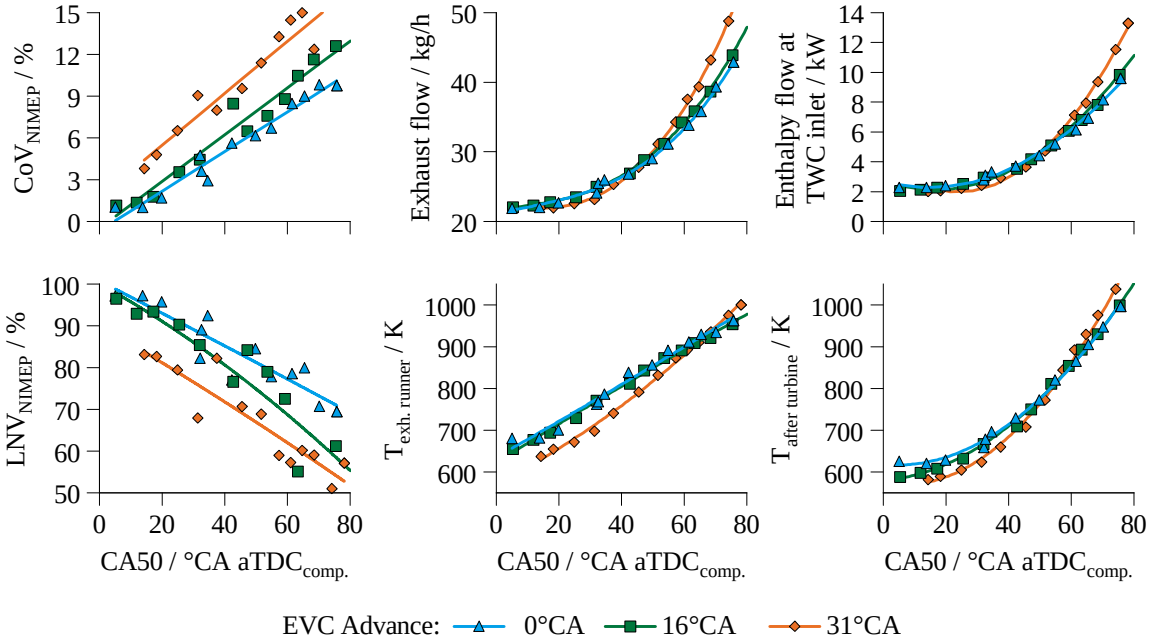

Figure 6-19: Combustion stability and exhaust thermal enthalpy as a function of CA50 for baseline and two early EVC settings

Figure 6-19 shows the combustion stability metrics and the feed gas enthalpy flow to the catalyst. The increase in residual gas fraction from early EVC reduces the flame propagation speed and consequently deteriorates the CoV and LNV of NIMEP. The moderate exhaust advance increases the slope of the CoV trace in 20%, while the most advanced EV results in a similar increase in slope with an additional offset of 3.5% CoV. Regarding the enthalpy flow, moderate exhaust advance has no influence

on the exhaust temperature and mass flow when compared to the baseline. On the other hand, 31°CA exhaust advance results in lower exhaust temperatures for CA50 earlier than 60°CA $aTDC_{comp.}$ and an increase in exhaust mass flow for CA50 later than 50°CA $aTDC_{comp.}$ as a consequence of the losses in GIMEP from early EVO (see Fig. 5-19).

6.5.2 Symmetric NVO

Symmetric NVO is the result from equal exhaust advance and intake delay. As such, the analysis done in Section 6.5.1 for early EVC also applies to the symmetric NVO cases presented in this section. The present discussion focuses on the impact that late intake timing has on the emissions, combustion stability and exhaust enthalpy.

Figure 6-23 presents the engine out emissions performance of the two symmetric NVO cases investigated; EV advance and IV delay of 12°CA and 24°CA respectively. The engine-out NOx trend resemble the results presented in the previous section for EVC advance alone; that is 35% NOx reduction for moderate symmetric NVO and 60% reduction for the larger symmetric NVO. However, in comparison to the early EVC alone strategy, less exhaust advance is necessary; in other words, the same reduction in NOx emissions is achieved with a lower residual gas fraction. As shown in the cycle simulation results in Fig. 6-20, NOx emissions are mainly a function of peak temperature at constant air-fuel ratio. The Zeldovich-Keck mechanism for NO formation [47] tells us that the logarithm of the NO formation rate is proportional to the inverse of the in-cylinder temperature. This effect is clearly shown in Fig. 6-20. Given that the air-fuel equivalence ratio was held constant for all valve timings, the explanation for observing the same NOx reduction with reduced residual gas fraction must be a reduction in peak cylinder temperatures brought alone by the delayed intake timing of the symmetric NVO valve setting.

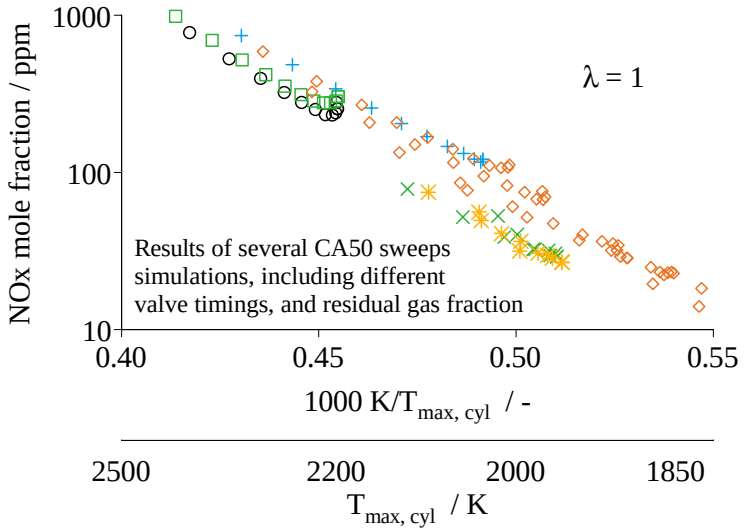

Figure 6-20: Simulated engine-out NOx emissions during cold fast-idle for different operation strategies at stoichiometric combustion

As shown in Fig. 6-21, delayed intake timing reduces the effective compression ratio of the engine due to late intake valve closing. The result is a reduction in charge temperature at the end of compression and consequently a reduction in the peak temperature of combustion. This reduction in temperature compensates for the lower residual gas fraction trapped in comparison to the early EVC strategy, resulting in similar NOx reduction.

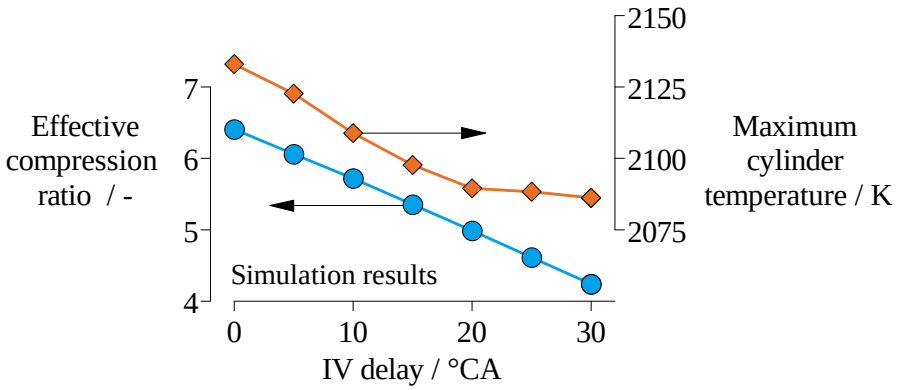

Figure 6-21: Effective compression ratio and modeled cylinder peak temperature as a function of intake valve timing delay during cold fast-idle

Regarding the HC emissions (Fig. 6-23, middle), the moderate symmetric NVO valve setting results in a reduction of HC emissions for combustion phasing with a CA50 later than 20°CA $aTDC_{comp.}$. For the larger NVO setting, the HC emissions deteriorate significantly as it was the case for the early EVC strategy. To understand the differences between the HC emissions behavior of the baseline, early EVC and symmetric NVO, it is worth to take a closer look at the traces of the HC mole fraction.

Fig 6-22 shows the crank-angle resolved HC mole fraction and mass emissions during the exhaust stroke for the three valve timing settings. The HC concentration traces feature two peaks; the first one related to the HC bulk concentration in the burned gases; the second one associated to the roll-up vortex caused by the scraping of the HC-rich boundary-layer formed by the remaining of the crevice HC and those desorbing and evaporating from the cylinder wall [30].

In comparison to the baseline, early EVC results in marginally lower HC emissions, while the symmetric NVO strategy shows a greater improvement in HC emissions than early EVC alone. The cumulative HC mass trace of the case with delayed intake timing (symmetric NVO) exhibits a lower blow-down value, compared to the stock intake timing (baseline and early EVC). The blow-down trend can be explained as follows: Late intake timing reduces the in-cylinder pressure at EVO (due to the lower effective compression ratio), therefore lowering the exhausted mass during blow-down. On the other hand, early exhaust timing lowers the HC concentration through charge dilution with residual gases, while at the same time increasing the exhausted mass during blow-down due to higher cylinder pressures at the advanced EVO. Moreover, advanced exhaust timing results in flow reversal close to the maximum exhaust valve lift. As a result, the exhausted mass is higher towards the end of the exhaust event, and slope of the cumulative HC trace is steeper for the advanced exhaust timing. Nevertheless, the end-of-stroke HC peak concentrations are lower for the symmetric NVO in comparison to early EVC.

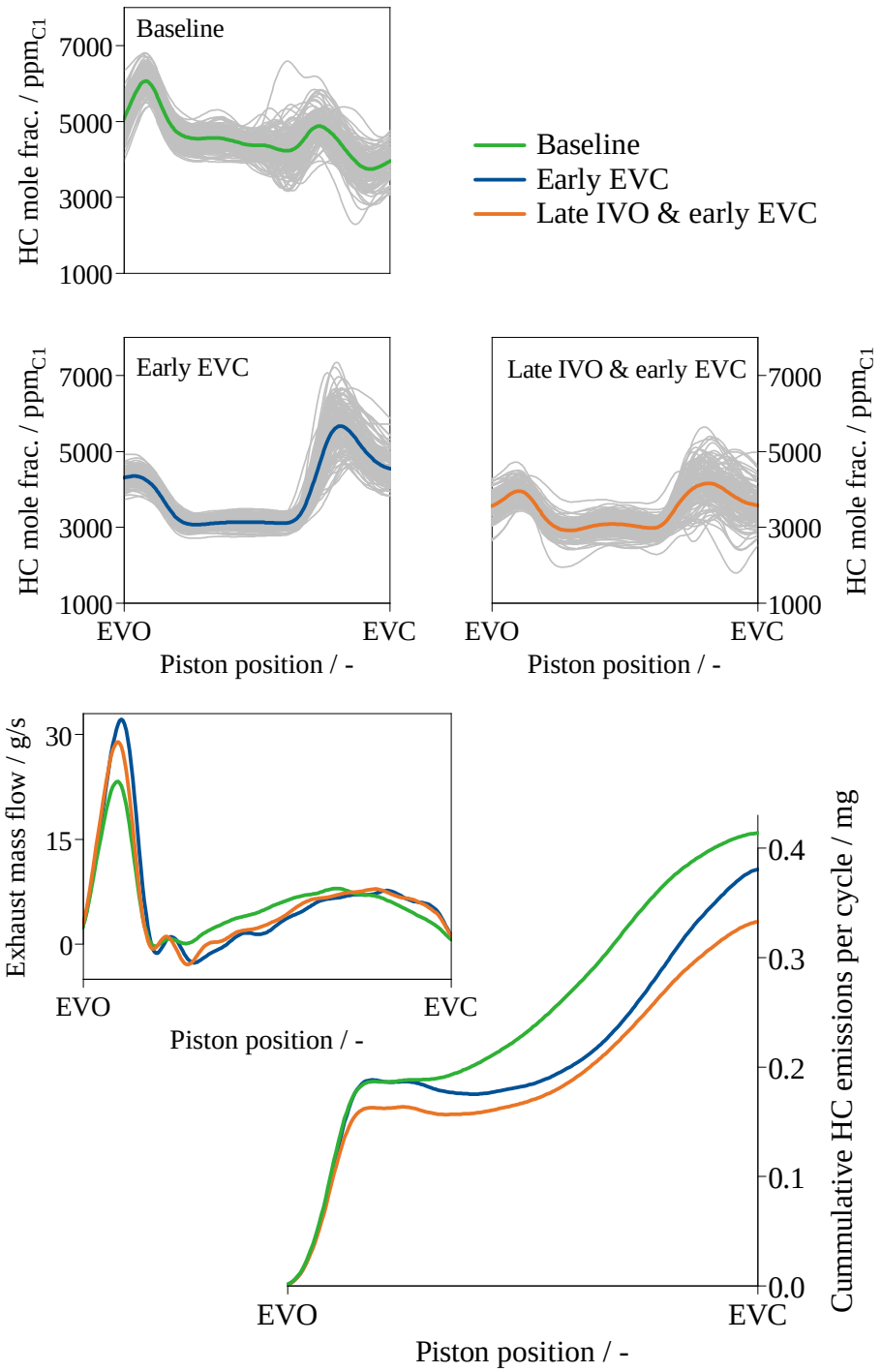

Figure 6-22: Crank angle resolved port-measurements of the HC emissions at cold fast-idle conditions for 3 different valve timings at CA50 $= 40°$CA aTDC$_{comp.}$. Color lines represent the average over 150 cycles

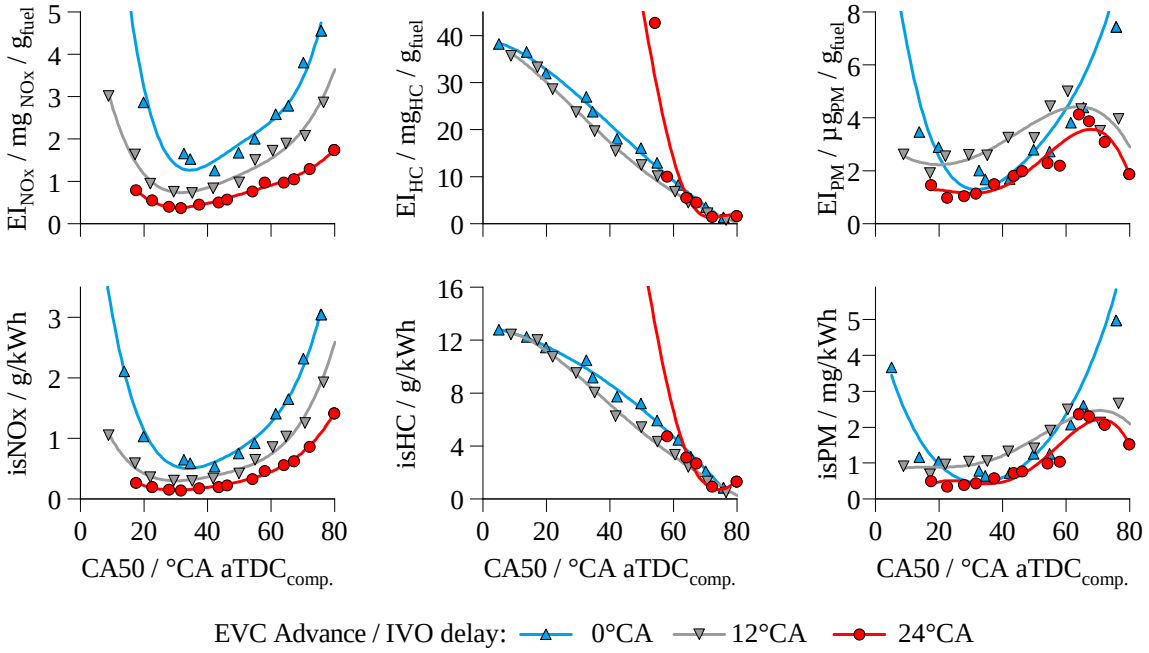

Figure 6-23: Emissions indices and indicated specific emissions of NOx, HC and PM as a function of CA50 for baseline and two symmetric NVO settings

The PM emissions of the two stages of symmetric NVO are shown in the right end of Fig. 6-23. Opposite to what was observed in the early EVC case in the previous section, the use of moderate NVO resulted in higher particulate emissions. Given the complexity of the particle formation and oxidation processes and the competing effects of temperature, it is difficult to determine the source of the observed trends. Nevertheless, by examining the size distribution of the particle spectrum further insight can be gained. Early EVC results in a significant reduction in PN, while simultaneously increasing the particle size. The symmetric NVO strategy shows a slight increase in PN concentration and a minor reduction in particle size compared to the early EVC strategy. Higher residual gas fraction lowers the flame and post-flame temperatures lowering the nucleation and oxidation rates. It is also possible that the lower HC concentrations achieved with early EVC reduce the particle growth through HC agglomeration.

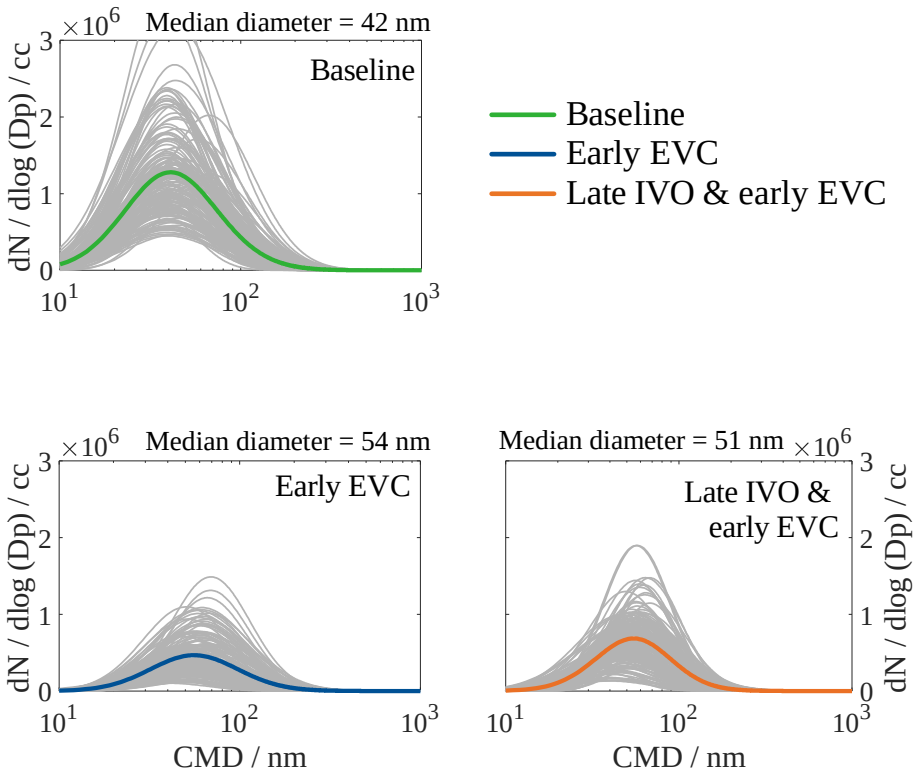

Figure 6-24: Accumulation mode particle spectrum at cold fast-idle conditions for each valve timing CA50 $= 40°$CA aTDC$_{\text{comp.}}$. Measurements were fitted to a lognormal distribution. Color lines represent the average over 150 cycles

Regarding combustion stability and cycle-to-cycle variability, Fig. 6-25 shows that the CoV of NIMEP suffers a 20% deterioration with moderate symmetric NVO and more than doubles with the more aggressive NVO strategy. Similarly, the LNV of NIMEP deteriorates in approximately 10% with moderate symmetric NVO and in approximately 30% with the more aggressive NVO strategy. As it was the case in the early EVC strategies, the moderate symmetric NVO has no impact on the exhaust gas temperature or exhaust mass flow; therefore, the exhaust enthalpy flow versus combustion phasing curve overlaps with the baseline results. On the other hand, the larger symmetric NVO results in a sharp reduction in exhaust temperature and slightly lower exhaust mass flow when compared to the baseline. As CA50 is delayed after 60°CA aTDC$_{\text{comp.}}$ these trends are reversed.

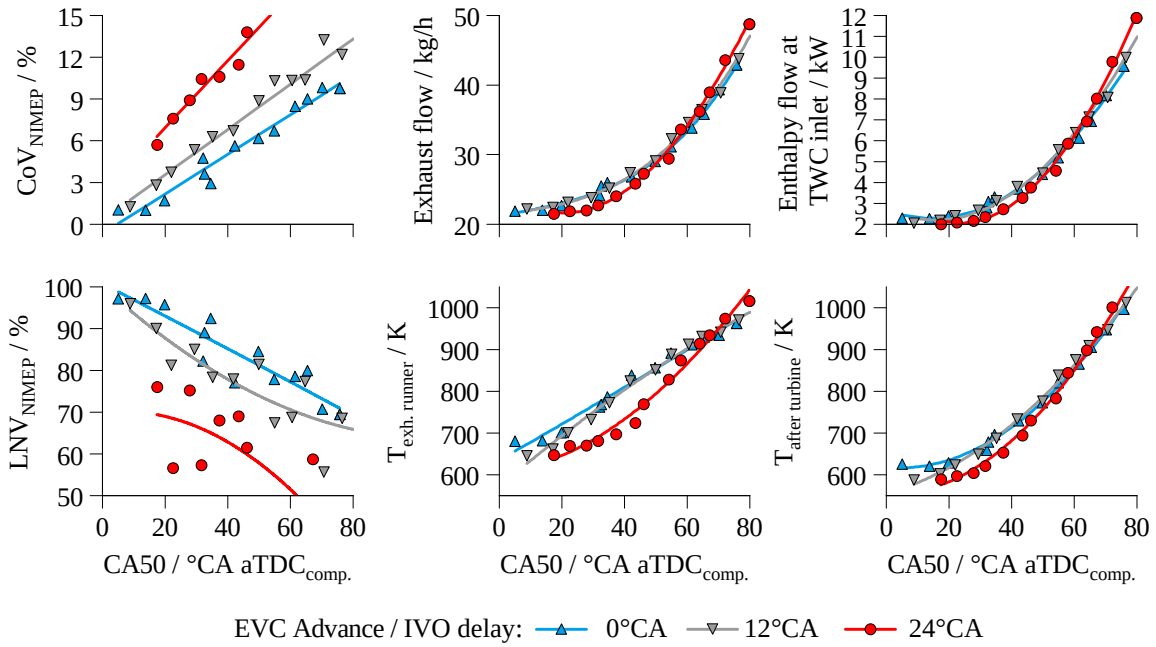

Figure 6-25: Combustion stability and exhaust thermal enthalpy as a function of CA50 for baseline and two symmetric NVO settings

6.6 Findings

The effect of different injection and valve timing strategies on the emissions performance, combustion stability and exhaust thermal enthalpy of a GDI engine during cold fast-idle were studied in detail. The following conclusions are drawn:

- The cold fast-idle period is not constrained by the stoichiometric requirements of normal engine operation given that the three-way catalyst is inactive. The use of lean air-fuel mixture results in a significant reduction of NOx, HC and PM engine-out emissions. However, the applicability of mixture enleanment is limited by combustion stability.

- Depending on the selection of the injection timings, the use of split injection strategies during cold fast-idle can result in the reduction of engine-out emissions while at the same time improving the combustion stability. A 50/50 split strat-

egy, where the first injection event occurs during maximum intake valve lift and the second close to bottom dead center exhibited the best performance. Earlier injection timings may result in interaction between the piston crown and the fuel stray leading to a drastic increase in particulate formation and emissions. The use of a very short injection immediately before spark timing improves the combustion stability but deteriorates significantly the PM emissions.

- The engine-out emissions have a high sensitivity to combustion phasing. Initial retard results in a significant reduction in NOx emissions up CA50 $\approx$ 40°CA $aTDC_{comp.}$. After this point the increase in fuel use from the lower engine efficiency and the reduction of residual gas mass fraction from the hotter exhaust gases reverse the trend leading to an increase in NOx emissions as the combustion phasing is further retarded. HC emissions on the other hand exhibit a monotonic decrease with combustion phasing; as the expansion and exhaust temperatures increase with late spark timing, the post-oxidation rate of HC increases. PM emissions exhibit a similar dependence on CA50 as NOx. PM emissions drop sharply as combustion is initially delayed achieving a minimum between 20 and 40°CA $aTDC_{comp.}$; thereafter, the larger amount of fuel necessary to compensate the decrease in engine efficiency promote the formation of fuel films and increase the PM emissions.

- The thermal enthalpy flow of the feed-gas to TWC increases proportionally to the square of CA50.

- Moderate exhaust valve timing advance is beneficial for engine-out emissions, has no impact on the exhaust enthalpy and deteriorates slightly combustion stability. The observed trends are mainly a result of the higher residual gas fraction of early EVC strategies. More aggressive exhaust timing advance reduces the expansion and exhaust temperatures significantly resulting in an increase in HC emissions.

- The combined use of intake timing delay and exhaust valve advance, dubbed symmetric NVO, exhibits the same emissions trends as early EVC alone. The decreased effective compression ratio from late IVO reduces slightly the peak cylinder temperature and pressure. As a result, similar improvements in NOx and HC can be achieved at lower residual gas fraction, when compared to the early EVC valve settings.

- There are clear tradeoffs present between engine-out emission, combustion stability and exhaust enthalpy flow. To minimize NOx emissions high residual gas fractions are beneficial; however HC emissions and combustion stability can be significantly affected. The reduction of HC emissions and of exhaust enthalpy is favored at very late combustion phasing; however, the emissions of PM and NOx increase and the combustion stability is deteriorated. PM emissions are favored at relatively early combustion phasing CA50 $\approx$ 30°CA aTDC$_{\text{comp.}}$; on the other hand this level of exhaust enthalpy flow would result in a longer light-off time of the catalytic converter, increasing the cumulative emissions of NOx and HC.

Chapter 7

Conclusion

The cold-start phase is responsible for a disproportionate share of the pollutant emissions of internal combustion engines. The purpose of the work presented in this dissertation was to expand the understanding of the mechanisms leading to the production and emission of regulated pollutants (CO, NOx, HC, and PM) during the cold-start phase of light-duty gasoline direct injection engines and to investigate the potential of different operation strategies for their mitigation.

The results indicate that the pollutant formation mechanisms have a strong dependence on the mixture formation process and on the temperature and pressure history during combustion. The strategies with the largest potential for the reduction of pollutant emissions during cold-start are the use of unconventional valve timing featuring a large, symmetric, negative valve overlap and of delayed combustion phasing.

The following sections provide an overview of the experimental approach used for the investigations, present the key contributions of this study and their significance, and propose recommendations for future research in the area of cold-start emissions of gasoline direct injection engines.

7.1 Overview

The experimental research was divided into the two phases of the cold-start period, the engine crank-start and the steady-state fast-idle. The experimental engine results were supplemented by modeling of the processes that were not measurable during the experiments, such as the crank-angle resolved exhaust mass flow rate, the cylinder temperature and the residual gas fraction. The experiments performed can be grouped into three categories.

1. **Cycle-by-cycle experiments:** The first three combustion cycles during the crank-start process were studied under several operation parameters including the amount of fuel injected, injection timing, combustion phasing, fuel pressure, throttle position and engine speed. The cycle-resolved mass emissions of CO, NOx, HC and PM were recorded during the experiments as a function of the aforementioned parameters.

2. **Crank-start experiments:** Complete crank-start experiments were conducted for four different valve settings including the stock valve setting of the engine as a baseline, delayed intake timing, advanced exhaust timing and a combination of late intake with early exhaust timings, dubbed negative valve overlap (NVO). The combustion phasing and the combustion equivalence ratio were kept constant across the different valve settings. The cumulative engine-out pollutant emissions were recorded.

3. **Fast-idle experiments:** The steady-state experiments at 20°C, 2.3 *bar* of NIMEP and an engine speed of 1200 *rpm* were carried out for different engine operating parameters including equivalence ratio, split injection schedules, combustion phasing and valve timing. The output variables of interest were the pollutant emissions flow rates as well at the enthalpy flow of the exhaust gas at the inlet of the three-way catalyst.

7.2 Contributions

This section presents the main contributions of this study in explaining the mechanisms for pollutant formation during cold-start and identifying the emissions reduction potential of different operation strategies in gasoline direct injection engines. The findings are presented separately for the cold crank-start and the fast-idle phases.

7.2.1 Cold crank-start in GDI engines

Compared to all other engine operation regimes, the cold crank-start experiences two extreme conditions: the lowest temperature and lowest engine speed. The evaporation process of the fuel spray is strongly dependent on the combustion chamber surfaces and bulk gas temperatures as well as on the charge turbulence. Consequently, the mixture formation process is negatively impacted during cold crank-start and significant over-fueling is necessary to obtain an ignitable mixture.

The fuel mass required to obtain robust combustion in the 1^{st} cycle during cold crank-start depends on the injection schedule, as it affects the degree of charge stratification. In the case of fuel injection during the intake or early compression strokes, approximately 75 mg of fuel are required; this amounts to circa 2.5 times the amount of fuel necessary to form a stoichiometric air-fuel mixture, that is, if all the fuel would evaporate and fully mix. The fraction of the fuel injected that evaporates and participates in the combustion process is approximately one third of the total injected amount. Of that third of fuel injected being converted to CO_2 and other combustion products, only a quarter, or around 8% of the total injected fuel energy, is converted to work. The remaining part of the energy released from the fuel is lost as heat transfer to the cold cylinder walls or is exhausted in the form of sensible enthalpy. In the case of mixture stratification through late injection, the reduction of spray

interaction with the liner increases the fuel mass participating in combustion.

The use of higher fuel pressure reduces the fuel spray droplet size and increases the turbulence during the injection event. Higher engine speeds result in higher turbulence during the intake and compression processes. Both effects improve the evaporation process, increasing the fraction of fuel being oxidized to CO_2.

The 1^{st} cycle emissions of NOx, HC and PM, exhibit a high sensitivity to the injection and spark timings. The injection timing determines the location and degree of the interaction between the fuel spray and the combustion chamber surfaces. Injection events during the early part of the intake stroke result in spray interaction with the piston crown which deteriorates the fuel evaporation and, in some cases, leads to misfiring of the cycle. As the injection timing is delayed to the mid part of the intake stroke, the interaction of the spray with the intake valve becomes dominant, resulting in a sharp increase in HC emissions. However, the spray/intake valve interaction does not affect the PM emissions and results in a reduction of the peak temperatures, leading to lower NO production. Injection events near bottom dead center result in the best emissions performance. Further delay in the injection timing results in increasing mixture stratification leading to an increased share of unburned HC and a higher formation rate of particulates. NO formation, on the other hand, is reduced as the mixture becomes more stratified.

Spark timing has a direct influence on the temperature history of the combustion process and on the time available for the post-combustion processes to occur before opening of the exhaust valve. Delaying the combustion phasing reduces the time available for particle formation through fuel pyrolysis and affects the formation and oxidation rates through changes in temperature. The end result is a significant reduction of PM emissions with late combustion phasing. Late spark timing reduces the peak cylinder temperatures leading to a reduction in NO formation. On the other hand, HC emissions are insensitive to spark timing for most of the range studied.

For the 2nd and 3rd cycles, the warming of the combustion chamber surfaces and the presence of residual fuel from previous injection events results in a reduction in the over-fueling requirement for robust combustion. The over-fueling required corresponds to 1.7 and 1.5 times the stoichiometric fuel amount, for the 2nd and 3rd cycles respectively. The amount of residual fuel leftover from the 1st cycle that is available to participate in the 2nd cycle mixture formation accounts for approximately 20% of the fuel participating in combustion during the 2nd cycle. Additionally, the warming up of the cylinder liner during the 1st cycle combustion and exhaust processes has a large influence on the evaporation process of the 2nd cycle fuel injection; an increase in roughly 100 J of heat transfer to the walls during the 1st cycle results in an additional 1 mg of fuel evaporating from the injection event in the 2nd cycle.

The emissions trends for the 2nd and 3rd cycles as a function of the injection timing and combustion phasing are very similar to those of the 1st cycle described above. However, the magnitude of the emissions changes significantly as the crank-start goes from the 1st to the 3rd cycle. NOx emissions are reduced as the engine runs up to the speed flare due to a reduction in the work output from the lower intake manifold pressure. The peaks observed in the HC emissions as a function of the start of injection are reduced in magnitude as the engine accelerates; however, the minimum value stays at a comparable level for all three cycles. Lastly, PM emissions are reduced by more than an order of magnitude as the engine accelerates during crank-start.

The use of unconventional valve timing provides an additional degree of freedom for controlling the engine-out emissions during cold crank-start. Delaying the intake valve opening decreases the cylinder pressure in the early part of the intake stroke favoring the flash boiling of volatile fuel species. It also increases the air speed through the intake valve increasing the turbulent intensity , and results in higher temperatures at the end of the intake stroke. Additionally, intake cam retarding delays the closing of the intake valve. As a result, the volumetric efficiency is reduced and less fuel

mass is required for robust combustion. These mechanisms lead to an improved mixture formation process, reducing the formation of fuel films, and therefore of HC and PM emissions. The reduced effective compression ratio also leads to lower peak temperatures during combustion which slow down the formation of NO.

Advancing the exhaust cam phasing increases the amount of burned gases trapped at the end of the exhaust stroke due to the earlier exhaust valve closing. The early exhaust timing strategy has no impact on the mixture formation of the 1st cycle, due to the absence of residuals. From the 2nd cycle on, advance exhaust timing improves the NOx emissions due to the lower temperatures achieved by the dilution of the fresh mixture with the larger amount of burned gases. On the other hand, early exhaust valve closing resulted in worse HC and PM emissions during crank-start. The combined strategy of late intake phasing with early exhaust phasing results in a significant reduction in NOx emissions and in an improvement of HC and PM similar to what was observed by only delaying the intake cam phasing.

7.2.2 Cold fast-idle in GDI engines

The cold fast-idle is a critical period in the engine homologation procedure. The main objective during the 20-second fast-idling period before the first acceleration event in the driving schedule is to provide enough thermal enthalpy to the three-way catalyst to achieve a fast light-off. Simultaneously, due to the catalytic inactivity of the after-treatment system, the engine-out emissions must be minimized and the engine stability must be preserved.

Due to the three-way catalyst inactivity, the cold fast-idle is not constrained to stoichiometric operation. The use of a slightly fuel-lean equivalence ratio ($\lambda = 1.05$) provides an oxidizing environment adequate for the reduction of HC and PM emissions, while it has little impact on the NO formation. The use of an even split injection

strategy, with both injection events occurring in the second half of the intake stroke, resulted in a reduction of the fuel spray penetration and of the fuel films associated with the latter. In comparison to the single injection strategy, the even split injection results in lower HC and PM emissions while simultaneously improving combustion stability.

The exhaust enthalpy flow, engine-out emissions, and combustion stability all exhibit a strong sensitivity to the combustion phasing. As combustion phasing is delayed, the thermodynamic efficiency of the engine decreases, resulting in higher post-combustion temperatures of the burned gases as well as in higher mass flow rates to compensate for the loss in efficiency. The combined effect results in a quadratic dependence of the exhaust enthalpy flow on the combustion phasing as quantified by CA50. The higher exhaust temperatures together with the oxygen availability of the slight lean equivalence ratio result in a monotonically decreasing trend for the HC emissions with later combustion phasing. The NOx and PM emissions, on the other hand, increase as combustion phasing is delayed after a certain point. The larger amounts of fuel required to maintain a constant load at late combustion phasing result in an increase in fuel film formation and in higher cylinder temperatures during combustion leading to higher PM and NO formation respectively.

The use of moderate advance exhaust phasing increases the internal exhaust gas recirculation through early exhaust valve closing. The higher residual gas fraction lowers the peak cylinder temperatures reducing the NO formation rate. Furthermore, the dilution effect of the residual gases reduces the HC concentration of the unburned mixture stored in the crevices resulting in a slight reduction in HC emissions. The PM emissions are not affected by the selection of valve timing for most of the combustion timings studied. The use of moderate, symmetric, negative valve overlap, with its reduced effective compression ratio, results in similar trends as the case of exhaust advance alone, despite the lower residual gas fraction.

7.3 Outlook

The scope of this research was constrained to regulated pollutants, certification relevant temperatures and to a specific engine plant and fuel. The following research ideas could expand the understanding of cold-start emissions of GDI engines.

- Investigation of the impact of alcohol fuels on the low temperature evaporation process and on the chemistry of the pollutant formation in GDI engines.
- Cycle-resolved HC speciation of the exhaust gases during cold-start for studying the effects of incomplete combustion on HC emissions.
- Extension of the cold-start particulate study to the non-regulated sub 23 nm semivolatiles, and the catalyst's effect on their reduction
- Impact of secondary air injection on the trade-off between pollutant emissions, exhaust enthalpy flow, and combustion stability
- Extension of the cold-start testing to temperatures lower than 20°C
- Investigation on the synergies available between hybridized powertrains and the cold-start performance of GDI engines

7.4 Closing remarks

The study of the cold-start phase of internal combustion engines will continue to be a relevant research topic given its impact on the overall emissions. The insights gained from this study on the cold-start behavior of GDI engines and the operation strategies proposed are useful for improving the emissions performance of modern gasoline engines, thus decreasing the societal impact of combustion-based transportation.

Bibliography

[1] Ball, Douglas and Negohosian, Corey and Ross, Deven and Moser, David and McClaughry, Richard. Comparison of Cold Start Calibrations, Vehicle Hardware and Catalyst Architecture of 4-Cylinder Turbocharged Vehicles. *SAE International Journal of Engines*, 6(4):1922–1933, October 2013. ISSN 1946-3944. doi:10.4271/2013-01-2593.

[2] Bertola, A. and Stadler, J. and Hwing, J. and Boland, D. and Berner, H. -J and Philipp, U. Indizierbasierte Analyse von Motor-Start-Stopp-Vorgnge. In *9. Internationales Symposium fr Verbrennungsdiagnostik*, volume 8. - 9. Juni 2010, Kurhaus Baden-Baden, 2010. Conference Proceedings.

[3] Brunt, Michael F.J. and Rai, Harjit and Emtage, Andrew L. The Calculation of Heat Release Energy from Engine Cylinder Pressure Data. In *SAE Technical Paper*, February 1998. doi:10.4271/981052.

[4] Burke, David and Foti, David and Haller, James and Fedor, William J. Fuel Rail Pressure Rise during Cold Start of a Gasoline Direct Injection Engine. In *SAE Technical Paper*, April 2012. doi:10.4271/2012-01-0393.

[5] Cambustion. Cycle-by-cycle AFR measurement of a cold start using an NDIR500 and HFR500. Technical Report Application Note NDIR03v02, Cambustion, 2011. Report.

[6] Castaing, Brigitte M. and Cowart, Jim S. and Cheng, Wai K. Fuel Metering Effects on Hydrocarbon Emissions and Engine Stability During Cranking and Start-up in a Port Fuel Injected Spark Ignition Engine. In *SAE Technical Paper*, October 2000. doi:10.4271/2000-01-2836.

[7] Cedrone, Kevin and Cheng, Wai K. Using Valve Timing and Exhaust Back Pressure to Improve Catalyst Warm-Up Time. In *SAE Technical Paper*, October 2013. doi:10.4271/2013-01-2656.

[8] Cedrone, Kevin and Cheng, Wai K. SI Engine Control in the Cold-Fast-Idle Period for Low HC Emissions and Fast Catalyst Light Off. *SAE International*

Journal of Engines, 7(2):968–976, April 2014. ISSN 1946-3944. doi:10.4271/2014-01-1366.

[9] Cedrone, Kevin David. *Control strategy for hydrocarbon emissions in turbocharged direct injection spark ignition engines during cold-start*. PhD thesis, Massachusetts Institute of Technology, 2013. Dept. of Mechanical Engineering.

[10] Chen, Kuo Chiang and Cheng, Wai K. and Van Doren, Jane M. and Murphy, James P. and Hargus, Matthew D. and McSweeney, Sarah A. Time-Resolved, Speciated Emissions from an SI Engine During Starting and Warm-Up. In *SAE Technical Paper*, October 1996. doi:10.4271/961955.

[11] Cheng, Wai K. and Zhao, Fuquan. Transient Engine Startup and Shutdown Processes. In *Technologies for Near-Zero-Emission Gasoline-Powered Vehicles*, pages 1–29. SAE International, 2006. ISBN 978-0-7680-1461-7.

[12] Cheng, Wai K. and Hamrin, Douglas and Heywood, John B. and Hochgreb, Simone and Min, Kyoungdoug and Norris, Michael. An Overview of Hydrocarbon Emissions Mechanisms in Spark-Ignition Engines. In *SAE Technical Paper*, October 1993. doi:10.4271/932708.

[13] Cheng, Wai K. and Summers, Tim and Collings, Nick. The fast-response flame ionization detector. *Progress in Energy and Combustion Science*, 24(2): 89–124, 1998. ISSN 0360-1285. doi:10.1016/S0360-1285(97)00025-7.

[14] Costanzo, Vincent S. and Heywood, John B. Effect of In-Cylinder Liquid Fuel Films on Engine-Out Unburned Hydrocarbon Emissions for an SI Engine. In *SAE Technical Paper*, September 2012. doi:10.4271/2012-01-1712.

[15] Costanzo, Vincent S. (Vincent Stanley). *Effect of in-cylinder liquid fuel films on engine-out unburned hydrocarbon emissions for SI engines*. PhD thesis, Massachusetts Institute of Technology, 2011. Dept. of Mechanical Engineering.

[16] Cowart, Jim S. Post-Combustion In-Cylinder Vaporization During Cranking and Startup in a Port-FuelInjected Spark Ignition Engine. *Journal of Engineering for Gas Turbines and Power*, 128(2):397–402, August 2005. ISSN 0742-4795. doi:10.1115/1.2061307.

[17] Dagefrde, Helge and Kubach, Heiko and Koch, Thomas and Spicher, Ulrich. Innermotorische Ursachen für Partikelemissionen bei Ottomotoren mit Direkteinspritzung. In Michael Bargende, Hans-Christian Reuss, and Jochen Wiedemann, editors, *14. Internationales Stuttgarter Symposium*, Proceedings, pages 435–459. Springer Fachmedien Wiesbaden, 2014. ISBN 978-3-658-05129-7 978-3-658-05130-3. doi:10.1007/978-3-658-05130-3_30.

[18] Davis, Richard S. and Patterson, Gary J. Cylinder Pressure Data Quality Checks and Procedures to Maximize Data Accuracy. In *SAE Technical Paper*, April 2006. doi:10.4271/2006-01-1346.

[19] Davis, Stacy and Diegel, Susan and Boundy, Ridge and Moore, Sheila. Vehicle Technologies Market Report 2014. Technical report, Oak Ridge National Laboratory, 2015.

[20] Eiglmeier, C. and Pfalzgraf, B. and Helbig, J. and Adam, S. and Grigo, M. and Dornhfer, R. and Eiser, A. Der neue R4 2,0l TFSI SULEV/PZEV-Motor von Audi. In *16. Aachener Kolloquium Fahrzeug- und Motorentechnik*, page 67, 2007. Conference Proceedings.

[21] Eng, James A. The Effect of Spark Retard on Engine-out Hydrocarbon Emissions. In *SAE Technical Paper*, October 2005. doi:10.4271/2005-01-3867.

[22] EPA and NHTSA. Final Rulemaking for 2017-2025 Light-Duty Vehicle Greenhouse Gas Emission Standards and Corporate Average Fuel Economy Standards. Technical Report EPA-420-R-12-901, EPA; NHTSA, 2012.

[23] Faanha, Cristiano and Blumber, Kate and Miller, Josh. Global transportation energy and climate roadmap. Technical report, International Council on Clean Transportation, Washington, DC, 2012.

[24] Fan, Q. and Bian, J. and Lu, H. and Li, L. and Deng, J. Effect of the fuel injection strategy on first-cycle firing and combustion characteristics during cold start in a TSDI gasoline engine. *International Journal of Automotive Technology*, 13(4):523–531, June 2012. ISSN 1229-9138, 1976-3832. doi:10.1007/s12239-012-0050-3.

[25] Fan, Qianwang and Li, Liguang. Transient Characteristics of Cold Start Emissions from a Two-Stage Direct Injection Gasoline Engines Employing the Total Stoichiometric Ratio and Local Rich Mixture Start-up Strategy. In *SAE Technical Paper*, April 2012. doi:10.4271/2012-01-1068.

[26] Gatowski, J. A. and Balles, E. N. and Chun, K. M. and Nelson, F. E. and Ekchian, J. A. and Heywood, J. B. Heat Release Analysis of Engine Pressure Data. SAE Technical Paper 841359, SAE International, Warrendale, PA, October 1984.

[27] Hallgren, Brian E. and Heywood, John B. Effects of Substantial Spark Retard on SI Engine Combustion and Hydrocarbon Emissions. In *SAE Technical Paper*, October 2003. doi:10.4271/2003-01-3237.

[28] Haynes, B.S. and Wagner, H.Gg. Soot formation. *Progress in Energy and Combustion Science*, 7(4):229–273, 1981. doi:10.1016/0360-1285(81)90001-0.

[29] Hedge, Michael and Weber, Phillip and Gingrich, Jess and Alger, Terrence and Khalek, Imad A. Effect of EGR on Particle Emissions from a GDI Engine. *SAE International Journal of Engines*, 4(1):650–666, April 2011. ISSN 1946-3944. doi:10.4271/2011-01-0636.

[30] Heywood, John B. *Internal combustion engine fundamentals*. McGraw-Hill, New York, 1988. ISBN 0-07-028637-X 978-0-07-028637-5 0-07-100499-8 978-0-07-100499-2.

[31] Hoard, John and Rehagen, Larry. Relating Subjective Idle Quality to Engine Combustion. In *SAE Technical Paper*, February 1997. doi:10.4271/970035.

[32] Hoffmann, Guy and Befrui, Bizhan and Berndorfer, Axel and Piock, Walter F. and Varble, Daniel L. Fuel System Pressure Increase for Enhanced Performance of GDi Multi-Hole Injection Systems. *SAE International Journal of Engines*, 7(1):519–527, April 2014. ISSN 1946-3944. doi:10.4271/2014-01-1209.

[33] Jimnez-Cruz, Federico and Laredo, Georgina C. Molecular size evaluation of linear and branched paraffins from the gasoline pool by DFT quantum chemical calculations. *Fuel*, 83(16):2183–2188, November 2004. ISSN 0016-2361. doi:10.1016/j.fuel.2004.06.010.

[34] Kaiser, E. W. and Rothschild, W. G. Storage and Partial Oxidation of Unburned Hydrocarbons in Spark-Ignited Engines - Effect of Compression Ratio and Spark Timing. *Combustion Science and Technology*, 36:171–189, 1984. ISSN 0010-2202. doi:10.1080/00102208408923732.

[35] Ketterer, Justin E. and Cheng, Wai K. On the Nature of Particulate Emissions from DISI Engines at Cold-Fast-Idle. *SAE International Journal of Engines*, 7(2):986–994, April 2014. ISSN 1946-3944. doi:10.4271/2014-01-1368.

[36] Ketterer, Justin Edward. *Soot formation in direct injection spark ignition engines under cold-idle operating conditions*. PhD thesis, Massachusetts Institute of Technology, 2013. Department of Mechanical Engineering.

[37] Kim, Sung-Jun and Hyun, Soungjae and Park, JaeIn. Optimization of Cold Start Operating Conditions in a Stoichiometric GDI Engine with Wall-guided Piston using CFD Analysis. In *SAE Technical Paper*, October 2013. doi:10.4271/2013-01-2650.

[38] Klein, Daniel and Cheng, Wai K. Spark Ignition Engine Hydrocarbon Emissions Behaviors in Stopping and Restarting. In *SAE Technical Paper*, October 2002. doi:10.4271/2002-01-2804.

[39] Knop, Vincent and Essayem, Eddie. Comparison of PFI and DI Operation in a Downsized Gasoline Engine. *SAE International Journal of Engines*, 6(2): 941–952, April 2013. ISSN 1946-3944. doi:10.4271/2013-01-1103.

[40] Koga, Nobuhiko and Miyashita, Shigeki and Takeda, Keiso and Imatake, Nobuo. An Experimental Study on Fuel Behavior During the Cold Start Period of a Direct Injection Spark Ignition Engine. In *SAE Technical Paper*, March 2001. doi:10.4271/2001-01-0969.

[41] Kudo, H. and Hirose, I. and Kihara, T. and Yamakawa, M. and Hitomi, M. MAZDA SKYACTIV-G 2.0l Gasoline Engine. In *20th Aachen Colloquium Automobile and Engine Technology*, page 111, 2011. Conference Proceedings.

[42] Kufferath, Andreas and Samenfink, Wolfgang and Gerhardt, Jrgen. Die neue Emissionsstrategie der Benzin-Direkteinspritzung. *MTZ - Motortechnische Zeitschrift*, 64(11):916–923, November 2003. ISSN 0024-8525, 2192-8843. doi:10.1007/BF03227138.

[43] Kuratle, Rolf H. and Mrki, Balz. Influencing Parameters and Error Sources During Indication on Internal Combustion Engines. In *SAE Technical Paper*, February 1992. doi:10.4271/920233.

[44] Landenfeld, Tilo and Kufferath, Andreas and Gerhardt, Juergen. Gasoline Direct Injection - SULEV Emission Concept. In *SAE Technical Paper*, March 2004. doi:10.4271/2004-01-0041.

[45] Lang, Kevin R. *Reducing cold start hydrocarbon emissions from port fuel injected spark ignition engines with improved management of hardware & controls*. PhD thesis, Massachusetts Institute of Technology, 2006. Dept. of Mechanical Engineering.

[46] Lang, Kevin R. and Cheng, Wai K. and Borland, Mark and Thomas, Chris and Zhao, Fuquan. Effect of Intake Cam Phasing on First Cycle Fuel Delivery and HC Emissions in an SI Engine. In *SAE Technical Paper*, June 2004. doi:10.4271/2004-01-1852.

[47] Lavoie, George A. and Heywood, John B. and Keck, James C. Experimental and Theoretical Study of Nitric Oxide Formation in Internal Combustion Engines. *Combustion Science and Technology*, 1(4):313–326, February 1970. ISSN 0010-2202. doi:10.1080/00102206908952211.

[48] Lee, Dongkun. *Effects of secondary air injection during cold start of SI engines*. PhD thesis, Massachusetts Institute of Technology, 2010. Dept. of Mechanical Engineering.

[49] Lejsek, David and Kulzer, Andr and Kufferath, Andreas and Hohenberg, Gnther and Bagende, Michael. Berechnung des Wandwrmebergangs im Motorhochlauf von Di-Ottomotoren. *MTZ - Motortechnische Zeitschrift*, 71(4):250–257, April 2010. ISSN 0024-8525, 2192-8843. doi:10.1007/BF03225562.

[50] Lejsek, David and Kulzer, Andre and Hohenberg, Gnter and Bargende, Michael. Novel Transient Wall Heat Transfer Approach for the Start-up of SI Engines with Gasoline Direct Injection. *SAE International Journal of Engines*, 3(1):1053–1070, April 2010. ISSN 1946-3944. doi:10.4271/2010-01-1270.

[51] Linstrom, P.J. and Mallard, W.G. *NIST Chemistry WebBook, NIST Standard Reference Database Number 69*. National Institute of Standards and Technology, Gaithersburg MD, 20899, 2016. URL http://webbook.nist.gov.

[52] Malaguti, S. and Cantore, G. and Fontanesi, S. and Lupi, R. and Rosetti, A. CFD Investigation of Wall Wetting in a GDI Engine under Low Temperature Cranking Operations. In *SAE Technical Paper*, April 2009. doi:10.4271/2009-01-0704.

[53] Malaguti, Simone and Fontanesi, Stefano and Severi, Elena. Numerical Analysis of GDI Engine Cold-Start at Low Ambient Temperatures. In *SAE Technical Paper*, October 2010. doi:10.4271/2010-01-2123.

[54] Mock, Peter. European vehicle market statistics, 2015/2016. Technical report, International Council on Clean Transportation, November 2015.

[55] Myung, Cha-Lee and Kim, Juwon and Jang, Wonwook and Jin, Dongyoung and Park, Simsoo and Lee, Jeongmin. Nanoparticle Filtration Characteristics of Advanced Metal Foam Media for a Spark Ignition Direct Injection Engine in Steady Engine Operating Conditions and Vehicle Test Modes. *Energies*, 8(3):1865–1881, March 2015. doi:10.3390/en8031865.

[56] Park, C. and Kim, S. and Kim, H. and Lee, S. and Kim, C. and Moriyoshi, Y. Effect of a split-injection strategy on the performance of stratified lean combustion for a gasoline direct-injection engine. *Proceedings of the Institution of Mechanical Engineers, Part D: Journal of Automobile Engineering*, 225(10):1415–1426, October 2011. ISSN 0954-4070, 2041-2991. doi:10.1177/0954407011406469.

[57] Pritchard, Joseph James. The effects of secondary air injection on particulate matter emissions. Thesis, Massachusetts Institute of Technology, 2014.

[58] Radovanovic, Michael S. Assessing the hydrocarbon emissions in a homogeneous direct injection spark ignited engine. Thesis, Massachusetts Institute of Technology, 2006.

[59] Rai, Harjit S. and Brunt, Michael F.J. and Loader, Colin P. Quantification and Reduction of IMEP Errors Resulting from Pressure Transducer Thermal Shock in an S.I. Engine. In *SAE Technical Paper*, March 1999. doi:10.4271/1999-01-1329.

[60] Rodriguez, J. Felipe and Cheng, Wai K. Effect of Operation Strategy on First Cycle CO, HC, and PM/PN Emissions in a GDI Engine. *SAE International Journal of Engines*, 8(3), April 2015. ISSN 1946-3944. doi:10.4271/2015-01-0887.

[61] Rodriguez, J. Felipe and Cheng, Wai K. Fuel carbon pathway in the first cranking cycle of a gasoline direct injection engine. *International Journal of Engine Research*, October 2015. doi:10.1177/1468087415609852.

[62] Rodriguez, J. Felipe and Cheng, Wai K. Cycle-by-Cycle Analysis of Cold Crank-Start in a GDI Engine. *SAE International Journal of Engines*, 9(2), April 2016. ISSN 1946-3944. doi:10.4271/2016-01-0824.

[63] Rodriguez, J. Felipe and Cheng, Wai K. Reduction of Cold-Start Emissions through Valve Timing in a GDI Engine. *SAE International Journal of Engines*, 9(2), April 2016. ISSN 1946-3944. doi:10.4271/2016-01-0827.

[64] Roth, David and Sisson, James and Gardner, Marty and Wing, Braman. Valve-Event Duration Reduction Through Ultra-Fast Phaser Actuation. In *SAE Technical Paper*, April 2007. doi:10.4271/2007-01-1281.

[65] Santoso, Halim and Cheng, Wai K. Mixture Preparation and Hydrocarbon Emissions Behaviors in the First Cycle of SI Engine Cranking. In *SAE Technical Paper*, October 2002. doi:10.4271/2002-01-2805.

[66] Schmitz, Ingo and Ipp, Wolfgang and Leipertz, Alfred. Flash Boiling Effects on the Development of Gasoline Direct-Injection Engine Sprays. In *SAE Technical Paper*, October 2002. doi:10.4271/2002-01-2661.

[67] Sellnau, M. and Kunz, T. and Sinnamon, J. and Burkhard, J. 2-step Variable Valve Actuation: System Optimization and Integration on an SI Engine. In *SAE Technical Paper*, April 2006. doi:10.4271/2006-01-0040.

[68] Silvis, William M. An Algorithm for Calculating the Air/Fuel Ratio from Exhaust Emissions. In *SAE Technical Paper*, February 1997. doi:10.4271/970514.

[69] Silvis, William M. The Algorithmic Structure of the Air/Fuel Ration Calculation. *Readout HORIBA Technical Reports*, 15:17–24, 1997.

[70] Spindt, R. S. Air-Fuel Ratios from Exhaust Gas Analysis. In *SAE Technical Paper*, February 1965. doi:10.4271/650507.

[71] Tang, Huayin and Burke, Richard and Akehurst, Sam and Brace, Chris and Smith, Les. Behaviours of a GDI Gasoline Engine during Start. In *SAE Technical Paper*, April 2014. doi:10.4271/2014-01-1374.

[72] Tharp, Ronald S. Hydrocarbon emissions in a homogeneous direct-injection spark engine : gasoline and gasohol. Thesis, Massachusetts Institute of Technology, 2008.

[73] Walters, David Mark. *Characterisation of Particulate Matter Emitted from Aviation Gas Turbines and Spray-Guided Direct Injection Gasoline Engines*. PhD thesis, Cardiff University, 2014.

[74] Whitaker, Paul and Kapus, Paul and Ogris, Martin and Hollerer, Peter. Measures to Reduce Particulate Emissions from Gasoline DI engines. *SAE International Journal of Engines*, 4(1):1498–1512, April 2011. ISSN 1946-3944. doi:10.4271/2011-01-1219.

[75] Wiemer, S. and Kubach, H. and Spicher, U. Investigations on the Start-Up Process of a DISI Engine. In *SAE Technical Paper*, October 2007. doi:10.4271/2007-01-4012.

[76] World Meteorological Organization. Guide to Meteorological Instruments and Methods of Observation. *Secretariat of the World Meteorological Organization*, Geneva(8th Edition), 2008. Generic.

[77] Woschni, G. A Universally Applicable Equation for the Instantaneous Heat Transfer Coefficient in the Internal Combustion Engine. In *SAE Technical Paper*, February 1967. doi:10.4271/670931.

[78] Xu, Zheng and Yi, Jianwen and Wooldridge, Steven and Reiche, David and Curtis, Eric W. and Papaioannou, George. Modeling the Cold Start of the Ford 3.5l V6 EcoBoost Engine. *SAE International Journal of Engines*, 2(1):1367–1387, April 2009. ISSN 1946-3944. doi:10.4271/2009-01-1493.

List of Nomenclature

Abbreviations

AFR	Air Fuel Ratio
BDC	Bottom Dead Center
CA	Crank Angle
CLD	Chemiluminescence Detector
DMA	Differential Mobility Analyzer
ECR	Effective Compression Ratio
EVC	Exhaust Valve Closing
EVO	Exhaust Valve Opening
FEF	Fuel Enrichment Factor
FID	Flame Ionization Detector
GDI	Gasoline Direct Injection
HC	Hydrocarbon
IVC	Intake Valve Closing
IVO	Intake Valve Opening
MBT	Maximum Brake Torque
NDIR	Non-Dispersive InfraRed detector
NEDC	New European Driving Cycle

NVO	Negative Valve Overlap
OEM	Original Equipment Manufacturer
PCV	Positive Crankcase Ventilation
PFI	Port Fuel Injection
PM	Particulate Mass
PN	Particulate Number
PW	Pulse Width
ROPR	Rise of Pressure Rate
SoC	Start of Combustion
SOI	Start of Injection
TDC	Top Dead Center
TWC	Three Way Catalyst
VVT	Variable Valve Timing
WGSR	Water-Gas Shift Reaction

Symbols

$\dot{m}_{C,y}$	Carbon mass flow from species y	$[g/s]$
$\dot{m}_{exh}$	Exhaust mass flow	$[g/s]$
η_{vol}	Volumetric efficiency	$[\%]$
$\hat{x}_y$	Mole fraction of species y	$[-]$
λ	Relative air fuel ratio	$[-]$
ρ_{int}	Intake air density	$[kg/m^3]$
$\mathrm{CoV}_{\mathrm{NIMEP}}$	NIMEP covariance	$[\%]$
$\mathrm{LNV}_{\mathrm{NIMEP}}$	Lowest normalized value of NIMEP	$[\%]$
CMD	Count Median Diameter	$[nm]$

$EFME$	Equivalent Fuel Mass Exhausted	$[mg]$
$GIMEP$	Gross Indicated Mean Effective Pressure	$[bar]$
H_{abs}	Absolute Humidity	$[g/kg]$
LHV	Lower Heating Value	$[MJ/kg]$
m_f	Fuel mass	$[mg]$
MAP	Manifold Absolute Pressure	$[bar]$
MFB	Mass Fraction Burned	$[-]$
MW	Molecular Weight	$[g/mol]$
N_{eng}	Engine speed	$[rpm]$
$NIMEP$	Net Indicated Mean Effective Pressure	$[bar]$
P_{sat}	Saturated vapor pressure	$[bar]$
RH	Relative Humidity	$[\%]$
SMD	Sauter Mean Diameter	$[\mu m]$
t_{10-90}	10% to 90% response time	$[ms]$
V_d	Engine displacement volume	$[cc]$
V_{cyl}	Cylinder volume	$[cc]$